Design, fabrication, and characterization of TIP-enhanced Raman spectroscopy probes based on metallic nano-antennas

Damien Eschimese

Université de Lille

Communauté d'Universités et d'Établissements Lille Nord de France

Université de Lille

École doctorale Sciences Pour l'Ingénieur

INSTITUT D'ÉLECTRONIQUE,
DE MICROÉLECTRONIQUE ET DE NANOTECHNOLOGIE
&
HORIBA SCIENTIFIC

THÈSE DE DOCTORAT :

DESIGN, FABRICATION, AND CHARACTERIZATION OF TIP-ENHANCED RAMAN SPECTROSCOPY PROBES BASED ON METALLIC NANO-ANTENNAS

CONCEPTION, FABRICATION ET CARACTÉRISATION DE SONDES DE SPECTROSCOPIE RAMAN À EXALTATION DE POINTE À BASE DE NANO-ANTENNES METALLIQUES

Thèse préparée et soutenue publiquement par **DAMIEN ESCHIMESE**
le **03 MAI 2019**, *pour l'obtention du grade de Docteur de l'***UNIVERSITÉ DE LILLE** *en :*

ÉLECTRONIQUE, MICROÉLECTRONIQUE, NANOÉLECTRONIQUE ET MICRO-ONDES

Membres du jury :

• Thierry MELIN	Directeur de Recherche CNRS, IEMN Villeneuve d'Ascq, **co-directeur**
• Steve ARSCOTT	Directeur de Recherche CNRS, IEMN Villeneuve d'Ascq, **co-directeur**
• Gaëtan LÉVÊQUE	Maître de Conférences, Université de Lille, Villeneuve d'Ascq, **co-encadrant**
• Frédérique DE FORNEL	Directrice de Recherche CNRS, Université de Bourgogne, **rapporteur**
• Cédric AYELA	Chargé de Recherche CNRS, IMS Bordeaux, **rapporteur**
• Anne-Laure BAUDRION	Maître de Conférences, UTT, L2n Troyes, **examinateur**
• Bernard HUMBERT	Professeur Université de Nantes, IMN, **examinateur & président du jury**
• Philippe de BETTIGNIES	Ingénieur, HORIBA Scientific, Villeneuve d'Ascq, **invité**

iemn
Institut d'Electronique, de Microélectronique et de Nanotechnologie
UMR CNRS 8520

HORIBA Scientific

« *New directions in science are launched by new tools much more often than by new concepts. The effect of a concept-driven revolution is to explain old things in new ways. The effect of tool-driven revolution is to discover new things that have to be explained.* »

Freeman Dyson

À mes parents et mon frère,

Je vous dédicace ce travail pour tout l'amour, le soutien, la force et le courage que vous m'avez apportés, et pour avoir toujours cru en moi....

... Objectif atteint !

5, 3, 12, ... 45 !

Résumé

Depuis les années 2000, le développement de la spectroscopie Raman à exaltation de pointe (TERS) a permis l'accès de manière extrêmement localisée aux propriétés structurales et moléculaires à la surface de la matière et à des analyses physico-chimiques combinées. La technologie TERS associe les techniques de microscopie à sonde locale - ici le microscope à force atomique (AFM) - avec le champ proche optique. Elle bénéficie en particulier de la génération, à la surface de métaux nobles, de plasmons de surface à l'origine d'exaltation d'ondes électromagnétiques pouvant être confinées dans un volume sub-longueur d'onde à l'extrémité des sondes AFM-TERS.

Aujourd'hui le principal verrou technologique en TERS est la conception des sondes AFM en termes de reproductibilité à échelle nanométrique, et de fabrication en série. Ce travail de thèse effectué dans le cadre d'une thèse CIFRE (HORIBA Scientific) a eu pour but de concevoir un nouveau type de sonde AFM-TERS excédant aux exigences de performances et de fabrication actuelles.

Pour atteindre cet objectif, une étude de simulation numérique a conduit à proposer une nanostructuration métallique de l'extrémité d'un levier AFM, afin de conduire à une exaltation électromagnétique optimisée. Un procédé de nano- et micro-fabrication a été développé au sein de la plateforme de micro et nanofabrication de l'IEMN, combinant lithographie électronique et optique, évaporation métallique et gravure sur wafers silicium. Il permet la réalisation en série de sondes AFM dont chaque extrémité est composée d'une nano-antenne métallique de taille sub-longueur d'onde, composée d'un nanodisque supportant un nanocône. La méthode de fabrication proposée permet un contrôle des réponses plasmoniques en termes d'amplification du champ et d'accordabilité de la résonance, qui sont la clé des performances en spectroscopie Raman à exaltation de pointe.

Une étude sur l'évaporation inclinée lors du procédé de nano-fabrication développé par lithographie électronique a également été réalisé dans le but de contrôler la forme des nanoparticules – de forme conique à cylindrique avec des parois poreuses – isolées ou en réseaux denses. Les simulations numériques suggèrent que de tels objets peuvent être des candidats potentiels pour le TERS ou le SERS (spectroscopie Raman à exaltation de surface).

Abstract

Since the start of the 2000s the evolution of tip-enhanced Raman spectroscopy (TERS) has enabled the simultaneous measurement of localized structural, molecular, and physicochemical properties. TERS technology combines scanning probe microscopy – atomic force microscopy (AFM) – with near field optical microscopy. The combined technique is referred to as AFM-TERS. The technique harnesses and exploits the generation of surface plasmons on metal surfaces. These plasmons lead to the generation of confined electromagnetic waves in a sub-wavelength volume at the very tip of the AFM-TERS probe.

The main technological challenge today is the design and optimization of an AFM-TERS probe having nanometer-sized dimensions – and the controlled, reproducible batch fabrication of such structures. The objective of the work presented in this PhD thesis was to design, fabricate, and characterize a new type of AFM probe capable of bettering the current state-of-the-art performances. The PhD was carried out in collaboration with HORIBA and funded partly by a French 'CIFRE' grant.

In order to reach these goals, comprehensive numerical modelling led to the design of an optimized metal nanostructuring having maximum electromagnetic exaltation – placed at the extremity of a silicon-based AFM cantilever. A new combined micro and nano fabrication process was developed to achieve this – to be performed using the existing equipment found in the IEMN cleanroom. The process encompasses techniques such as masking using electron beam (Ebeam) lithography and UV photolithography, thermal evaporation of metals and 'lift-off' techniques, and highly-controlled dry etching of small silicon mesas structures and deep etching for MEMS cantilever releasing. The process enables the batch-fabrication manufacture of AFM-TERS probes containing matter on the millimeter scale (the silicon probe support), the micrometer scale (the silicon cantilever), and the nanometer scale (the combined metallic disk and cone having sub-wavelength dimensions). This method allows nanostructuring on the optical/plasmonic behavior of TERS probes, the key factor which will lead to higher performance in TERS.

Finally, a further study concerning the inclined evaporation of metallic nanostructures via an Ebeam-derived lithographic shadow mask was performed in order to control the size and shape of the nanostructuring. The study proved this approach to be feasible. Furthermore, numerical modelling of such structures suggests that they are potential original candidates for both TERS and SERS (surface-enhanced Raman spectroscopy).

Acknowledgements

I would like to express my sincere gratitude to my supervisors Thierry MELIN [1] and Steve ARSCOTT [1], as well as my advisor Gaëtan LÉVÊQUE [1], for their continuous support during my Ph.D study and related research, for their patience, motivation, and immense knowledge. Their guidance helped me during the research period of the Ph.D. and for the writing of this thesis. I could not have imagined having a better mentors for my Ph.D study.

Besides them, I would like to thank the rest of my thesis committee: Philippe De BETTIGNIES [2], Joachim SCHREIBER [2], Marc CHAIGNEAU [2], for their insightful comments and encouragement, but also for the hard questions which inspired me to widen my research from various perspectives.

My sincere thanks also goes to Patrick HSIA [2], François VAURETTE [1], Dominique DERESMES [1], Dmitri YAREKHA [1], Pascal TILMANT [1], Ophélie LANCRY [2], Catalina DAVID [2], Djamila HOURLIER [1], David TROADEC [1], and Isabelle ROCH-JEUNE [1] for their invaluable technical help during the course of the Ph.D. Without their precious support it would not have been possible to conduct the research. I am also grateful to Céline Ha and Oliver KERIVEL for their great help as being my interns for several months of my thesis.

I thank my fellow labmates, Nathali FRANCHINA VERGEL, Louis THOMAS and Nemanja PERIC for their stimulating discussions, and for all the fun we have had in the last four years!

Last but not the least, I would like to thank my family: my parents and my brother for their loving support throughout my scientific studies and my life in general, as well as my beloved girlfriend who have been there for me during both the good and less good periods for the last 5 years, and decided to follow me to Singapore for the next page of my scientific career and in our life together...

1. Institut d' Électronique, de Microélectronique et de Nanotechnologie (IEMN), Université de Lille, CNRS UMR 8520, Avenue Poincaré CS 60069, 59652 Villeneuve d'Ascq Cedex, France.

2. HORIBA France SAS, HORIBA Europe Research Center, Avenue de la Vauve, Passage Jobin Yvon, CS 45002, 91120 Palaiseau, France.

Contents

Introduction

Going beyond the diffraction limit of the light has been for many decades one of the main challenges to investigate the so-called 'nano-world'. New tools from brilliant scientists such as Gerd. Binnig and Heinrich Rohrer have given birth to the development of different instruments which give access to materials' properties at the nanometric scale. Other researchers have been working on chemical aspects using the interaction that exists between light and matter such as Raman scattering, which tells us about the vibrational properties of molecules. Here, we will see how the combination of the Scanning Probe Microscopy with the near-field optics allows the extremely localized investigation of Raman scattering from molecules with a sub-wavelength resolution. This technique is called Tip Enhancement Raman Spectroscopy (TERS) and at the time of writing mostly involves the use of an Atomic Force Microscope (AFM) equipped with a metallized probe (usually silver and gold), called AFM-TERS probes. This technique simultaneously performs topographical and chemical imaging with high lateral resolution via scanning the probe over the sample surface. By using surface plasmons – a resonant collective electron oscillation at the metallic surfaces that compose the probes – one creates an enhanced electromagnetic near-field that enhances the surrounding electromagnetic far-field. This near-field is confined at the vicinity of the probe apex into a volume of the order of a few to few tens of nm^2, which forms the nano-source required for Raman nano-spectroscopy. The Raman enhancement factor (EF) mostly depends on the structural quality of the TERS probes themselves, and more particularly the metallic apex size and shape which partly determine the plasmon frequency, from which the excitation laser frequency must be as close as possible. Today, the main challenge in TERS is centered around the EF optimization which, for some methods, uses a 'machining process' to create an isolated and single optical nano-antenna that forms the AFM-TERS probe apex. In this context, the main problem that limits TERS experiments is related to the fabrication process, which needs to fulfill simultaneously challenging requirements like plasmonic control of the localized near-field at the apex, high reproducibility and mass production compatibility.

This thesis was supported by a CIFRE (*Conventions Industrielles de Formation par la REcherche*) grant and undertaken in the context of a collaboration between HORIBA scientific and the *Institut d'Électronique, de Microélectronique et de Nanotechnologie* (IEMN). HORIBA Scientific is the world leader in Raman spectroscopy, with a long history in this technique and has pioneered systems for Raman spectroscopy, designing and manufacturing them for over four decades. From 2006, Horiba started developing the optomechanical instrumentation that couples an AFM with a Raman spectrometer. Today, Horiba commercializes TERS proven systems for scientific institutes around the world. IEMN is an internationally-recognized research laboratory whose design, micro and nanofabrication, and characterization equipment are at the best European and world levels. Research at IEMN covers a wide range from materials physics and nanostructures to telecommunications systems and acoustic and microwave instrumentation.

To respond to the challenge concerning the fabrication of AFM-TERS probes, a bibliographic study combined with numerical calculations have driven us to propose a new type of MEMS-based probes which incorporate a single metallic nanoparticle at their extremity, called optical nano-antenna. The probes are fabricated within the IEMN micro- nanofabrication cleanroom – using several techniques such as electron beam and thermal evaporation – on the basis of lithographically-patterned metallic nanostructure either on glass substrates or on silicon for the TERS probe. The studies around optical nano-antennas have driven us to design an optical characterization bench to measure the scattering spectrum of isolated nano-objects. Once coupled with an AFM, the final aim of the experimental set-up is to characterize any kind of AFM-TERS probes to better understand differences between entirely metalized rough tips and isolated metallic nanostructures. On silicon wafers, the integration of our designed nanostructures at the extremity of silicon cantilevers has been performed using several steps of lithography and silicon etching. The whole fabrication process developed here constitutes the beginning of the manufacturing of AFM-TERS promising high reproducibility, plasmonic tunability control, and mass production. Moreover, the investigation of tilted metallic evaporation during the lithographically-patterning conception has given us access to an entire family of nanostructures with a precise control of shape. Optical properties of such original structures, isolated or into a dense and perfectly organized array, suggest their application in enhanced Raman spectroscopy (Tip-ERS or Surface-ERS).

In this thesis, I will recall in the first chapters the basics concerning the nano-optics domain (chapter 1) and Raman scattering (chapter 2). In the first chapter, we will see that the barrier imposed by the diffraction limit of the light has led scientist

to developed new techniques requiring sharp tips to collect or create electromagnetic near-field. The notion of surface plasmon will also be explained to see how the electromagnetic enhancement may be controlled by the optical and structural properties of the materials involved.

In the second chapter, I will address the basics of Raman scattering, and describe the instrumentation for standard Raman spectroscopy, co-localized AFM-Raman microscopy, and TERS. Special care will be taken to the description of the fabrication of TERS probes together with several optimization methods reported from the literature.

Chapter 3 will focus on the tools that I used or developed in the frame of the thesis, including: (i) a numerical model from finite element method for the design and study of the plasmonic response according to the size, shape and environment properties of the metal nanosystem, (ii) an experimental set-up allowing the detection and the study of single and isolated nanostructures fabricated on glass substrate, and commercial AFM-TERS probe. The modelling and experimental results on the different types of nano-emitters will suggest in chapter 4 the elaboration of the new kind of TERS probes. Again, I used numerical modelling to optimize the enhancement response of isolated nano-antenna, giving the specification from the upstream micro- and nanofabrication processes that I developed. The final result of probes will be tested in real TERS experimentation conditions on reference samples as graphene oxide and carbon nanotubes.

Finally, chapter 5 will show how I have obtained other nanostructures with controllable shape by tilted evaporation during the developed lithographically-patterning process, including the fabrication and the study of isolated nano-object and dense nanostructured array.

Chapter 1

Near-Field optics

1.1 Introduction

1.1.1 Resolution in optical microscopy

Humans eyes are sensitive only to a tiny part of the electromagnetic (EM) spectrum with wavelengths ranging from 400 nm to 750 nm ('visible light'). Other wavelengths can be accessible only through specific optical equipment. For a physicist, an optical wave contains rich information about the absorption and emission properties of atoms and molecules. Having relatively low energy, an optical photon provides, for instance, a non-destructive tool to investigate biological processes and materials science. Over the years, conventional optical tools have been developed to meet the needs of laboratories regarding their versatility, ease of operation under ambient conditions, and compatibility with *in vivo* experiments.

Like most people who have already looked into a microscope, we are impressed about seeing the fine details of any object using magnifying lenses. Unfortunately, we also come up against the limits of magnification since we always want to see more and more closely. Due to the wave nature of the light, optical devices such as a telescope, camera or microscope have a limited resolution, defined as the minimum distance r for which two points of an object can be distinguished from each other. This limit is due to the diffraction phenomenon and can be estimated from Abbe and Rayleigh criteria. The difference between the two criteria is based on the different way used either by Abbe [1] or Rayleigh [2] to define how to distinguish two points of an object. Here, what we need to keep in mind is that the diffraction limit criterion r is around:

$$r \simeq 0.5 \frac{\lambda}{NA} \tag{1.1}$$

with n the index of refraction of the surrounding medium, NA $(= n\sin(\theta))$ the numerical aperture and θ the collection angle. In practice, r can be approximated for the moment at $\lambda/2$. For Rayleigh convention, two points are not distinguishable if the intensity at the 'overlap intersection' (red dot) must be at least 26% lower than the maximum (I_{max}).

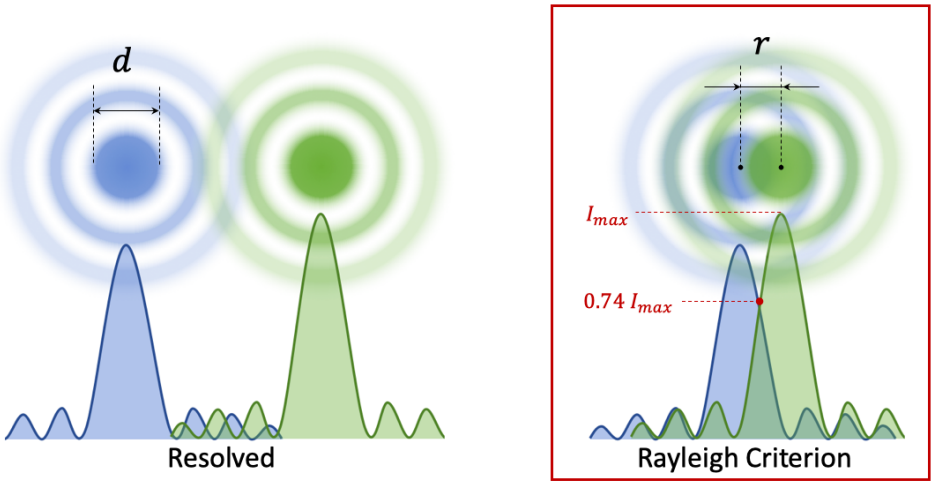

FIGURE 1.1 – Illustration of the Airy pattern from two successive points, separated enough to be resolved until it reaches the Rayleigh criterion, minimum distance between the center of Airy disks.

However, a tiny object can be indirectly observed by the far-field that it can emit under specific conditions (see localized plasmon in paragraph § 1.4 for example) even if details are not large enough to be observed with a standard far-field illumination, i.e. a radiative optical wave propagating into the entire space. It can exist nevertheless some surface information relative to these details that cannot reach the objective – or every kind of far-field collector – but stays at the vicinity of the object. In other words, optical propagation can be compared to a low-pass filter and cuts out fine surface details. This comment suggests a first definition for the near-field. This field is not only the region where the far-field approximation is not valid anymore; it is also the region of the so-called evanescent EM waves which contribute significantly to the global field. In an article from 1928, Synge suggested a method to obtain optical images beyond the diffraction limit with a simple idea based on a sub-wavelength aperture in an opaque screen [3]. Under far-field illumination, evanescent waves can appear at the aperture to form a source spot that can be brought close to the sample and laterally moved along the surface for scanning. By recording any transmitted or reflected light, it may be possible to produce an image with a resolution below this diffraction limit of the light, called super-resolution microscopy.

We will see that instead of a sub-wavelength aperture, a very sharp tip may be able to investigate samples by keeping contact or a certain distance between its extremity, called apex, and the sample while scanning surfaces, analog to a blind person that reads a braille book with his fingers.

1.1.2 Scanning probe microscope

For many decades in science, we have been talking about the visualization, study, and control of individual atoms, molecules, or nanostructures. Unfortunately, conventional experimental studies are typically performed on large groups of particles. Indeed, any signal containing precious information from single particles is many orders of magnitude weaker than groups of particles and is often in the same range of the noise-signal from sources or detectors implemented in the measurement. Nevertheless, over the past three decades, scientists have made significant progress in the study of individual nanoparticles, in particular with the development of Scanning Probe Microscopy (SPM) techniques. From the first micro/nanofabrication techniques, it became possible to create such sharp tip ending with apex dimensions well below than visible wavelengths, typically a few tens of nanometers, which allows interacting with very small areas of samples, from a few to hundreds of nm^2, where free propagating light cannot.

Historically, Russell Young was the first to demonstrate in 1972 that an electrical current can be measured between the sample and a sharp tip to allowed surface imaging [4], performing a lateral et vertical resolution respectively around 400 nm and 3 nm. In 1981, G. Binnig et al. from the IBM research labs invented the first scanning tunneling microscope (STM) where the basic concept is the detection of a quantum tunneling current between a metallic tip and a conductive sample surface [5]. They have obtained topographical information with a spatial resolution around a few angstroms. With such precision, this team obtained first an image of silicon reconstruction with atomic resolution in 1983 [6], and then the Physics Nobel Prize "for their design of the scanning tunneling microscope" in 1986 for reaching and horizontal and vertical resolution respectively about 2 and 0.1 Å.

Such a breakthrough in science comes with expensive equipment and severe environment conditions (extremely clean surface and high vacuum) which restraints the application variability and the access to this technique. Moreover, since the probe is a tunneling current, STM works only on conductive samples. The same

year, G. Binning and C. F. Quate proposed a solution to address the surface by mechanical properties which may operate on any kind of sample. They developed a new method based on the motion measurement of a cantilever with a tiny mass on a measurable distance (10^{-4}Å), which is sensitive to forces as small as 10^{-18} N [7]. Called atomic force microscopic (AFM), the sensitivity of this technique comes from the inter-atomic forces regime between single atoms as well as EM forces, using conductor or insulators probes/samples under ambient conditions.

Since then, individual atoms and molecules have been detected and manipulated using STM [8] or AFM [9]. A lock-in amplifier (LIA) extracts a signal at a given frequency and phase from a noisy environment. Thus, a frequency modulated analysis allows a very sensitive reading and at least one LIA is integrated inside AFM electronics. Three main types of feedback loop mechanisms are used to keep the tip in contact with the surface, i.e.: tunneling current (STM), shear force (or normal force) involving quartz tuning fork, and optical deviation of cantilevers in contact/tapping mode AFM – illustrated respectively in Figure 1.2.a, b, and c.

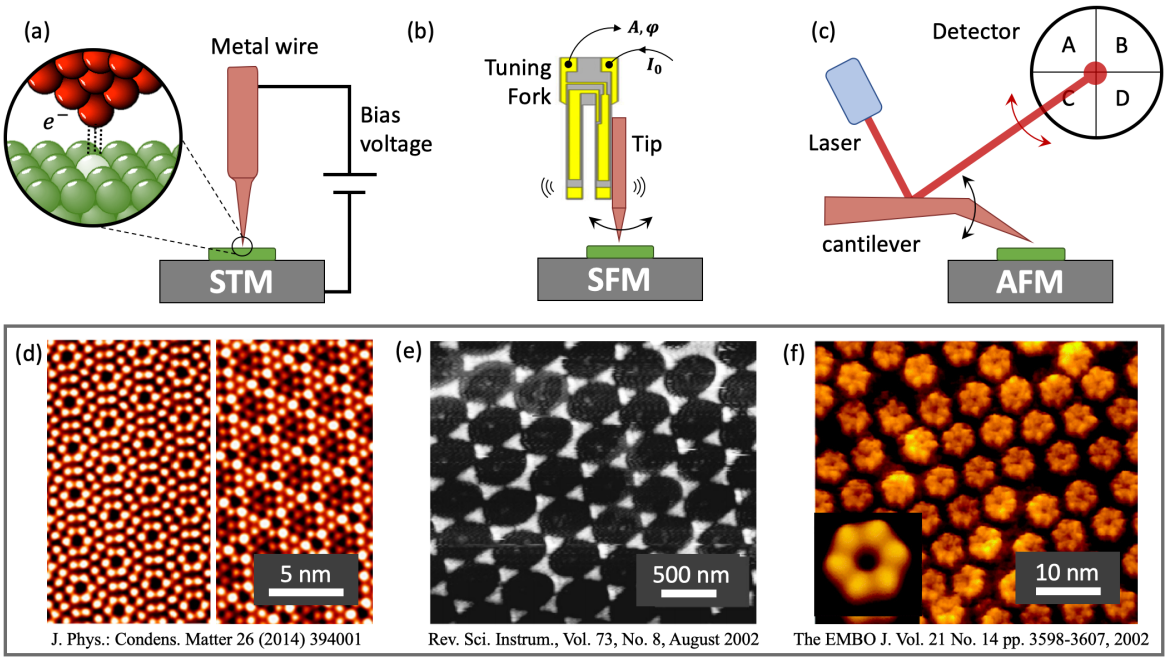

FIGURE 1.2 – Schematic illustrations of SPM feedback mechanisms used in TERS: (a) STM, (b) Shear-force, and (c) AFM feedback mechanisms. (d) STM images of Si (111)-7×7surface. (e) Shear-force imaging of Al islands on a SiO_2 surface. (f) High-resolution liquid cell AFM image of proteins connexin 26.

STM can work under two modes: constant height and constant current. In the first configuration, the tip remains at a constant height via piezoelectric motors, and

the signal is based on the difference in the detected tunneling current. The piezo-actuators are off which allows a faster scan. Its main drawback is that if the tip encounters an obstacle, it will surely be damaged. In the second case, the current is set as a set-point and the tip/sample distance will be regulated to keep it constant. The change in height allows imaging the topography of the sample. The very high vertical sensitivity of this technique is due to the tunnel current which varies exponentially with the tip-surface distance. The impressive lateral resolution is due to the fact that only the last atom at the extremity of the tip that is involved in the tunnel effect. Haiming Guo et al. showed atomically resolved images of Si(111)-7×7 surfaces using STM where the bright protrusions correspond to the Si surface adatoms dangling bonds – immobilized atoms that lie on a crystal surface assimilated to the opposite of surface vacancies on resulting SPM images – [10]. Depending on the sample bias voltage, they were able to image atoms arrangement of the silicon surface through imaging of either empty states or occupied states (see Fig. 1.2.d). The application in biology requires the immersion of the sample and thus the probe in aqueous solution. One of the valuable feedbacks used in the case to investigate both conductive and non-conductive samples is based on shear-forces – unaligned forces pushing in the opposite direction – existing between the sample and a probe attached on piezoelectric quartz tuning-fork (TF). Here, a voltage is introduced into specifically designed electrical-contacts – patterned onto the TF prongs – and excites mechanical oscillation of the attached tip parallel to the sample surface (see Fig. 1.2.b). This technique uses the frequency response of this TF during the apex-sample interactions, which can produce a resonance shift in the oscillations amplitude and phase. Usually, the sample topography is imaged since these oscillations are maintaining a suitable set-point value by the feedback system. For instance, A. Kramer et al. [11] successfully performed topographic imaging with shear-force distance control to investigate small hexagonal patterned Al islands on a glass substrate (see Fig. 1.2.e). Since the oscillations of the tip are parallel to the sample surface, the lateral resolution is naturally less impressive than the STM (from a few to tens of nanometers). We can note that the TF (as presented in Figure 1.2.b) can be tilted at 90° for its arms oscillate perpendicular to the sample surface. If a tip (fabricated from electrochemically etched wire for example) is attached to one of the arms extremities, the tip will undergo vertical displacement instead of horizontal, called normal-force imaging, providing better lateral resolution.

AFM based on optical beam deflection is convenient for experiments in atmospheric environments. Its feedback mechanism consists of a tip at the end of a cantilever to form the probe. A laser beam is reflected backward from a cantilever to

a position-sensitive photo-diode in order to detect its movement. With piezoelectric motors piloting either the probe or the sample holder, the tip approaches the substrate and undergoes intermolecular attraction or repulsion depending on distance [12], causing the cantilever to move towards/away from the surface. Then, the laser beam deflects off and the photo-detector registers the position change (see Fig. 1.2.c). AFM then uses a feedback loop system to maintain a constant force of interaction to generate imaging. For topography mapping, two main modes can be exploited: contact or tapping mode. While scanning, the former brings the tip directly in contact with the surface of the sample. Using the photo-diode signal, the z-axis of the piezoelectric motor is tuned to maintain a constant deflection at different locations, which provides the topography image. This method nevertheless degrades the apex of the tip during use. Tapping mode is a semi-contact mode where the cantilever beam is led by piezoelectric materials to oscillate around its resonance frequency above the sample surface at a convenient distance. The cantilever oscillation generates laser spot oscillation on the photo-diode used as the feedback signal. To maintain a constant oscillation amplitude, the cantilever (or the sample) is moved up and down and this movement is used to reconstruct the surface profile of the sample. Since this technique does not require a conductive sample, it can be used to probe any kind of sample, such as semiconductor materials or biological samples. For example, Daniel J. Müller et al. [13] used AFM for imaging biological samples such as the human communication channel protein connexin 26 in a dense array (see Fig. 1.2.f).

Electrostatic and magnetostatic forces can also be recorded between the sample and the SPM probe to form other techniques called Electrostatic Force Microscopy (EFM), Magnetic Force Microscopy (MFM), Kelvin Probe Force Microscopy (KPFM), Piezoelectric Force Microscopy (PFM), etc.

1.2 Scanning Near-Field Optical Microscopy

From Abbe's or Rayleigh's criteria, the resolving ability of standard optical microscopes is restricted by the light diffraction limit which is about some hundreds of nanometers. However, reducing the size of the light-collector (or scatterer) and moving it into the near-field (also called evanescent waves) makes possible to overcome this limit, localized only a few angstroms to a few nanometers from the sample surface. Scanning probe microscopy combined with optical microscopy leads to the so-called scanning near-field optical microscopy (SNOM). Since the near-field can

only be extracted locally, the size of the probe is then a very critical parameter: the smaller, the better. A large probe would inevitably scatter the evanescent waves from a large area and thus lead to averaging out the details.

In 1989, a demonstration of an SNOM had been assigned to as Photon Scanning Tunneling Microscope (PSTM) [14]. In this case, the specimen is deposited on a prism to be excited in total internal reflection (TIR). This configuration is equivalent to an STM where the tunneling process involves photons instead of electrons, or called frustrated total internal reflection [15], and allows the mapping of the optical distribution in the evanescent field with low background [16].

Two types of techniques can be used here: called aperture-SNOM which uses a sharp optical fiber, and scattering-SNOM (or also called 'apertureless'-SNOM) which involves typically bulk probe used for SPM, for example, electrochemically etched probe in STM or silicon cantilever in AFM.

1.2.1 Aperture-SNOM

This method is performed by using an optical fiber glued to one of the tuning-fork arms involved within the scanning shear-force feedback [17]. In figure 1.3.a we present the basic principle of an aperture-SNOM probe.

A tapered optical fiber is metal-coated with a certain angle to leave a minuscule opening ($d < \lambda$) at the apex tip where light can exit (or enter). In this configuration, it is the probe which generates evanescent fields at the exit of its sub-wavelength aperture and the sample scatters this illuminating near-field. During the scattering process, evanescent waves lead to propagating waves, which are detected in reflection (or transmission) using far-field detectors. This configuration has here the advantage that the sample is locally excited with any far-field background. However, the metal coating is not uniform on the nanoscale. Indeed, roughness at the tip may influence the optical imaging process. In addition, we could think that an optimized probe would have an aperture as small as possible and that one day all technological problems could be addressed. Unfortunately, the finite skin depth in metals as a function of EM source frequency imposes a fundamental lower limit to the aperture size, over some nanometers. Typically, a probe aperture should then be at least of 30 nm large [18, 19].

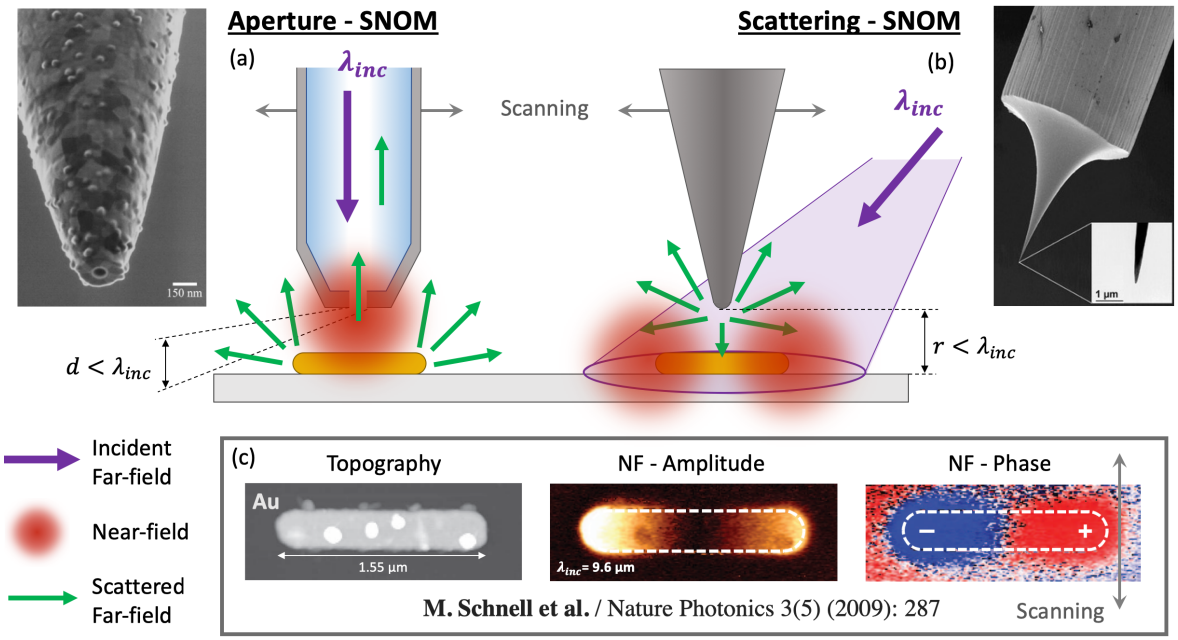

FIGURE 1.3 – Illustration of (a) Aperture- and (b) scattering-SNOM experimental configuration (c)Topography, near-field amplitude, and near-field phase images of a 1.55μm long Au nano-rod with a diameter about 230 nm on Si substrate.

1.2.2 Scattering-SNOM

The concept of scattering SNOM is to illuminate both the probe and the sample system and locally scatter the near field components from the excited region. This technique may work as a collection-mode instrument: some evanescent waves are created by the sample under an external EM source and converted into propagating waves by the tip (see Fig. 1.3.b). Note that in both cases – a-SNOM and s-SNOM – the sample can be illuminated in transmission mode through far-field radiation, and furthermore, under a critical angle which leads to evanescent wave occurring at the interface of the sample. Under TIR illumination, only the signal that is scattered at the junction between the tip and the sample enters the fiber (for a-SNOM) or reaches the far-field detector (for s-SNOM). As the a-SNOM configuration does with an excitation via the fiber provides, the TIR excitation combined with far-field collection lead to background-free experiment. Unfortunately, only s-SNOM can provide a collector probe dimension under the minimum of the a-SNOM aperture size ($\sim 30nm$). If an AFM is involved in driving the probe, tapping mode can provide a strong modulation of the near-field scattering. Therefore, the system electronically removes any signal from the illuminated area by a propagating excitation field.

Apertureless-SNOM was reported by U. Fischer and D. Pohl [20] by overcoating an aperture probe which creates a small protrusion in a gold film. Here, the sample is imaged using the scattering emitted from this protrusion. On the same concept, Specht et al. performed mapping on rough conducting samples by using a metallic probe from STM [21]. With a silicon probe (from AFM), the group of K. Wickramasinghe has recorded a resolution down to 1 nm on mica droplets [22].

On the previous figure, we illustrated the application of a scattering-SNOM reporting some results from M. Schnell et al. [23] using transmission-mode excitation and a silicon AFM probe as a near-field collector. They imaged 1.5 μm long gold nanorods designed for a dipolar plasmon resonance at mid-IR frequencies (9.6 μm) by electron-beam lithography on a silicon substrate. Note that the antenna length is significantly shorter than $\lambda/2$ due to the high aspect ratio of the rods (230 nm wide), the presence of a dielectric as the substrate, and plasmonic effect [24]. Figure 1.3.c regroups the topography, IR near-field amplitude and phase images of the nanorod. This study reveals strong electric amplitudes at its both extremities with field oscillation in opposition of phase as expected for the dipolar near-field mode.

Crystallization of organic films can also be investigated via IR s-SNOM to characterize molecular vibrations. Figure 1.4.a shows some interesting results from C. Westermeier et al., studying two different recrystallization forms of the pentacene film under the nanoscale Fourier transform infrared (FTIR) spectroscopy [25]. A small variation of the resonance frequency was observed between both molecular configurations – thin-film phase (TFP) and bulk phase (BP) pentacene) – which led to the mapping of a thin layer of the sample deposited on a glass substrate. The optical image gives details which are hardly distinguishable on the AFM topography. To develop nano-optoelectronic devices requires electric control of light which can be obtained through surface plasmons coupled with charge carriers in a graphene sheet, such as the one demonstrated by J. Chen et al. [26] also with IR s-SNOM. Employing metal-coated AFM tips as near-field probes, they performed real-space images of propagating and localized graphene plasmons. We can see in Figure 1.3.b that they successfully imaged the surface plasmon intensity on a tapered graphene ribbon on SiC. The images show evidence of two different localized modes (red and white arrows) – showing the existence of resonance conditions for the generation of plasmons according to the width of the ribbon and the incident wavelength. Numerical calculations were also performed to confirm the experimental data.

The geometry of the tip plays an important role in imaging. A sharp probe can be modeled in a first approximation as a spheroid or a cone. Scattering from

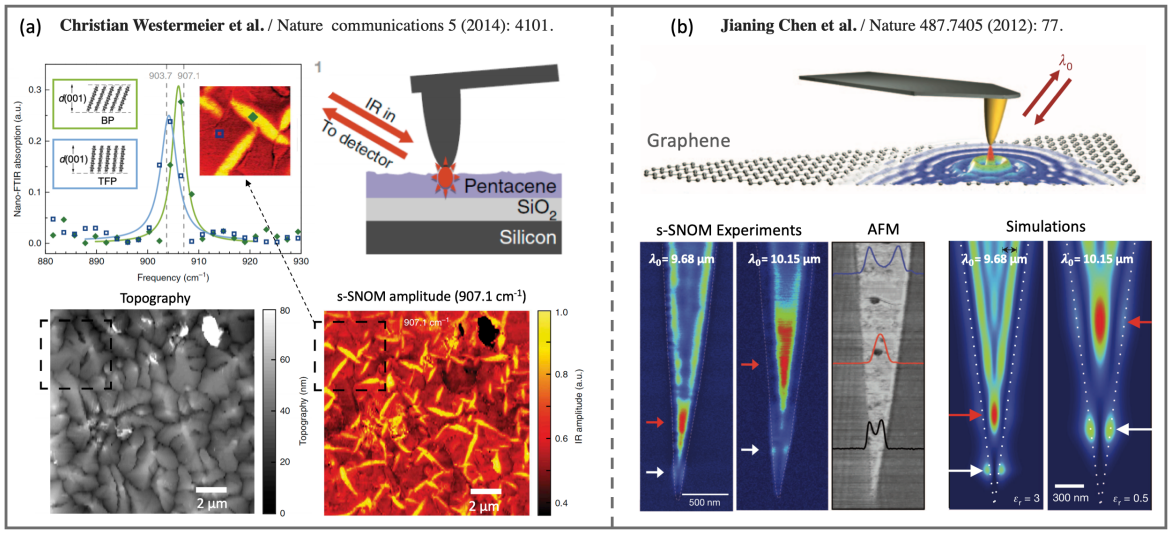

FIGURE 1.4 – (a) AFM topography and IR s-SNOM of a 40-nm thick pentacene thin film on a SiO2 substrate, and Nano-FTIR spectra taken at two different locations: TFP (blue) and BP (green) molecular arrangements perpendicular to the substrate and presenting a shift in resonance frequency.(b) Schematic of the experimental configuration of propagating waves in graphene. Near-field optical and topography images of a tapered ribbon with comparison with the theoretical model.

a spheroid can be solved analytically in a similar way than a nano-sphere. An elongated spheroid leads to scattering one order of magnitude larger than a sphere. However, a combination of the geometrical effects and plasmon resonances in metals could give rise to an up to several orders of magnitude increase in the scattering coefficient. Analog to antenna theory for the radio frequencies, this field enhancement is often referred to as the lightning rod effect (geometric-dependent), and such metallic probe can then be called as an optical antenna. For a separation distance with a sample under 5 nm, the extremely confined optical field sees its EM intensities enhanced as the tip becomes sharper. The scattered signal from such a sharp tip exhibits a specific wavelength depending the size and shape of the tip (see § 2.3.2).

After more than fifteen years, reproducible and efficient fabrication of scattering SNOM probes still remains an open technological issue. Several methods have been proposed for producing sharp tips and for their metal coatings. However, these techniques still have problems that vary depending on the design of the probe which makes nanotechnology a central topic to control the properties of an SNOM tip.

Today, the recent applications involving s-SNOM are mostly dedicated to the visible range of the EM to investigated the Raman spectroscopy field which strongly dependent on the plasmon properties, as proven in Surface (see § 2.2) and Tip (see § 2.3) enhanced Raman scattering.

1.3 Plasmonics

One of the first revolutions in optical-science technology began with the invention of the laser in 1960, followed by the revolution of optical fiber communications in the 1980s. The continuous progress of nanotechnology techniques in the early 1990s has driven the third revolution in photonics: nano-photonics, which can be defined as studying the light-matter interaction at the nanoscale [27]. Nanophotonics use sub-wavelength confinement and EM enhancement for potential applications in different scientific and engineering fields such as sensors, lasers, energy, and photonics chips [28–30]. Further research on metallic nano-objects exploits their optical properties which strongly depend on their size and shape [31], as well as their environment, including substrates [32].

The area of photonics which concerns metallic nanostructures is then called nano-plasmonics [33]. This term refers to the collective oscillation of free electrons moving with respect to the positive ions that compose a metallic lattice. Called plasmon, they are referred to as a quantized plasma (charge density) wave, also called volume or bulk plasmon (see 1.5.a). Plasmons that confine to a metal-dielectric interface are called surface plasmons (SP). When light is coupled to these SP under certain conditions, it generates enhanced evanescent electromagnetic fields, called surface plasmon polaritons (SPP, see Fig.1.5.b) [34], propagating on extended surfaces and exponentially decaying away from the boundary into the surrounding materials. Moreover, a metallic object with a sub-wavelength dimension may also couple its electron oscillations with incident light and create localized enhanced field nearby its surfaces, as we already saw in the case of the SNOM [35], called localized surface plasmons (LSP, see Fig.1.5.c). The specific properties of metallic nanoparticles are important for applications such as biosensors [36], surface enhanced Raman spectroscopy (SERS) [37], light trapping in solar cells [38], and novel metamaterials [39].

When the far-field illumination reaches the resonance plasmon frequency, the coherent displacement of electrons enters in phase with the scattered electromagnetic field and oscillate with greater amplitude than other frequencies, called localized surface plasmons resonance (LSPR). The EM enhancement generated reaches then its maximum of intensity. A sharp resonance peak is seen for conductive materials, especially noble metals such as gold and silver, in the visible range of the light spectrum [40].

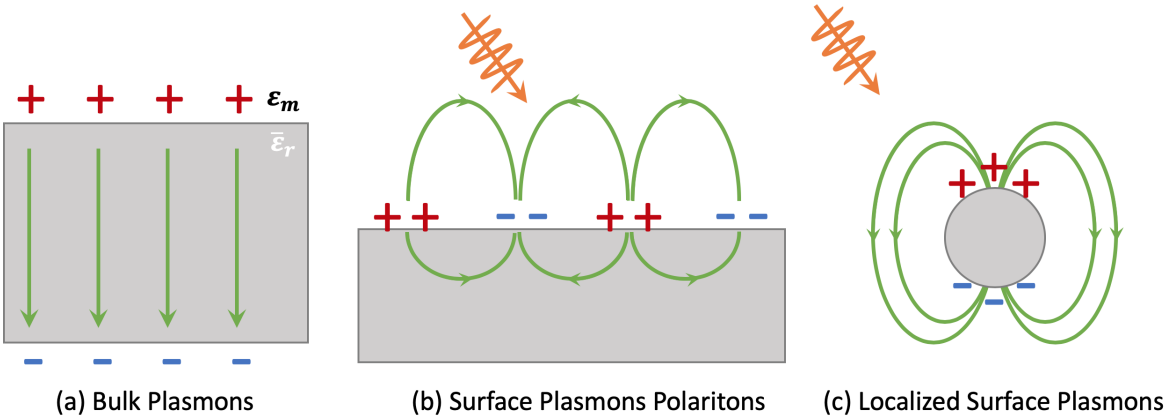

FIGURE 1.5 – (a) Electron oscillation into metal volume. Light-plasmon coupling at the metal/dielectric interface generating, (b), propagative plasmon along a planar metallic surface or, (c), localized plasmon at the vicinity of a metallic nanoparticles.

Nano-plasmonics is thus a new frontier that combines electronics, photonics, and nanotechnology. First, the great developments in nanofabrication techniques have allowed numerous studies to create metallic nanostructures such as nanoparticles or nano-thin films. Secondly, the development of computational techniques has stimulated researchers to perform theoretical experiments, design nano-optical devices, and study new-optical phenomena. Finally, nano-plasmonics devices are compatible with standard CMOS microfabrication techniques [41,42]. Hence, nano-plasmonics has the potential to provide a large variety of sub-wavelength optical components, also called optical nano-antennas, and integrate them in particular for the conception of efficient s-SNOM probe to perform optical trapping by plasmonic nanotips [43] or for enhanced spectroscopy [44].

Some conditions in terms of materials and illuminations are however required to allow the existence and excitation of a surface plasmon. We first need to describe the frequency-dependent permittivity of the metals and the boundary condition at the interface when it is excited by far-field radiation.

1.3.1 Plasmonic materials

In metals, the plasmonic properties result from interactions between EM waves and conduction band electrons. The dielectric constants of metals can explain their very high reflectivity in the visible range and absorption for higher frequencies as the blue-range for gold and UV-range for silver. The collective motion of the electrons can be mechanically described by applying Newton's law on single electron of mass m_e as a simple harmonic oscillator. The Drude model [45] is referred to

a as damped-electron model which describes the motion of electrons as a damped Lorentz oscillator when illuminated by a time harmonic electric radiative field of a pulsation ω in a linear medium $\mathbf{E}(\mathbf{r},t) = \mathbf{E}(\mathbf{r})e^{-i\omega t}$, where $\mathbf{r}(t)$ is the position vector of the electron which is solution of the motion equation:

$$m_e\frac{d^2\mathbf{r}}{dt^2} + m_e\Gamma\frac{d\mathbf{r}}{dt} = e\mathbf{E_0}\exp(-i\omega t) \quad \rightarrow \quad \mathbf{r}(t) = \frac{e\mathbf{E}(t)}{m(\omega^2 + i\Gamma\omega)} \tag{1.2}$$

with Γ the damping term. According to Maxwell's equations, a single free-electron's displacement can be associated with a dipole moment $\mathbf{p} = e\mathbf{r}$ in any direction giving the macroscopic polarization as the sum of all individual dipole per unit volume as $\mathbf{P} = n\mathbf{p}$. The optical properties of nobles metals depends on the excitation frequency described by dielectric function, called relative permittivity ε_r expressed as:

$$\varepsilon_r(\omega) = 1 + \chi_e(\omega) \quad ; \quad \mathbf{P} = \chi_e\varepsilon_0\mathbf{E} \tag{1.3}$$

with the electric susceptibility χ_e, electric constant of materials. The dielectric function is a complex function: $\varepsilon(\omega) = \varepsilon'(\omega) + i\varepsilon''(\omega)$. Using these relations, the complex permittivity of metal is expressed as [46]:

$$\varepsilon_{Drude}(\omega) = 1 - \frac{\omega_p^2}{\omega^2 + i\Gamma\omega} = \varepsilon' + i\varepsilon'' = 1 - \frac{\omega_p^2}{\omega^2 + \Gamma^2} + i\frac{\Gamma\omega_p^2}{\omega(\omega^2 + \Gamma^2)} \tag{1.4}$$

with ω_p the plasma frequency [47], depending on the volume density of free-electrons n involved in the motion in the metal, such as:

$$\omega_p = \sqrt{\frac{ne^2}{m_e\varepsilon_0}} \tag{1.5}$$

with e the elementary electric charge and ε_0 the electric permittivity of the vacuum. A quantum of this frequency corresponds then to the plasmon energy ($\hbar\omega_p$).

The imaginary part of the metal permittivity characterizes the absorption, or dissipation, of the energy related to the motion of the electrons in the metals. Thus the Drude model is well suited for metals whose optical properties are mainly due to the behavior of conduction electrons as for alkali or trivalent metals. Nevertheless, the experimental results for higher energy photons significantly diverge from the prediction of the Drude theory. This model does not consider the fact that electronic transitions between the valence and the conduction band can occur. In the case of noble metals, this model then needs an additional term related to interband transitions, called the Lorentz model, to form The Drude-Lorentz theory [48].

1.3.2 Surface plasmons

Since light-plasmon coupling is the main interest for nanophotonics, only surface plasmons are considered here. There are two different surface plasmons modes. If a least one the three-dimension of a metallic object is infinite with respect to the plasmon wavelength (nanowire, s-SNOM probe, thin surface, waveguide, ect.), evanescent waves localized at the metallic-dielectric interface can propagate along this (these) directions(s). These waves, called Surface Plasmon Polariton (SPP), penetrate the media where they decay exponentially along the perpendicular direction from the interface plane. For a finite metallic object with a characteristic size from tens to hundreds nanometer, surface plasmons stay localized nearby the metallic surfaces and can resonate under conditions depending on the nature, size, and shape of the object, and environments. These modes are called localized surface plasmons (LSP). LSP result in strong signatures in terms of absorption, scattering, and enhancement of the EM field, confined in the volume with sub-wavelength extension. This localized and intense near-field is usually called *hot-spot* in the scientific community.

1.3.2.1 Surface Plasmon Polariton

Surface plasmons polaritons (SPP) are longitudinal and coherent electron oscillation mode at an interface ($z = 0$) between a transparent medium of real permittivity ($\varepsilon(\mathbf{r},\omega)_{z>0} = \varepsilon_d$) and a metal with a complex permittivity ($\varepsilon(\mathbf{r},\omega)_{z<0} = \varepsilon_m = \varepsilon'_m + i\varepsilon''_m$). The charge motion in a surface plasmon generates the existence of an electromagnetic fields ($\mathbf{E}_{spp}(\mathbf{r},t) = \mathbf{E}(\mathbf{r})e^{i(k_{spp}\cdot\mathbf{r}-\omega t)}$) which decays exponentially in the metal and dielectric layer (see Fig.1.6.a). The SPP relation dispersion [49] (relation between pulsation ω and wavevector k) is expressed as:

$$k_{spp} = \frac{\omega}{c}\sqrt{\frac{\varepsilon_d\varepsilon_m(\omega)}{\varepsilon_d + \varepsilon_m(\omega)}} \tag{1.6}$$

with k_{spp} the complex tangential k-vector of the SPP. The plasmon wavelength (λ_{spp}) is defined with the real part of k_{spp}, while the imaginary part measures the propagation length of the SPP. In both medium, the length for which the intensity of the electric field inside a medium decreases to 1/e is called the penetration depth (δ_d,

δ_m) and along the interface is called propagation length (L_{spp}), and are expressed as:

$$\lambda_{spp} = \frac{2\pi}{k'_{spp}} \quad ; \quad \delta_d = \frac{1}{k''_{z,d}} \quad ; \quad \delta_m = \frac{1}{k''_{z,m}} \quad ; \quad L_{spp} = \frac{1}{2k''_{spp}} \tag{1.7}$$

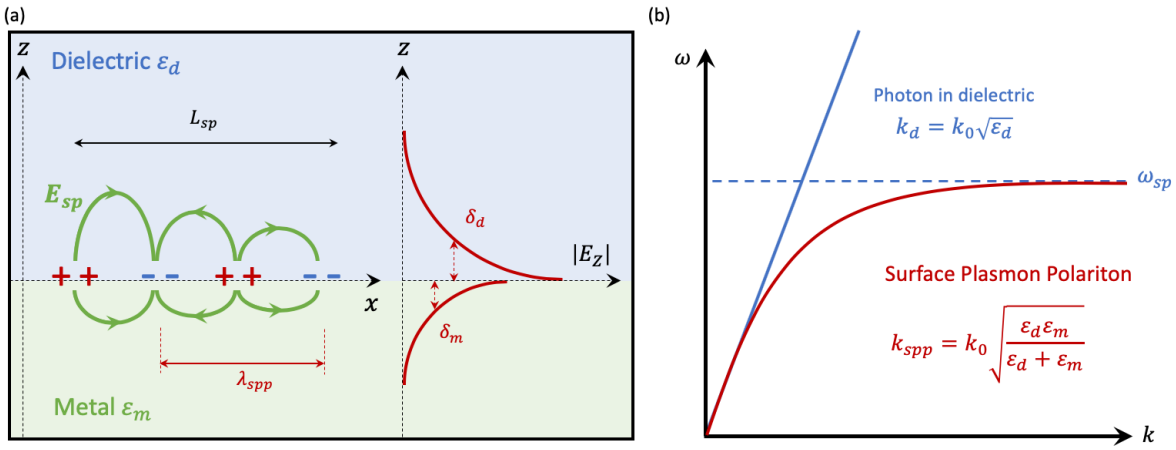

FIGURE 1.6 – (a) Schematic illustrations of surface plasmon polariton with penetration depths into both media. (d) Light dispersion relation in the medium $\sqrt{\varepsilon_d} > n_{air}$ (blue), and SPP dispersion relation (red).

We observed in Figure 1.6.b the SPP that the k_{spp} tends to an asymptote for a frequency proportional to the plasmon frequency ω_{sp}. This value can be extracted for the Drude model and the Eq. 1.4 such as:

$$\varepsilon'_m \approx 1 - \frac{\omega_p^2}{\omega} \quad ; \quad \omega_{sp} = \omega_p \sqrt{\frac{1}{1+\varepsilon_d}} \tag{1.8}$$

The difficulty of the observation of surface plasmons can be explained by the fact that these modes are linked to the metallic interface: the evanescent wave is exponentially decreasing in the air and cannot be excited or observed from the far field if the surface is perfectly flat. Indeed, in this case, we see that the SPP dispersion relation is entirely below the light dispersion. A direct optical propagating excitation thus cannot excite SPP since $\omega = \omega_{sp}$ and $k_x = k_{sp}$ cannot be simultaneously fulfilled.

1.3.2.2 SPP excitation

If an incident planewave propagates through air ($\varepsilon_d = 1$), it is impossible to excite SPP between an air/metal interface. However, a light wave can penetrate

the metal up to a distance comparable to the skin depth, and it may be possible to increase the parallel wavevector k_x using a second medium, with a large dielectric constant, or by changing the roughness of the metallic surface. Based on total internal reflexion configuration (TIR), Kretschmann [50] and Otto [51] configuration use both a prism with higher permittivity which can increase the value of incident k_x (see Fig.1.7.a). In Kretschmann configuration, a metallic layer is deposited on a prism and excited through it under an angle of incidence leading TIR. The light stemming from the prism goes through the metal film and reaches the metal/air interface. As we see on the corresponding dispersion relation (see Fig. 1.7.b), the prism permittivity gives the required increase of the incident k-vector (blue line) that crosses the metal/air plasmon dispersion (red). At a certain incidence angle of θ_{spp}. For this value, the incident planewave can be coupled to SPP.

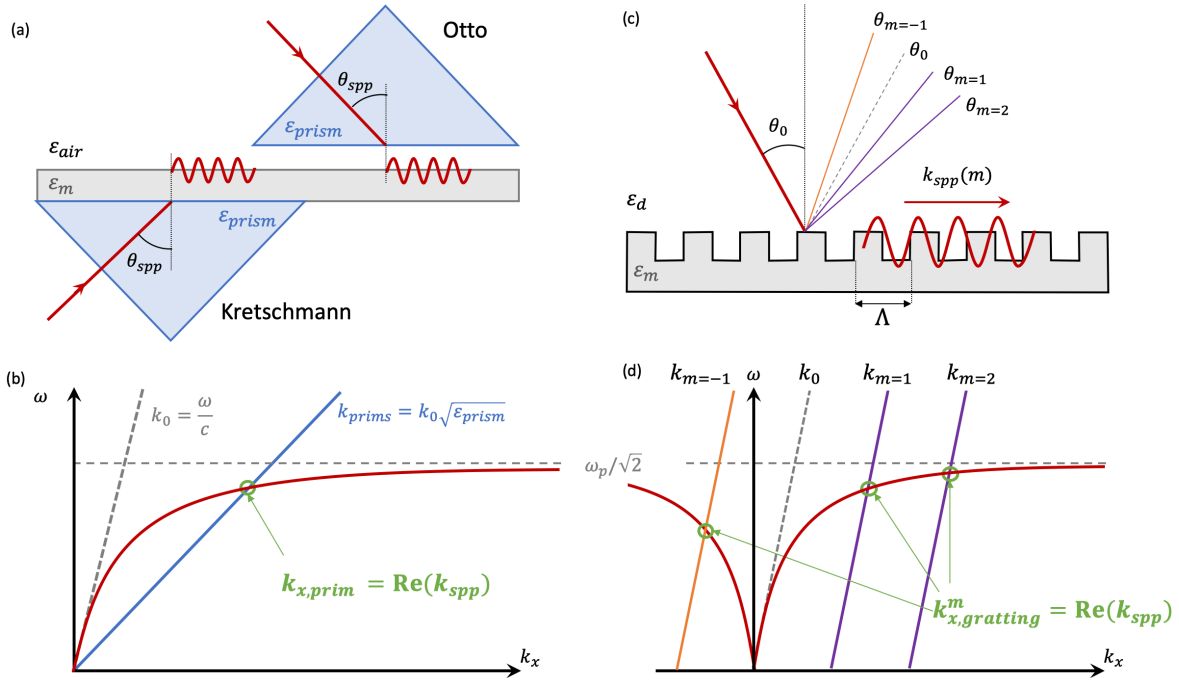

FIGURE 1.7 – Surface plasmon polariton excitation by (a) total internal reflexion – Kretschmann and Otto set-up configuration – or by (c) diffraction grating to generate SPP. (c) and (d) respective dispersion relations revealing light-plasmon coupling conditions

The Kretschmann configuration is not adapted anymore for metal films thicker than skin depth, however, SPP can be still excited using the Otto configuration. In this case, the prism (and the TIR excitation) is placed above the metal surface and the photon tunneling takes place in the air between the surface and the prism. In

both configuration, the resonant conditions are expressed as:

$$k_{x,prism}(\omega_{sp}) = \frac{\omega}{c}\sqrt{\varepsilon_{prism}}\sin(\theta_{spp}) \;=\; \mathrm{Re}\left(k_{spp}\right) \tag{1.9}$$

It is also possible to increase the k_x vector of the incident excitation by changing the roughness of the metallic surface. For instead, a grating pattern on the metal surface diffracts the incident light propagating through any transparent medium ε_d (see Fig.1.7.c) [52]. With an one-dimensional grating of grooves with a period Λ, the diffracted waves of order n can see their k-vectors higher than the incident wave (see Fig. 1.7.d), and excite SPP if phase-matching condition k_x is fulfilled:

$$k^{m}_{x,gratting}(\omega_{sp}) = \frac{\omega}{c}\sqrt{\varepsilon_d}\sin(\theta_0) + m\frac{2\pi}{\Lambda} \;=\; \mathrm{Re}\left(k_{spp}\right) \tag{1.10}$$

Moreover, plasmon excitation of the metallic surface structure can be also performed at the end of a sharp probe (a- /s-SNOM), by irradiation of a metallic nanoparticle, or excitation of fluorescent molecules. Each of these method generates of a confined near field with large spatial frequencies, containing parallel component that matches the real part of the k-vector of the SPP mode.

In the visible range, the ratio between the metal skin depth and the incident wavelength (λ_0) becomes large and intense. This strongly confines surface plasmon modes with effective indexes larger than the environment. The refractive index of an SPP, n^{eff}_{spp}, is defined as: [53]

$$n^{eff}_{spp} = \frac{\lambda_{spp}}{\lambda_0} \tag{1.11}$$

Similar to standard refractive optics, which diffracts the light according to the Snell-Descartes law, a discontinuity in ε_d along a metallic surface supporting surface plasmon leads a 'plasmon' interface where at one side the refractive index is $n^{eff}_{spp,\,die1}$, for example an air/metal, at the other side $n^{eff}_{spp,\,die2}$, for example glass/metal [54].

1.4 Localized Surface Plasmons

We introduce now non-propagating plasmon excitation on metallic nanostructures. If we consider a small isolated and spherical metallic nanoparticle with a size ranging the penetration depth of an EM wave (e.g., $\sim$ 20 nm to 100 nm for Ag or Au excited with the visible spectrum), the concept of volume plasmon disappears.

In this case, the excitation field goes into the bulk matter and moves the conduction electrons with respect to the ion lattice. The resonance condition occurs when the frequency of light corresponds to the electrons oscillation frequency against the restoring force from the ion lattice (see Fig. 1.8.a), called localized surface plasmon resonance (LSPR). The interaction between light and metallic nanostructures for LSPR leads to the concentration and exaltation of light into sub-wavelength volumes (localized evanescent waves). In addition to light being confined, the intensity of light is also enhanced by several orders of magnitude.

The excitation of LSP mode is responsible for the bright colors that metallic nanoparticles exhibit in both transmitted and reflected light seen, for example, in windows or ornamental cups [55, 56]. LSPR modes of a metallic nanoparticle have strong signatures in scattering and absorption properties, which are strongly dependent on the particle morphology, size, composition, and environment. We will base our understanding of the involved mechanism using the electrostatic approximation [57] on the simplest case of a metallic nanosphere, and see what the factors influencing on the plasmon resonance conditions are.

1.4.1 Electrostatic approximation

For a spherical metallic nanoparticle smaller than the EM wavelength, the electrostatic approximation can be studied from a theoretical point of view. Here, we consider a static electric field $\mathbf{E} = E_0\mathbf{e}_z$ in a isotropic surrounding medium exciting a metallic sphere with a radius $R \ll \lambda$ and a complex dielectric constant $\varepsilon_m(\omega) = \varepsilon'_m(\omega) + i\varepsilon''_m(\omega)$ depending on the incident frequency. According to Maxwell's equation and the induced relation: $\mathbf{P} = \varepsilon_0\varepsilon_d\alpha\mathbf{E}_{NF}$, with $\mathbf{E}_{NF}$ the local field surrounding the nanoparticle, we can extract the complex polarizability of the sphere α, proportional to the excitation amplitude:

$$\alpha_{sph} = 4\pi\varepsilon_0 R^3 \frac{\varepsilon'_m - \varepsilon_d}{\varepsilon'_m + 2\varepsilon_d} \tag{1.12}$$

The polarizability then transcribes the spectral response of nanoparticles, in the way that they absorb and scatter EM radiation. For this, we introduce the absorption and scattering cross section (σ_{abs} and σ_{scat}) [58]. These quantities are expressed as the ratio between the absorbed power, or the scattered power, by the nanoparticle and the intensity of the incident wave. The sum of both cross sections give the so-called extinction cross-section σ_{ext}. For a nanosphere in the electrostatic approximation, it

can be shown that these cross sections can be directly expressed as:

$$\sigma_{abs} = \frac{P_{abs}}{I_{inc}} = \frac{k}{\varepsilon_0}\,\mathrm{Im}(\alpha(\omega)) = 4\pi k R^3\,\mathrm{Im}\left(\frac{\varepsilon'_m - \varepsilon_d}{\varepsilon'_m + 2\varepsilon_d}\right) \tag{1.13}$$

$$\sigma_{scat} = \frac{P_{scat}}{I_{inc}} = \frac{k^4}{6\pi\varepsilon_0^2}|\alpha(\omega)|^2 = \frac{8\pi}{3}k^4R^6\left|\frac{\varepsilon'_m - \varepsilon_d}{\varepsilon'_m + 2\varepsilon_d}\right|^2 \tag{1.14}$$

$$\sigma_{ext} = \sigma_{abs} + \sigma_{scatt} \tag{1.15}$$

with and $k = 2\pi/\lambda$. A resonance occurs when the denominator of this relation tends to zero, only dependent on the excitation frequency (into electrostatic approximation). The resonance occurs then when the illumination reaches the plasmon frequency $\omega_{inc} = \omega_{lsp}$ which fulfills the condition $\varepsilon'_m(\omega_{lsp}) = -2\varepsilon_d$.

Numerical modelling based on finite elements have been used here to illustrate the case of a single Au nanosphere with a radius R ranging from 20 to 60 nm (via COMSOL Multiphysics - see more details in § 3.1.1). Figure 1.8.b shows both the absorption and scattering response in the green range of the optical spectrum. The peak that exhibits the spectra is characteristic of the fundamental dipolar resonance mode. A tiny variation with R of the resonance wavelength ($\lambda_{lsp} = 2\pi c/\omega_{lsp}$) appears for both signals and shift towards the red by only 10-20nm (red-shift). Nevertheless, the distribution of the energy contained in the incident wave between the absorption and the scattering strongly depends on the size of the nanoparticle ($\sigma_{abs} \propto R^3/\lambda$, and $\sigma_{scatt} \propto R^6/\lambda^4$). Here, the absorption signal is 25 times increased from the smallest to the largest nanoparticles, while the scattering signal is amplified up to 750 times. There is another fundamental property LSPR for applications. It lies in the distribution of the field radiated by the nanoparticles [59]. This field can be expressed from the dipole moment $\mathbf{p}$ of the particle so that the field scattered in the direction $\mathbf{n}$ by a localized dipole placed in a position $r(0,0)$. Two area can be distinguished as being the near-field for a region where $rk \ll 1$, approximately corresponding to the distance smaller than $\lambda/10$, and the far-field for a region respecting $rk \gg 1$, from a distance large than a wavelength unit (10λ - 100λ). The far-field $\mathbf{E}_{FF}$ scattered by the nanoparticle can be written as:

$$\mathbf{E}_{FF} = \frac{3\mathbf{n}(\mathbf{n}\cdot\mathbf{p}) - \mathbf{p}}{4\pi\varepsilon_0\varepsilon_d}\frac{1}{r^3} \tag{1.16}$$

In Figure 1.8.c, we see on the NF field map along the XZ plane the localized field nearby the nanoparticles, along the symmetry plane of the particle containing $\mathbf{E}$. The enhancement factor EF_{lsp} of this localized field is obtained from the intensity ratio

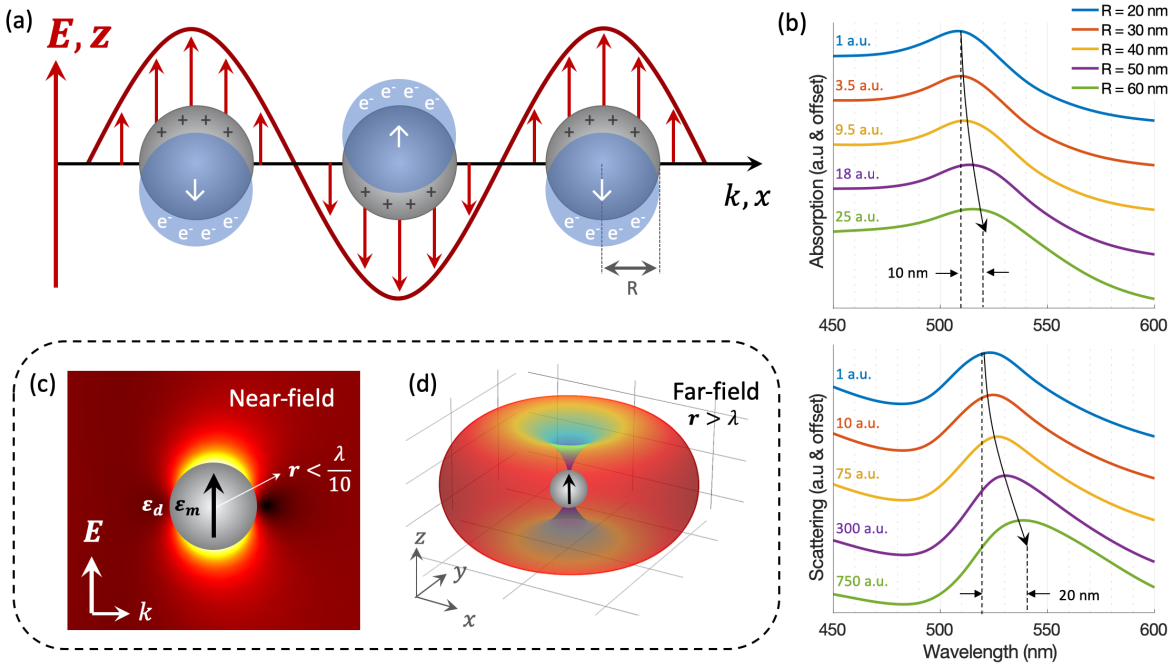

FIGURE 1.8 – (a) Schematic illustration of collective motion of electron from a metallic nanosphere oscillating under with the incident far-field excitation. (b) Absorption and scattering spectra of Au nanosphere for different radius ranging from 20 to 60 nm. (c) Electric field map of the near-field confinement and (d) three-dimensional far-field radiation pattern.

between the near-field just outside the surface of the nanoparticle and the incident excitation:

$$EF_{lsp} = \left| \frac{\mathbf{E}_{NF}}{\mathbf{E}_0} \right|^2 = \left| \frac{3\varepsilon_d}{\varepsilon_m + 2\varepsilon_d} \right|^2 \tag{1.17}$$

The 'scattering amplitude' based on the integration of the energy flux of the time-averaged Pointing vector $\mathbf{S}_{av}$:

$$\oint_S \mathbf{S}_{av}\, \mathbf{dS} = \frac{1}{2} \oint_S \mathrm{Re}\left(\mathbf{E}_{FF} \times \mathbf{H}^*\right) \mathbf{dS} \tag{1.18}$$

with $\mathbf{dS}$=dS$\mathbf{n}$. $\mathbf{S}_{av} \cdot \mathbf{n}$ forms then the far-field radiation pattern presented in Figure 1.8.d, that shows how the nanoparticle radiates in three-dimensions. The scattered intensity is maximum in the perpendicular plan to the dipole axis.

1.4.1.1 Nanoparticle shape

The LSPR of a nanosphere is independent on the incident field polarization. We will see that for an asymmetric shape, the behavior of the LSPR becomes polarization-dependent and can be understood by treating the case of spheroids,

elongated spheres along a single direction called major axis [60]. We start by considering a small metal spheroid with sub-wavelength semi-axes a_x, a_y and a_z as illustrated in Figure 1.9.a. In the quasi-static approximation, the dipole moment $\mathbf{p}_i$ along the principal axes ($i = x, y, z$) responds linearly to the incident polarized field $\mathbf{E}^i_{inc}$ and where the complex polarizability α_i can be extracted such as [61]:

$$\mathbf{p}_i = \varepsilon_0 \varepsilon_m \alpha_i \mathbf{E}^i_{inc} \quad ; \quad \alpha^i_{spheroid} = \frac{4}{3}\pi\varepsilon_0 a_x a_y a_z \frac{\varepsilon_m - \varepsilon_d}{\varepsilon_m + L_i(\varepsilon_m - \varepsilon_d)} \tag{1.19}$$

with L_i the depolarization factors. We can evaluate the effect of the shape on the polarizability of a prolate nanoparticle ($a_z > a_x = a_y$), and then on the optical cross sections. For that, we start from a Au nanosphere with a radius of 40 nm. We increase the radius a_z along the major axis to form the spheroid. We adapt the minor axes ($a_x = a_y$) in order to keep the same volume of matter than the original nanosphere. The depolarization factors are given by:

$$L_z = \frac{1-e^2}{e^2}\left[\frac{1}{2e}\ln\left(\frac{1+e}{1-e}\right) - 1\right] \quad \text{and} \quad L_x = L_y = \frac{1-L_z}{2} \tag{1.20}$$

with $e = \sqrt{1-(AR)^{-2}}$ and the aspect ratio (length/width) of the spheroid expressed as $(AR) = a_z/a_x$. We see that now the resonance condition in Eq. 1.19 strongly depends on the shape parameter L_i in addition to the frequency: $\varepsilon'_m(\omega)(1+L_i) = L_i\varepsilon_d$. Since two different values of L_i exist in the spheroid case, two resonances can occur for a polarized excitation E_i along the long (called longitudinal mode) and along the short (called transverse mode) axis. Here, the key to control plasmon resonances resides thus in the aspect ratio of the metallic nanostructures. First, we look at the influence on the scattering signal and the EF when the incident field is polarized along the major axis of the spheroid. We note in Figure 1.9.b a strong red-shift of the LSPR over 220 nm from a nanosphere of 40 nm radius (AR=1) to a 200 nm long spheroid (AR=4) with an identical volume.

We also see in Figure 1.9.c that the longitudinal mode is amplified more as the major axis a_z increases. When measured 1 nm from one of the extremity, the EF shows amplification of the field at resonance from 25 up to 3800, for respectively the original nanosphere excited ($\lambda_{lsp} = 530$ nm) and the longest spheroid ($\lambda_{lsp} = 750$ nm). The LSPR splits thus into two modes: (i) a longitudinal mode α_z that corresponds to the free electrons oscillations along the major axis, and (ii) two degenerated transverse modes α_x and α_y related to the oscillations perpendicularly to it (see Fig. 1.10.a).

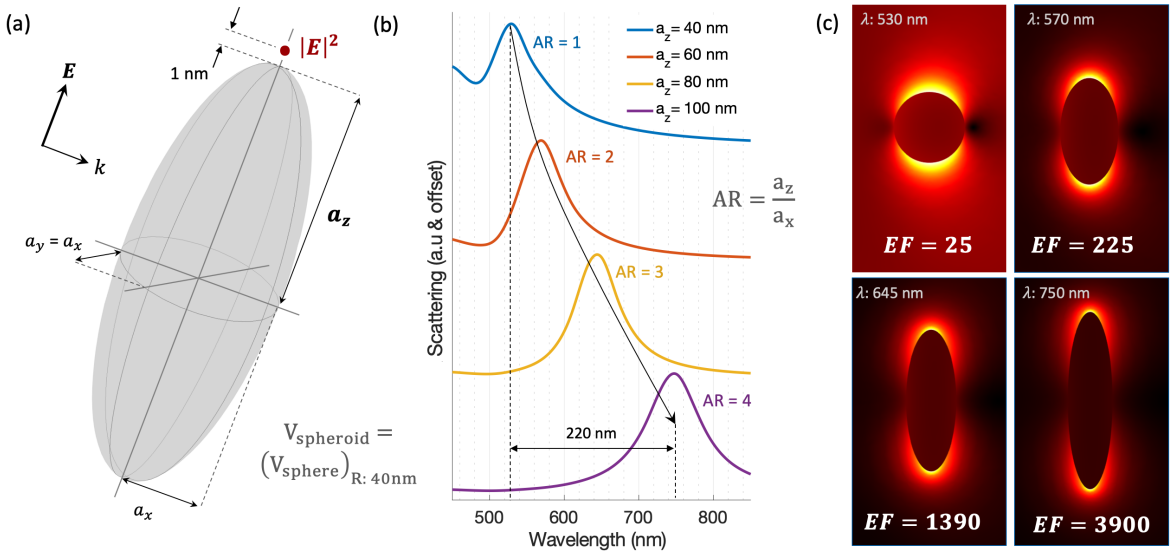

FIGURE 1.9 – (a) Gold spheroid excited by electric field polarized along the major axis a_z. Enhancement factor calculated 1 nm away from the extremity. (b) Scattering spectrum of spheroid with different aspect ratio (AR) and identical volume. (c) Electric field maps under resonance conditions.

The transverse oscillation does not seem to be the privileged mode for an elongated shape compared to the longitudinal mode. Indeed, we observe on the EF maps that the localized field is quasi-uniformly distributed along the particle surface with a weak EF around 10. The longitudinal mode presents a much more confined field at its extremities, increasing the EF between two and three orders of magnitude. The difference can also be observed on the scattering spectrum of Figure 1.10.c. Considering the previous nanosphere resonance at 530 nm, the transversal mode exhibits a small blue-shift as the aspect ratio increases, driven by a minor radius going down to 25 nm. The longitudinal mode, as we saw, strongly depends on the AR with a scattering signal 220 times more intense. We saw what conditions should be imposed on the shape of the metallic nanoparticles to strongly influence the LSPR in term of frequency and the field intensity that reigns into the localized evanescent waves. Several studies in literature focus on more specific shape as well as nanodisks and nanocones that will be discussed in our theoretical and experimental studies (see § 3.1.2.1).

1.4.1.2 Nanoparticle material

Plasmons materials properties as seen above suggest that several metals can be used to generate plasmonic resonances. Here, we use the previous example of the

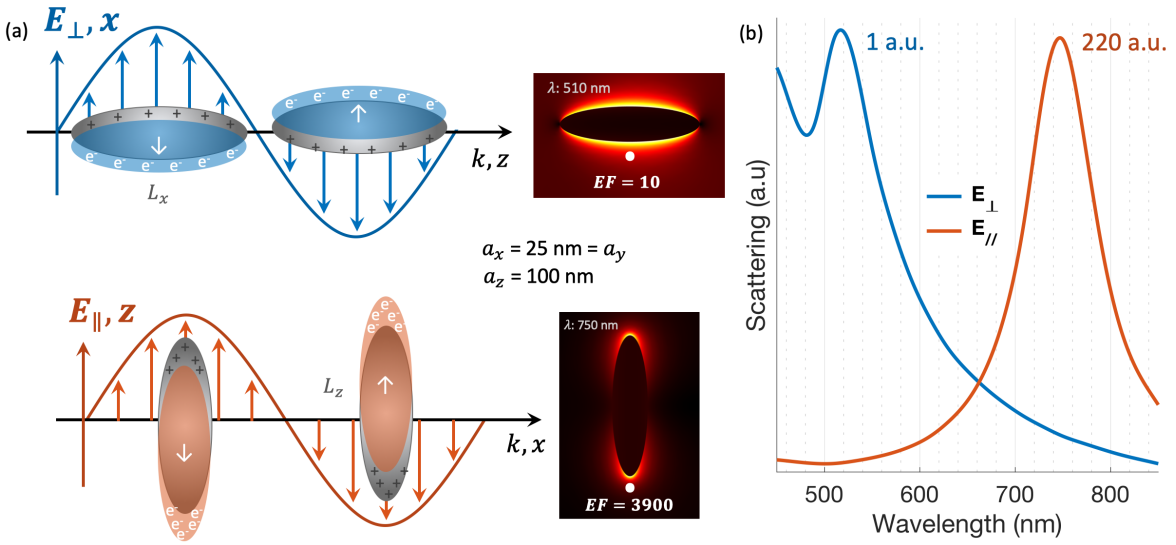

FIGURE 1.10 – (a) Schematic illustration of electron motion of metallic nanospheroid under a polarized electric field along the mirrors axes (transverse mode - in blue), or along the major axis (longitudinal mode - in orange) with respective electric field map of the near-field. (b) Scattering spectra for both excitations on Au spheroid with an aspect ratio around 4.

longest spheroid (a_z = 100 nm; a_x = 25 nm) and we compared the scattering spectra and the EF at the resonance frequency for an object made in aluminum, silver, copper, and gold. The influence on the LSPR resides into their complex dielectric constant (see Fig. 1.11.a), where plasmon resonances occur for negative real parts, with an absolute value extending the corresponding imaginary part. As we can see in Figure 1.11.b, a consequent red-shift occurs from aluminum resonating in the green range, until gold excited in the red range.

Moreover, the polarizability relation (Eq. 1.19) shows that the environment properties may also affect the resonance conditions. Another set of numerical modelling was then performed on the Ag spheroid immersed into air, water, or glass medium, with a refractive index $n = \sqrt{\varepsilon_d}$ respectively of 1, 1.33 and 1.5 (see Fig. 1.11.c). As expected, we observe a strong red-shift of the optical responses as the medium index increases. The plasmonic properties of nanostructures can also be strongly influenced by the presence of a substrate that supports the metallic nanoobject [63]. In that case, instead of being immersed into a single medium, the plasmonic structure is embedded in an asymmetric environment which drastically affects the plasmon resonances depending on the interaction between the object and the substrate [64].

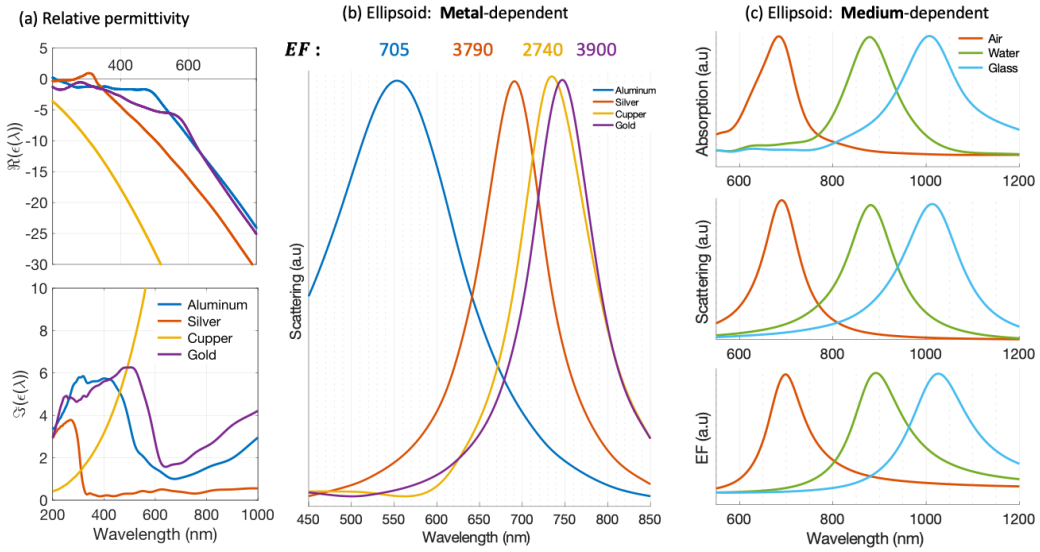

FIGURE 1.11 – (a) Real and imaginary part of the relative permittivity of several metals from the near UV to near IR wavelength, extracted by interpolation of Johnson and Christy's [45] (for Ag, Cu, Au), and McPeak [62] data (for Al). (b) Scattering spectra for the same spheroid (AR=4) in each metals. (c) Optical responses spectra for the silver spheroid immersed into air, water and glass medium.

1.4.1.3 Excitation angle

Excitations of plasmonic higher order modes in metallic nanoparticles are dependent on the incidence angle θ of the EM excitation. Figure 1.12.a shows the EF spectra of a silver nano-spheroid into glass medium at different angles from 0° to 90°. It shows three distinct peaks, namely the dipole at 1020 nm, a quadrupole at 625 nm, and a sextupole at 500 nm. The mode nature of these three resonances is confirmed by their near-field distribution maps and the z-component of the electric field map illustrated in Figure 1.12.b.

As expected, the EF is maximal for the dipole resonance excited at 0° and is zero at 90°. Due to the charge distributions, the quadrupole mode responds most strongly at 45°, while the sextupole mode appears for 0° and 60°. There is no signal at 90° due to the modes symmetry not compatible with the incident polarization. There is an excitation of LSPR modes with a planewave when the overall dipole moment of the spheroid does not disappear. These modes are radiative, or called bright modes, are related to an asymmetric charge distribution, and can strongly couple to the incident planewave excitation and exhibits a large scattering cross-section. For some modes, the charge distribution is centrosymmetric and have a reduced light scattering efficiency, called dark modes [65].

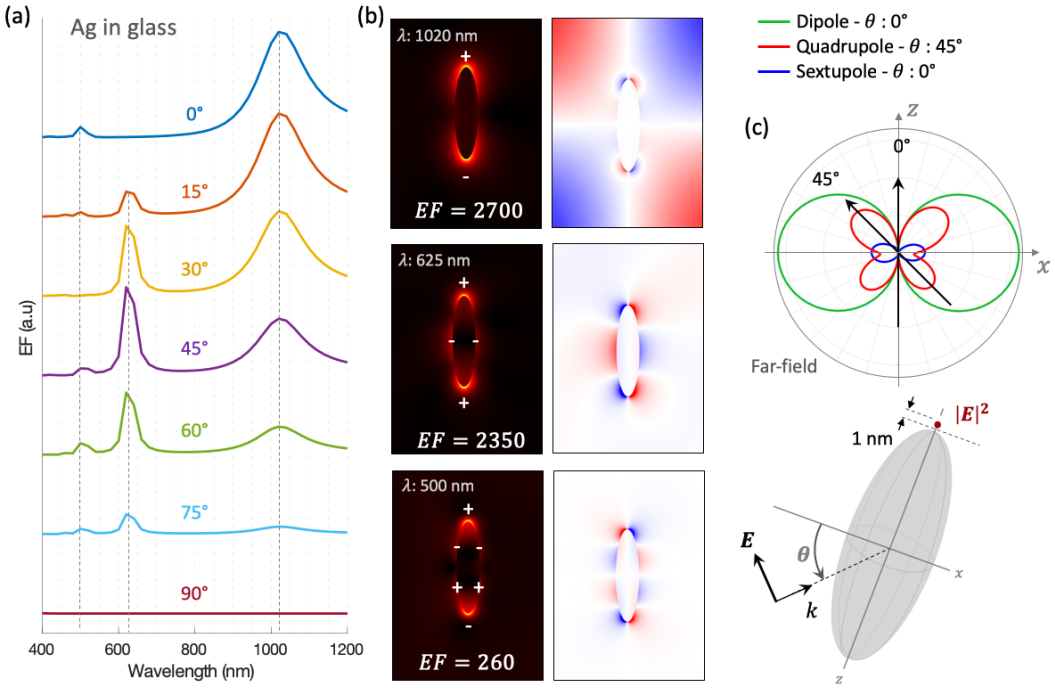

FIGURE 1.12 – (a) Scattering spectra of a silver spheroid of AR=4 in a glass environment excited at different incidence angles of a p-polarized electric field. (b) Plasmon modes representation of amplitude and x-component of the electric field maps, at optimal angle and frequency. (c) Two-dimensional far-field radiation pattern in the XY plane for each mode at the optimal angle.

Far-field radiation patterns are presented in Figure 1.12.c in the XY plane and show how the radiated light from the nanostructure is emitted into the far-field. Here, the dipole typically emits as a donut shaped pattern, with a maximum of the scattered signal in the direction perpendicular to the dipole axis, as well as the sextupole mode. For the quadrupole mode, the maximum is emitted within an angle around 45° from the spheroid axis [66].

It is clear that manipulation of the shape, dimensions, metal nature and environment allows controlling the light emission under a certain directivity, characteristic of the field scattered by a metallic elongated nanostructure. Finite plasmonic nano-object also offers strong confinement of the EM field, characterized by the enhancement factor. With an adequate choice of all the plasmonic parameters, we can tune the scattering and near-field enhancement over the entire visible spectrum. Finite and elongated metallic nanostructures are thus considered as the building blocks of optical nano-antennas.

1.4.2 Optical nano-antennas

It is interesting to note that for strongly elongated particles, the quasi-static approximation eventually breaks down. To provide a qualitative understanding of the longitudinal LSPR, we focus on the example of a long nanorod assimilated to a finite wire supporting SPP since it is excited by a polarized side illumination. The extremities of the wire act as discontinuities at which the mode is partly reflected depending on the geometry. Called Fabry-Pérot cavity, the condition for longitudinal resonances can be expressed as [67]:

$$k'_{lsp}(\omega)L + \Phi_R(\omega) = n\pi \tag{1.21}$$

with L the rod length and n the order of the resonance. For a fixed rod length, the respective resonances can be found, called dipole for the first order $n = 1$, quadrupole $n = 2$, sextuple $n = 3$, etc. $\Phi_R(\omega)$ corresponds to reflexion coefficient that depends on the exact geometry of the extremities. The resonance efficiency of Fabry-Pérot resonators is limited by. In the case nanorod antennas, three different ways for losses affect the plasmon frequency: (i) the radiative damping due to oscillating electron, (iii) ohmic losses due to absorption of metal at optical frequencies, and (iii) reflection losses at the particle extremities, similar to mirror losses in conventional optical Fabry-Pérot cavities [68]. This plasmonic cavity can be considered as an antenna for optical frequencies and has many applications, such as high-resolution spectroscopy [69], optical sensors [70], photovoltaics [71], or lasing [72].

In the same way than their radio wave analogs, optical antennas mediate the information contained into the far-field [73]. Optical antennas then convert propagating optical radiation to localized near-field, and vice versa [74]. Radio antennas are metal-independent as used metals can be considered as perfect conductors for radio frequency waves.

Moreover, radio wave antennas are designed with a size proportional to the half-wave of the incident wavelength $L = n\lambda/2$. Again, this fails at optical frequencies because the penetration of EM waves into metals has to be considered. For a finite plasmonic nanowire, there is a delay between the excitation field and the response of the electron motion. Lucas Novotny showed that electrons do not respond to the wavelength λ but to an effective wavelength λ_{eff} [75]. The effective optical half-wave that interacts with the antenna is then $\lambda_{eff}/2 < \lambda/2$, depending on geometrical factors. For Au nanowire with a radius of 10 nm longitudinally excited by illumination at 800 nm, For instance, then the effective wavelength

is about 230 nm. Rather than $\lambda/2$, the Au nanowire must then exhibit a length $L_{rod} = \lambda_{eff}/2 \sim 115nm$.

Conclusion

In this chapter, we have introduced the concepts of the light diffraction limit inherent to standard optical microscopes imposing a spatial resolution of sample imaging around $\lambda/2$. Scanning probe microscopy (SPM) breaks the diffraction limit by using a very sharp probe with a sub-wavelength apex. These techniques collect information on the sample surface with a lateral nanometric resolution. Nevertheless, SPM gives only physical information while chemical data still required EM excitation to reveal crystalline structures or molecular vibrations of a sample.

However, we have explained the concept of near-field and evanescent waves nearby small aperture or object with a sub-wavelength dimension. Evanescent waves have the characteristic to enhance the surrounded EM field locally and can be used as a (nano)sources for local spectroscopy. SPM technology and near-field optics form together scanning near-field optical microscopy (SNOM) which allows a precisely manipulate the EM *hot-spot* over a sample.

We have also introduced the plasmonic theory which also deals with the near-field optics. An illuminated metal/dielectric interface generates surface plasmon either propagating along a surface or localized nearby an isolated nanoparticle. We have seen how localized surface plasmon resonances strongly depend on the shape, size, and nature of each material (metal, media, substrate). With a plasmon responding in the visible range of the spectrum, optical nano-antennas offer a large number of applications that required strong EM confinement and directivity of the far-field scattering.

We will see that the heart of the thesis deals with a single optical nano-antenna, specifically designed to efficiently enhance the EM field in the visible range, that constitutes the apex of an AFM probe to perform both s-SNOM experiments on Raman spectroscopy with topography imaging.

Chapter 2

Application to Enhancement of Raman Scattering

2.1 Raman scattering

2.1.1 Introduction

Basic concepts: When a medium or an object is illuminated by light, the interaction can produce many kinds of optical phenomena. Light can indeed be reflected, transmitted, absorbed, re-emitted (through fluorescence or luminescence) and scattered, depending on its energy and frequency, but also on material properties. All these effects help us to better understand the nature of light-matter interactions and the inner structure of materials. The scattering effect is a common phenomenon in nature that appears when particles hits a in a certain direction. This direction and even the energy of this particle may be changed due to the interaction, and these changes may inform us on properties that concern either the particle and the target. Spectroscopy is thus defined as being the study of these interactions. Based on the different kinds of incident particles, scattering can be categorized as neutron, electron, and photon scattering. Photon represents the quantification of the electromagnetic energy of light, and its scattering can be sub-divided into gamma, X-ray and visible light scattering. Each of these bands of energy gives different information. For instance, X-rays are suitable for detecting atoms or ions in the matter to inform us of their arrangement in space by diffraction, while visible light is suitable for studying the molecular vibrations. Since AFM probes for Raman spectroscopy is the final aim of this thesis, we will see that only a small range of electromagnetic waves are concerned by such interactions, located around the visible spectral range, from near ultraviolet (UV) until near infrared (IR), leading *in situ* analysis.

Chandrasekhara Venkata Raman reported in 1928 the light-scattering phenomenon known today as the Raman effect [76], which led him to win the Nobel prize in Physics in 1930. His discovery was not based on theoretical expectations but only on experimental work in which the molecules scatter light in liquids or gases. In addition to a diffuse radiation having the same wavelength as the incident beam, he observed a "new scattered radiation" with a different frequency. He has deduced it from the observation of a narrow range of wavelengths separated from the incident beam by "a dark space" between lines from a mercury lamp spectrum. Any line is accompanied by other lines (more or less intense) which satisfy the famous relation:

$$\omega_{Raman} = \omega_{excitation} \pm \omega_{vibration} \tag{2.1}$$

which describes the exchange of energy between the incident light and the scattering medium corresponding to vibration energies of the molecules. Indeed, each molecule bond vibrates at a specific frequency which depends on the nature of involved atoms but also the molecule geometry. Thus, each mode of molecular vibrations corresponds to a specific energy.

Nowadays, these energies are known and constitute references – depending on the used method – which makes possible the recognition of vibration modes of unknown samples and enables, for instance, a chemical identification, called vibrational spectroscopy. Among light scattering effects, Raman scattering is a fundamental form of spectroscopy. It is a very versatile, non-destructive technique and does not require specific sample preparation [77].

Concerning chemical identification, the predecessor of Raman spectroscopy is infrared (IR) spectroscopy, based on the light absorption by matter involving a single photon (one-photon event). An IR photon can disappear when it meets a molecule by being absorbed entirely, elevating then the molecule in a higher vibrational mode by a value corresponding to the photon energy. In contrast, Raman scattering is a two-photon event which comes from the change in the molecule polarizability with respect to its vibrational motion direction. To obtain these properties in Raman spectroscopy, the sample is illuminated by a laser beam with an energy $\hbar\omega_0$. During interaction with an external source, the polarizability generates an induced dipole moment in the molecule. The light scattered by this dipole consists of altogether Rayleigh and Raman scattering. Rayleigh scattering, mostly privileged compared to Raman scattering, corresponds to the light scattered with the same frequency than the excitation light (elastic scattering), whereas the Raman light is shifted in frequency and, hence, in energy (inelastic scattering). Just a single photon over 10^7

comes from Raman scattering, which explains the known intrinsic weakness of the Raman efficiency, depending on the laser intensity and the number of molecules. The frequency difference between Rayleigh and Raman photons corresponds thus to a gain or a loss of the incident energy by a value equal to the vibrational state of the molecule $\hbar\omega_k$.

As represented in the energy-level diagram in Figure 2.1.a, Rayleigh and Raman scattering are both generated after an incident photon with an energy $\hbar\omega_0$ is absorbed to elevate the molecule from the fundamental vibration state (real energy state - black lines) to a virtual energy state (dashed lines). Rayleigh photon is emitted with the same energy than the excitation $\hbar\omega_0$ restoring the initial vibration state of the molecule. Both IR absorption and Raman scattering are involved in the passage from one vibrational state (initial state, $\nu = 0$) to another (higher state, $\nu = k$). While IR absorption achieves this passage by a single step (black arrow) – with an energy equal to the energy of one vibrational state – scattering involves two steps from two photons with much higher energy than the IR photon, one regarding the excitation and the other for the scattered radiation. This scattered photon with a loss is frequency/energy is called Stokes Raman scattering (green arrow), whereas with a gain corresponds to anti-Stokes Raman scattering (purple arrow). In the spectrum, the energy positions of the Raman peaks $\hbar(\omega_0 \pm \omega_k)$ are symmetric with respect to the Rayleigh scattering due the Stokes and anti-Stokes mechanisms, which lead to respectively a positive or negative value of the frequency-shift for the same vibration mode.

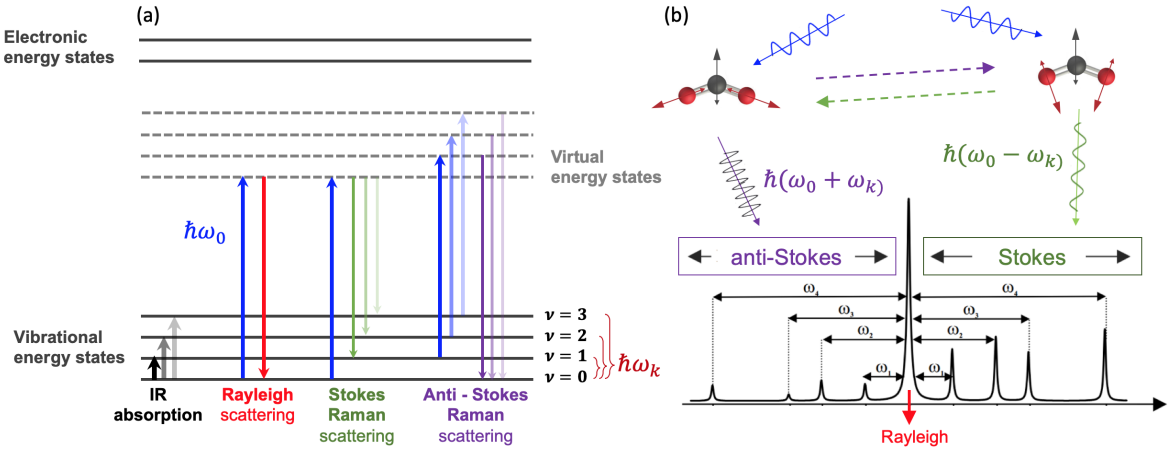

FIGURE 2.1 – (a) Diagram based on real (black) and virtual (grey) energy states. (b) Illustration of Raman scattering process, taking as an example the case of a water molecule under two successive vibration modes. Blue, green, and purple arrows respectively correspond to the excitation, Stokes and anti-Stokes Raman scattering

In addition, the schematic illustration of the spectrum in Figure 2.1.b illustrates differences regarding the peak intensities where Stokes peaks (I_S) are much more intense than anti-Stokes ones (I_{AS}). The Stokes/anti-Stokes intensity ratio defined by the Bose-Einstein distribution function represents the occupation of particles in available discrete energy states (phonons), such as :

$$\frac{I_{AS}}{I_S} = C\frac{n_k}{1+n_k} \quad ; \quad n_k = \frac{1}{e^{\frac{\hbar\omega_k}{k_B T}} - 1} \tag{2.2}$$

with k_B the Boltzmann constant, T the temperature, C a proportionality constant depending on the setup, and n_k the vibration state population at the level $\nu = k$, i.e. a phonon with an energy $\hbar\omega_k$. If phonons have energies larger than the thermal energy $k_B T$, then $n_k \ll 1$ and then the Raman scattering under Stokes mechanism is much more intense than anti-Stokes. A higher energy state has thus less probability of being populated than a lower state, thermally dependent. The ratio should be close to 1 for temperature high enough to activate a large population of phonons over higher states.

Today, Raman spectroscopy has numerous advantages, such as being a relatively fast technique and adequate for studying solids, liquids, solution, and gases. For solids, only a positioning under the microscope and a focused monochromatic light are required. In contrary to IR spectroscopy, liquids can be measured through the glass and the water does not disturb the measurements.

However, there are some selection rules which allow or not a vibration to be excited under Raman spectroscopy (the transition is referred to as Raman-active). To understand which are the authorized vibration modes of the molecule, we introduce the dipolar moment $\boldsymbol{\mu}_{ind}$ induced on the molecule by the incident electric field $\mathbf{E}$:

$$\boldsymbol{\mu}_{ind} = \overline{\overline{\alpha}} \cdot \mathbf{E} \quad ; \quad \text{with} \;\; \mathbf{E} = \mathbf{E}_0 \cos(\omega_0 t) \tag{2.3}$$

with $\overline{\overline{\alpha}}$ the polarizability tensor which is specific to the molecule. Depending on the molecular symmetry, the tensor can be expressed as:

$$\overline{\overline{\alpha}} = \overline{\overline{\alpha}}_0 + \sum_{k=1}^{N} \left(\frac{d\overline{\overline{\alpha}}}{dQ_k}\right)_0 \cdot \mathbf{Q}_k \quad ; \quad \text{with} \;\; \mathbf{Q}_k = \mathbf{Q}_k^0 \cos(\omega_k t) \tag{2.4}$$

with N the number of possible vibrations ω_k, and with Q_k the amplitude vibration of the mode from the original position Q_k^0. By introducing this expression into Eq. 2.3, we can express the induced dipolar moment of the molecule as:

$$\boldsymbol{\mu}_{ind} = \overline{\overline{\alpha}} \cdot \mathbf{E}_0 \cdot \cos(\omega_0 t) + \frac{1}{2} \sum_{k=1}^{N} \left(\frac{d\overline{\overline{\alpha}}}{dQ_k} \right)_0 \cdot (\mathbf{Q}_k^0 \cdot \mathbf{E}_0) \cdot [\cos(\omega_0 - \omega_k)t + \cos(\omega_0 + \omega_k)t] \tag{2.5}$$

The scattered light intensity is directly related to the induced dipole. We can observe in Eq.2.5 that the dipole is defined by three terms with different frequencies corresponding to the three kinds of light scattering – Rayleigh (ω_0), Raman Stokes ($\omega_0 - \omega_k$), and anti-Stokes ($\omega_0 + \omega_k$). We can then deduce the selection rules of the inelastic scattering: only vibration modes that modify the molecular polarizability of the molecule are 'active' in Raman spectroscopy; i.e., when:

$$\left(\frac{d\overline{\overline{\alpha}}}{dQ_k} \right)_0 \neq 0 \tag{2.6}$$

Moreover, if the dipolar moment does not change during the vibration of the molecule – meaning that there is a center of symmetry of the vibration mode – it is a Raman active vibration. If the mode does not have such symmetry, the dipole changes and vibration is also IR active.

Figure 2.2 presents and compares Raman and IR spectra obtained on mesitylene molecules. We observe that certain peaks are present in one spectrum but not in the other. Usually, IR spectra are obtained in transmission configuration leading to a curve with several dips for the frequencies for which the molecules have absorbed to move to a higher vibrational states. Each transition of vibration mode corresponds to a specific wavelength, so IR spectroscopy requires excitation over a broadband spectrum to cover a maximum of vibrational energies. For Raman spectra, vibration modes are identified with emission of the sample after excitation (using either by reflexion, transmission configuration), the results consists in a curve with a peak for each detected mode. Raman has this advantage to obtain an important number of identified vibrations using a unique (up to a few) visible laser(s). Both IR and Raman spectra plot the intensity in term of wavenumber (in cm^{-1}) such has:

$$\begin{aligned} \bar{\nu}_{vib,\,\mathrm{IR}}\,(cm^{-1}) &= \frac{10^7}{\lambda_{0,\,\mathrm{IR}}(nm)} \\ \Delta\bar{\nu}_{vib,\,\mathrm{Raman}}\,(cm^{-1}) &= \pm 10^7 \left(\frac{1}{\lambda_{0,\,\mathrm{VIS}}(nm)} - \frac{1}{\lambda_{\mathrm{S\ or\ AS}}(nm)} \right) \end{aligned} \tag{2.7}$$

In the case of IR absorption, we express the spectra in terms of the wavenumber

$\bar{\nu}$ of the absorbed IR wavelength $\lambda_{0,\,\mathrm{IR}}$. Whereas, for Raman scattering, we called the spectra in term of Raman-shift $\Delta\bar{\nu}$ which refers to the emitted Stokes or Anti-Stokes radiations slightly shifted from the visible excitation wavelength $\lambda_{0,\,\mathrm{VIS}}$.

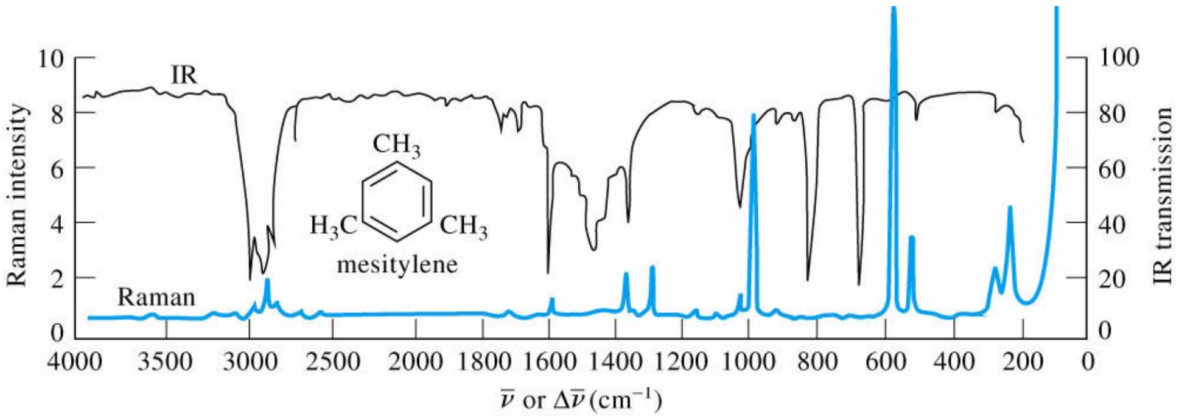

FIGURE 2.2 – Comparison of Raman and IR spectra for mesitylene
@2007 Thomson Higher Education

With a better selectivity than IR spectroscopy, parasite interferences coming from the experiment or the preparation method of the sample do not exist with Raman spectroscopy. For some molecule (centrosymmetric) a vibrational mode may be either IR active or Raman active but not both. Raman and Infrared analysis are then complementary and allow a complete study of the vibrational modes of the studied sample.

Applications: Typically, Raman spectroscopy probes chemical properties of a material and gives information regarding the structure, phase, polymorphism, intrinsic stress, contaminations or impurities in the sample. Since a Raman spectrum can be assimilated to a chemical fingerprint of a molecule, it can be used to identify materials or distinguish them from each other quickly. Spectral libraries containing thousands of reference Raman spectra are used to find a match with the acquired spectrum and identify which molecules compose the sample.

Raman spectroscopy can also provide stress measurements on silicon-based materials, a topic of interest for micro-electromechanical systems community [78, 79]. Some of the results from works of both research teams led by Kilian Wasmer et al. from Switzerland [80] and Qiu Li et al. from China [81] are presented in Figure 2.3.

The former combined nanoindentation and Raman spectroscopy to locally detect microstructural changes – such as phase transformations and stress gradients –

induced by uniaxial stress (compression) applied to silicon micro-pillars. The shift study of Raman peaks – the ability to shift peaks of Raman spectrum from an initial position while the sample undergoes any kinds of external modification – is in agreement with the applied stress. A correlation between cracks formation and dislocation activity was observed (see Fig. 2.3.a).

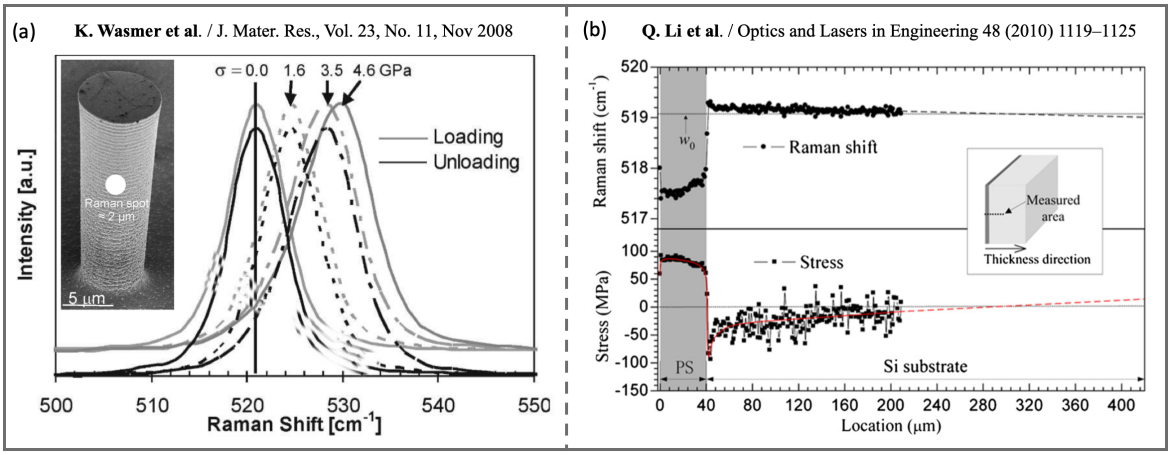

FIGURE 2.3 – Adapted from K. Wasmer et al.: (a) SEM image of micro-pillar subjected to a compressive stress of -4.6 GPa with the Raman spot represented in white. Raman shift measured during loading–unloading with a velocity of 0.7 mN.s^{-1} and a maximum load of 200 mN. Adapted from Q. Li et al.: (b) The distribution of (upper part) Raman shift and (lower part) residual stress in the PS-film structure along the thickness direction (the red line indicates the change trend of residual stress).

The latter uses micro-Raman spectroscopy to numerically and experimentally establish a relation between Raman shift and stress on porous silicon (PS) layer deposited onto silicon. Raman spectroscopy was performed to measure the distribution of the residual stress along the depth in the structure which is in agreement with stress measurements (see Fig. 2.3.b). The results show evidence of residual stress inside the PS layer which drastically switches from tensile into compressive stress on each side of the interface. These results demonstrate that Raman scattering combined with mechanical forces is an efficient technique to determine material properties in the micrometer range, and identify crack propagations for potential process control.

2.1.2 Instrumentation and limit of confocal microscopy

The current implementation of Raman spectroscopy is significantly different from earlier approaches. Since the first experimental demonstration of the Raman effect, the first improvements were made by the use of mercury lamps as excitation sources. However, optical alignments required for measurements remained difficult and Raman spectroscopy historically a restricted research topic, leaving IR spectroscopy as being the commonly used technique in the 1960s. With lasers development and their availability at the end of the 1980s, instrumentation has evolved significantly, which has consequently reduced the size of samples and the duration of the acquisition. Later, progress has also been brought by new optical filters, detectors, and various optical components.

Lasers and filters: The evolution of equipment that enables routine Raman spectra – recorded in few seconds or minutes – took about half of a century to be developed due to the weakness of the Raman signal itself. For this purpose, the excitation source ideally should be intense, coherent, polarized, and monochromatic with small divergence. Two main kinds of Raman spectrometers co-exist depending on the wavelength of the laser λ. Raman spectrometers based on a dispersive optical component can be used with lasers from UV (200 nm) to the near-IR (1064 nm), while Fourier-transform (FT-) Raman spectrometers are involved for the largest wavelengths (up to the near-IR), described later. The choice of laser wavelength strongly affects the scattering efficiency, since Raman intensity is inversely proportional to λ^4 [82]. Thus, Raman scattering might be 15 times less intense using IR rather than blue or green lasers. Moreover, the laser needs also to be in adequacy with the detectors which signal-to-noise ratio and sensitivity are also wavelength-dependent. Regarding the sample, lowest frequencies (red, near-IR) are used for fluorescence suppression, while higher (blue, green) are adapted for inorganic material. With UVs, it is also possible to study bio-molecules, such as proteins or DNA, but also probe thin surface layers of semi-conductor samples, due to the very small penetration depth of the UV light.

With the selected laser, a suitable filter must be placed in the Raman beam path to block the scattered laser line from the Rayleigh scattering and only let the inelastically scattered photons go through to the spectrometer and detector (see Fig. 2.4). Two main kinds of filters can be used: edge filters or notch filters. The former absorbs all light up to a specific value of wavelength while the latter has a sharp and discrete absorption band that coincides with the excitation laser. Notch filters have,

hence, the advantage to allow measurement made for both Stokes and anti-Stokes Raman scattering, whereas edges filters limit experiments to study only one of these scattering groups, either with long or low pass filters.

Components must be selected according to the tasks and options. There are two main types of spectrometers on the market based on back-scattering detection to focus the laser beam on the sample and also to collect Raman photons. With the general set-up in Figure 2.4, we described: (i) dispersive spectrometers and (ii) Fourier-transform Raman spectrometers.

Dispersion systems: Any spectrometer analyze the collected light as a function of their wavelength. This chromatic analysis can be made as a function of space (with light diffraction) or time variation (with FT). The simplest dispersive instrument is a prism – or a grating nowadays – where the angle of refraction – or reflexion – of light is wavelength dependent (see Fig. 2.4, orange dashed frame). A diffraction grating consists of a repetition of reflective lines (called grooves) where the distance between them matches with the visible wavelengths range. The groove periodicity gives rise to constructive or destructive interferences depending on the incident angle and, obviously, the wavelength. Each one will be further focused into the detector at thus different locations (space-function). Then, a rotation of the grating allows the selection of the spectral range of the acquisition, while groove spacing affects the spectral resolution as well as the spectrum width.

With regards to FT-Raman instruments, spectral analysis is given through a Michelson interferometer constituted of two mirrors, one fixed and one translating during the experiment, and a beam-splitter (BS) (see Fig. 2.4), purple dashed frame). With a laser as an excitation source, the recombined beams – after separation by the BS and reflexion onto both mirrors – are out of phase (time-function) with each other depending on the displacement of the mobile mirror. According to the difference between beam path-lengths, the different interferences lead to the detector records the Raman signals or not. During Raman experiment, all frequencies of the scattered light from the sample give a specific fringe pattern to be superimposed and form an interferogram. These data undergo then a Fourier-transform to obtain the Raman spectrum. The spectral resolution here depends on the translation distance that the mirror is traveling. Indeed, the more fringe patterns collected at different distances to form this interferogram, the more precise is the chemical analysis.

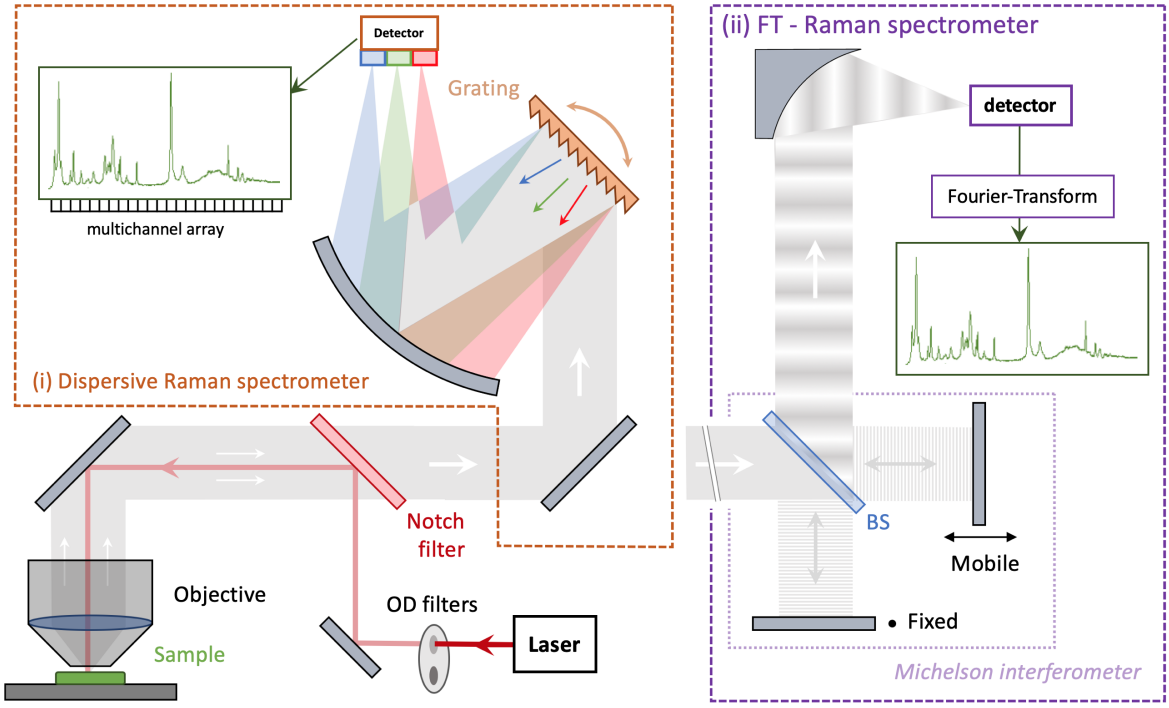

FIGURE 2.4 – General set-up of a dispersion and a Fourier-transform Raman spectrometers

Detectors: it is crucial to have sensitive detectors due to the very weak Raman signals. In addition to high quantum efficiency, it is also essential to have a low dark signal generated by the detector – not exposed to light – which is sensitive to the temperature, and this is at the origin of noise signals. Therefore, these detectors are cooled using, for example, liquid nitrogen. Charge-coupled device (CCD) is a kind of multi-channel detectors consisting on a two-dimensional array of optical elements called single-channel detectors – based on photomultiplier tubes or semiconductor (silicon) – sensitive to a specific wavelength each and create detectable electron/hole pairs. To avoid parasitic fluorescence signal – produced by an electronic transition, more intense than molecular vibration – it is common to use an excitation with higher wavelength, insufficient to excite the molecule to an excited electronic state. When the excitation wavelength is too large, detectors based on other semiconductors can be used (e.g., InGaAs, Ge) with a forbidden band (band gap) small enough to create detectable electron-hole pairs.

Confocal Raman microscopy: The principle of Raman microscopy consists of a sequence of Raman spectra with a displacement of the excitation spot along the sample between each spectrum. The exact position of the spot, as well as all information into each corresponding spectrum, can be retrieved to form a Raman mapping. Indeed, all pixels of the image contains a complete spectrum and can be interrogated,

all together or individually, according to specific properties, such as the intensity of several characteristic peaks. A false-color image can then be generated by assembling each pixel according to the coordinates of the acquisitions (2.5.a). Raman spectral imaging can hence perform detailed images of the sample based on its composition or structure.

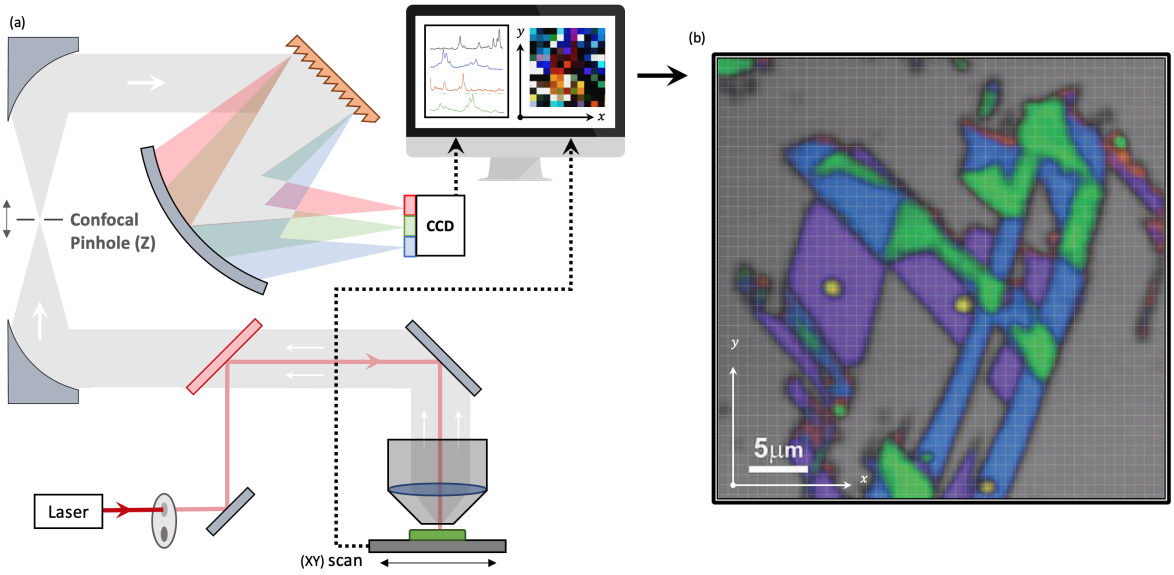

FIGURE 2.5 – (a) General diagram of confocal Raman microscopy. (b) 256 × 256 points Raman mapping of superimposed graphene flakes.

For instance, as presented in figure 2.5.b, Raman signal leads to the imaging through chemical information of graphene flakes, where the number of layers superimposed can be distinguished – mono-, bi, and tri-layers respectively in purple, blue, and green – as well as structural defaults and impurities (in yellow) – Copyright HORIBA Scientific. Here, we quickly understand that size of the laser spot should affect the so-called spatial resolution of the Raman imaging (see § 1.1.1).

For instance, a 633 nm laser with a standard 0.9/100x objective would predict a spatial resolution of 429 nm. Unfortunately, incoming laser and out coming scattered light undergo many interactions with the sample interfaces as well as with optical components that constitute the microscope, and this can reduce the resolution. Thus, typical spatial resolution for Raman spectroscopy is often quoted as being around 1 μm. We can note that this law is only related to lateral (XY) resolution. It is more complicated for the depth (Z) resolution since it strongly depends on the confocal configuration of the experimental set-up. By using an adjustable confocal pinhole aperture after the couple of optical lenses (objective and tube lens)

of the microscope (see Fig. 2.5.a), it is possible to probe the volume of a transparent-enough sample by a simple translation of the pinhole along the optical path, or the substrate holder along the vertical direction. Depth resolution is located between 1 and 2 μm which allows mapping individual thin layers of the sample to then form a 3D imaging.

Co-localized AFM et Raman: Raman imaging and atomic force microscopy (AFM), or any SPM, can be combined to form a system providing new capacities to collect chemical and physical information on the same area altogether. Co-localized AFM et Raman measurements [83] can be performed through either successive or simultaneous acquisitions and allow overlapping of AFM and Raman maps matching pixel-to-pixel. On one side, confocal spectroscopy provides Raman chemical information form local analysis or imaging with a spatial resolution led by the Rayleigh criterion ($< \mu$m); on the other side, AFM gives access to topographic, mechanical, thermal, electrical and magnetic information with a spatial resolution down to few nm.

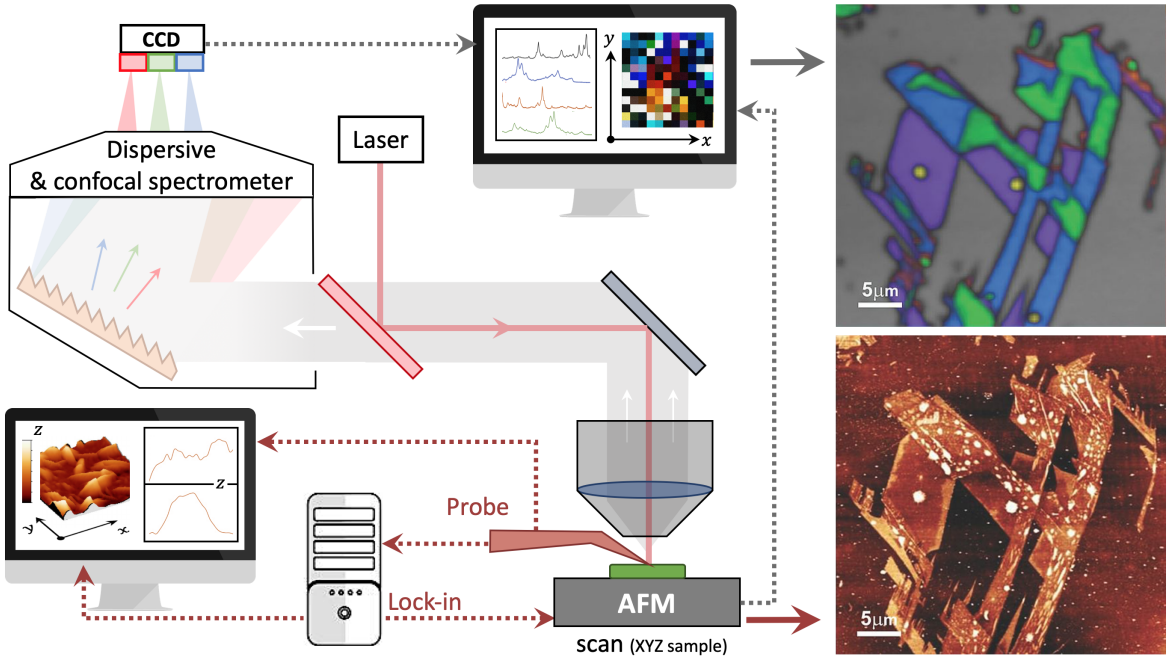

FIGURE 2.6 – General diagram of co-localized AFM et Raman resulting of 256 × 256 points simultaneously acquired topography and Raman mapping of superimposed graphene flakes.

One possible set-up configuration is illustrated in Figure 2.6 and based on the previous example. Regarding Raman mapping, Raman spectra are collected while

the scanner of the AFM provides the piezoelectric displacement along the same area. Concerning the AFM part, the XY scan is led by either substrate holder or tip holder and provides topography – or any kind of physical properties – by recording the interactions of the probe in contact with the surface of the sample during the scan. Here, the probe-sample distance data are then combined with the lateral displacement of the substrate to form a high resolved physical imaging. We then obtain two images of graphene flakes containing information of different natures with a perfect overlapping at a sub-micrometer scale.

Today, providing chemical data at the nanometric scale is one of the biggest challenges in the Raman community. Beyond the spatial resolution limit that is imposed by the light diffraction phenomenon, there is also exists the issue regarding the very low Raman cross-section, which is weaker as we go down through the scales until the intensity of the Raman signal cannot be resolved anymore with the noise signal of the detector. Indeed, for quantitative Raman analysis, we can study the intensity of a spectrum which is proportional to the concentration of the molecule in the sample.

2.2 Surface Enhancement Raman Spectroscopy

2.2.1 Mechanisms of Raman signal enhancement

In 1974, Fleischman et al. recorded an unexpected strong Raman scattering on a monolayer of pyridine adsorbed on a rough silver electrode, by a factor of 10^6 times compared with the pyridine without of the metal [84]. It is well known today that this amplification effect is due to the excitation of surface plasmons of the metallic substrate [85]. Surface Enhancement Raman Spectroscopy (SERS) is a technique which enhances the Raman scattering of molecules when deposited on rough patterned metal surfaces, usually by noble metals (e.g., gold, silver) nanoparticles. This technique can be used to sensor application. It is important to choose the nature of the metal, the particle size or the roughness of the substrate, altogether with adequate laser wavelength. As seen before (§ 1.4.1.2), silver substrates (respectively gold substrates) are more efficient while using green or blue lasers (respectively red lasers).

The adsorbed molecules are assumed to be located in a favorable environment where the EM field is intense and locally confined by localized plasmon modes. For

example, metallic cracks on surfaces or junctions between nano-structures exhibit the highest field enhancements [86]. Today, SERS is a technique which offers improvement of many orders of magnitude in Raman intensity with an enhancement factor typically around 10^6-10^7. SERS and coherent anti-Stokes Raman scattering (called SECARS) can be combined to lead to an EF around 10^{10} [87], while combined with resonant-Raman effect (called SERRS) allows to further improve signal up to 10^{12} [88]. However, two independent works have reported giant EF of 10^{14}, which are sufficient to allow very sensitive detection down to a single molecule [89,90].

The Raman-scattered field is generally assigned to from either chemical and/or electromagnetic mechanisms. The former mechanism is based on the formation of chemical bonds between the adsorbed molecule and the metal, allowing charge-transfer excitations. The latter, which is widely predominant [91], is related to surface-plasmon excitations at the metal-dielectric interface.

Chemical enhancement: Due to interactions between the adsorbed molecule and the metal surface of the substrate (physisorption or chemisorption) chemical contribution participates for an enhancement factor up to 100. Physisorption is relative to weak interactions (e.g., dipole-dipole effects, electrostatic, or Van der Waals interactions) and chemisorption explains the chemical bonds origins between the molecule and the substrate. It is then possible to use Raman spectroscopy to measure such bonds. Moreover, some anisotropic molecules have a preferential orientation once grafted on a substrate which affects the enhanced Raman signal.

Another effect is due to charge-transfer considering the overlapping between electronic orbitals of the molecule and the metals. Since interaction between molecules and the metal can disturb the electron cloud of the molecule, electronic levels can shift until the resonance conditions are fulfilled. Besides, there are possible excitations to a (real state) energy level in the conduction band of the metal, which contributes to the enhancement phenomenon.

Field Enhancement: The measured Raman signal is proportional to the intensity of the electromagnetic field. A field enhancement occurs for roughened or nanostructured metal surfaces – leading propagating or localized (*hot-spots*) evanescent waves – which increases the EM intensity experienced by the analyte molecules. Figure 2.7 presents an illustration extracted from the review of Jian-Feng Li [92], synthesizing the two main SERS configurations corresponding of both natures of

surface plasmons.

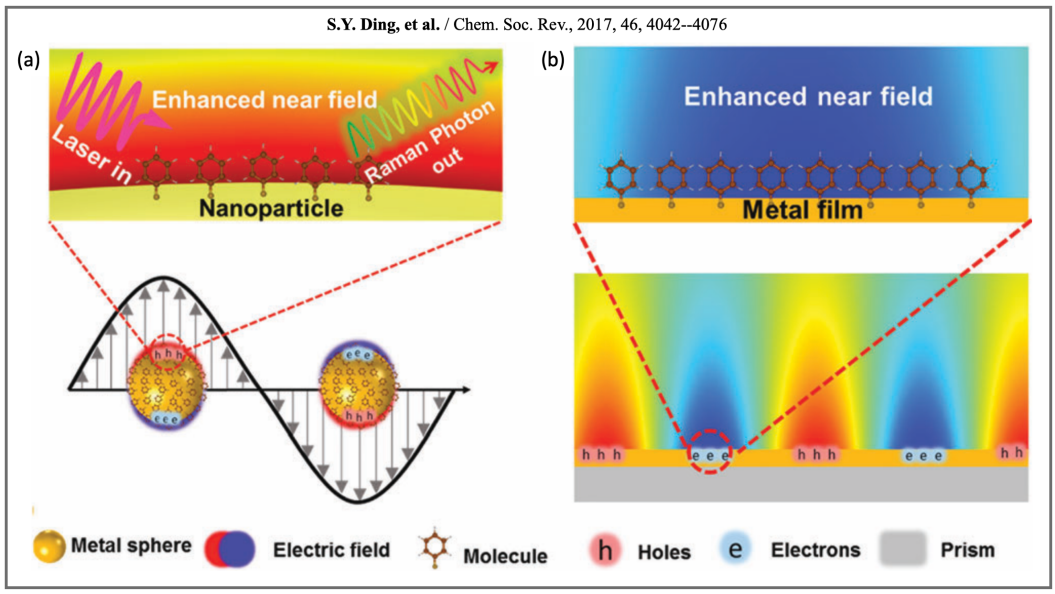

FIGURE 2.7 – Adapted from S.Y. Ding et al.: Enhanced Raman scattering effect due to the excitation of (a) LSP at a Au nanosphere/air interface or by (b) SPP excited by incident laser beam at Au thin film/prism interface in the Kretschmann mode (see § 1.3.2.2).

EM enhancement can be localized nearby metallic nanostructures (LSP – see Fig. 2.7.a) in which electrons oscillate over the nanostructure surface, or propagating along metallic surfaces (SPP – see Fig. 2.7.b). Since metallic surfaces are functionalized with molecules, the induced EM source interacts with them in addition to the EM field of the excitation laser.

Raman-active molecules interact with the enhanced near-field, the inelastically Raman scattering occurs, and emitted light can interact with the plasmon modes of the metal. In this case, it is commonly known that Raman scattering enhancement is proportional to the fourth power of the electric field EF [93,94] when the incident and scattered frequency match or are close to the plasmon frequency, based on a complex scalar phenomenological theory [95]. However, this mechanism can be easily explained by a two-step EM process.

According to the electromagnetic model presented in Figure 2.8, we take as an example the case of molecules in the vicinity of a metallic nanosphere. First, the enhanced Raman scattering arises from the incident EM field $\mathbf{E}_i$ with a frequency corresponding to the plasmon resonance ω_{LSP}, and generating a local field (red)

scattered by the nanostructure into the far field $\mathbf{E}_{i,scat}$.

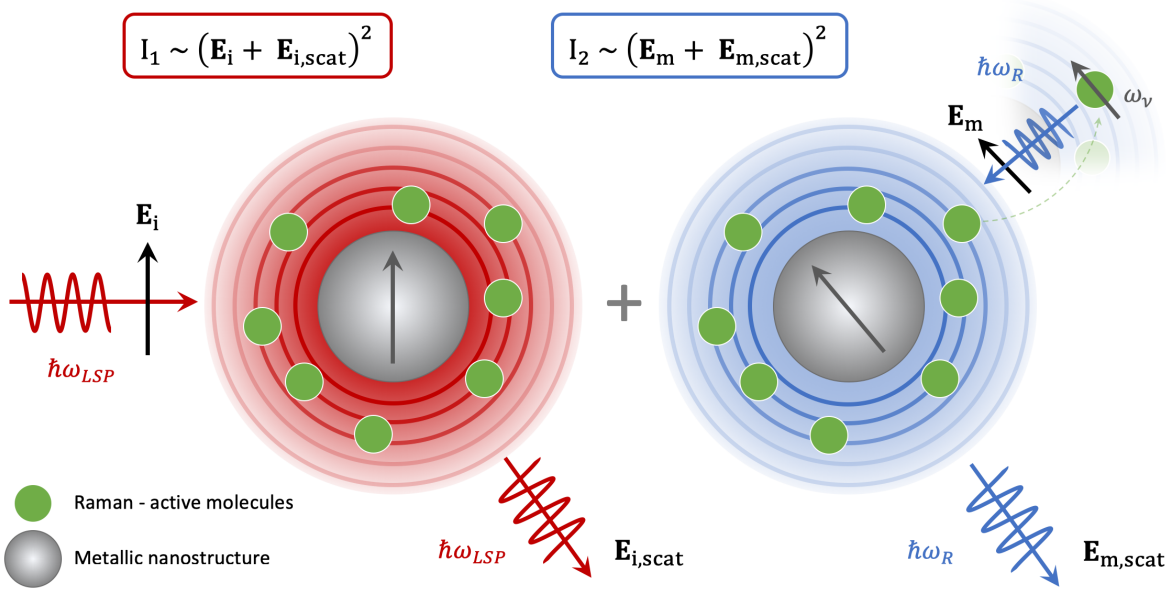

FIGURE 2.8 – Illustration of the two-step process EM enhancement involve during SERS experiment in the case of molecules nearby the surface of an Ag nanosphere. A first enhancement is originally due to the excitation laser set at the plasmon frequency (in red) and the second due to the Raman scattered light from the molecule at the Stokes or anti-Stokes frequency (in blue).

A first enhancement factor EF_{LSP} can then be established assuming that $|\mathbf{E}_{scat}| > |\mathbf{E}|$ such as:

$$EF_{LSP} = \frac{|\mathbf{E}_i(\omega_{LSP}) + \mathbf{E}_{i,scat}(\omega_{LSP})|^2}{|\mathbf{E}_i(\omega_{LSP})|^2} \approx \frac{|\mathbf{E}_{i,scat}(\omega_{LSP})|^2}{|\mathbf{E}_i(\omega_{LSP})|^2} \tag{2.8}$$

Firstly, the plasmonic nanosphere acts as a receiving optical antenna to transform the incident laser source into localized near-field, which can interact with the molecules by exciting their molecular induced dipole at the Stokes or anti-Stokes frequency $\omega_R = \omega_{LSP} \pm \omega_v$, with ω_v the vibration frequency of the molecule. Secondly, the emitted Raman field $\mathbf{E}_m$ from the molecules can also polarize the nanostructure. The enhancement phenomenon stems from the apparent Raman polarizability between the nanosphere and the molecules. It was observed that one or two orders of magnitude larger than the polarizability for isolated molecules. Then, the plasmonic nanosphere acts as an optical transmitter of the near field into the far field $\mathbf{E}_{m,scat}$. Like above, we establish a second enhancement factor EF_{mol} induced by the

molecular dipole as:

$$EF_{mol} = \frac{|E_m(\omega_R) + E_{m,scat}(\omega_R)|^2}{|E_m(\omega_R)|^2} \approx \frac{|E_{m,scat}(\omega_R)|^2}{|E_m(\omega_R)|^2} \tag{2.9}$$

The difference in terms of frequency between the incident light and the Raman signal determines the magnitude of the enhancement. This difference corresponds to the vibration frequency of the molecule ω_v. We can assume that $\omega_{LSP} \approx \omega_R$ since the frequency difference is very small compared to the excitation – or Raman – frequency. Then, both fields from the excitation and the molecular dipole can be nearly resonant with the surface plasmon. We then defined the total factor EF_{Raman} as:

$$EF_{Raman} = \frac{|E_{i,scat}(\omega_{LSP})|^2}{|E_i(\omega_{LSP})|^2} \times \frac{|E_{m,scat}(\omega_R)|^2}{|E_m(\omega_R)|^2} \approx \left| \frac{E_{i,scat}(\omega_{LSP})}{E_i(\omega_{LSP})} \right|^4 \tag{2.10}$$

and meet up the $|\mathbf{E}^4|$ enhancement law for SERS. The field enhancement associated with surface plasmons has hence been extensively used to increase the interaction between a molecule and optical radiation. Practically, the advantages of SERS can be implemented on any Raman spectrometer without changing parameters of basic Raman acquisition. It is essential to use a laser wavelength matching with the SERS substrate properties (metal and topography). For instance, silver provides the highest enhancement factor because of interband transitions which occur in the ultraviolet range. Then, there will be less absorption in the visible or near-IR Raman wavelengths, resulting in large SERS intensities in the blue-green range. Copper and gold have interband transitions for optical frequencies which results in a lower SERS intensity. Despite the greater enhancement capability of silver, gold is more often used due to its internal stability in ambient environments and its ease of use during the fabrication of SERS substrates.

2.3 Tip Enhancement Raman Spectroscopy (TERS)

2.3.1 Technique description

The investigation of chemical properties of molecules or individual nanostructures by Raman spectroscopy with a spatial resolution less than the diffraction limit requires an electromagnetic field confined at the nano-scale. This was introduced as tip-enhanced Raman spectroscopy (TERS) [96–99], a impressive analytical method for correlated chemical and physical surface mapping with nanoscale spatial resolution [100–103]. This technique is a combination of co-localized Raman microscopy and plasmonics properties of the SPM probe surface – such as with Apertureless SNOM probes § 1.2.1 – here called TERS probes. Such probes provide Raman signal amplification obtained by excitation of propagative and/or localized surface plasmons (SPP and LSP), resulting in an enhanced optical evanescent field confined in a nanometric volume at the tip apex, which governs the spatial resolution in TERS. The corresponding TERS amplification factor strongly depends on the shape of the tip, and ranges from 10^4 to 10^8 [104], enabling TERS mapping with a nanometric resolution [102, 105]. To better understand the TERS configuration, we based our description on the co-localized AFM-Raman configuration presented above in Figure 2.6. As a reminder, this set-up provides physical information down to the molecular resolution by using an AFM and other information given by SPM techniques such as STM, Shear-Force microscope.

It has been demonstrated with SERS that Raman scattering can be enhanced enough to detect very small amount of sample using localized enhancement field (hot-spots) acting as excitation nano-sources for the adsorbed molecules. If a very sharped tip, such as an SPM one, is made from a SERS layer then the enhancement effect is also expected nearby the tip extremity (or called apex) and generates a single *hot-spot*. Since the tip apex has sub-wavelength dimensions (a few tens of nm) the enhanced field also has similar dimensions and then can act as a single nano-source, with an ability for scanning the sample. Thus, TERS combines SERS and SPM probe and allows then the investigation of chemical properties of samples on a nanometric area – Nano-spectroscopy Raman – as well as to acquire discretized Raman spectrum of two successive points with spatial resolution related to the *hot-spot* size – working at Super-resolution Raman spectroscopy.

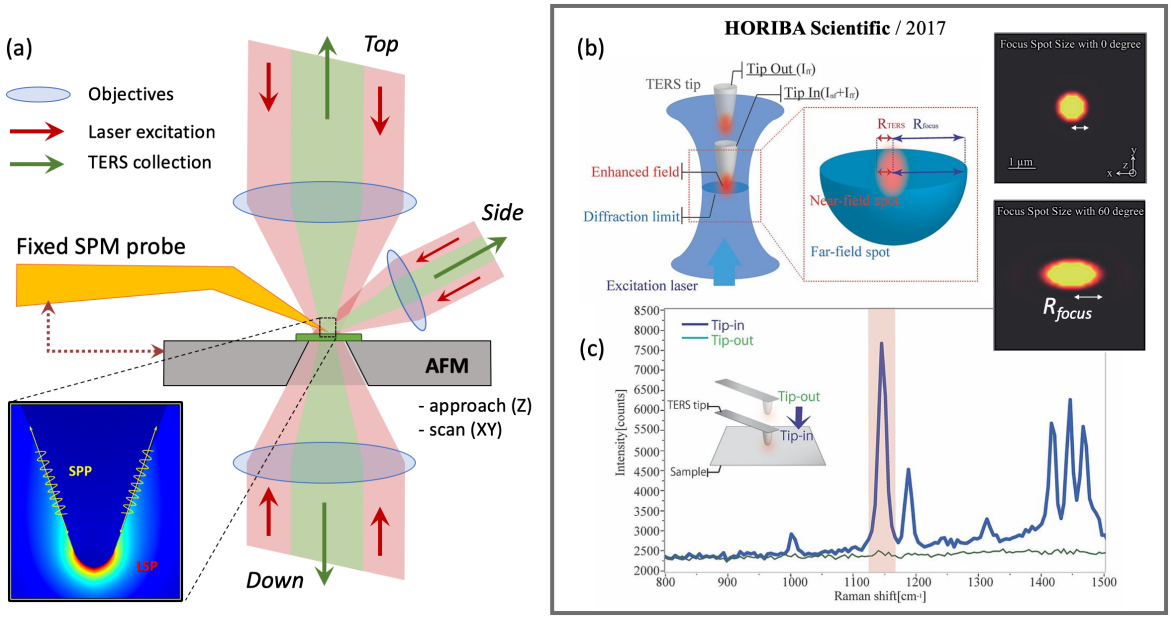

FIGURE 2.9 – (a) Illustration of the main TERS configurations, leading either top, down, or side excitation and collection. To keep the right laser-tip alignment, only the sample holder moves (piezo) in the three directions, i.e., in the XY plane for mapping, and Z for approaching the tip respecting the feedback guideline on the tip. (b) Schematic representation showing both far-field and near-field volume to consider for Raman scattering EF estimation – Copyright (2017) HORIBA Scientific. (c) Comparison of a Far-Field Raman scattering spectrum with the TERS spectrum of Azobenzene molecules grafted on a flat Au substrate – Copyright (2017) HORIBA Scientific.

The focusing of an excitation laser beam through standard microscope objectives towards the extremity of the plasmonic-active probe is usually required for TERS experiments. Among others, different configurations are possible corresponding to top, down, or side collection and excitation (see on Fig. 2.9.a). Combinations involving two objectives are possible, but the most common configuration is called back-scattering, in which the excitation and collection are done with a single objective, requiring then a different objective-tip alignment. As a function of the objective and laser wavelength, the spot size of the excitation is close to the Rayleigh criterion, such as $\sim$0.5 - 1 μm. The light-metal interaction generates evanescent waves at the air/metal interface of the tip, with a maximum of intensity at the correct polarization – i.e., an electric field along the tip axis. Two distinct mechanisms are involved in the enhancement field at the probe apex. Due to the geometric singularity of a sharp probe, the electrostatic lighting rod effect is combined with propagative surface plasmons (SPP) traveling along the tip combined with localized surface plasmons (LSP) to enhance EM field (see electric field map on the inset on Fig. 2.9.a).

The schematic illustration of Figure 2.9.b illustrates the required parameters for the calculation of the enhancement factor (EF_{Raman}). 'Tip-in' corresponds to the situation where the probe is in contact with the Raman-active sample. Here, molecules are excited by the focused laser in a volume V_{ff} (in blue) to generate a Raman scattering intensity defined as I_{ff}. The same molecules are also excited in the small volume V_{nf} by the enhanced field nearby the probe apex (in red), and generating a Raman intensity I_{nf}. When the probe is retracted, only far-field Raman intensity needs to be considered. The Raman EF is taken as the ratio between the near field and far field components [106]:

$$EF_{Raman} = \left(\frac{I_{ff} + I_{nf}}{I_{ff}} - 1 \right) \frac{V_{ff}}{V_{nf}} \tag{2.11}$$

Each volume can be defined according to R_{focus} and R_{TERS}, the excitation radii at the sample surface for respectively the laser spot and the localized *hot-spot*:

$$V_{ff} = R_{focus}^2 \pi h_{ff} \quad ; \quad V_{nf} = R_{TERS}^2 \pi h_{nf} \tag{2.12}$$

with h_{ff} and h_{nf} the effective heights respectively for the laser excitation and LSP excitation. For fine radii of curvature (<20 nm), an additional contribution of the far field comes from the mirror dipole of the tip. When the tip is in contact, we finally measure $\left(2I_{ff} + I_{nf}\right)$ [107]. For a sufficiently thin layer of adsorbed/deposited molecules, we can consider that $h_{ff} \sim h_{nf}$. Moreover, in many experimental cases, the incidence angle θ of the laser is nonzero (relative to the normal of the surface) and consequently the far-field area on the sample surface has an elliptical shape (see calculations in inset of Fig 2.9.b) with a surface as $\pi R_{focus} \times R_{focus} \cos(\theta)$. Finally, the near-field radius can be approximated as being half of the radius of curvature of the apex tip ($R_{TERS} \sim \frac{1}{2} R_{apex}$). Altogether, these approximations lead to another expression of the enhanced Raman factor such as:

$$EF_{Raman} = \left(\frac{I_{ff} + I_{nf}}{I_{ff}} \right) \left(\frac{R_{focus}}{\frac{1}{2} R_{apex}} \right)^2 \cos(\theta) \tag{2.13}$$

Far-field and near-field Raman scattering intensities are determined on the Raman spectra as shown in Figure 2.9.c revealing an intense enhancement of the Raman signal of Azobenzene molecules grafted on a flat Au substrate. We usually consider the most intense peaks of the enhanced Raman spectrum to calculate the Raman EF (here at 1150 cm^{-1}).

Despite many apparent advantages of TERS analysis – centered around chemical identification at the nanoscale – one of the main technical challenges of TERS experiments is the comparability of TERS probe performances. The estimation of the enhancement depends on all these parameters described above which are not precisely measurable. Errors of 20–50% of the obtained value of EF_{Raman} can result in large over or underestimations. Moreover, errors are also caused by inhomogeneities in sample composition, its density, and its molecular thickness, which adds difficulties for reproducible comparisons. Advanced preparation protocols, both for the tip and sample are then required for more precise EF calculation.

To show the advantages of TERS techniques, we present in Figure 2.10 a comparison between confocal Raman and TERS mapping on the same sample-area. HORIBA Scientific performed this example on graphene oxide (GO) flakes and carbon nanotubes (CNT) deposited on a gold substrate.

Confocal results show the poor lateral resolution of the optical set-up for such a sample, where no clear information can be easily distinguished (see Fig. 2.10.a). Note here that the focused laser is fixed and only the sample-holder is moving.

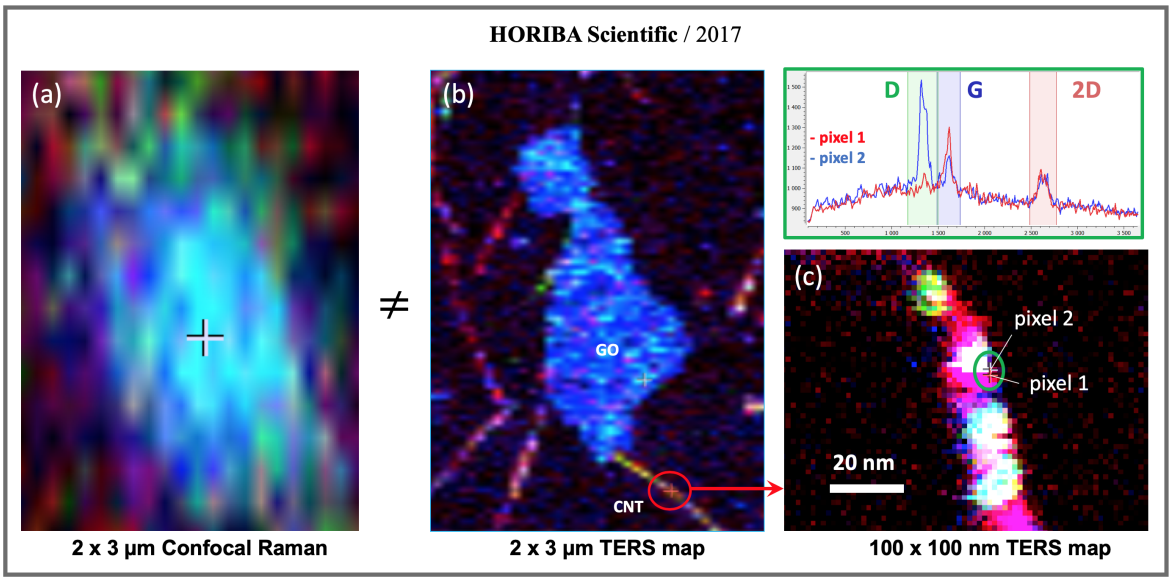

FIGURE 2.10 – Comparison of 2 x 3 μm mapping on GO flakes and CNT on Au substrate using (a) Confocal microscopy and (b) TERS imaging. (c) 100 x 100 nm TERS mapping of a single CNT showing a cross section resolved down to 8 nm; and chemical sensitivity at the pixel size 1.3 nm, proved by the Raman spectra for two successive pixels (1 et 2) – Copyright (2015) HORIBA Scientific.

For TERS mapping, a metallic probe – here a Ag-coated AFM probe – is brought at the focus point of the laser spot center, and the AFM sample holder brings the sample surface in contact with the probe before undertaking the planar scanning.

Here, there is a clear difference since GO flakes, as well as several CNTs, are well resolved (see Fig. 2.10.b) as compared to the confocal Raman image of Fig. 2.10.a. A zoom of a certain area can be obtained by reducing the scanned sample area and increasing the number of pixel acquisition per line. We observed in Figure 2.10.c a 100x100 nm TERS mapping on a single CNT revealing specific zones inside it, such as either defects or pure graphitic arrangement. Indeed, two successive pixels (for instance, pixel 1 and 2) show differences in Raman spectra, as shown here the D- and G-band intensity. TERS techniques provide then here an optical resolution around 8 nm – considering the CNT cross-section – with a chemical sensitivity about the pixel step size (here 1.3 nm).

2.3.2 Probe fabrication and enhancement optimization

Various plasmonic probes with several designs have been seen in the literature, including smooth tips such as electrochemically etched metallic wires [108–110] – preferably used for STM – or granular metallic coatings onto silicon cantilevers for TERS [111, 112] usually used in AFM. It was shown that the roughness of the metallic layer deposited on AFM probes [113] but also the size of the metallic apex itself have a strong influence on enhancement factors. These two types of TERS probe will be more detailed here, together with some manipulation in the aim of controlling the spectral plasmonic tunability of the localized near-field, and thus improve the Raman EF. However, we make a non-exhaustive reference list of some original techniques to complete the overview of TERS probes fabrication better:

— Attaching a TERS-active element at the extremity of an AFM probe such as: a single Ag nanowire [114, 115] or Au caps on silicon nanowires [116, 117]

— Angle-griding process on an AFM probe before several metallic evaporations, called nano-prism vertex TERS probes [118]

— Focused ion beam assisted fabrication such as: FIB sculpting [119], FIB milling [120], or FIB-growing [121] on several SNOM or A-SNOM probes.

— Template-Stripped Gold Pyramids [122], combined with FIB milling and integrated a C-shaped nanogap [123]

The majority of TERS probes involves today the use of gold as a metallization layer, which is interesting for its intense plasmonic activity in the visible region but also for its chemical inertness providing long lifetime probes. However, gold layers only produce plasmonic resonances with wavelengths in the red region, which

limits applications, e.g. in the fields of semiconductors or biology or semiconductors that require to lower the penetration depth of the Raman excitation laser in the sample but also to avoid parasitic fluorescence signal. Silver [124, 125] and aluminum [126, 127] can be used to reach lower wavelengths for such experiments — indeed, the plasmonic activity of silver takes place in the blue-green region, while aluminum can even reach the UV [128, 129] region. Unfortunately, these materials suffer from sulfidation / oxidation in air, which limits the probe lifetime [130, 131]. Reliable control of the spectral response of TERS probes, i.e., their spectral tunability, is still a key aspect for TERS experiments and developments.

2.3.2.1 STM based-probe

Among all fabrication techniques, electrochemical etching is the most popular due to its low cost procedure and have been widely used to create sharp and smooth metallic probes [132]. It consists of a metallic wire connected to an electrode altogether immersed with a second electrode in an electrolyte solution. While applying a bias current, etching starts at the junction between the wire and the solution interface (meniscus). For instance, Sergey S. Kharintsev et al. [133] have applied dc-pulsed low-voltage on Au wire into a solution from hydrochloric acid and ethanol with a ring gold counter-electrode encompassing the wire to ensure symmetric etching (see Fig. 2.11.a). Cl^- anions – from the salt dissolution in an aqueous medium – act as complexing agents and react with Au – from anodic oxidation reaction – to generate chloroaurate complexes. Varying the etching voltage parameters while the gold wire is moving enables to create different geometries as smoothed and roughened sharp probe, spheroidal and conical antennas, all susceptible to perform specific optical responses during TERS experiment.

This technique requires numerous parameters such as the electrode (e.g., Au, Ag, W, Pt), the electrolyte, (e.g., NH_3 for silver and HCl for gold), and the solvent nature, the voltage magnitude and type (dc, ac), the etching timing (including the stopping conditions), the wire-electrode distance, the immersion depth, and the mechanical stability of the solution as well as its environment (temperature, humidity, pressure). Unfortunately, it is impossible to control all of the parameters perfectly.

For a certain number of research topics, it would be desirable to excite Raman-active molecules only with a near-field excitation rather than both far-field and near-field together to significantly reduce the contribution of the background from far-field illumination. In this case, the excitation radiation spot should not overlap with

the supposed localized field between the apex and the sample during standard illumination. The well-known ability to generate an optical nano-confinement of SPPs holds significant promise for background-free TERS experiments [134, 135]. To generate and 'launch' plasmon through a plasmonic guide, we can use the traditional attenuated total internal reflection, but also dielectric waveguides, photonic crystal elements, or grating coupling. The latter is seen here as an example through the studies of Ropers C. et al. [136]. They have shown an efficient nonlocal optical illumination of the apex of an electrochemically etched gold tip using grating-coupling. This grating was created far away from the apex using sputtering from a focused gallium ion beam. Called super-focusing, these SPPs are launched from the grating under illumination and propagate around 10 μm toward the apex of the tip to confine and form the localized near-field, useful for free-background TERS (see Fig.2.11.b). The far-field light scattered by spectroscopy, reveals the efficient SPP propagation from the grating to the tip apex. This research group also demonstrates the spectrally tunable emission from the apex with the illumination angle, proving a fine control of the plasmon resonance frequency.

Still with the aim of improving the plasmonic response of TERS probes, recent work has started to go beyond standard fabrication process in order to design the apex itself of SPM tips by using focused ion beam (FIB) reshaping in order to isolate the metallic part that composes the apex from the rest of the metallic tip [137]. This machining breaks the conventional semi-infinite plasmonic tip model ('non-resonant' tip) by creating an electromagnetic cavity – Fabry-Pérot type – of controlled shape at the tip apex, with spectrally well-defined resonances related to localized surface plasmon modes (i.e. 'resonant tips').

In practice, Thiago L. Vasconcelos et al. [138] created such structured tips using FIB milling to engrave a single groove at only 180 nm away from the apex. Electron energy-loss spectroscopy (EELS) was applied here to obtain images of the milled tips with a high spatial and spectroscopic resolution. It reveals a well-defined LSPR at 2.1 eV (λ $\sim$590 nm) after the milling which is the sign of a plasmonic cavity resonating between the apex and the groove. (see Fig. 2.11.c). The comparison before and after FIB milling was applied to TERS experiments by successfully performing TERS on graphene, and it shows a larger enhanced Raman after FIB milling. The groove-apex distance can then considerate as the only parameter to control the LSPR frequency, under a linear relation that depends on the geometry and material properties.

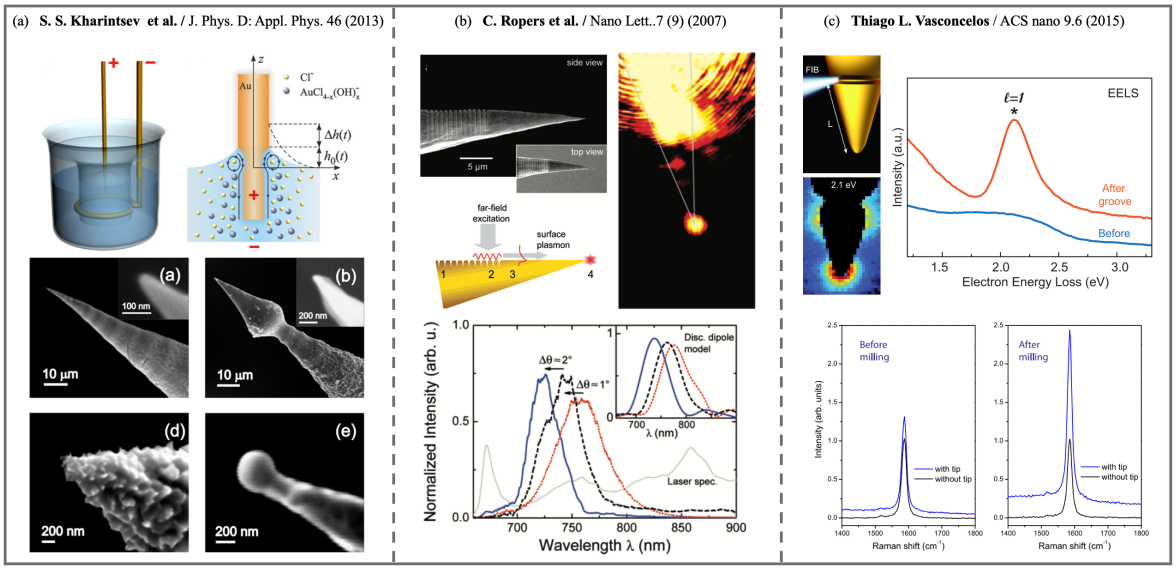

FIGURE 2.11 – Adapted from S. S. Kharintsev et al.: (a) Illustration of an electrochemical cell and etching mechanism. SEM images of electrochemically etched plasmonic optical antennas at different dc-pulsed voltage regimes. Adapted from C. Ropers et al.: (b) SEM images of the tip with a grating coupler with a schematic representation of the plasmon launch mechanism. Optical image recorded demonstrates the efficient nonlocal excitation of the apex via the grating illumination. Recorded scattering spectra for three different incidence angles. Adapted from T. L. Vasconcelos et al.: (c) Illustration of the FIB-milled probe and EELS intensity mapping plotted at 2.1 eV. EELS spectra acquired at the apex before (blue) and after (red) FIB manipulation). Graphene G-band spectra obtained before and after the milling, when the probe is away (black) or in contact (blue).

Electrochemically metallic wire as bulk metal is usually used under a STM feedback, which constrains the study of conductive samples and usually under specific environments. Plasmonic-active electrochemically etched metallic wire can be then used for AFM Feedback since it can be glued on tuning forks.

2.3.2.2 AFM based-probe

For routine TERS characterization, metal-coated AFM-TERS probes appear simpler to use than STM-TERS probes and allow non-conductive samples to be analyzed. Metallic deposition processes on commercially available AFM probes can be performed in many ways with different roughness properties such as, for example, a mechanical dipper which transfers colloidal nanostructured film onto an AFM probe [139], by electroless metal-plating [111, 112] or photoreduction deposition [140]. However, most metallizations are performed by thermal evaporation, widely used in microfabrication clean-rooms.

Depending on the evaporation rate and the surrounding temperature, it is possible to control the surface aspect to reach an optimized near-field enhancement. Atsushi Taguchi et al. [141] demonstrated that at high evaporation rate, silver could be deposited relatively uniformly along the surface to obtain a smoothed metallic surface. At slow evaporation rate, the higher surface free energy of Ag as compared to SiO_2 overrides the coating uniformity by forming clusters and thus leads to a rougher surface where Ag grains are all connected to each other. There is a third case where a high temperature during low evaporation rate increases the deposited atoms mobility, which induces larger distance between clusters and thus leads to a coating made from disconnected Ag grains. Figure 2.12.a first shows the result from smoothed and roughed surface and A. Taguchi reported an EF respectively about 230 and 800 on the G-band of graphene. An AFM probe coated with disconnected grains was also used, and it revealed an EF up to 5500. Finally, they successfully applied this latter probe for high resolution Raman and AFM imaging on CNTs. The three characteristic peaks of graphene seem to be all equally enhanced and give a similar contrast in Raman imaging.

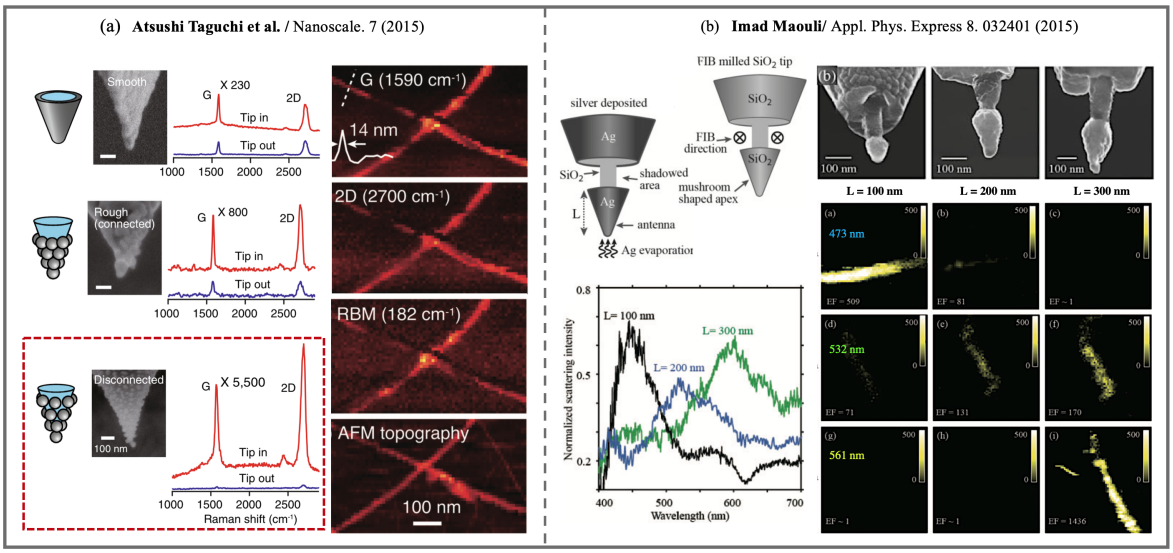

FIGURE 2.12 – Adapted from A. Taguchi et al.: (a) Illustration, SEM image of the used probe for corresponding Raman spectra of graphene sheets scattered with Ag tip having smooth (down) and rough (middle) surface as well as disconnected Ag grains coated on SiO_2 probe. TERS images of CNTs measured with the disconnected multiple grain tip are shown at G-band, radial breathing mode (RBM), and 2D-band, respectively with a topographic image of CNT simultaneously. Adapted from I. Maouli et al.: (b) Illustration of FIB-milling on SiO_2 AFM probe at a distance L from the apex, followed by silver evaporation. SEM images for L = 100, 200, and 300nm. Scattering spectra of fabricated antennas. TERS images (320 x 320 nm) of CNT samples, contrast coming from the G-band intensity.

In another work, Imad Maouli et al. [142] have demonstrated a fabrication method to obtain metallic nano-antennas of different size using FIB to create a groove on a SiO_2 AFM probe before thermal deposition of silver (see Fig. 2.12.b). The groove etched at a distance L from the apex acts as a shadow area during deposition and three nano-antennas with different lengths about 100, 200, and 300 nm were fabricated. An experimental characterization set-up based on an AFM head on an inverted microscope which is settled in dark-field scattering configuration is used for plasmonic measurements (see more details § 3.2). It reveals that each probe presents its resonance at a specific wavelength that red-shifts when increasing antenna length. Each probe has then its own spectral efficiency range that should be in adequacy with the excitation laser required for Raman spectroscopy. Using then three different lasers, they performed TERS mapping on CNTs using each probe on the same sample. Based on the G-band intensity, high resolution Raman imaging confirmed the probe efficiency ranges. TERS images show higher enhancements for the mappings where the incident wavelengths are in near-resonance with the nano-antennas. This technique can thus precisely tune the plasmon resonance for optimized TERS experiments by controlling the antenna length during the fabrication process.

From these reported works, we observe that disconnecting a tiny metallic part from the rest of metallic (in the case of electrochemically etched STM probes) or metalized probe (in the case of AFM dielectric tip) suggests being the key element to precisely control the plasmonic properties involved in enhanced Raman scattering. AFM imaging has the advantage to also provide physical information, such as topography, on any kind of sample. Disconnected Ag grains coated on SiO_2 probe is a nice solution for low cost but it does not ensure a good tip-to-tip reproducibility regarding the grain sizes of the gaps, and small variations drastically affect the enhanced field.

The last example seems then to be the best idea to obtain nano-antenna ending AFM probes with control of the optical properties since free-background Raman spectroscopy – as grating-coupling would offer – is not required. A nanometric design of a metallic apex playing the rule of efficient nano-antenna requires however here costly FIB instrumentation rejecting any fabrication solution for mass production.

Conclusion

In this chapter, we have introduced the concepts of the Raman scattering phenomenon. We have seen that chemical identification tools required specific instrumentation. Optical Lasers are driven toward a sample and focus on the surface over a small area ($\sim \mu m$) and the emitted Raman signal from the sample is analyzed with dispersion systems. A lateral scanning of the sample during confocal Raman experiment offer chemical imaging of the sample.

Confocal Raman microscopy can be coupled with SPM techniques for co-localized experiments. To nevertheless bring the chemical resolution toward a nanometric resolution, Raman excitation source must be an intense smaller than standard illuminations. Plasmonic materials are the best candidate to offer both EM confinement with an intense enhancement factor. A first demonstration of the plasmonic effect on Raman active molecule has been studied with surface enhancement Raman spectroscopy. Based on nanostructured metallic substrates, the localized plasmons generate EM *hot-spots* which interact with the molecules adsorbed on the metal surfaces. A factor can then enhance the Raman signal from 10^7 and up to 10^{14}.

To obtain a nanometric resolution for Raman spectro/microscopy, the single *hot-spot* generate at the apex of an s-SNOM probe can be used as the Raman nano-source. Called tip enhancement Raman spectroscopy, this technique provides a great non-destructive characterization tool for nano-spectroscopy Raman allowed with an EF up to 10^8.

In concern for the continuous improvement of the TERS performances, plasmon at the origins of the enhancement must be tuned with respect to the Raman excitation laser. Optical nano-antennas deliver a perfect plasmonic control of the resonant properties. We have seen different optimization of the probe fabrication processes where the goal was to the machining of the apex probe and isolate a single metallic nanostructure. However, the use of FIB to obtain efficiency TERS probe is costly methods. Based on a single optical nano-antenna ending a silicon probe, the thesis is centered around the conception of a new TERS probe promising fabrication technique compatible with mass production, high reproducibility, and plasmonic tunability.

Chapter 3

Characterization Tools for Optical Antennas

The understanding of physical phenomena always requires interaction between theory and experimentation. In nanophotonics, we can understand and predict the electromagnetic behavior of metal nanostructures in both far-field and near-field domains. In this third chapter part of the thesis, we describe the numerical and experimental tools which have been used and developed in our studies. To assess the efficiency of these tools, we investigate and compare the results with well-known cases from published literature concerning plasmonics. Then, other cases will be studied in order to: (i) better understand the EM field enhancement that takes place at the tip apex of commercially-available TERS probes, and (ii) propose a new design of probes based on a single optical nano-antenna ending a silicon tip.

Numerical modelling has been used to design plasmonic nano-objects and understand the role of the specific parameters involved in the generation of localized resonances (or localized-surface-plasmon-resonance – LSPR – see § 1.4), embedded in a homogeneous medium or deposited onto a dielectric interface.

In this part, we will investigate using numerical modelling:

— the effect of the refractive index of transparent media surrounding typical metallic nanospheres on their LSP properties (§ 3.1.2.1);

— the tunability of the plasmon in the air, and EM enhancement factor (EF) of conically shaped nanostructures (§ 3.1.2.1);

— the improvement of light-matter interaction with evanescent rather than radiative excitation, under total internal reflection on the substrate/air interface (§ 3.1.2.2);

— the link existing between optical properties and perfectly smoothed micrometric metal tips (§ 3.1.2.3);

— the scattering response of lithographically-patterned gold nanodisks as a function of the disk diameter (§ 3.3.1) for later comparison with experimental results in order to validate our in-house characterization set-up (§ 3.2.2).

On the experimental side, we describe an experimental set-up specially constructed at IEMN to investigate the field enhancement properties of TERS probes. It consists of an achromatic coupling involving an inverted microscope equipped with an oil immersion total-internal-reflection (TIR) fluorescence objective and a broadband excitation light in the visible range. With a thin glass substrate, such an optical spectroscopy set-up can perform both an evanescent excitation and a dark-field collection. The TIR excitation and detection scheme also provides the possibility to couple the TIR microscope with an AFM-head. Hence, the optical field emitted from the apex of TERS-probes can be recorded by a spectrometer, when approaching to the substrate and interacting with the incoming evanescent waves on the glass surface.

First, the characterization set-up will be validated with individual antennas (Au nanodisks or nanocones) lithographically-patterned on a glass substrate. Dark-field spectra will be compared with numerical modelling performed on modeled nano-objects, of shape and dimensions extracted from scanning electron microscope (SEM). Then, we have investigated a series of state-of-the-art metal-plated AFM cantilevers commonly used for TERS experiments.

The results from such scattering analyses will be correlated with the SEM observations of the tip apex to help answering the probe fabrication problematics.

3.1 Numerical Modelling

3.1.1 Single nano-antenna models description

Numerical modelling in nanophotonics allows to determine EM field distributions nearby nanostructures and the associated radiation or absorption properties. In this case, modelling the system allows us to limit the size of our sample to a

unique nano-structure and save time on experiments that can be difficult to implement. A strong theoretical comprehension of the field distribution gives us access to the conception, development, and optimization of optical devices controlling the light beyond the Rayleigh criterion. In the frame of optical nano-antenna investigation, popular methods based on the resolution of Maxwell's equations are Mie-scattering calculation [143, 144], Green's function method [145, 146], Finite-Difference Time-Domain method (FDTD) [147, 148], Discrete Dipole Approximation (DDA) [149], Boundary Element Method (BEM) [150–152], Multiple Multipole Program (MMP) [153, 154], and Finite Element Method (FEM) [155, 156].

To study the plasmonic properties of metallic nano-antenna, we performed simulations with the Finite Element Method (FEM), implemented in the Radio-Frequency module of COMSOL Multiphysics. This commercial software solves problems in the general field of electromagnetic waves, in a wide frequency range including microwave or visible light. We describe this method in the case of a single nanoparticle deposited on a substrate of refractive index n_1 and surrounded by a second medium n_2. The program solves, from Maxwell equations, the following relation:

$$\nabla \times \nabla \times \mathbf{E} - k_0^2 \varepsilon_r(\mathbf{r}, \omega)\mathbf{E} = 0 \tag{3.1}$$

where $\mathbf{E}$ the electric field at location $\mathbf{r}$ and pulsation ω, and ε_r the dielectric constant that depends on the object. FEM modelling requires then: (i) a simple geometry with application of boundary conditions at its extremities, (ii) dielectric properties of each material, (iii) an optimized geometrical discretization (called mesh), (iv) initialization of the EM source, and (v) the interpretation of calculations.

Geometry: First, we must start by the geometric elaboration of the system, considering any symmetry planes to reduce to size and therefore the calculation time. As presented in figure 3.1.a, our model consists in an EM excitation along the x-positive direction to a single nano-disk with a symmetry plane along the XZ-plane. The entire system is delimited by a spherical – or cylindrical in certain cases – domain such as the interface plane of the substrate is centered. Specific boundary conditions must be implemented to imitate the EM wave propagation in the entire space: (i) an outer layer set as a perfect-matched-layer (PML) to allow all outgoing waves to be absorbed, to prevent unwanted reflections of the scattered field onto boundaries, and hence to simulate EM waves that propagate into an unbounded domain; (ii) the anti-symmetry – *or symmetry* – plane (XZ) set as a perfect electric – *or magnetic* – conductor port since the incoming waves will a transverse-electric (TE or s-polarization)

– *or transverse-magnetic (TM or p-polarization)* – polarized plane-wave.

Materials: The minimum data required to create a virtual model are related to the nature of material such as dielectric functions extracted by interpolation of Johnson and Christy's data [45] for metals and the refractive index of surrounding mediums. The relative permittivity $\varepsilon_r(\omega)$ can be expressed as:

$$\varepsilon_r = \varepsilon_r^{'}(\omega) + i\varepsilon_r^{''}(\omega) \tag{3.2}$$

with $\varepsilon_r^{'}$ the real part which represents the refractive coefficient and $\varepsilon_r^{''}$ the imaginary part which defines losses associated with the oscillation damping of the electron in metals. Moreover, the generation of surface plasmon occurs when the real part is negative with an absolute value exceeding the imaginary part ($|\varepsilon_r^{''}| << |\varepsilon_r^{'}|$). The optical properties which define the surrounding and the substrate are mainly set as dielectric material such as air, glass, or silicon using the refractive index representatively 1, 1.5, and 3.48.

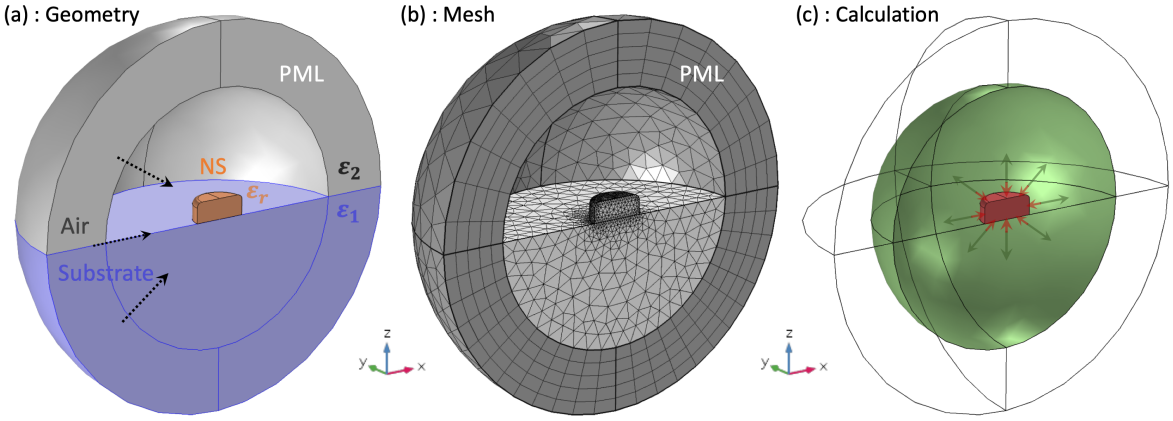

FIGURE 3.1 – Schematic representation of: (a) the studied geometry showing the air medium (in grey) the substrate (in blue) and the metallic nanostructure (in orange) altogether delimited by the spherical out-layer (PML); (b) the mesh of the entire geometry showing a finner mesh around the nanostructures and an surface defined to compute the PML layer in order to limit the number of elements; (c) Scattered waves by the nanostructure in the 3D-space (in green), and volume where absorption response is evaluated (in red).

Mesh: The next step consists in the geometrical discretization of our entire system into a certain number of sub-domains (see Fig. 3.1.b), to solve Maxwell's equations inside each element depending on the optical properties defined above. The number of elements influences the quality of the solution approximation, especially for regions where the EM field varies rapidly. Such a geometrical decomposition is called

the mesh and generally consists in tetrahedral elements –except for the PML layer which is meshed by a homogeneous distribution of triangular prisms (pentahedral elements) again for calculations memory optimization purposes.

EM source: Then, we must initialize the calculation with the exact solution of the reflected and transmitted fields at the interface from the incident field $\mathbf{E}_j$, taking from:

$$\begin{gathered} \mathbf{E}_j = \mathbf{E}_j \, e^{i(\mathbf{k}_j \cdot \mathbf{r} - \omega \cdot t)} \\ \text{with} \quad \mathbf{k}_j = \left(k_x, k_y, \pm k_z^i\right) \quad \text{and} \quad \left|\mathbf{k}_j\right| = k = \frac{\omega}{c} n_j \qquad j \in \{1;2\} \end{gathered} \tag{3.3}$$

with $\mathbf{E}_j$ the amplitude, $\mathbf{k}_j$ the wave-vector, and n_j the refractive index. As presented in Figure 3.2, when a plane wave falls onto a boundary between two homogeneous media with different optical properties, it is split into two waves. One is a transmitted wave proceeding into the second medium while the other is a reflected wave propagated back into the first medium. Two polarizations of the electric field is studied here as being perpendicular $\mathbf{E}_j^{(s)}$ or parallel $\mathbf{E}_j^{(p)}$ to the plane of incidence and propagating along $\mathbf{k}_j$. We consider here, for both polarizations, an incoming plane wave propagating in the first medium ($n_1 = \sqrt{\varepsilon_1}$) along $\mathbf{k}_1$ with an incident angle θ_1 from the normal interface and a transmitted wave diffracted in the second medium ($n_2 = \sqrt{\varepsilon_2}$) along $\mathbf{k}_2$ and with an angle θ_2.

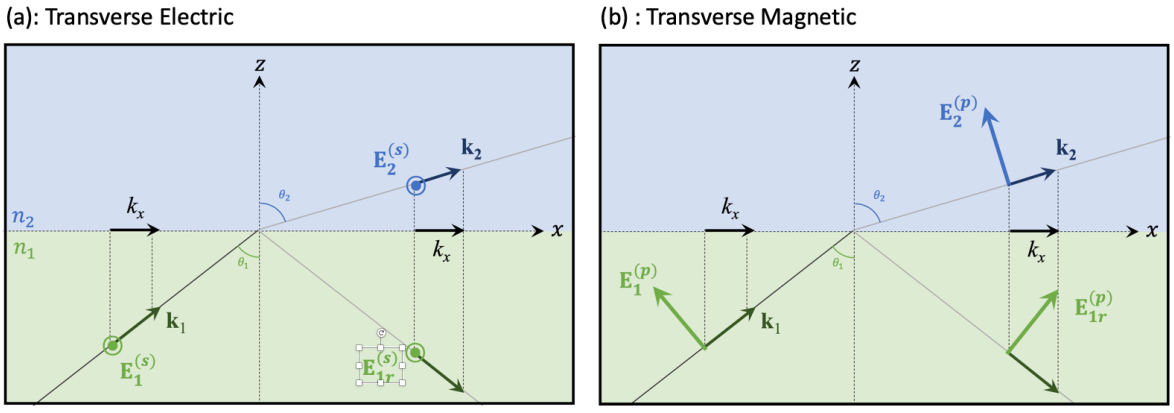

FIGURE 3.2 – Refection and refraction of a plane wave at a plane interface: (a) s-polarization when the electric field $\mathbf{E}^{(s)}$ is along the y-axis (TE) and (b) p-polarization when the electric field $\mathbf{E}^{(p)}$ is along the xz-plane (TM).

In the both medium the total electric field is expressed as:

$$\begin{aligned} &\text{in medium } n_1 : \ \mathbf{E} = \mathbf{E}_1^{s/p}\, e^{i(k\cdot x-\omega t)}\, e^{ik_{z1}} + \mathbf{E}_{1r}^{s/p}\, e^{i(k\cdot x-\omega t)}\, e^{-ik_{z1}} \\ &\text{in medium } n_2 : \ \mathbf{E} = \mathbf{E}_2^{s/p}\, e^{i(k\cdot x-\omega t)}\, e^{ik_{z2}} \end{aligned} \tag{3.4}$$

with $\mathbf{E}_1$, $\mathbf{E}_{1r}$, and $\mathbf{E}_2$, the amplitudes of respectively the incident, reflected, and transmitted field. The boundary conditions through the interface give the expression of the Fresnel coefficients, in reflection r or transmission t [157]:

$$r^{(s)} = \frac{E_{1r}^{(s)}}{E_1^{(s)}} = \frac{k_{z_1} - k_{z_2}}{k_{z_1} + k_{z_2}} \quad ; \quad t^{(s)} = \frac{E_2^{(s)}}{E_1^{(s)}} = \frac{2k_{z_1}}{k_{z_1} + k_{z_2}} \tag{3.5}$$

$$r^{(p)} = \frac{E_{1r}^{(p)}}{E_1^{(p)}} = \frac{\varepsilon_2 k_{z_1} - \varepsilon_1 k_{z_2}}{\varepsilon_2 k_{z_1} + \varepsilon_1 k_{z_2}} \quad ; \quad t^{(p)} = \frac{E_2^{(p)}}{E_1^{(p)}} = \frac{2n_1 n_2 k_{z_1}}{\varepsilon_2 k_{z_1} + \varepsilon_1 k_{z_2}} \tag{3.6}$$

Assuming an amplitude of the incoming field E_1 set as 1 V/m, we have for the s-polarization a total electric field only defined along the y-axis and with a total amplitude independent of the incident and transmitted angle as:

$$\mathbf{E}_{n_1}^{(s)} = e^{i(k_x\cdot x-\omega t)}(e^{i(k_{z_1}\cdot z)} + r^{(s)}e^{-i(k_{z_1}\cdot z)})\mathbf{e}_y \quad ; \quad \mathbf{E}_{n_2}^{(s)} = t^{(s)}e^{i(k_x\cdot x+k_{z_1}\cdot z-\omega t)}\mathbf{e}_y \tag{3.7}$$

For the p-polarization the total electric has components along both x- and z-axis with amplitudes depending on the incidence angle:

$$\begin{aligned} \mathbf{E}_{n_1}^{(p)} &= \begin{pmatrix} e^{i(k_x\cdot x-\omega t)}(-e^{i(k_{z_1}\cdot z)} + r^{(p)}e^{-i(k_{z_1}\cdot z)})\frac{k_{z_1}}{k_1} \\ 0 \\ e^{i(k_x\cdot x-\omega t)}(e^{i(k_{z_1}\cdot z)} + r^{(p)}e^{-i(k_{z_1}\cdot z)})\frac{k_x}{k_1} \end{pmatrix} \\ \mathbf{E}_{n_2}^{(p)} &= \begin{pmatrix} -t^{(p)}e^{i(k_x\cdot x+k_{z_2}\cdot z-\omega t)}\frac{k_{z_2}}{k_2} \\ 0 \\ t^{(p)}e^{i(k_x\cdot x+k_{z_2}\cdot z-\omega t)}\frac{k_x}{k_2} \end{pmatrix} \end{aligned} \tag{3.8}$$

with $k_x = k_1 \sin\theta_1$ and $k_{z_j} = \sqrt{k_j^2 - k_x^2}$.

Calculations: To characterize the optical signatures specific to the metallic nanostructure, we can calculate both the absorption inside the object and the scattering field intensity from the structure to the far-field, which gives the radiation diagram

in the three-dimensions. To obtain these optical properties, we use the Poynting theorem [158] which provides the relationship between the EM field and its energy content (see § 1.18).

3.1.2 Preliminary studies

3.1.2.1 From metallic nano-sphere to nano-cone

The first set of numerical modelling has been performed to study well-known cases from the literature, in order to build the model and set the methodology. Gold and silver nano-spheres (NS) have been used here to investigate three parameters that affect the resonance frequency of localized-surface-plasmon (LSP) such as the size of the NS, the metal and the surrounding medium nature. Figure 3.3.a presents a NS located at the center of a 1 μm large spherical domain enclosed by a 250 nm thick outside shell set as a PML. A p-polarized electric wave ($|\mathbf{E}| = E_z$) is used as an excitation, and propagates along the x-axis ($\mathbf{k}_x$). The graph (see Fig. 3.3.b) shows the spectrum of the enhancement factor (EF), calculated 1 nm under the metal surface, and defined as:

$$EF_{LSP} = \frac{|\mathbf{E}(\omega)|^2}{|\mathbf{E}_0(\omega)|^2} \tag{3.9}$$

where $\mathbf{E}$ is the total field and $\mathbf{E}_0$ the incident (or transmitted) field. For silver (left) and gold (right), three transparent media – such as air (n=1), water (n=1.33) and glass (n=1.5) – have been studied while the diameter of the NS variates from 20 to 100 nm.

The resonances in the curves are representative of a LSP with a maximum corresponding to the plasmon-resonance (LSPR – § 1.4). Here, the maximum of the EF corresponds to the excitation of the dipolar plasmonic mode, first-order mode of optical nano-sphere. We observe that the resonance frequency of this dipole redshifts when the diameter is increased. The tunability of the plasmon – redshift or blueshift – according to its geometry is here relatively weak in the air. The LSPR from silver NS shifts from the near-UVs to the blue range (70 nm shift) while the gold NS scans the green region (15 nm shift). This difference is explained by the relative permittivity functions of the metals, as described before (§ 1.3.1). We can note that this redshift gets more sensitive while the refractive index of the medium increases, i.e., a shift from 60 to 150 nm for water and from 90 to 175 nm for glass. For a higher

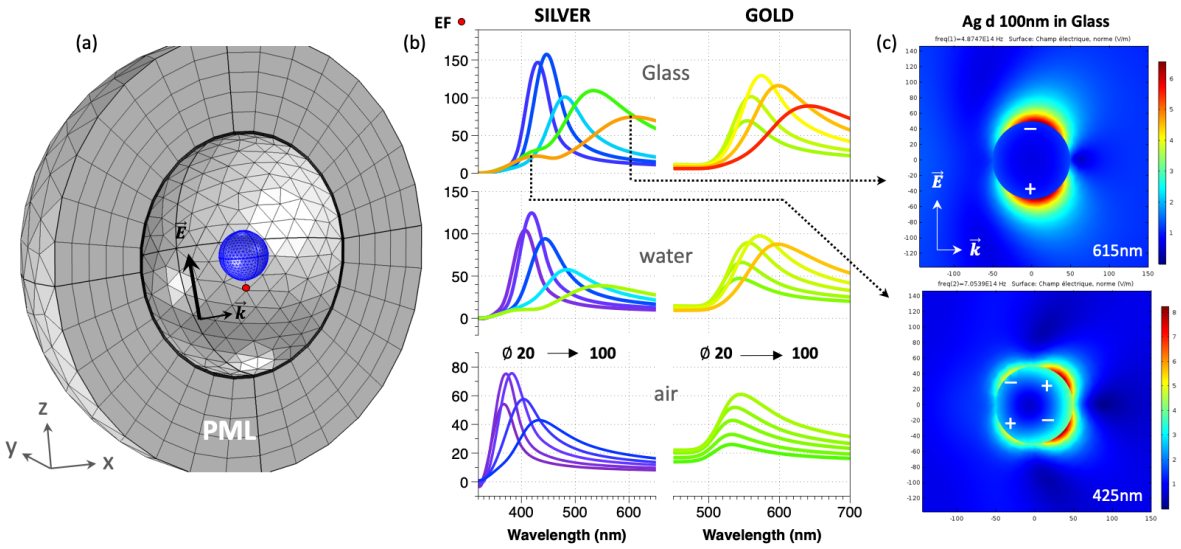

FIGURE 3.3 – (a) Schematic representation of a nano-sphere at the center of the numerical domain. (b) EF spectra of gold and silver nanospheres with a varying diameter in different media. (c) Distribution of the electric field amplitude in the XZ plane for a 100 nm large silver NS into glass medium. Dipolar (top) and quadrupole (bottom) plasmonic modes exhibiting surface-charges accumulation characteristic of evanescent field lobes.

refractive index and larger diameter, a higher order mode appears at a higher excitation frequency. Figure 3.3.c shows the distribution of the electric field amplitude along the XZ plane for 100 nm large silver NS in the glass. The peak at 615 nm represents the dipolar mode while a higher mode, here the quadrupole, appears at 425 nm. The electric field plots of the figure reveal the localized and enhanced field as lobes nearby the nanoparticles surfaces. Finally, we measured that the EF intensity of these nanospheres is about 10^2. The spherical shape is the most basic to describe nanoparticles. We will see that for a similar volume of matter, elongated shape of the structures will strongly affect the plasmon in terms of its tunability and intensity of the enhanced field.

For the next study (see Fig. 3.4.a), the nano-antenna takes the shape of a nanocone (NC) with a fixed half-angle of 20°, a radius of curvature of 10 nm at the apex, and a height H ranging from 60 to 140 nm. Both gold and silver are be studied in air.

In comparison with the previous case, two strong effects of the conical shape can be noticed. The first one is shown in the spectra in Figure 3.4.b revealing a plasmonic tunability in the air of 90 nm with Au and 140 nm with Ag. As was the case previously, both metals can cover the whole visible spectrum with the appearance

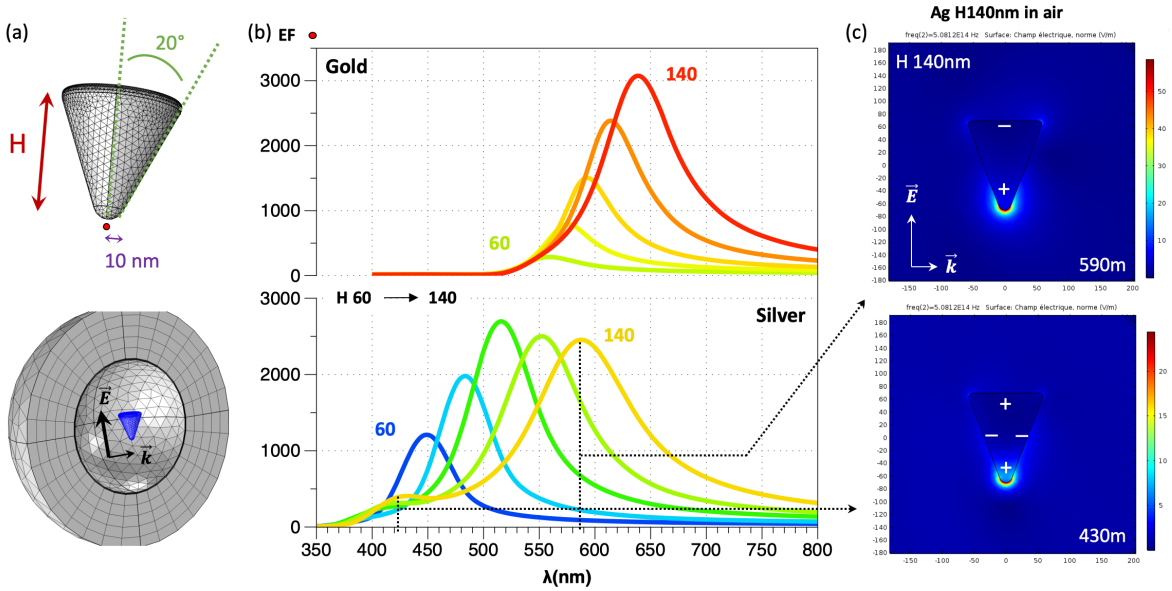

FIGURE 3.4 – Schematic representation of geometric characteristics a nano-cone (NC) at the center of the numerical domain. (b) EF spectra of gold and silver NCs with varying height in the air media. (c) Distribution of the electric field amplitude in the XZ plane for a 140 nm height silver NC. Dipolar (up) and quadrupole (down) plasmonic modes exhibiting very strong surface-charges accumulation signature of the localized evanescent field at the apex of the cone.

of a well-defined resonance in the blue region for silver and green for gold. The second interesting aspect is the intensity of the EF measured 1 nm below the apex of the cone growing up from 10^2 for spherical nanoparticle, to 3.10^3 for NC for gold. For silver, both modes – dipolar at 590 nm and higher mode for 430 nm – present strong confinement of the electric field over the apex compared to the base of the nanostructure (see electric map along the XZ plane of Figure 3.4.c). Such optical nano-antenna present all the specifications required to create an intense nano-source of the light in the visible range (see § 2.3).

The finite element method can also study plasmonic nanostructures integrated on dielectric substrates (§ 3.3.1), which strongly affects resonances and scattering properties of metal nanostructures. We investigate now numerically this effect and focus in particular on linear polarization effects in the case of gold nanodisks disposed on a glass substrate.

3.1.2.2 Dielectric interface and incident polarization

A homogeneous environment is useful to study the basics of the plasmonics theory; however, to confront theoretical and experimental results, an interface needs to be added to take into account the sample substrate.

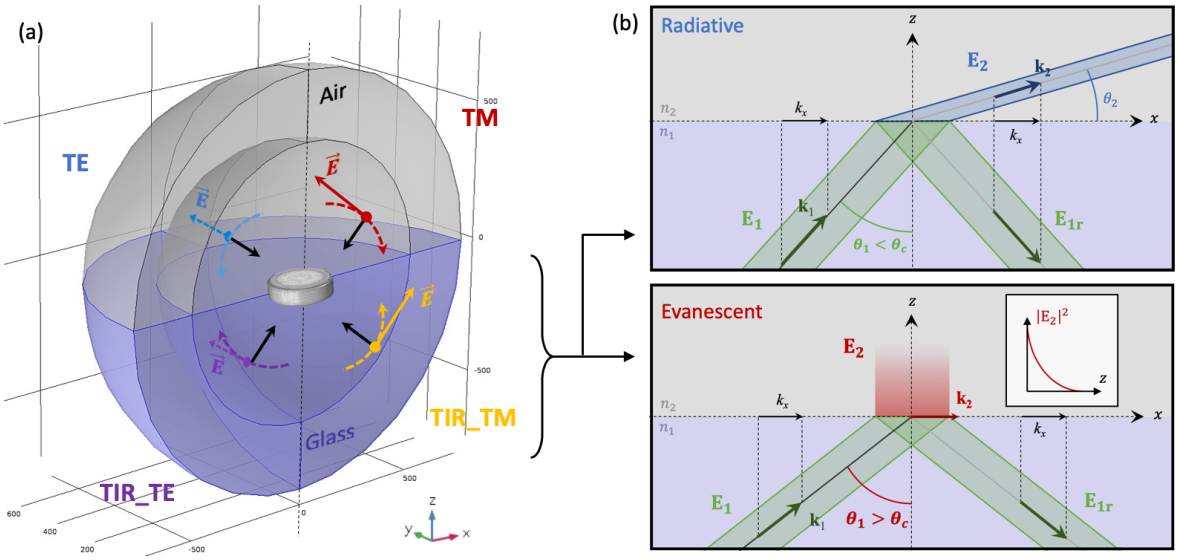

FIGURE 3.5 – (a) Schematic illustration of a AuND at the center of the calculation domain, deposited onto the glass surface. All possible linear polarizations of the electric field are illustrated under a varying incident angle (dashed arrows). (b) Schematic representation of radiative (top) and evanescent (bottom) excitation depending on the incident angle under (top) or above (bottom) the critical angle θ_c, propagating in a medium n_1 toward a dielectric interface with a second medium $n_2 < n_1$. In the inset, the graphical representation of the exponential decay of the EM intensity along the z-direction.

Here, we study a gold nanodisk (AuND) placed onto a transparent glass substrate where both linear polarized excitation planewaves – transverse electric and transverse magnetic – is sent first to the air/glass interface (TE and TM) and, second, onto the glass/air interface (TIR-TE and TIR-TM), as illustrated in Figure 3.5.a. The second case leads to a total-internal-reflexion and allows the transition from a radiative to an evanescent excitation (3.5.b) since the incidence angle reaches the critical angle $\theta_c = \text{asin}(n_2/n_1) = 41.8°$, with $n_2 = 1.5$.

The AuND is a test-sample to visualize the effect of each polarization on plasmonic resonances excited under illumination from the air domain – Transverse Electric (TE) and Transverse Magnetic (TM) – or the glass domain – called TIR-TE or TIR-TM. We have focused on three different plasmonic modes to reveal the effect of such evanescent excitations compared to linear plane-wave on the absorption

and scattering responses. Figure 3.6 presents these modes as being the plasmonic horizontal dipolar and quadrupole modes, and the vertical dipolar mode of the AuND at the resonance wavelength, respectively 800, 600 and 515 nm.

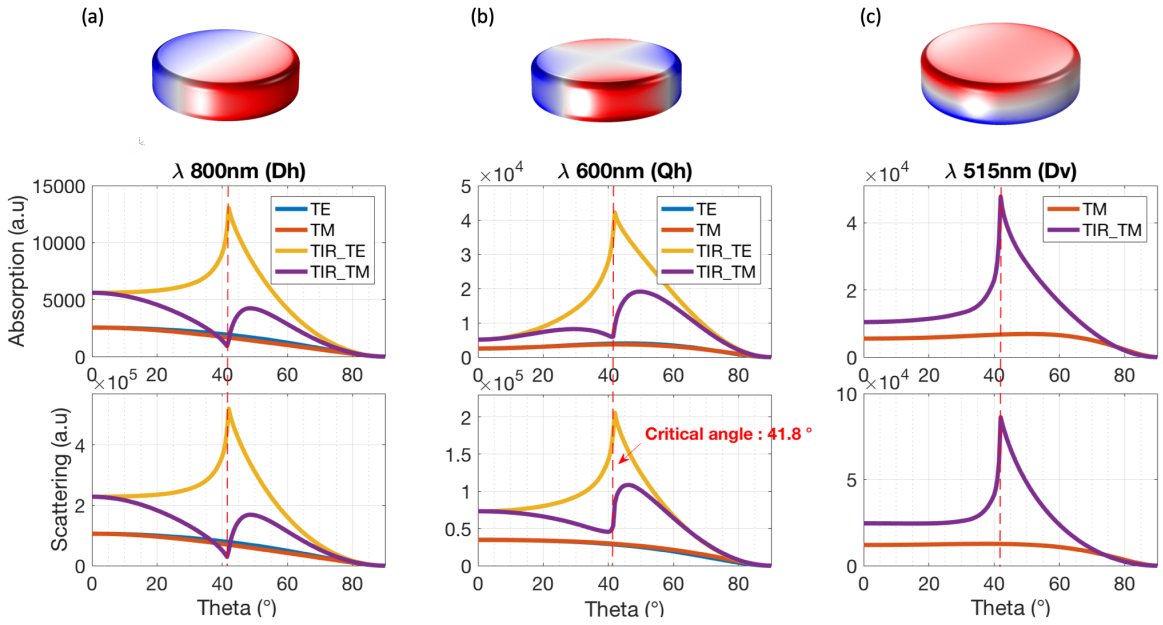

FIGURE 3.6 – Schematic illustrations of surface charge distribution of the plasmonic modes supported by AuND (top) and graphics representing the absorption (middle) and the scattering responses (down) according to the incident excitation angle for the horizontal dipole (a) and quadrupole (b) mode (with TE and TM curves confused), as well as the vertical dipole mode (c).

In horizontal planes, parallel to the substrate interface, fields with s-polarizations (TE and TIR-TE) have only a y-component of the electric field, independently to the excitation angle, while for p-polarizations (TM and TIR-TM) fields have a x-component which depends on the angle ($E_x = |\mathbf{E}| \cos\theta$). That is why horizontal modes (see Fig. 3.6.a and .b) are excited by all polarization states while the vertical mode can be excited only for p-polarizations which deliver the required z-component of the electric field, also depending on the excitation angle E_z (see Fig. 3.6.c). The corresponding graphics for each plasmon mode shows the absorption and scattering signals as a function of the excitation angle. Blue (TE) and orange (TM) curves represent the incoming plane-wave excitation from the air medium. Yellow (TIR_TE) and purple (TIR_TM) curves represent the excitation from the glass medium. The strong decay to zero observed for grazing angles (~60 to 90°) is explained by destructive interferences appearing between the incident and the reflected field. Each signal is amplified by a factor around 10 when the nanostructures are excited by the evanescent instead of the radiative plane-wave. The

result shows the interest to combine evanescent waves with conventional optical spectroscopy for plasmonic characterization techniques.

3.1.2.3 From nanometric to micrometric metallic antennas

We have just seen that single nanoparticles – in a unique medium or onto a dielectric surface – exhibit well-defined dipole or quadrupole plasmons. To numerically evaluate the behavior of current commercial TERS probes, we must start with a micrometric metallic tip from bulk gold metal, usually with a height between 10 and 15 μm. Here, a perfectly smoothed probe is studied with a radius of the apex about 50 nm, and a height of only 5 μm for computer memory reasons. The 3D model is presented in Figure 3.7.a where a perfectly smooth tip is pointing to the glass interface with a gap between the apex and the interface of 10 nm. The domains are here cylindrical to minimize the size of calculations. The TIR excitation can be visualized on the XZ cut-plane of the domain displayed in Figure 3.7.b and showing radiative waves into the glass substrate and evanescent wave generated onto the air/glass interface (x-component). Figure 3.7.c and 3.7.d shows the electric responses for respectively the x and the z-component of the electric field. In this case, surface plasmon polaritons (SPP) are traveling from the apex to be reflected at the base of the tip which creates a cavity mode for the plasmon (called Fabry-Pérot effect [159,160]) where many orders of resonance modes in the visible range can exist.

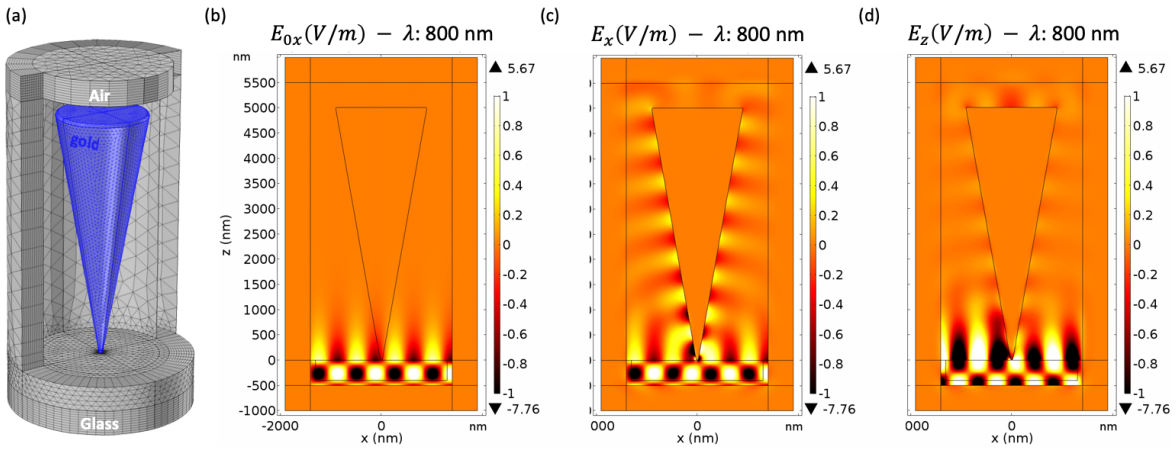

FIGURE 3.7 – (a) Schematic representation of the 5μm high gold tip in the center of a cylindrical domain. (b) x-component of the incident electric field. (c) x-component and (d) z-component of the total electric field on the XZ plane.

To simulate a semi-infinite case and be closer to real TERS probes conditions (from electrochemically etched gold nano-wire for instance – § 2.3.2.1), we have to look for

a geometric solution without using a too large modelling. We decided here to merge the base of the metal tip into the PML. Then, SPP traveling along the tip should not be back-scattered and should not be experienced any Fabry-Pérot effect like previously. To do that, we studied both cases with several heights of the tip under a range from 1 to 5 μm and the EF at 1 nm from the apex have been investigated. All the results are presented on the next figure 3.8 for the finite (a) and semi-infinite (b) case. Surface-plots show the spectral response for each signal for continuous variation of tip height while graphics represent spectra for particular values (1, 3 and 5 μm).

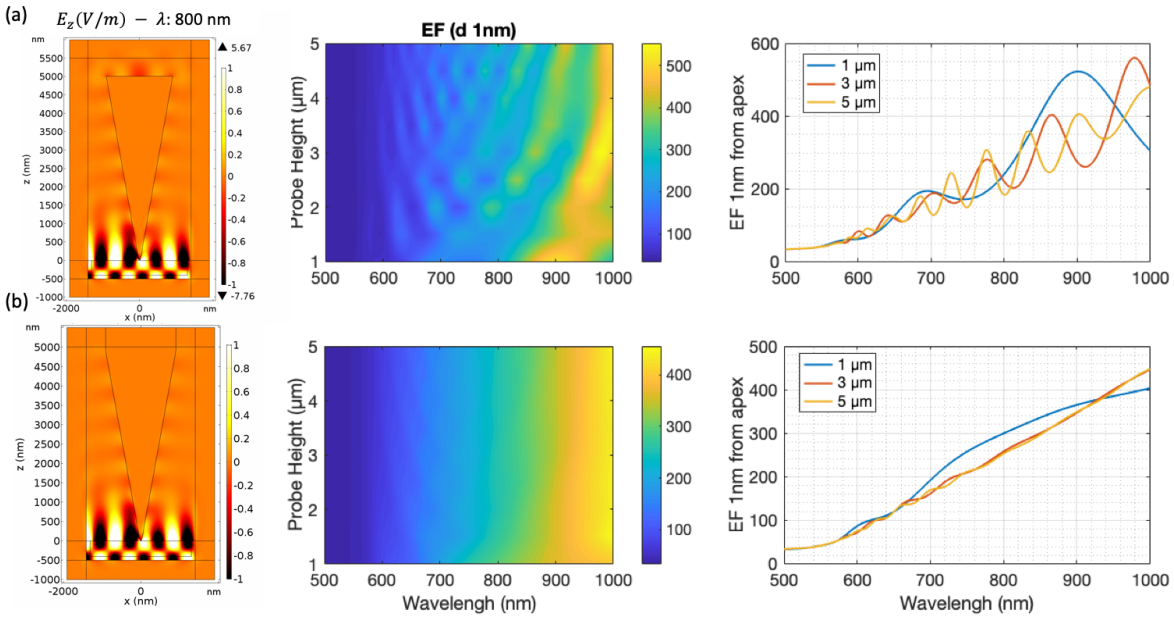

FIGURE 3.8 – From left to right: z-component of the electric field along the XZ plane, surface-plot of EF spectrum depending on the tip height, and EF spectrum for selected tip height. (a): Finite tip case. (b): semi-infinite tip case

In the finite case 3.8.a, optical properties exhibit a resonant characteristic according to the cavity length. Indeed, the higher the tip, the more numerous the number of modes. However, this resonant behavior of the micrometric tip can be almost completely canceled for the semi-infinite case 3.8.b, since SPP are not traveling between extremities of a cavity but seems to vanish at the PML interface: and this tends to smooth the responses. The EF spectra do not change significantly for tip height > 3 μm, and it results in an enhancement in the broad visible spectrum range without resonance making this system a 'non-resonant' tip.

In practice, resonant responses are attributed to granularity or roughness of metal probes but modelling such a surface is complex. To give a resonant characteristic of our perfectly smoothed and semi-infinite tip, we decided to reproduce

the FIB milling at the vicinity of the apex as shown in the literature [138] and as illustrated in Figure 3.9.a. In order to isolate a nano-antenna from the rest of the tip, we show the effect of a 10 nm width and 10 nm deep trench away from the apex with a distance from 50 nm (in blue) to 200 nm (in yellow). The surface-charges presented in Figure 3.9.b show a plasmon mode inside the apex-trench cavity. As expected we can observe the occurrence of a particular resonance on the optical properties for a wavelength excitation shifting from 520 to 600 nm according to the location of the trench (see Fig. 3.9.c).

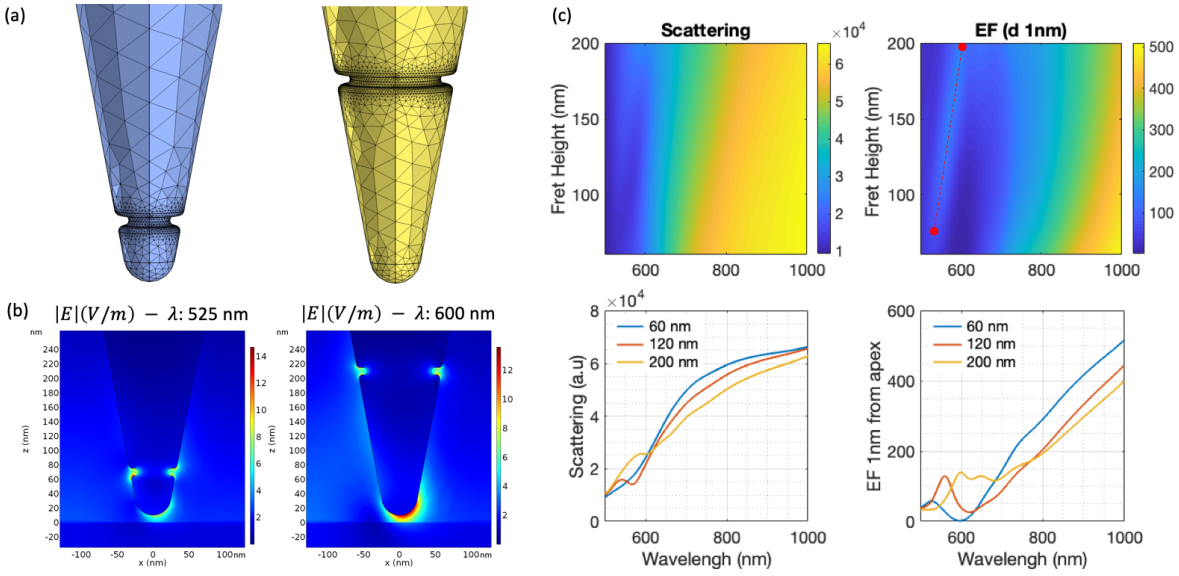

FIGURE 3.9 – (a) Illustration of the numerical discretization of the geometry (mesh) for a trench distance of 50 nm (blue) and 200 nm (yellow). (b) Corresponding electric field imaging along the XZ plane. (c) Top: Surface-plots of the scattering and EF spectra depending on the distance of the trench from the apex. Bottom: Spectrum of scattering and EF for particular trench location.

These preliminary studies were performed in order to confirm the interest to reach simple plasmonic modes with nanometric particles rather than a micrometric metallic tip in terms of efficiency and reproducibility. Controlling the size of the isolated apex in the aim matching the plasmon frequency with Raman excitation laser must then maximize the EF in a TERS experiment. To study such plasmonic control, we need, in addition to a numerical approach, to develop an experimental set-up optimized to characterize plasmonic objects and investigate the effect of certain machining of the extremity of TERS probes.

3.2 Experimental Set-up

3.2.1 Plasmonic characterization

In order to experimentally characterize the objects talked about in the previous section, we have developed in this work an optical bench based on evanescent waves as being the excitation source in order to probe the spectroscopic scattering response of AFM-TERS probe, as well as engineered plasmonic nanostructures [161, 162]. The operating principle is close to dark-field scattering [163–165], however we use a TIR illumination [166–171] for the purpose of measuring the AFM tip scattering spectrum under scanning conditions, i.e. when an AFM tip is brought into contact with a transparent substrate as seen in the latest numerical results.

We have thus developed a spectroscopic tool starting from an AFM mounted on an inverted microscope. We rebuilt the microscope using optical components based on silver-coated mirrors so that it ensures an achromatic behavior over the visible spectrum. The set-up uses a 100x TIR objective in which a white light source is introduced with a large incidence angle at the objective/glass interface to create an evanescent optical field. The plasmonic response of metallic nanostructures (gold, silver or aluminum) is located mostly in the visible range but also the near-IR and UV range, that is why a broadband white light source needs to be used to assure the excitation of the plasmons. The TIR objective is used in dark-field mode, by blocking the light reflected at the interface. Thus, all properties of the scattered light can easily be extracted and analyzed through a spectrometer without parasite light from the excitation since the optical device is settled in such a configuration. We present here our assembly combining AFM mounting with white light TIR illumination and dark-field collection.

3.2.2 Description of the set-up

3.2.2.1 Illumination and collection

The set-up shown in Figure 3.10 is based on an inverted microscope (Olympus IX71, Germany). We replaced the original conventional microscope objective by a high numerical aperture TIR objective (NA 1.49 - UAPON 1000XOTIRF – Olympus).

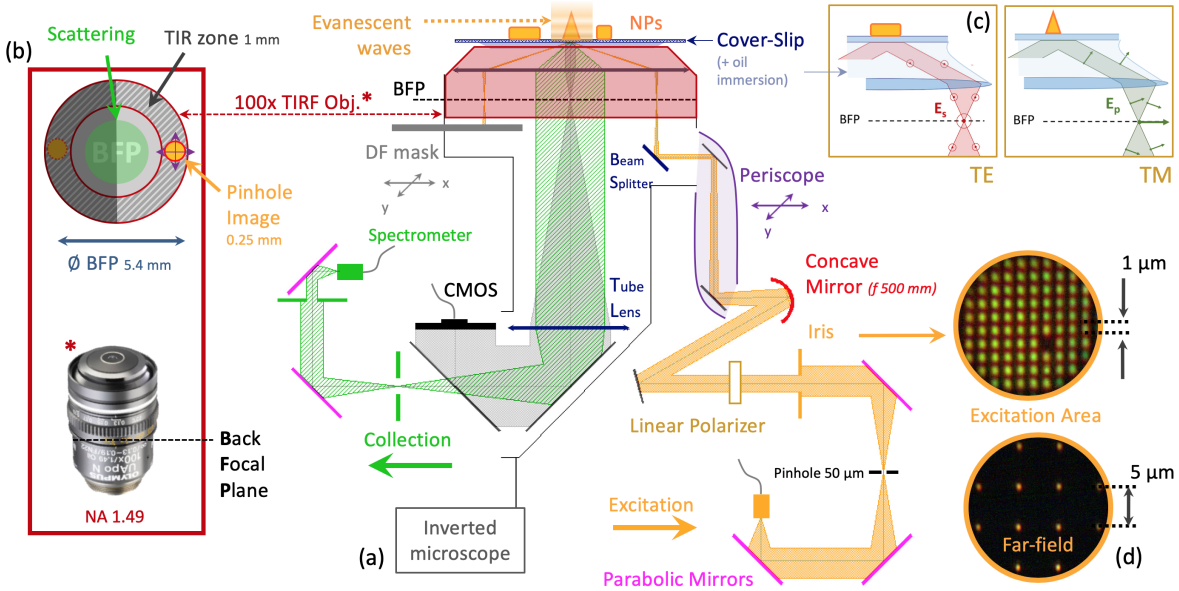

FIGURE 3.10 – Schematic illustration of the experimental set-up, see (a). Orange path: excitation guided on the objective BFP, see (b); a linear polarizer is used to excite nano-antennas either in TE or TM modes, see (c). Green path: the scattered light is collected via the same objective, enabling either the dark-field imaging, see (d), or the spectral analysis via a visible spectrometer. (b) Cross-section in its BFP, showing the incident pinhole image (orange spot), the specular reflection blocked by the dark-field mask, and the collected scattered signal. (d) Example of acquired far-field images on arrays of metallic nano-antennas on a glass cover-slip (1 μm or 5 μm pitch).

A broadband white light source (LDLS EQ-99XFC, ENERGETIQ, US) is used as an intense and unpolarized illumination. To avoid chromatic aberrations, silver coated parabolic, concave and plane mirrors are used in the set-up. The incident light from the fiber is first collimated and focused into a 50 μm pinhole before being collimated again to cross an iris and a linear polarizer – three parabolic mirrors are involved here. The filtered and polarized pinhole point source is then reflected by a long-focal concave mirror and enters the microscope through a periscope. The light is reflected onto a beam splitter and finally focused on one side of the objective back focal plane (BFP) to allow TIR excitation at the coverslip/air interface. The incident beam gets reflected on the glass-air interface, goes back into the objective and is blocked by a mask on the other half of the BFP. This mask, as well as the focal image of the pinhole source, can be finely positioned using XY micrometric screws (see Fig. 3.10.b). The substrate thickness is in the 150-200 μm range (Schott D 263®M cover glass), and immersion oil (IMMOIL-F30CC, Olympus, Germany) ensures the lens-substrate contact and index matching. The light scattered by the evanescent field at the coverslip/air interface is collected in the center of the TIR objective, travels through the beam splitter and is focused by the tube lens of the

microscope onto a CMOS camera to obtain scattered far-field imaging. The first tunable iris allows us to control the excitation spot size on the substrate interface, while the scattered light is focused on a second one to control the collection area and acquire the spectra. It is then collimated and focused onto the input slit of the spectrometer (VS7000 – HORIBA Scientific, France) equipped with an uncooled CCD camera. For an incident light source with an optical power around 80mW/nm in the visible range – giving a surface power of about 4 mW/μm^2 for an excitation spot with diameter of typically 5μm –, this set-up performs the scattering spectrum analysis of single gold nano-antennas within a typical 100 ms acquisition time.

Figure 3.11 shows in more details the alignment specifications. The first condition was to use a white-light source with as less as possible contact with transparent features such as standard optical lenses.

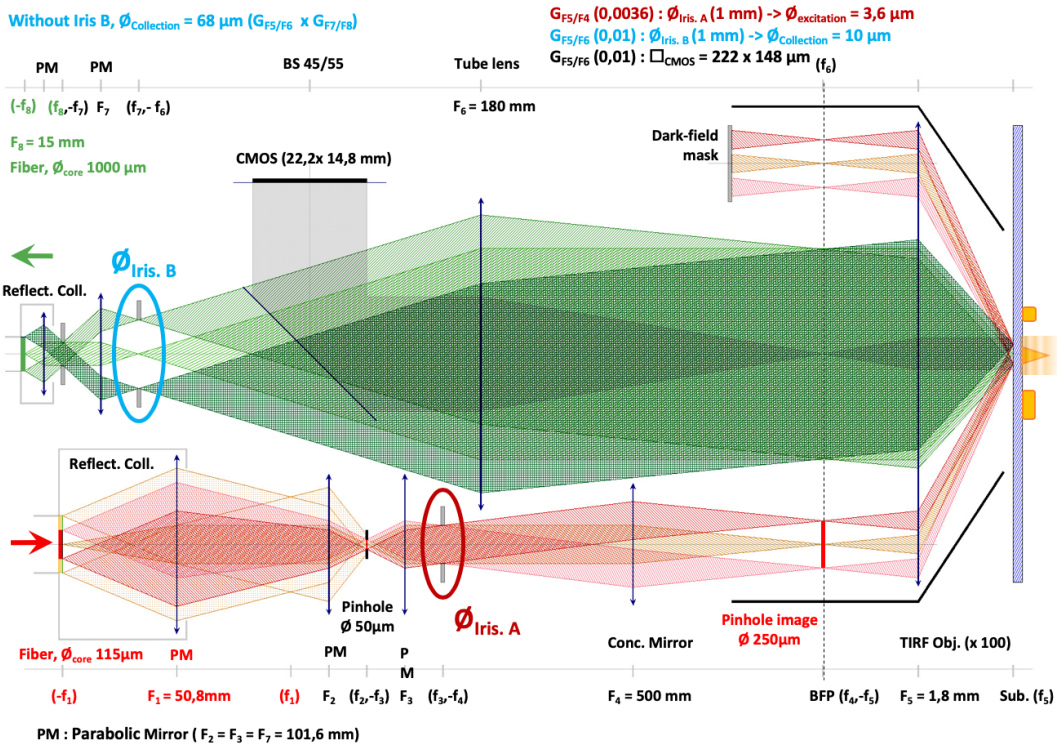

FIGURE 3.11 – Schematic illustrations of the experimental set-up with the previous vertical axis now represented horizontally. Red path: light ray path from source points of the excitation. A focal-object was performed by a 50 μm width pinhole to obtain focal-image on the BFP of 250μm. The iris A defines the excitation area with a magnitude of 0.0036. Scattering light rays from emitter points of the sample to the spectrometer (green path) or the CMOS camera (gray path), iris B defines the collection area with a magnitude of 0.01.

Reflecting collimators are also based on similar parabolic mirrors, ensuring the

junction with optical fiber apertures for the incoming light and the out-coming scattered light into the spectrometer. We also observe in Figure 3.11 the optical path characteristics in term of focal lengths between optical components. Parabolic mirrors are thus illustrated as simple concave lenses while plane mirrors are not represented at all as well as the beam-splitter inside the microscope.

As an illustration, Figure 3.12 presents the optical path through optomechanical elements (Throlabs, US). It can be noticed that the compact disposition enables to introduce the entire optical set-up on a 75x75 cm optical table inside the original AFM frame for a vibration-free environment.

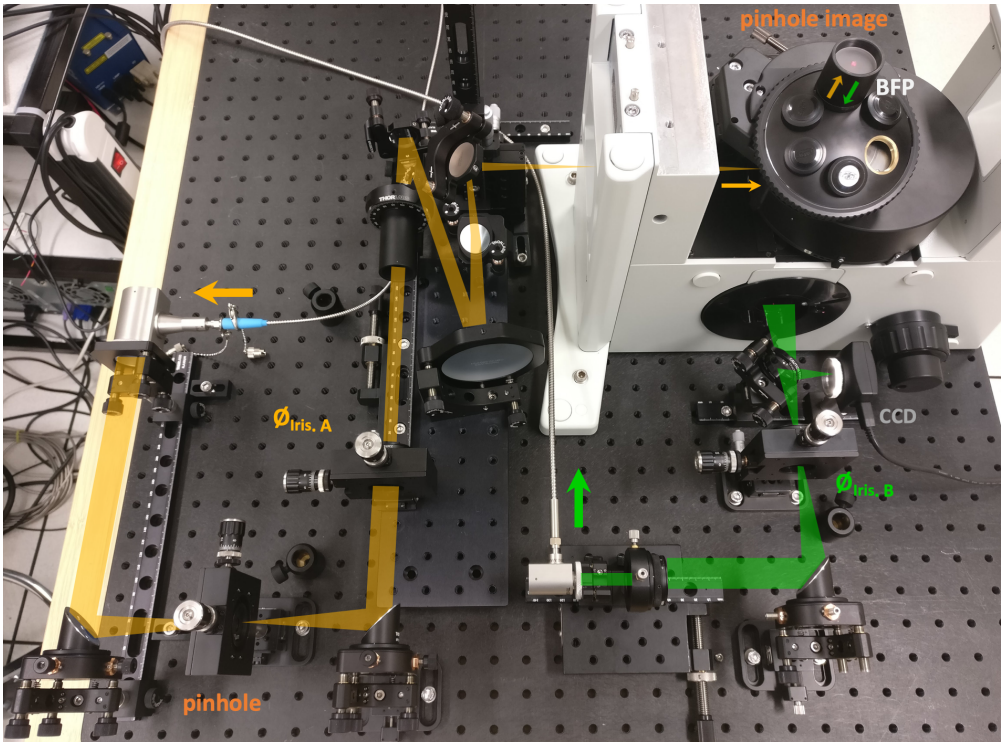

FIGURE 3.12 – Photograph of the set-up showing the optomechanical equipment. Orange path: the excitation beam is first focused on the pinhole, and the pinhole image is spatially filtered by the iris A and focused on the BFP. Green path: Using a flip mounting beam-splitter, collection beam is focused either onto the CMOS camera or onto the spectrometer fiber after being spatially filtered by the iris B.

As seen in Figure 3.10.b, the TIR objective focuses light with a high NA required for total-reflexion since light enters the objective BFP with enough distance from the optical center. We can define then a TIR area on the external part BFP. To ensure that all the incoming light reaches this region only, the focal spot on the BFP should not exceed 1 mm. The pinhole together with the parabolic mirror and the concave mirror determine the spot size. With the combined focal lengths giving a magnification of about 5 and a pinhole focal-object of 50 μm, we obtain the focal-image on

the BFP of width about 250μm – small enough to fit in the TIR area. Also, two iris in the optical path allow a control of the spot size under the sample or the collection surface area of the sample. The excitation spot responds to a combined focal length from the concave mirror and the TIR objective lenses with a magnification of 0.0036 while the collection spot is determined by the objective and tube lenses focal of the microscope with a magnitude of 0.01. For instance, both iris settled to exhibit an aperture of 1 mm give an excitation area about 4 μm while the collection zone is about 10 μm.

Moreover, samples consist mostly here in an array of lithographically-patterned metallic nanostructures. It is hence necessary to anticipate the sample fabrication before the characterization tests in terms of the pitch size of the grid array. We have seen in Figure 3.10.d what the excitation area looks like with a pitch array of 1 and 5 μm. In these conditions, the excitation iris easily gives the possibility to light up a single nano-object. Unfortunately, we can also see on far-field images an optical iridescence – red on upper left, and green on bottom-right – which is a signature of chromatic aberrations caused by the TIR objective lenses and due to the intense refraction of a high NA. It is thus better to privilege a larger excitation spot size on a large pitch array sample so that all wavelengths are roughly focused on the same point and allow excitation of the nanostructures within the whole visible spectrum. The iris of the collection can potentially filter parasite noise from the entire device.

For an easy acquisition of a multitude of particles, we must choose a pitch array for our sample to target a single nano-object among others properly. Indeed, the detector size of the CMOS camera and the microscope magnification imposes a small field of view of the sample, about 220$\times$150 μm. A motorized scanning stage (SCANplus IM120x80, Marzhauser, Germany) has been installed to move the substrate above the microscope finely without damaging the oil-contact between the objective and the cover-slip. It also allows an easy investigation of each nanoparticle that forms the array with a pitch from 5 to 12 μm as used for later experiments.

3.2.2.2 AFM-head adaptation

One of the main goals of this experimental device is ultimately to optically characterize the response of metal tips or microfabricated TERS probes by the scattered field. We can then obtain information about the approximative geometrical aspect of the probe apex through plasmonic properties, or predict the Raman scattering

enhancement range for downstream spectroscopy measurements done under a specific excitation wavelength. Our set-up requires then an adaptation of the AFM microscope. We have placed such a microscope (Bioscope, Brüker, Germany) on the scanning table of the inverted microscope (see Fig. 3.13).

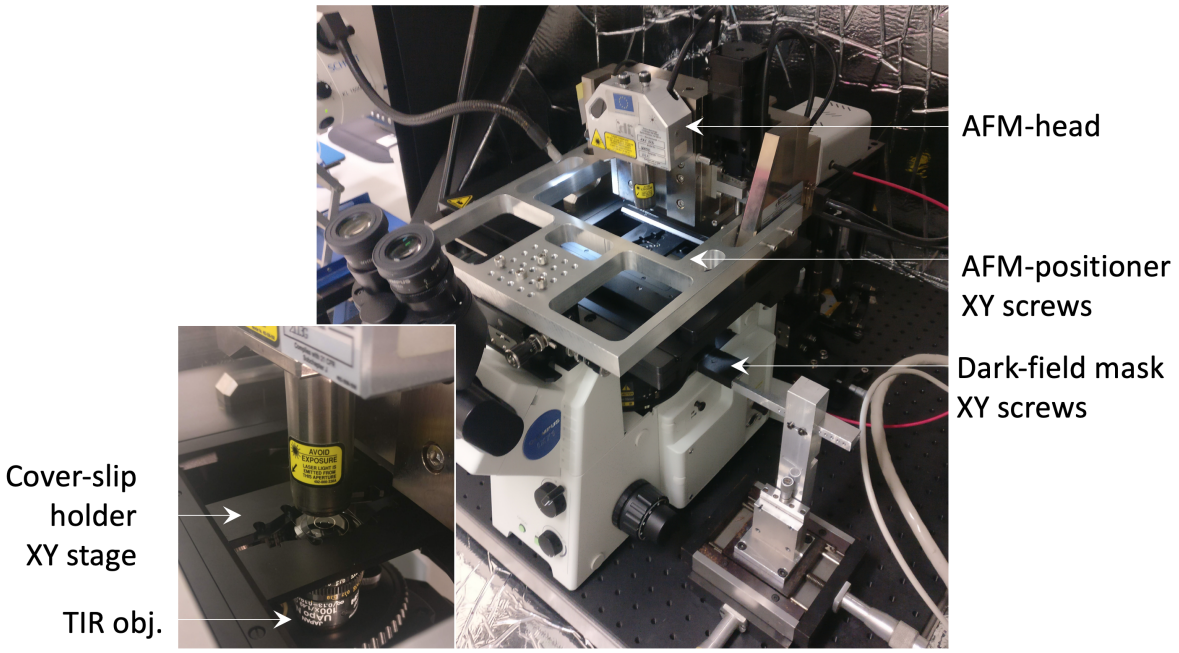

FIGURE 3.13 – Photography of the set-up coupled with the AFM microscope. Aluminum plate positioner moves the AFM-holder on the scanning table with XY micrometric screws. The dark-field mask under the objective is also displaced with micrometric screws. In the inset, a zoom on the system AFM-head/sample/TIR objective.

While a blank glass cover-slip is enough to characterize TERS probes, we have anticipated future SNOM experiments where the displacement of the probe must be independent of the sample displacement. The AFM head has a motorized translation range about 1 cm with (a pitch around 1μm) in the vertical direction and piezoelectric translation ranges of 100 μm in the XY-plane and 6 μm in the z-direction. This displacement constitutes a limitation for a first coarse alignment of the AFM with the optical microscope. To solve this issue, a homemade positioner from a bulk aluminum plate was machined and fixed on a manual XY translation stage and the microscope without interacting with the scanning stage. Two arms embrace the AFM-holder posts and screws ensure the contact between the positioner and the AFM-holder. After a coarse alignment, loosen the screws releases all the contact points and allows precise alignment for the piezo-scanners of the AFM-head.

3.3 Comparative Results - Numerical vs Experimental

3.3.1 Optical nano-antennas

This set-up is first tested with individual plasmonic nano-antennas consisting either in Au nanodisks or in Au nanocones lithographically-patterned onto a glass substrate. The structures have been fabricated by Au evaporation through a PMMA resist lift-off mask written by electron beam lithography (EBL, § 4.2.1.1). Each nanoparticle has been, after optical characterization, measured using electronic microscopy to evaluate dimensions that are introduced in the theoretical modelling for comparison and interpretation of the scattering spectra.

We then tested TERS-efficient commercial Au-coated AFM-TERS probes. For that purpose, the AFM-head is installed on the upper part of the inverted microscope. Under piezoelectric control, these probes are brought into the evanescent field at the TIR objective/glass interface in tapping or contact mode (§ 3.3.2). Their optical properties are compared with the results of individual plasmonic nanostructures, and in particular Au nanocones.

3.3.1.1 Gold nano-disks

We start with a series of Au nanodisks, with a thickness of about 50 nm and diameters in the 100-160 nm range, fabricated on a glass substrate. Both transverse electric and transverse magnetic linear polarizations (see Figure 3.10c) have been probed under TIR conditions, and are hereafter labelled TIR-TE and TIR-TM. For every single nano-antenna, we have recorded the associated scattering spectra in the 400-900 nm wavelength range. A background signal spectrum (recorded on the glass substrate, S_{bg}) has been subtracted from raw data (S_{raw}) and normalization by the white light reference (measured by collecting the incident light reflected without the dark-field mask, S_{WL}) has been applied. The scattering response of the nano-antennas (S_{LSP}) is thus defined as:

$$S_{LSP} = \frac{S_{raw} - S_{bg}}{S_{WL}} \tag{3.10}$$

For comparison sake with experiments, theoretical scattering spectra have been computed together with three-dimensional representations of the far-field radiation for each TE or TM polarizations (§ 3.1.1).

Experimentally obtained and theoretically computed data are shown in figures 3.14a and 3.14b – colors are used in the rest of the figure to label the nanodisks diameters). We observe in the TIR-TE polarization a single resonance, which exhibits a redshift for increasing nanodisks diameters. This mode corresponds to the plasmon associated with the horizontal dipole (HD, see illustration in Fig. 3.14b), for which a spectral redshift with larger diameters is predicted by the plasmon theory and is linked to the lowering of the restoring force exerted on free electrons at the surface of the particle [172] (see the grey arrow as a guide for the eye). [173, 174].

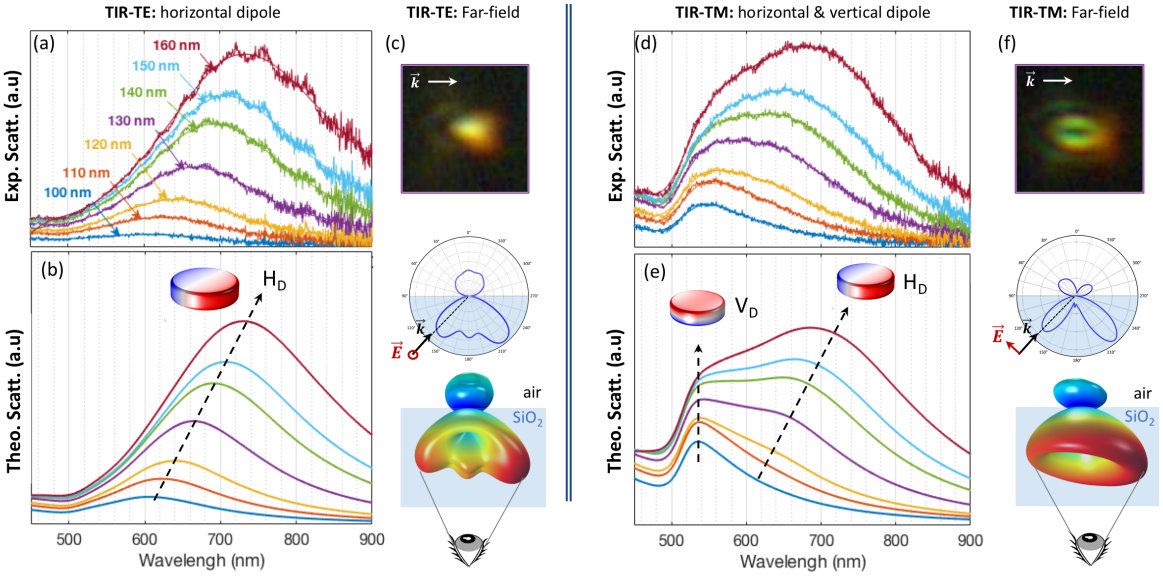

FIGURE 3.14 – (a) Experimental TIR-TE scattering spectra for a series of individual Au nanodisks for different diameters. (b) Corresponding calculated spectra, showing a horizontal dipole (HD) resonance in the inset. (c) Far-field image of a single Au nanodisk (top) of 130 nm diameter, and radiation diagrams of the HD mode in the plane normal to the air/glass interface (middle), and in a three-dimensional representation (bottom). (d) Experimental TIR-TM spectra for the same series of Au nanodisks. (e) Corresponding calculated TIR-TM spectra, showing a resurgence of the HD mode at a larger wavelength, and a second resonance at a lower wavelength, corresponding to a vertical dipole (VD) mode, insensitive to the diameter. The insets show schematic illustrations of the two dipolar modes surface charges (in air). (f) Calculated radiation patterns associated with the VD mode (bottom) showing a donut-like shape, together with an experimental far-field image of the same Au nanodisk used in (c).

The experimental data are in excellent agreement with theoretical scattering spectra. Experimental far-field images (see Fig. 3.14c) also show similarities with the calculated radiation patterns, and are comparable with calculations found in the literature [175]. We can see in the calculations the appearance of two side lobes

in the excitation plane which might be explained by the electric quadrupole mode contribution [173, 174].

However, the situation is more complex for TIR-TM polarization. Experimental scattering spectra exhibit two resonances, one can be seen by the shoulder of the dipole response, which are well accounted for by numerical modelling (Fig. 3.14.d). The resonance at a larger wavelength corresponds to the same horizontal dipolar mode and exhibits the same redshift with increasing nanodisk diameter. This reminiscence of the HD mode is due to the tilt angle of the optical excitation in the TIR objective (see the schematic illustrations of the TIR-TE and TIR-TM polarizations in Fig. 3.10) which imposes a non-zero value of the horizontal component E_x of the excitation. In contrast, the shorter-wavelength resonance is almost insensitive to the nanodisk diameter (driven by the fixed thickness of 50 nm). This resonance is well accounted for in numerical calculations and corresponds to a vertical dipolar (VD) mode [176] (see inset of Fig. 3.14.e for an illustration). The experimental evolution of the wavelength and amplitude of the two resonances as a function of the nanodisk diameter is accurately predicted by numerical modelling, taking the incidence angle of the illumination equal to 44°. The calculated far-field radiation diagrams of the VD mode, shown in Figure 3.14.f, presents a typical 'donut-like' shape, observed in the experiments, and is due to the cancellation of far-field radiation in the direction of the induced dipole.

3.3.1.2 Gold nano-cones

Au nanocones were studied as a second set of samples. As proposed by preliminary studies of the numerical modelling, conical nano-antenna seems to be an interesting plasmonic structure (§ 3.1.2.1) with great variability of LSPR properties. Indeed, nanocones offer a large plasmonic tunability with the size and exhibit intense enhancement of the EM fields at its tip. The nanofabrication process – detailed in § 4.2.1.1 – leads also to the fabrication of nanocones on a glass substrate by playing on the aspect ratio of the lithographically-patterned nano-hole written onto the resist by EBL (grey part on Fig. 3.15.a) combined with the amount of metal evaporated which tends to reduce the aperture until it closes completely (orange part). The next part focuses on characterization and modelling of individual gold nanocones with several heights but with a constant cone half-angle of about 12.5°, which depends on the nature of the metal [177].

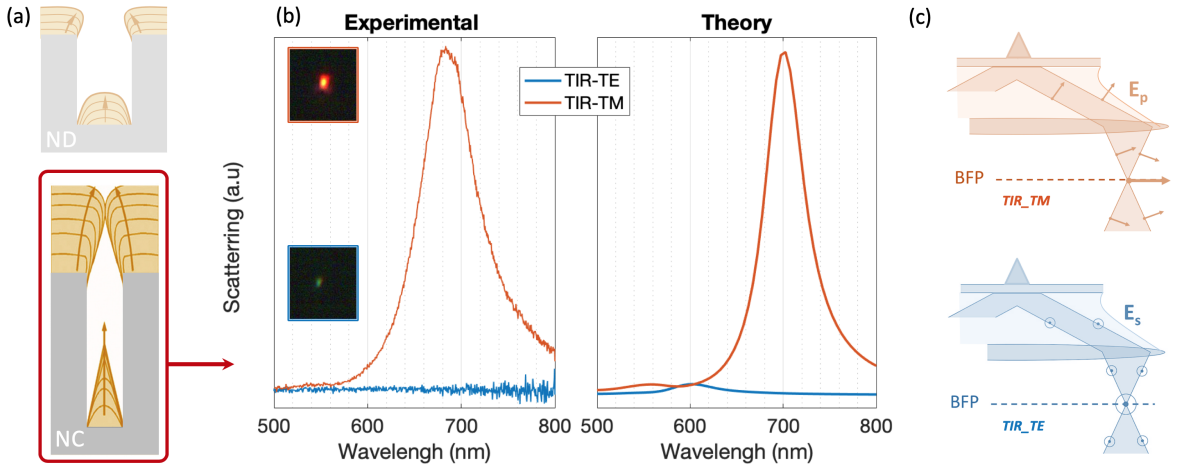

FIGURE 3.15 – (a) Brief schematic illustration of the fabrication process of ND and NC. (b) Experimental spectra for a single 120 nm high Au nanocone with a base diameter about 65 nm (left) showing far-field inset for both polarization with corresponding calculated spectra (right). (c) Schematic of the orientation of the electric field, defined parallel to the paper plane for the TM or perpendicular for TE.

Such structures exhibit intense plasmon resonances with vertical dipole behavior due to their large vertical aspect ratio, since they have been probed under p-polarization (or TIR-TM). Indeed, we see on the first figure 3.15.b a clear difference in comparison with TIR-TE where no resonance is clearly identified. Figure 3.15.c presents illustrations to remind the polarization state at the TIR objective influenced by the linear polarizer of the experimental set-up (§ 3.2.2). For p-polarization, the electric field is defined on the paper plane (XZ), and the z-component is privileged since the point source is focused out of the optical center of the objective and onto the back focal plane (BFP). The vertical dipole can be thus excited and resonates at a wavelength excitation of 700 nm (orange curves) for the corresponding height of the nanocone (here about 120 nm), as it can be seen in the signature of the far-field, red spot observed in the insert. For s-polarization (blue curves), the incident electric field is perpendicular to the paper plane (along Oy) and excites the horizontal dipole which resonates for a higher frequency (600 nm according to the calculations) located close to the base of the cone (here about 65 nm) and it is at the origin of the green spot observed in the far-field. To assess the plasmonic tunability, we performed a series of spectral acquisitions of gold nanocones with heights in the 105-250 nm range. Experimental scattering spectra are shown in figure 3.16, together with numerical calculations.

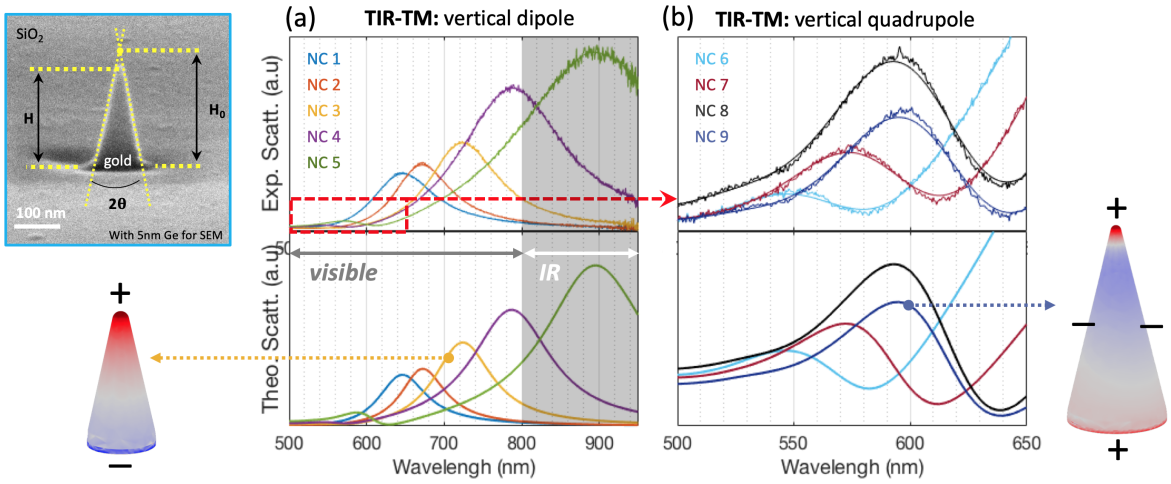

FIGURE 3.16 – Experimental spectra recorded (top) and calculated (bottom) for a TM optical excitation. Data for nanocones NC1-NC5 are shown in (a) and exhibit dipole resonances in the 500-900 nm wavelength range. For taller nanocones NC6-NC9, (b), they exhibit quadrupole resonances in the 500-650 nm wavelength range. Insets show a typical SEM of the nanocone geometry, and 3D numerical representations of the Poynting's vector to illustrate the plasmon modes.

The dimensions of the Au nanocones (height H, half-angle θ, and apex radius r) have been measured individually from scanning electron microscopy (SEM) images, and all data are reported on the table 3.1. The dimensions used in the numerical modelling correspond to dimensions obtained experimentally with an accuracy of a few percents. We will describe later in details the measurement procedure of the geometric parameters and the correction procedure introduced in numerical modelling. TIR-TM scattering spectra and numerical calculations both reveal a dipolar and a higher-order vertical plasmonic mode. The first series of nanocones (NC 1 to NC 5), with heights ranging from 105 to 205 nm, exhibits a pronounced dipolar resonance in the visible range (550-800 nm) except for NC 5. In the latter case, both experimental and theoretical results show the emergence of a higher order mode in the green region, of quadrupolar type, since the dipolar resonance falls in the infrared. For taller nanocones (here, labelled from NC 6 to NC 9, with heights ranging from 195 to 245 nm), the quadrupole dominates in the 500-650 nm wavelength range. As before, the evolution of experimental TIR spectra is consistent with the numerical analysis conducted as a function of the Au nanocone dimensions.

The nanocone geometric properties have been measured experimentally from SEM observation (example shown in Fig.3.17 - left). Nanocones have been covered for this purpose by a 5 nm layer of Ge to ensure imaging without charging effects. Experimentally, we measured the nanocone half angle, the nanocone nominal height

	Nanocone parameters derived from SEM					Nanocone parameters used in numerical modelling					
	Parameters measured by SEM			Base diameter D (nm)	Apex radius r (nm)	*Correction*		Base diameter* D* (nm)	err (%)	Apex radius* r (nm)	err (%)
	θ (°)	H_0 (nm)	H (nm)			θ* (°)	err (%)				
NC 1	12	175	107.3	74.4	17.8	-	-	-	-	-	-
NC 2	12.15	143.6	108.1	61.8	9.5	12.25	0.8	62.4	0.8	9.6	1
NC 3	12.95	158.7	130.8	73	8.1	12.65	2.4	71.2	2.5	7.8	3
NC 4	10.4	206	158	75.6	10.6	10.75	2.2	74	2.3	10.3	2.7
NC 5	10.5	235.1	203.3	87.2	7.1	10.65	1.4	88.4	1.4	7.2	1.7
NC 6	15.85	217	195.8	123.2	8	16.5	3.9	128.6	4.2	8.4	5.3
NC 7	13.7	234.5	213.1	114.4	6.6	14.25	3.9	119.2	4	7	5
NC 8	17.75	263.7	243.4	129	6.3	13.75	0	129	0	6.3	0
NC 9	11.8	259	229.8	108.2	7.5	11.5	2.6	105.4	2,7	7.3	3.2

TABLE 3.1 – Geometrical parameters of nanocones NC 1 to NC 9 as measured from SEM imaging. Left columns: the parameters θ, H_0 and H have been measured from SEM (see Figure 3.17, left) and the base diameter D and apex radius r are derived from geometrical considerations. The right column shows the parameters used in numerical modelling: the parameter θ has been adjusted in order to fit the main scattering spectrum resonance wavelength (the error indicates the variation with respect to the value of θ measured from SEM); the values of D and r have been recalculated (*), taking into account the corrected value of θ.

H_0 (extrapolated height assuming an infinitely sharp cone), and the nanocone actual height H. Data for θ, H_0 and H extracted are shown in Table 3.1 (left column). The nanocone base diameter D is geometrically derived from θ and H_0. The finite apex radius is obtained using a sphere-cone description based on the nanocone half angle θ, base diameter D, and apex radius r. A source of error in these measurements lay in the Ge coating of nanocones and residual fuzziness of the nanocone edges upon SEM imaging. To account for this, we introduced a correction procedure in the simulations, in which the cone half-angle value has been slightly adjusted in order to fit the wavelength of the main resonance observed in experimental TIR scattering spectra of Figure 3.16., while keeping constant the values of H_0 and H extracted from SEM measurements. Adjusted values for θ are shown in Table 3.1 (right). They only differ from SEM values by a few percents at most, as well as the affected values of the nanocone base diameter D and nanocone apex radius. The corrected values of θ, D, and r (*) have been used in numerical simulations shown in Figure 3.16.

A particular situation is additionally found for the nanocone NC 1, for which corrected values for θ, D and r have not been shown in Table 3.1. This structure is, in reality, closer to a double nanocone as seen from the SEM image shown in Figure 3.17 (right) and compared with the NC 6 (left). It has been adequately treated as a double sphere-cone structure in numerical modelling.

From these results, we can conclude with no doubt that this optical characterization of localized plasmonic properties is a powerful solution for the

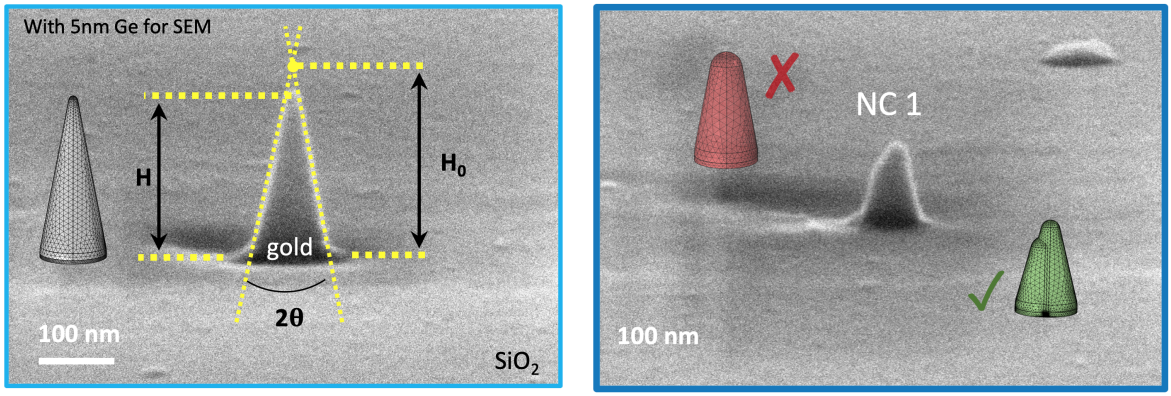

FIGURE 3.17 – Left image: SEM image of a nanocone (NC 6) with the measured parameters θ, H_0 and H. Right image: specific case of the nanocone NC 1, appearing as a double nanocone)

study of individual metallic nanostructures using basic optomechanical components. Moreover, the results obtained both on Au nanodisks and nanocones show the relevance of our TIR scattering spectroscopy setup to collect the plasmonic properties of nano-resonators and promote the ability of the finite element calculations used in this work to quantitatively account for the detailed optical properties of individual metallic nano-resonators as a function of their nanoscale geometry.

3.3.2 AFM-TERS probes

The final goal in this part is to characterize commercialized AFM-TERS probes and correlate the results with SEM observation in order to better understand which elements at the tip influence the plasmon properties at the apex. We have characterized individual TERS cantilever-based AFM-TERS probes fabricated by metal evaporation on standard commercial AFM tips (ACCESS-NC probes, Applied NanoStructures, Inc., USA). We describe in the following the acquisition of TIR spectra on the example of an Au-coated tip with an apex radius of curvature about 40 nm, and then we compare a set of three probes. AFM-TERS probes (see Fig. 3.18a) are brought into the evanescent optical field of the TIR objective covered with a blank glass substrate (see Fig. 3.18b and 3.18c). AFM-TERS probes are first coarsely centered above the objective and engaged in tapping mode. The position of the tip is finely adjusted in a second step, using the AFM head horizontal piezoelectric displacements, to bring the tip to the center of the optical excitation spot. As before, the plasmon responses are obtained after subtraction of the background noise in the absence of any tip and normalization with the excitation spectrum.

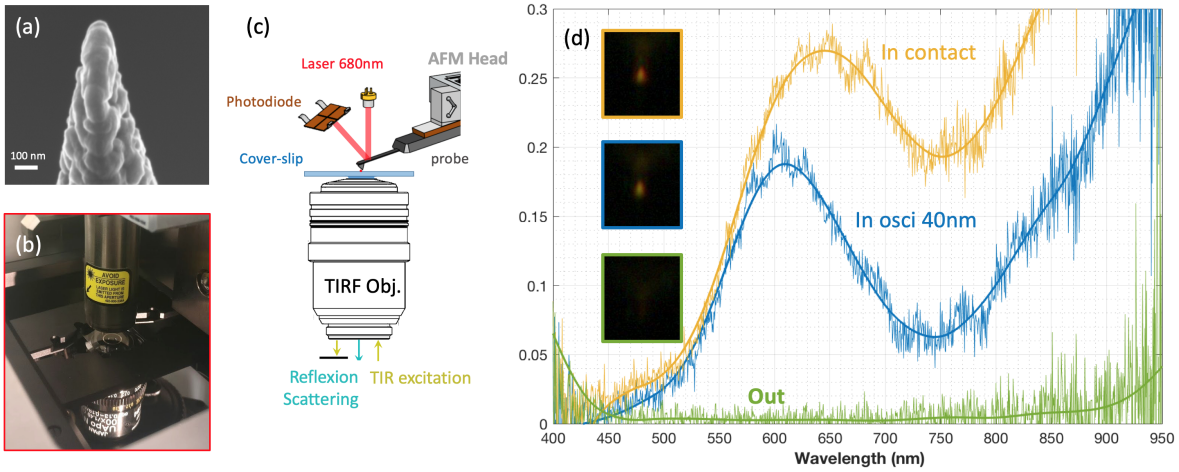

FIGURE 3.18 – (a) Scanning electron micrograph of the apex of a Au-coated AFM probe with 40 nm apex radius (b) mounted on the AFM head located above the TIR microscope. (c) Schematic illustration of the measurement configuration, in which the TERS tip is brought in the evanescent field of a glass coverslip above the TIR objective using the regulation of the AFM head. (d) TIR scattering spectra for the Au-coated tip shown in (a). The green, blue, and orange curves are the normalized TIR scattering spectra recorded respectively with the tip located 200 nm above the glass coverslip, with the tip engaged on the surface in tapping-mode with a 40 nm oscillation amplitude, and with the tip engaged in contact mode. Far-field optical images are shown as insets.

The TIR spectra for a Au-coated AFM-TERS probe is presented in Figure 3.18.d. The green curve corresponds to the TIR spectrum acquired with the TERS probes retracted ∼200 nm away from the substrate surface and exhibits almost no response, as would be expected for a probe out of the evanescent optical field from the substrate. The increased noise level at the edges of the recorded spectrum is due to the cut-off of the optical set-up (mainly, of the TIR objective) out of the visible range, which reduces the amount of light detected at such wavelengths. A TIR scattering spectrum of the TERS tip is first shown (blue curve in Fig. 3.18d) when the tip is engaged on the surface in tapping mode (average oscillation amplitude of ∼40 nm) also corresponding to a bright spot in the dark-field image (see insets in Fig. 3.18d). The TIR scattering spectrum shows a clear resonance at a wavelength of about 600 nm, while a background develops at larger wavelengths (> 800 nm). When the tip approaches the surface, and by switching the AFM regulation from tapping mode to contact mode (orange curve in Fig. 3.18d), the spectrum shows an enhanced signal and preserved the structure, with an observable redshift of the resonance now occurring at a wavelength of ∼650 nm. This redshift in the scattering spectrum can be explained by the interaction of the dipolar localized plasmon mode supported by the tip and its image in the glass substrate [178].

We also performed a comparison between a set of three Au coated AFM-TERS probes (see Fig. 3.19) using the same protocol as in the experiments shown in Figure 3.18. Probes appear almost identical in individual SEM images (see Fig. 3.19a). They exhibit a tip apex radius of curvature between ∼35 nm and ∼45 nm — this radius mainly depends on the metal coating local roughness at the tip apex. Scattering spectra are shown in Figure 3.19.b. The systematic sharp peak observed at a wavelength of 685 nm corresponds to a parasitic detection of the AFM head laser and needs to be disregarded. The third probes present a 'white' scattering background response, which is typical of a semi-infinite metallic (non-resonant) antenna. Besides, the scattering spectra also show a plasmon resonance around 630 nm and 850 nm for the tips with a radius of curvature about 35 nm and 40 nm respectively. For a larger radius of curvature (45 nm), the main resonance reaches the infrared region. We thus observe as a trend that sharper tips produce localized surface plasmon resonances with high oscillator strength, and occur at shorter wavelengths.

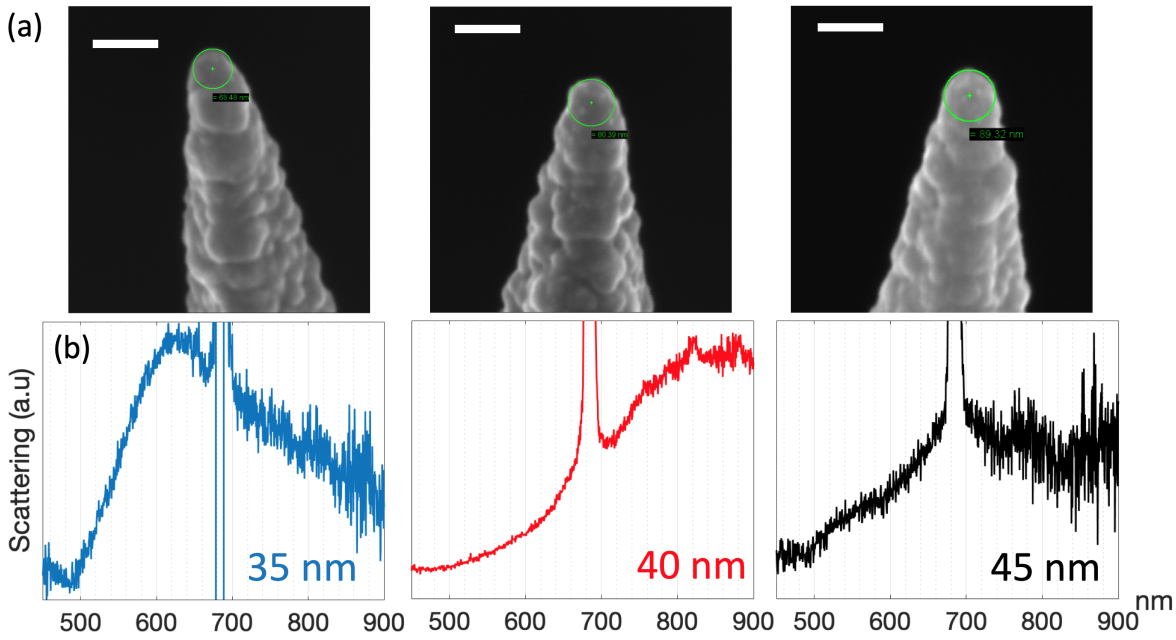

FIGURE 3.19 – (a) Scanning electron micrograph provided for a set of three commercial Au-coated AFM cantilevers. The scale bar is 100 nm. Apex radii are highlighted. (b) Corresponding TIR scattering spectra. The tip apex radii are shown in insets. The line or discontinuity at 680 nm corresponds to a parasitic detection of the laser line of the AFM head and should be disregarded.

This spectral dependence related to the variation of the probe radii of curvature of only 5 nm (most certainly due to the roughness at the tip vicinity) is strong and it

appears difficult to control during the thermal evaporation of the gold layer on the AFM tip.

Conclusion

In this chapter, we have performed finite element simulations to investigate the resonance properties of metal optical nano-antenna. Their plasmonic responses were studied according to the shape of the nanostructure and under nanometric variation of their dimensions. Nanocones present interesting characteristics for the optimization of plasmon properties, i.e., the large plasmon tunability in air (250 nm) and intense enhancement factor (3000) nearby the apex. Numerical modelling has also demonstrated the dependence on the illumination polarization of the excitation of resonance modes associated with nanodisks disposed on the glass surface. Under total internal reflexion configuration, inverted cone long as few microns was studied in order to simulate a perfectly smoothed tip probe. With a finite size tip, a plasmonic Fabry-Pérot cavity is created between both extremities of the tip. A semi-infinite model results in 'non-resonant' system, and it is possible to break the aspect by customizing the apex tip.

Using an inverted microscope equipped with a high NA oil immersion objective, we have recorded the spectral response of plasmonic nanostructures here lithographically-patterned onto a glass substrate. We have seen that precise alignment conditions on the BFP of the objective are required to ensure TIR illumination at the origin of evanescent waves. An additional mask placed right under the objective is required to block the excitation reflection to obtain a dark-field configuration. In addition to an analysis on a multitude of nanostructures, this tools combined with an AFM-head ensures the detection of the enhancement properties of marketed efficient AFM-TERS probes.

The result shows that a significant difference exists between metallic nanostructures fabricated by electron beam lithography and the AFM based probes commonly used in TERS experiments. It is striking that the former nanostructures reproducibly give rise to clear-cut localized surface plasmon resonances with a tunable and controllable wavelength, while the latter tips show variability of plasmon from tip to tip. Moreover, nanocones exhibit a reproducible apex radius of 9.9 ± 1.3 nm (the error bar corresponds to the standard deviation for a series of 168 nanocones), contributing to a narrowing of the electromagnetic field lines at the tip apex [179] as required for strong field enhancement for TERS experiments [145, 156].

Chapter 4

Design and Micro/Nano fabrication of AFM-TERS probes

4.1 Field-Enhancement Improvement

Following the work done in the previous chapter, we propose a new design for AFM-TERS probes providing large plasmon tunability, compatible with mass production processes, and high reproducibility. This idea is based on the integration of a single gold optical nano-antenna onto the extremity of silicon AFM-based probes. Taking into consideration the supporting layer effects on the localized surface plasmons, the geometrical properties of this nanostructure have been optimized by numerical calculations in terms of field enhancement. Our design consists of a combination of a metallic nanocone with a nanodisk. Micro- and nano-fabrication processes are developed using *MicroElectroMechanical Systems* (MEMS) in a cleanroom, including several electron beam- or photo-lithography, metallic evaporation and deep reactive ion etching steps on a silicon wafer. As a feasibility test, AFM imaging has been achieved as well as TERS analysis on carbon nanotubes. Such tips should ensure a spectral tunability as a function of the material, size, and geometry, together with high enhancement factors to be used for TERS experiments.

4.1.1 Nano-antenna supporting layer

The aim is be to study and test an s-SNOM probe design based on a single gold nanocone (AuNC) positioned at the extremity of a tip. Thus, the effect of a supporting layer under the AuNC is be here studied using the three-dimensional finite element method, as previously described (§ 3.1.1).

To obtain plasmonic resonances in the visible range of the spectrum, we studied the behavior of the LSP from a 100 nm high AuNC, with a half-angle of 20° and a tip apex curvature radius of 10 nm. The object is excited by a p-polarized EM plane wave ($|\mathbf{E}| = 1$ V/m) as a function of the excitation angle from the normal of the z-axis in three first cases, when the NC is: (i) in the air, (ii) on a glass substrate, or (iii) on a gold substrate (see Fig. 4.1). The graph represents the enhancement factor (EF) calculated half a nanometer away from the apex and in resonance conditions, i.e., for the excitation wavelength respectively 590, 610 and 733 nm. The electric field maps represent the z-component of the excitation for each case under the optimized illumination angle.

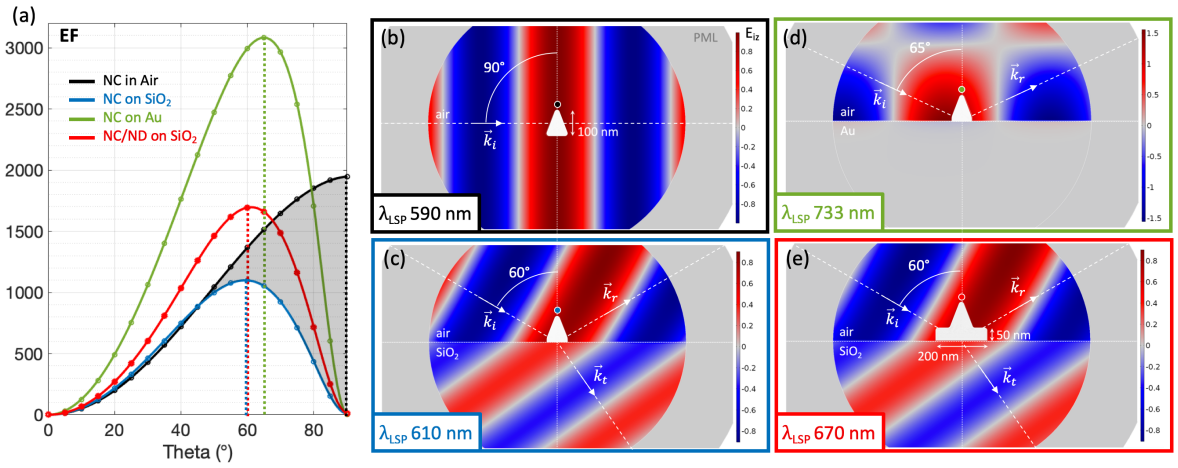

FIGURE 4.1 – (a) EF as a function of the excitation angle - at a specific excitation wavelength - for a single AuNC in air (in black - at 590nm), on SiO_2 surface (in blue - at 610nm), on a gold surface (in green - at 733nm) and a combination of AuNC-AuND on a SiO_2 surface (in red - at 670 nm). (b-e) Corresponding maps of the z-component of the incoming plane wave at the optimized value of the incident angle.

The AuNC in the air (black case) gets a maximum of the EF at 90°, about 2×10^3, when the vertical component of the incoming field is maximal. However, when the same NC in deposited of onto a glass substrate (blue case), its EF becomes null at 90°, due to the destructive interferences between the incident and reflected waves for grazing angle - represented in Figure 4.1.a with the grey area. A maximum of the EF about 1.1×10^3 is then obtained around 60°, i.e., under the best compromise between these interferences and the z-component of the electric field. It explains why the EF decreases from 2×10^3 to 1.1×10^3, in addition to the effect of the substrate on the plasmon [180], such as a redshift of the plasmon from 590 to 610 nm. We observe a similar behavior when the NC is disposed on the bulk gold surface. Here we also

observe an impressive increase of the EF up to 3.1×10^3 with a significant plasmon redshift from 610 to 733 nm. This case is very interesting in view of optimizing the EF generated by the apex of the nanostructure. However, we need to keep in mind that the main goal of this subject is the integration of such optical nano-antenna onto a micrometric tip for AFM-TERS applications. Tip-shaped dielectric materials, like silicon or silicon dioxide, need to be involved in top-down fabrication, so a bulk Au supporting layer is not relevant. The fourth case of the figure (red) shows the possibility to optimize the EF by adding a metal step under the NC. This step is here a 50 nm thick gold nanodisk with a diameter of 200 nm. It increases the EF of 55% with respect to the case where the NC is alone on the glass surface, and with an obvious red-shift of the plasmon from 610 to 670 nm.

4.1.2 Nanodisk-nanocone combination

The last numerical modelling demonstrates the advantage of adding a metal layer just under the AuNC (see Fig.4.1.e - at 60°). The effect of the layer's geometry on the EF needs to be studied to find an optimized configuration. We then vary the disk dimensions, such as the thickness from 0 to 50 nm (see Fig. 4.2.a) and the diameter from 120 nm to 1μm (see Fig. 4.2.b). Each study here contains a schematic representation of the nano-antennas, a plot of the EF spectra as a function of the dimension criterion as well as a graphical representation of the values of EF and plasmon resonance wavelength. The black circle represents the previous geometry with an AuND having a diameter of 200 nm and a thickness of 50 nm.

We can observe in both cases a strong influence of the AuND dimensions that shows the behavior for the EF and wavelength LSP when increasing the dimensions of the AuNd. In Figure 4.2.a, we observe a strong variation of the optical properties with an optimum regarding the EF (2.5×10^3) for a AuND thickness around 10 nm. Moreover, when the thickness is increased from 0 to 5 nm, the original vertical dipole at 610 nm (see Fig. 4.1.c) is slowly vanishing, while for a thickness of 6-7 nm we observe the emergence of another and intense resonance coming from the infrared region, that is strongly blue-shifted and stabilizes at 670 nm. We can see in Figure 4.2.b a strong increasing of EF from 670 nm of 1.1×10^3 with an optimum up to 5.8×10^3 for a diameter of 380 nm, followed by a stabilization around 4.8×10^3. The resonance wavelength is, to a lesser extent, also influenced and red-shifted up to 720 nm. These studies prove the complex plasmonic coupling between the cone and the

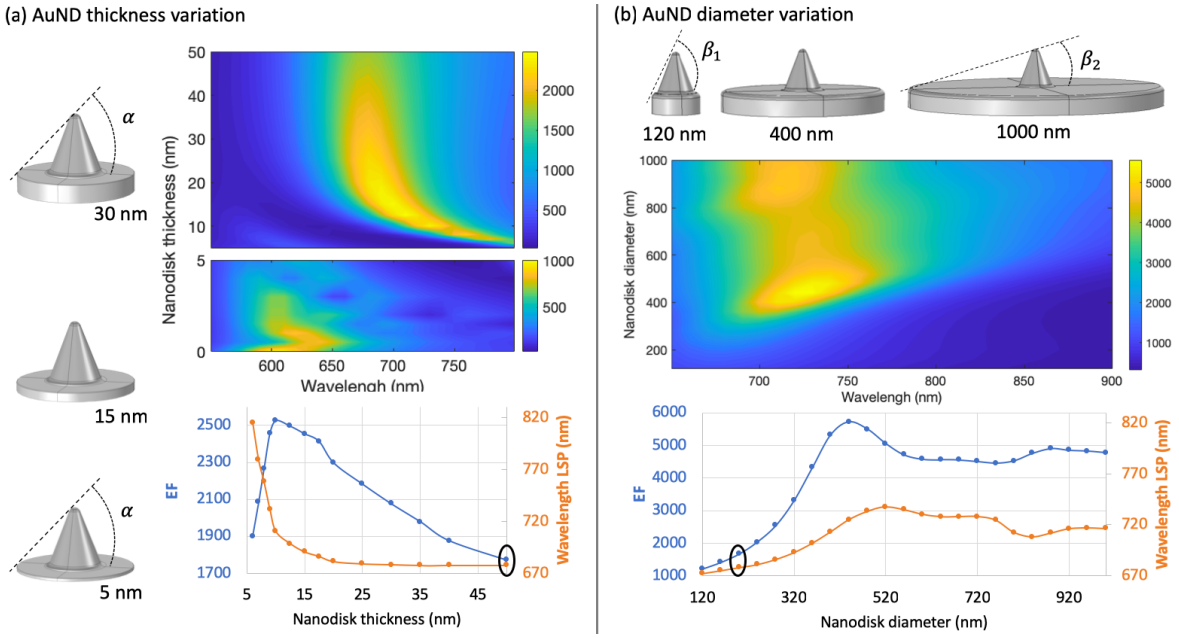

FIGURE 4.2 – **Nanodisk's dimensions study:**(a) AuND thickness variation from 0 to 50 nm non-influencing the angle α. (b) AuND diameter variation from 120 nm to 1 μm strongly influencing the angle β_i. Each study contains a schematic representation of the nano-antennas, a plot of the EF spectra as a function of the dimension criterion and a graphical representation of the values of EF and plasmon resonance wavelength. The black circle represent the initial geometry (diameter of 200 nm and thickness of 50 nm).

disk. The thickness optimum can be reached with a good compromise according to the shift of the plasmon for the conception of the optical nano-antenna at the end of a dielectric probe for TERS experiments. We need to consider that the AFM tip-holder that carries the probe is tilted at 10° from the horizontal. Thus, the optimal diameter cannot be reached without ensuring that only the apex of the AuNC will be in contact with the sample. In other words, the diameter of the AuND of around 400 nm combined with a 100 nm high AuNC will limit a potential tilt of the probe to around $\beta = 26°$ before the edge of the disk touches the sample, while a diameter of 200 nm will get a maximum tilt of the probe about $\beta = 45°$. Moreover, smallest AuND diameters are privileged due to 10° tilted probe facing the 30° tilted Raman laser excitation (see the optical alignment in Figure 4.9 in § 4.3.1). Indeed, the larger the AuND, the larger the supporting layer of the silicon tip, and the more important the shadowing effect of the laser spot on the AuNC.

It is important to remember that the Raman enhancement factor for TERS behaves like the square the EM enhancement, since the scattering Raman wavelength

is very close to the excitation one ($\omega_{inc} \approx \omega_{Raman}$):

$$EF_{TERS} \approx EF_{LSP}^2 = \left[\frac{\left|\mathbf{E}_{apex,\omega_{inc}}\right|^2}{\left|\mathbf{E}_{0,\omega_{inc}}\right|^2} \right]^2 \tag{4.1}$$

with $\mathbf{E}_0$ the intensity of the incoming plane wave. AuNC alone or combined with a AuND (50x200nm) should provide then – in principle – a Raman enhancement respectively up to $\mathbf{1}\times\mathbf{10}^8$ and $\mathbf{3}\times\mathbf{10}^8$ excluding the chemical enhancement part known to participate in enhanced Raman experiments - usually interpreted by the charge-transfer mechanism [181] and giving an additional factor from 10^1 to 10^2.

4.1.3 Study concerning the type of metal

The optical properties of gold are compatible with plasmonics mostly located in the red region of the visible spectrum and restricts the applications, e.g., in the field of biology or semiconductors, that requires to decrease the penetration depth of the excitation laser in the sample devoid from parasitic fluorescence signals. However, silver and aluminum can be used to reach lower wavelengths – and a comparative study between these metals and gold needs to be performed. In order to compare optical properties of these materials, we have presented in Figure 4.3.a-b the real part $\Re(\varepsilon_\lambda)$ and the imaginary part $\Im(\varepsilon_\lambda)$ of the dielectric functions for gold, silver and aluminum.

The conditions required for the generation of plasmons are: (i) $\Re(\varepsilon_\lambda) < 0$ and (ii) $|\Re(\varepsilon_\lambda)| >> |\Im(\varepsilon_\lambda)|$. A clearer representation of the spectral range of plasmon according to the metal can be done considering the quality factor for LSP, Q_{LSP}, which significantly depends on the shape of the metal nanoparticles [182, 183]. For instance, the Q_{LSP} from metallic nanospheres are given by $Q_{LSP} = -\Re(\varepsilon_\lambda)/\Im(\varepsilon_\lambda)$. For each metal studied here, we have represented these factors in Figure 4.3.c. We can see that $Q > 1$ for a Au nanosphere from an excitation wavelength above 500 nm while Ag has an interesting Q_{LSP} from the near UV-range (350nm). Only aluminum benefits from a plasmonic activity from the UV to the entire visible range despite a Q factor much lower than the others. These results are consistent with the calculated EF spectra - represented in Figure 4.3.d - of our designed optical nano-antenna made from each metal and disposed of SiO_2 substrate and illuminated under the optimized conditions (60° and p-polarized). Indeed, gold provides the best EF despite a plasmonic spectral range from 550 to 800nm. Silver matter brings plasmonic activity on the entire visible range despite an maximum EF around 30% lower than gold.

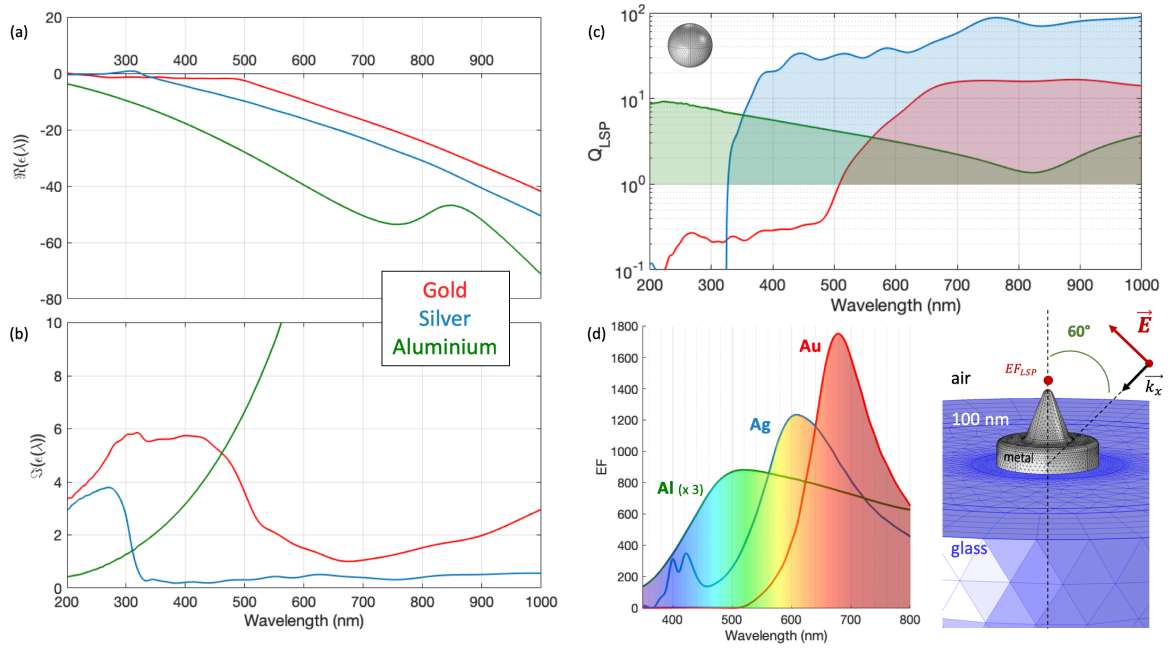

FIGURE 4.3 – **Metal study:**(a) real and (b) imaginary part of the relative permittivity as a function of the excitation wavelength. (c) The quality factor of LSP for a nanosphere. (d) left: EF spectra of the designed optical nano-antenna deposited on of a glass surface and excited by a TM excitation with an illumination angle of 60°. right: schematic representation of the model

The aluminum EF spectrum was multiplied by a factor 3 for clearer comparison with other metals, and we see that aluminum also provides then EM enhancement for highest frequencies despite a value of EF under 3×10^2, i.e. 4 to 6 time lower than for silver or gold.

Here, we have just theoretically demonstrated that this structured nano-object seems to be interesting for TERS experiments. For manufacturing such TERS probe prototype based on our design, we will focus on the common nano-fabrication processes involving gold, due to its inert feature and its ease of implementation. To meet the requirement of current TERS analysis – i.e. simultaneously topographic imaging and high resolution – we have based our probe development on dielectric AFM cantilevers, for which silicon offers a large variability of machining from the micro- to the nanoscale with good reproducibility.

4.2 Manufacturing Development

4.2.1 Nano-fabrication

As seen in the introduction (§ 2.3.2), common TERS probes are either electrochemically etched metallic wires leading to STM tip probes (which can be mounted on tuning forks) or metallized and/or processed conventional AFM probes. For some processes, tips need to be processed individually during their fabrication. We propose here a solution in a different direction, i.e., starting from the design of the metallic apex under which a full cantilever will be aligned and processed. We have also seen (§ 3.3.2) the close relationship between the geometric properties of apexes and the plasmon resonances - and thus the EM enhancement efficiency. It explains why reproducibility of marketed probes is one of the main issues in the TERS community. Hence, we have developed here processes within the cleanroom of the IEMN resulting in a TERS probes fabrication solution promising high reproducibility and compatible with mass production. In this section, we describe how such a combination of metallic nanostructures can result in efficient nano-antennas responding in the visible range, as required for Raman spectroscopy.

Being able to both precisely and accurately control the shape and dimensions of manufactured nano-objects is a fundamental challenge in nanotechnology. In the literature, we can find fabrication methods developed for the reproducible three-dimensional and sub-micrometer-scale objects. Such structures can be fabricated using either 'bottom-up' synthesis methods – such as assembly and self-assembly [184], or 'top-down' methods [185] – by wielding lithographic approaches [186–188]. Here, we demonstrate a simple top-down method whereby electron beam lithography [189, 190] can be combined the well-known 'lift-off' technique with thermal evaporation [191] to control the topography and size of metallic objects at the nanometer scale.

4.2.1.1 Metallic nanocones

Figure 4.4.a shows the fabrication sequences to obtain nanocones patterned onto a flat wafer (3-inch diameter, polished, (100) orientated crystalline silicon) using electron beam lithography (EBL – Raith EBPG 500 Plus at 100kV). The wafer is spin-coated with positive-tone Ebeam sensitive polymer termed the 'resist'. A copolymer methyl methacrylate-poly-(methyl methacrylate) bilayer – commonly referred to as

a 'COPO/PMMA' bilayer – is exposed under an electron beam (dose 400 and 1500 $\mu C/cm^2$ with beam current 1 to 12 nA for respectively AuND and AuNC). The focused electron beam is used to locally alter the dissolution rate of the resists during a later resist wet chemical development step which opens quasi-cylindrical shaped 'nano-holes' in the resist – revealing the underlying silicon wafer. Metallic evaporation is achieved and metallic structures are obtained after lift-off (Remover PG at 70°C). The evaporative deposition onto the resist surface has both a vertical and a horizontal component; the former effectively increases the 'height' of the mask while the latter leads to an effective reduction of the opening width of the hole as the evaporation proceeds. Thus, the key to obtain nanodisks or nanocones resides in the aspect ratio of the exposed cylindrical patterns and the amount of evaporated metal. To create AuND, only 50 nm of Au is evaporated onto a 200 nm thick resist layer. The evaporation tends to close the hole apertures, accounting for the observed tilted edges of the NC. For AuNCs, 250 nm of Au is evaporated on a 500 nm thick resist layer.

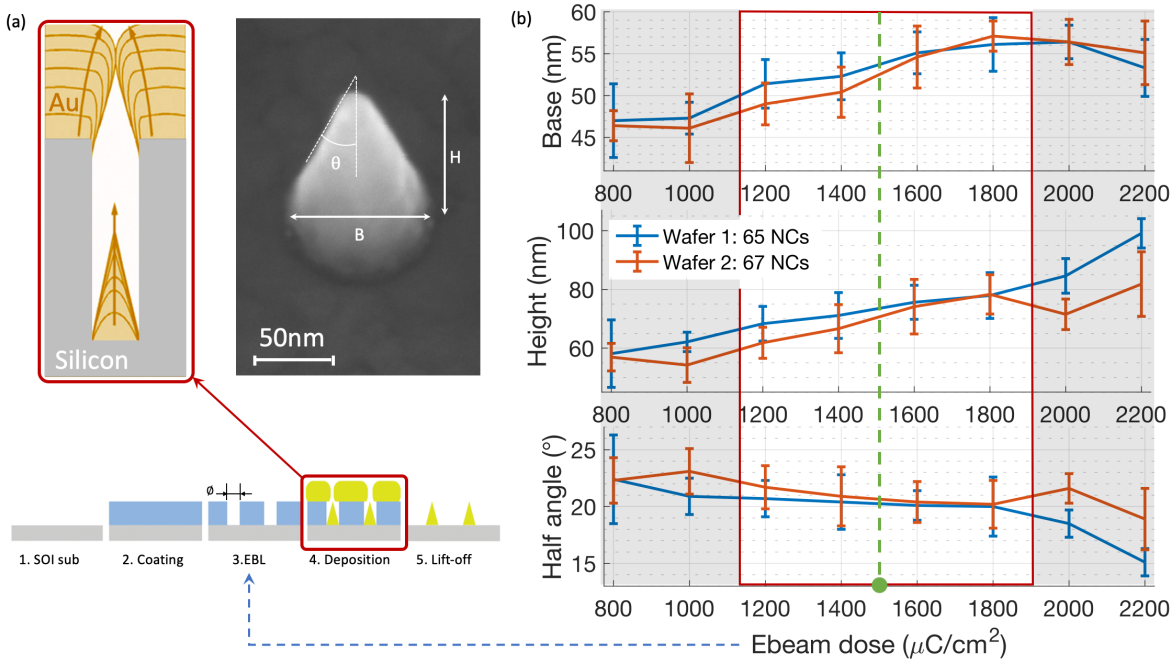

FIGURE 4.4 – (a) Fabrication sequence for Au nanocones and SEM image of a single nanostructure. (b) Statistic studies of AuNC fabrication process about 130 objects dispatched onto two wafers showing the average base, height and half angle of the cones with their respective error bars.

The value of the Ebeam dose is not critical to create nanodisk with respect to the nanocone. We used here 400 $\mu C/cm^2$ according to the basics protocols. For the nanocones, it requires a statistical study varying the Ebeam dose to select a stable value for the final fabrication process. About 130 nanocones were measured using SEM and the dimensions, such as the base, height, and half-angle, as reported in Figure 4.4.b. We can distinguish a dose range (1 200 to 1 800 $\mu C/cm^2$) where the relation with the parameters of the NCs seems being more stable/linear that the extreme values of the Ebeam dose. We chose a value of 1 500 $\mu C/cm^2$ in the following in order to control the size of our structures with the diameter guideline that is respected to open the resist.

4.2.1.2 Nanodisk-nanocone combination

By EBL alignment of a second mask onto pre-patterned AuNDs, it is possible to fabricate nanocones on nanodisks (AuNC/ND – see sequences on Fig. 4.5.a). Here, the disk diameter is given by the hole diameter guideline from the step EBL 1 while the height of the cone is obtained trough by the step EBL 2 diameter guideline. To control the size of the nanocones, a second statistic study has been performed on about 200 nanostructures to collect the geometrical specificities of the AuNC such as the height, base, and apex diameter of curvature at the apex as a function of the Ebeam hole diameter guideline. The data are reported on the graph shown in Figure 4.5.b, under two different gold evaporation rates.

According to the numerical modelling, we can represent the visible spectrum area under the curve corresponding to the evolution of the height of the nanostructures (vertical dipole - λ_{LSP}). We can also notice that the tip of the fabricated cones has a radius of curvature with a value of 9.9 $\pm$ 1.3 nm. This (reproducible) value is smaller than usual commercial silicon AFM tips ($\sim$15 nm) and commercial metal-plated AFM tips ($\sim$25 nm), which is of great interest for AFM-TERS tips. (see § 2.3).

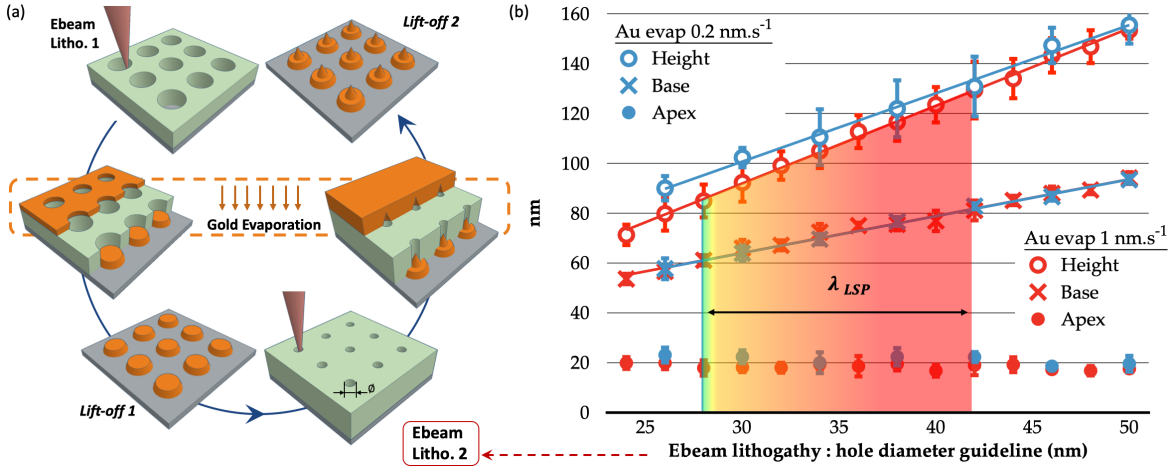

FIGURE 4.5 – (a) Fabrication sequence for Au nanocones combined with Au nanodisks. A PMMA resist layer is exposed by electron beam lithography; Au is then evaporated through the obtained mask, followed by a lift-off process leading either to nanodisks or nanocones at large evaporation thickness. The hole diameter guideline of Ebeam lithography is thus at the origin of the height of the AuNC. (b) Statistic studies of AuNC fabrication process: on 100 objects for each evaporation rates – 0.2 and 1 $nm.s^{-1}$ – showing the average height, base and apex diameter with their respective error bars.

4.2.2 Micro-fabrication

4.2.2.1 MicroElectroMechanical Systems

The story of microelectromechanical systems (MEMS) can be traced back to the fundamental work of Charles Smith in 1954 [192]. He found that the piezoresistivity coefficient depends on the semiconductors crystal orientation and the type and level of impurity doping in the material. These observations have since been greatly exploited in numerous devices and systems. Another major contribution to the development of MEMS technologies was being developed in the USA. Jack Kilby [193] (Texas Instruments) and Robert Noyce [194] (Fairchild Semiconductor) were developing integrated circuit technology under planar approaches. Kilby was awarded the 2000 Nobel Prize in physics for the importance of his work. The predictions of Feynmann had a profound effect on MEMs development [195] regarding the benefits of miniaturization or making tiny machines. The first prototype MEMS "device" could be the one developed by Harvey Nathanson et al. in 1967 [196] based on "resonant gate transistor" performing high-quality signal filtering. The first MEMS-type "laboratory-on-a-chip" was developed in 1979 by Stephen Terry et al. [197]. In 1982, Kurt Petersen suggested silicon can be shaped and used "as a mechanical material" to exploit its specific and advantageous properties [198]. Based on this idea, Calvin Quate pioneered the development of silicon-based atomic

force microscopy probes [199] using two major and powerful techniques: "bulk micromachining" [200] and "surface micromachining" [201]. In the early 2000s, nanoelectromechanical systems (NEMS) [202] have been developed as well as new methods of fabrication [203] to reduce more size of mechanical parts of such systems. The latter area of research has spawned a competition between the so-called "top-down" lithographic-based techniques [204] and the 'bottom-up' auto-assembly techniques [205]

Here, we demonstrate the possibility to integrate the designed nanostructures onto the extremity of silicon AFM-based tip for TERS applications. We have developed here a fabrication scheme enabling the mass production of such tips, by using processes commonly employed for micro- and nano-electronic research development, such as conventional silicon etching techniques from MEMS. The etching can be categorized into a wet and a dry process. While the wet etchant is in the liquid state, the dry etchant is usually in a gas or plasma state. Wet etching has the advantages of a high etching rate and high selectivity. However, it is not directional like in chemical dry etching where gaseous etchants encounter collisions with charged particles. The physical dry etching process is similar to the sputtering process for a thin-film deposition where the reactive ions bombard the material. A commonly used method in dry etching is reactive ion etching (RIE), where both chemical and physical etchings take place. Deep reactive ion etching (DRIE) is known as a process for silicon etching with vertical sidewalls, and a high aspect ratio called the Bosch process [206] and illustrated in Figure 4.6. It consists of an inductive coupled plasma (ICP) RIE with the capability to switch between several gases.

The Bosch process starts from a Si wafer masked by a first layer and exposed according to the area to engrave. At room temperature, it consists of two alternating cycles: (i) etching with sulfur hexafluoride (SF_6) plasma – illustrate in Figures 4.6.(1, 3, 5, 7) – and (ii) passivation of the sidewalls and bottom with fluorocarbon polymer deposited from plasmas containing in the octafluorocyclobutane (C4F8)– see Fig. 4.6.(2, 4, 6, 8). An SF6-based etching gas is first introduced into the chamber. Ions contribute to directional physical etching since a voltage has been applied to the substrate (bias) while the fluorine radicals SiF_x contribute to a chemical etching in all direction (isotropic etching). The gas in the chamber is then switched to C4F8 which forms a passivation fluorocarbon layer on the whole surface, with the bias off. After the passivation, the gas is switched back to SF6 with control of the bias to either remove the passivation layer – only the bottom part – and start another step of silicon etching.

ECS Journal of Solid State Science and Technology, 4 (6) N5067-N5076 (2015)

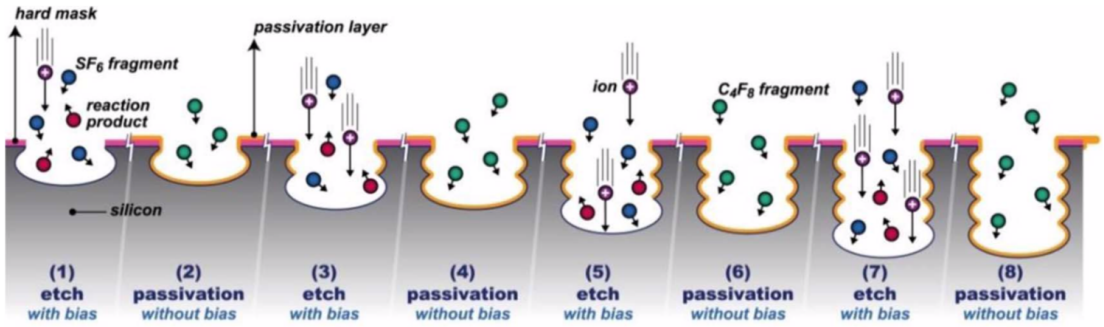

FIGURE 4.6 – Schematic illustration of conventional Bosch process for etching silicon wafer with a pre-patterned mask a top, using alternating etch and passivation half-cycles [207].

The remaining passivation layer on the sidewall functions as a protective layer, thus the sidewalls remain vertical. The process is repeated in cycles until the desired depth is achieved to finally obtain an anisotropic etching result.

4.2.2.2 Optical nano-antenna based AFM probes

The aim of the fabrication process is the integration of each designed nano-antenna previously lithographically-patterned onto the exact extremity of a standardly shaped AFM-based silicon probe. Three reactive ion etching (RIE) of silicon steps are involving here in order the create (i) a tip as a nano-antenna holder at the extremity of a (ii) micrometric cantilever attached the in one side of the front face of a millimetric chip. Then, (iii) the back face of this chip is obtained by piercing the wafer thickness from the back side of the wafer (see figure 4.7).

Ebeam lithography is again involved here to first protect the nanostructures (Fig. 4.7.a) by a first resist mask before an isotropic etching in order to create a silicon tip under them (Fig. 4.7.b). The entire wafer is once again protected with a second resist and Ebeam lithography is performed as drawing the front face of the AFM probe, including the cantilever and the chip, around each nanostructure (Fig. 4.7.c). An anisotropic etching using a Bosch process is used to create cantilevers. The last step consists in piercing the wafer from the back side to obtain the back face of the chip. Photolithography and deeper Bosch etching process are involved here. Then all the fabricated probes are extracted from the wafer by dissolution of the thick oxide layer in a fluorhydric acid bath (Fig. 4.7.d).

The SOI (silicon on insulator) wafer is composed by a first silicon layer (100) with a thickness of 5 μm, thick enough to create either the tip and the cantilever (2.5 μm each). The second layer is a 2 μm thick silicon dioxide layer, used to stop the etchings, and a final layer of silicon with a thickness of 380 μm.

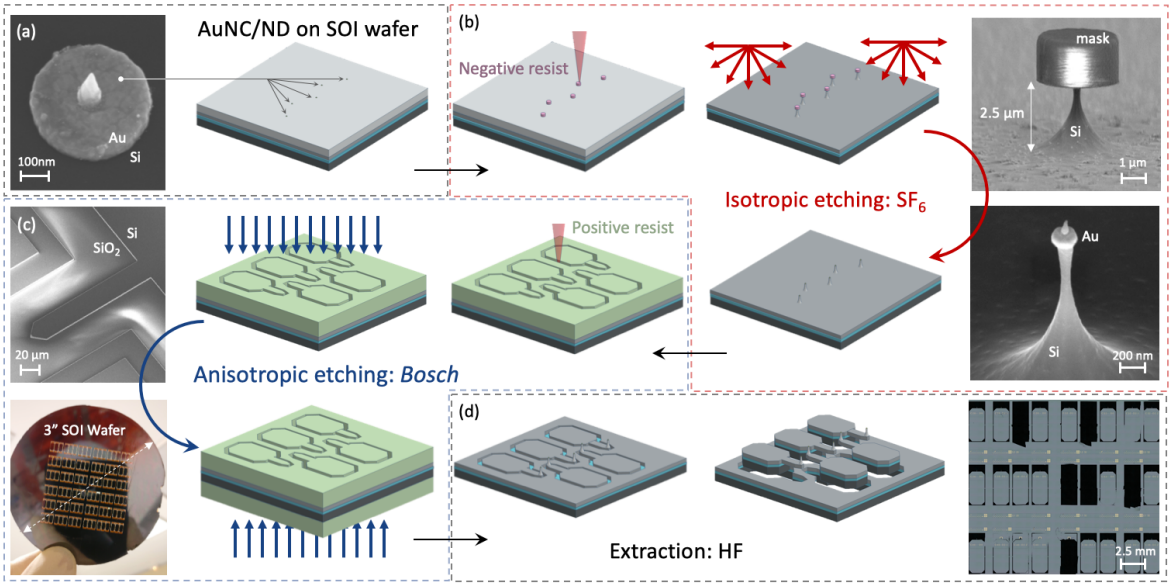

FIGURE 4.7 – Microfabrication sequence of AFM probe around the nano-antennas on SOI wafer (a) with sets of PMMA resist deposition, lithography and silicon etching processes – such as isotropic with SF6 plasma (b) and anisotropic with the Bosch etching methods (c). Acid bath ends the production by dissolving the silicon dioxide layer separating each probe from the parent wafer (d).

Our process has been calibrated to obtain an extremity of this tip made by a planar disk surface with a diameter of about 500 nm to carry the nanostructure (see Fig. 4.8.a). Au nano-antennas were protected with a 2 μm thick PMMA negative resist with a diameter of 3.5 μm using EBL. Once developed, the wafer is introduced in an RIE chamber (STS – SPTS) to undergo an SF6-based plasma etching (pressure: 10 mTorr / flow: 100 sccm) during 55s. It results in a tip with a base of 3.5 μm, a height of 2.5 μm (see Fig. 4.8.b). After the *lift-off* of this mask, the second step starts with another mask using Ebeam lithography on a positive resist. During the writing operation, the electron beam bypasses the silicon tip and draw the shape of the cantilever and the front face of the AFM chip. After the development of the insulated part of the resist, the parent wafer is introduced in a deep reactive ion etching (DRIE) chamber (ESTRELAS – Oxford Instrumental Plasma Technology) to apply an anisotropic etching of the silicon in the vertical direction (Bosch). The etching operation is then stopped once the SiO_2 layer of the wafer is reached giving

hence a 2.5 μm thick silicon cantilever (see Fig. 4.8.c and .d) attached to the front face of the chip (see Fig. 4.8.e). The third and last step consists in piercing the entire last layer of the wafer from the back side according to the shape of the AFM chip – cantilever excluded. For that, the front face of the wafer is physically protected with a 14 μm thick resist to work on the other side of the wafer without damaging the nanostructures. Photolithography is then used on a 7 μm thick positive photoresist since the alignment with the previous steps does not require high precision like previously. Using the same DRIE chamber, the Bosch recipes had been updated to pierce the silicon wafer over 380 μm to reach the other side of the oxide layer. At this current state, the wafer undergoes an HF bath to dissolve the reveal part of the SiO_2 layer and thus releasing all the probes out of the parent wafer still attached with small silicon bridges that need to be broken (see Fig.4.8.f).

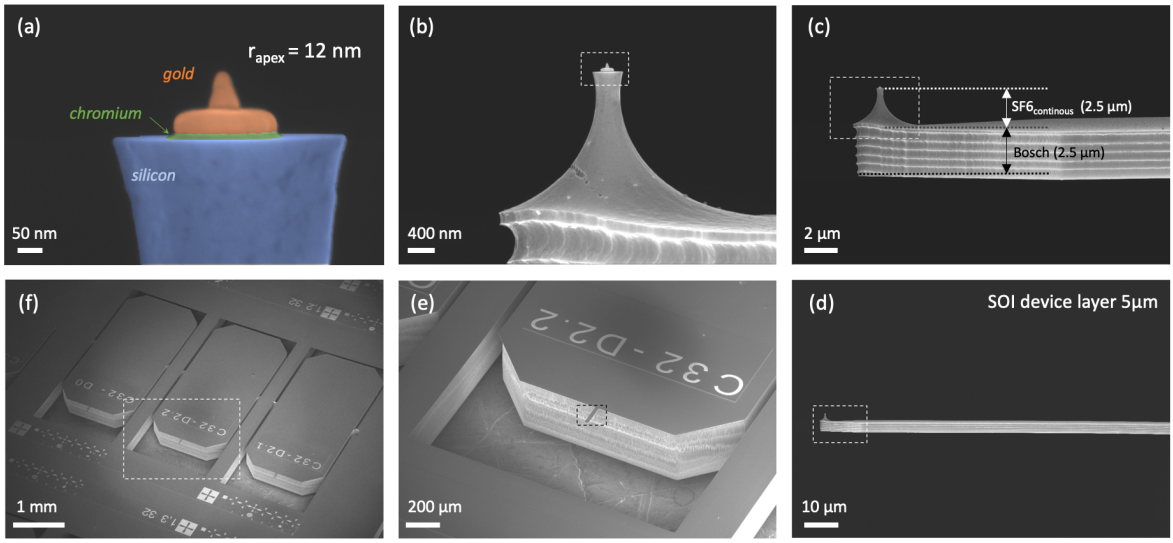

FIGURE 4.8 – Successive scanning electron micrographs of a new prototype of AFM-TERS probe. (a) AuNc/Nd integration on the silicon by 10 nm chromium layer adhesion. The apex of the nanocone exhibits a radius of curvature about 12nm. All materials are illustrated with artificial colors. (b) Optical nano-antenna onto the silicon tip. (c) 5 μm thick SOI device layer use for isotropic and anisotropic etching. (d) Profile view of the silicon cantilever. (e) Piercing of the wafer thickness around the AFM cantilever and chip outline. (f) A trio of probes showing series production on SOI wafer.

We have successfully obtained original nano-structures – for instance here a 75 nm high AuNC with an apex radius about 12 nm, itself on a 50 nm thick AuNDs with a diameter about 200 nm (Fig. 4.8.a). For our first success set, only 6% of the probes exhibit a viable nano-antenna for TERS experiments (7 probes on 108 along a three-inch wafer).

4.3 Application to AFM-TERS

4.3.1 Optical alignment of laser with tip

To evaluate the performances of the fabricated AFM-TERS cantilevers, we have installed these probes on the AFM-Raman system from Horiba Scientific similar as described before (see § 2.3.1). The AFM microscope combined with the Raman spectrometer is based on sample piezo-scanning and motionless probe to keep the right tip-laser alignment obtained under a specific procedure. Off-axis excitation/collection as represented of Figure 4.9.a imposes a three-dimensional alignment of the focused laser at the extremity of the tip using piezo-electric scanner holding the objective. It is, therefore, the Raman excitation laser which is scanned and aligned to the tip apex to optimize the alignment procedure. From the spectrum displayed on the figure 4.9.b, we have used Raman signal from the silicon matter (520 cm^{-1}, in green) as well as the gold luminescence response of the optical nano-antenna (under a random range, here 700-1200 cm^{-1}, in blue) to indirectly image the probe and distinguish the nanostructure from the rest of the probe.

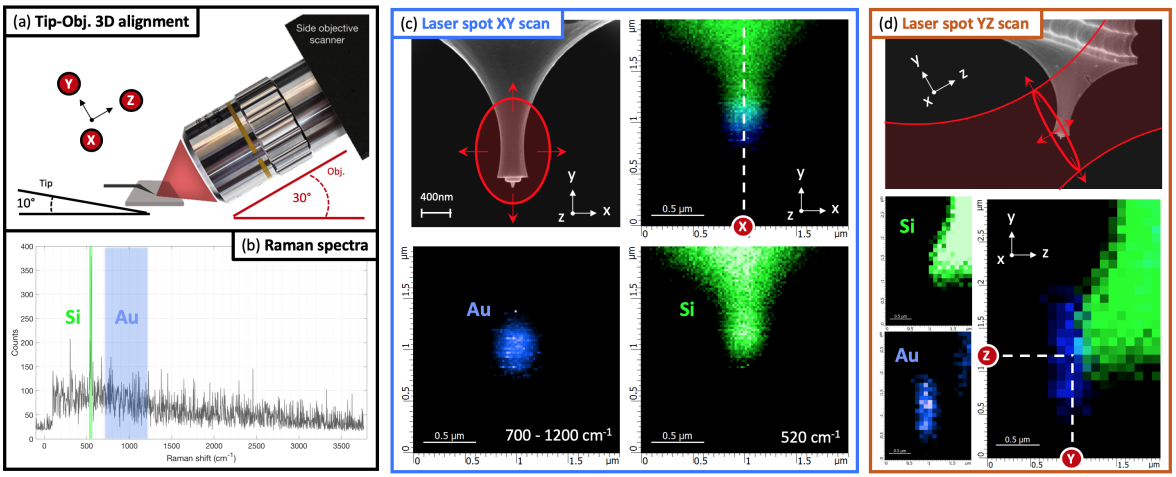

FIGURE 4.9 – (a) Schematic illustrations of the three-dimensional alignment to the off-axis excitation/collection with the probe. (b) Raman spectrum revealing silicon (green) and gold luminescence (blue) responses. (c) Laser spot XY scan: front view on SEM and chemical imaging on the tip fixing the x-coordinate. (d) Laser spot YZ scan: side view on SEM and chemical imaging on the tip fixing the y- and z-coordinates.

The first step of alignment is the scan of the objective in the XY plane corresponding to the front view of the tip's probe (see Fig. 4.9.c). We illustrate on the SEM image a coarse comparison between the spot size – of elliptical shape due to

the tilted illumination – and the tip. After scanning the laser on the body of the tip, we can reconstruct a Raman imaging based on the specific signals. Thus, the blue spot corresponds to the optical nano-antenna and the green shape to the silicon tip. Note that a difference between SEM (taken at 90° from the vertical plane) and the chemical imaging is due to the tilt of the objective (30°) and the tip (10°), and that gives rise to imaging the tip at 60° from the vertical plane. This procedure gives us the x-coordinate from where a second scan (in the plane YZ) will be achieved. This scan corresponds then to the trench of the tip which can be interpreted as the side view of the tip (see Fig. 4.9.d). As before we can distinguish between Au and Si to obtain the missing coordinate revealing the precise position of the nanostructure required for TERS experiment.

4.3.2 TERS of carbon nanotubes

In order to prove enhanced Raman or either AFM imaging efficiency of our new probes, we have studied carbon nanotubes (CNT) as well as graphene oxide (GO) flakes on a gold substrate as a reference test sample. This sample-substrate configuration leads to the so-called 'gap-mode' and gives the largest enhancement in TERS experiment. Indeed, in addition to the field confinement while the TERS probe is approaching any sample substrates, an mirror dipole is induced for metallic surfaces. It acts in the manner of a second nanoparticle with a gap resonance frequency also as a function of tip-substrate separation [208, 209]. This has the effect to highly improve the near-field enhancement of several orders of magnitude. In contrary, if the substrate surface is another material than metal, for instance, dielectrics or a semiconductors, the TERS configuration is then called 'non-gap mode'. In this case, it is more difficult to obtain a detectable signal for analyte molecules with a weaker Raman cross section.

First of all, a tapping-mode AFM imaging was done as shown in Figure 4.10.a using an AFM microscope (AIST-NT/Horiba France). The TERS measurements were achieved using a commercially available combination of this AFM with an Xplora spectrometer (Horiba France). The Raman spectra were collected in backscattering geometry and recorded with an EMCCD camera with gain.

The topographic results show the performance of the probe which is similar to what we can find in the literature in a non-controlled environment [210–212]. The cross-section of a single wall carbon nanotube (SWCNT) is shown in the inset of Figure 4.10.a as the height of the tip while is scanning the surface of the sample. The

SWCNT width is given as the full width at half of the maximum height (FWHM) and has a value of about 40 nm. This result is always larger than the real width due to the tip-convolution. To evaluate the Raman enhancement factor, we detect the response once the probe is away from the sample (see orange curve in Figure 4.10b) and once the probe is in contact with an SWCNT (see blue curve). When the tip is placed in contact, the Raman signal is strongly enhanced compared with the far field background and shows signature Raman peaks of sp^2 carbon materials [213], as being the G-band (1600 cm^{-1}) due to the C-C bonds of graphite, the D-band (1300 cm^{-1}) as being the defect-induced band which gives information about the structural quality of the carbon nanotubes. There is a third peak, 2D-band (2600 cm^{-1}), which occurs as an overtone of the D-band. [214–217].

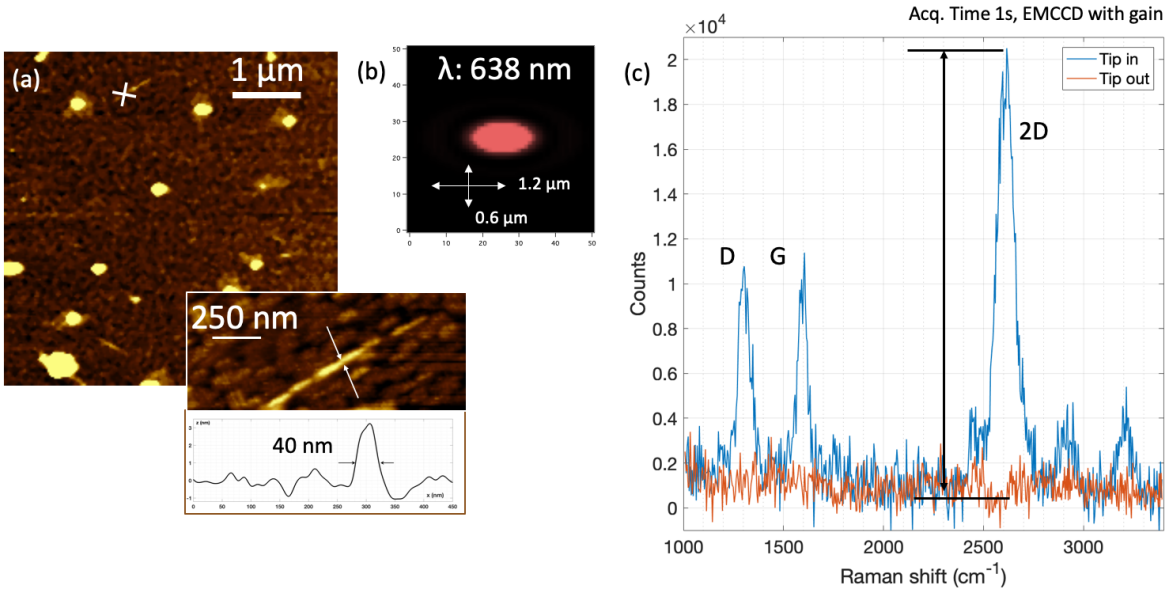

FIGURE 4.10 – (a) AFM imaging of the sample with a more resolved AFM imaging with a topography graph along the cross-section of the SWCNT on a gold substrate - in the inset. (b) Calculation of the excitation laser spot size. (c) Raman scattering spectra from the apex of the probe when the probe is away (in orange) and when the probe interacts in contact mode with the sample (white cross on AFM image).

Based on the equation 2.11 seen in the second chapter § 2.3.1, we can estimate the Raman enhancement factor, here on the largest Raman signal (2D-band). We assume that the studied system can be approximated as a two-dimensional case since the SWCNT thickness is too small to consider a probed volume of the sample under illumination. Thus, the probed volume ratio between the far-field (FF) led by the laser spot and the near-field (NF) by the SWCNT is reduced to a surface ratio. Figure 4.10.b shows the spot size of the excitation laser as being an ellipse

representing the A_{FF}. The surface of a disk gives the A_{NF} is given with a diameter corresponding to the width of the carbon nanotube (with an approximation of the tip deconvolution, FWHM: 30 nm). The EF is obtained by multiplying it with the intensity ration recorded on the Raman spectrum when the tip is in (I_{NF}) and out (I_{FF}) which is given by the noise intensity since any Raman signal can be used as a reference. For the specific band, we obtain an EF as:

$$\begin{aligned} EF_{Raman} &= \left(\frac{I_{FF}+I_{NF}}{I_{FF}}\right) \times \frac{V_{FF}}{V_{NF}} \approx \frac{I_{NF}}{I_{FF}} \times \frac{A_{FF}}{A_{NF}} \\ &= \frac{20200+1800}{1800} \times \frac{600 \times 300}{15 \times 15} \approx 1 \times 10^4 \end{aligned} \tag{4.2}$$

4.3.3 TERS on Graphene oxide flake

Figure 4.11.a presents the topographic and phase AFM imaging of another area of the sample where appear on the right a well define carbon nanotube, and on the left a part of a GO flake). This time, GO was locally investigated in TERS (white cross) and the results are shown in Figure 4.11.b.

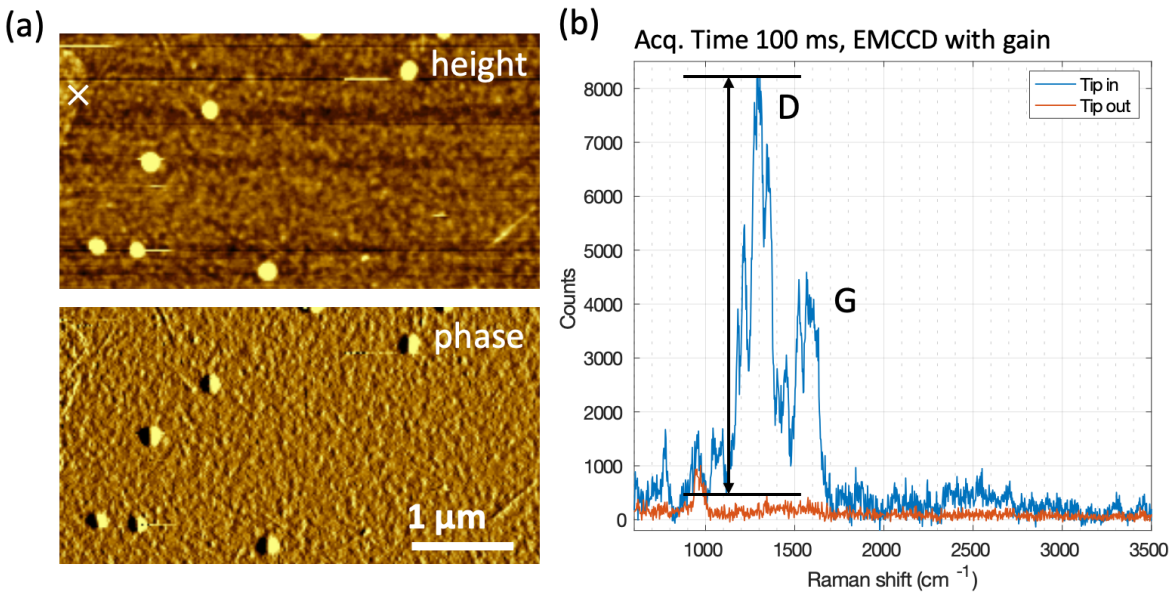

FIGURE 4.11 – (a) AFM imaging of the sample – height and phase (b) Raman scattering spectra from the apex of the probe when the probe is away (in orange) and when the probe interacts in contact mode with the sample (white cross on AFM image).

Both characteristic band, D and G, appear on the Raman spectrum once the TERS probe is in contact with the GO. Here, to obtain a close value of the EF, the

near-field area can be determinate only by knowing size of the apex since we do not know via the sample which area is excited under the near-field. Our probe prototype exhibits a radius of curvature from 10 to 20 nm, we thus based our EF calculation in Equation 2.13 (see § 2.3.1) with a $R_{apex} = 15$ nm:

$$\begin{aligned} EF_{Raman} &= \left(\frac{I_{FF} + I_{NF}}{I_{FF}}\right)\left(\frac{R_{focus}}{\frac{1}{2}R_{apex}}\right)^2 \cos(\theta) \\ &= \left(\frac{200 + 7600}{200}\right)\left(\frac{600}{7.5}\right)^2 \cos(60^\circ) \approx 1.2 \times 10^5 \end{aligned} \tag{4.3}$$

with R_{focus} the radius of the excitation spot and θ the incident angle from the normal. If we compare these experimental results with our numerical result from the Figure 4.3.d in the section § 4.1.2, regarding a AuNC/ND for excitation wavelength corresponding to the Raman laser used here (638 nm), the EM enhancement factor (EF_{LSP}) is about 1100. For Raman scattering, we can estimate theoretically as the square of this value, around 1×10^6, i.e. up to two order of magnitude more than we obtained in our experimental test (without considering chemical enhancement contribution).

We note that the estimation of the overall TERS enhancement depends on several parameters that are not precisely measurable, which leads between 20 and 50% of error resulting in over- or underestimation of the TERS enhancement [106]. It is one of the obstructions for the comparability of TERS tip performance. Moreover, main errors can be explained by inhomogeneities in sample composition which is challenging for reproducible comparisons among laboratory made TERS tips. More precise EF calculation requires then more advanced preparation protocols of both tip and sample.

Furthermore, the TERS equipment involved here – as being in off-axis excitation and backscattering collection – does not seem to be the adequate configuration for our probe prototype – with a right angle between cantilever and tip, pointing in the opposite direction than the objective. Because of grazing excitation are not allowed, the EM excitation is optimized for a side-illumination at 30° from the substrate plane. Common marketed AFM-TERS probes matching with this instrumental configuration are usually made with a tilted tip – between 30 and 40° – pointing forward, i.e., in the direction of the EM source, which as a consequence to reach an optimized configuration between the laser polarization and the tip axes. Here, due to the layer support that holds the nano-antenna (see § 4.1.1), an EF optimum calculated before was, for the same reasons, from a tilted illumination at 30° from the

horizontal axis. A perfect configuration might be, hence, reached with nanofabrication techniques allowing the creation of tiled silicon mesa (10°) pointing forward. Another solution would be the use of an AFM-Raman microscope based on an inverted microscope to lead an excitation from the bottom instead to the side, with a tunable EM polarization – with a radial polarization converter providing radially polarized excitation – to reach the optimal excitation of the nano-antenna dipole.

4.3.4 Protective coating

TERS probes suffer from their lifetime in term of enhancement efficiency regarding different kinds of degradation of metals. In the literature, Ag tips are well accepted to show a higher TERS enhancement than gold tips. However, used carefully, gold tips present today a longer lifetime and are only subject to mechanical degradation since the hardness of pure gold is very weak. For silver tips, it is more question about oxidation during the storage and the use that drastically affect the TERS efficiency over time. Altogether with unwanted chemisorption, all degradation suggest the study of a final coating acting as a protective layer. Among other, some solution was proposed by using pinhole-free silica shell [218] or aluminum oxide [219] coating against undesired chemisorption or chemical attack to provide longer lifetime than unprotected tips without to affect the SPM feedback mechanism or the enhancement efficiency.

With a look at future work within this project, we have performed here some numerical study of several coatings, which are potential solutions of protecting layer for optical nano-antenna. To anticipate the effect of such coating on the plasmonic properties, we have studied a gold nanocone deposited on a glass substrate and excited under total-internal-reflexion (see § 3.1.2.2 for more details). From a plasmon resonance at 600 nm for uncoated nanocone, we observe in Figure 4.12 the evolution of the optical responses – such as absorption, scattering and enhancement factor (EF) – for each coating with a thickness ranging from 0 to 10 nm.

The 2D graphs show the evolution of the spectra where the resonance peak is represented for the highest intensity (in yellow). Graphics on the right show the corresponding EF spectra for a coating thickness of 5 nm. Uncoated Au cones exhibit an EF up to 1.2×10^4 which exponentially decreases with the distance. With iridium and Alu/alumina coating, the EF of naked gold are strongly affected. While iridium [220] red-shits the resonance, aluminum [221] blue-shits it. For SiO_2, the coating

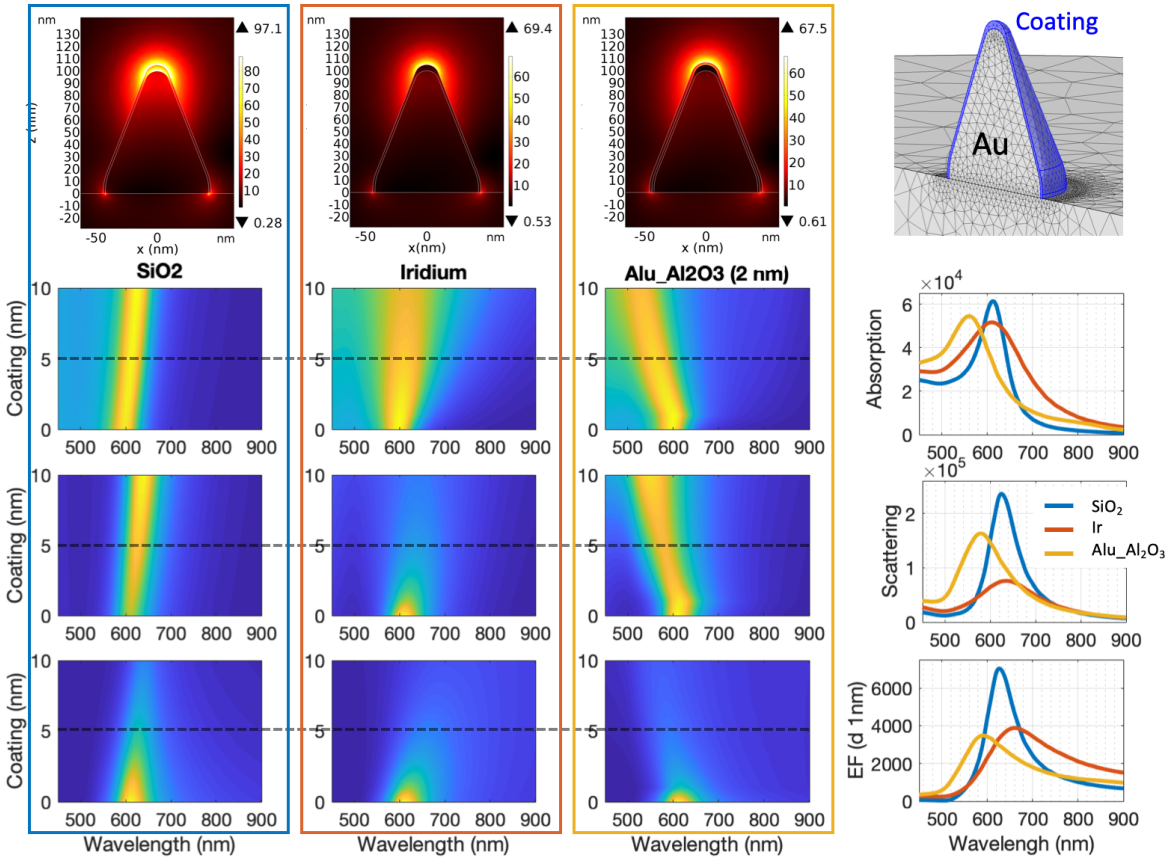

FIGURE 4.12 – **AuNC coating studies:** the upper images show the near-field maps on the longitudinal plane of $SiO2_2$, Iridium, and Aluminum coated Au nanocones. Aluminum coating is accompanied with a 2 nm thick alumina layer. Middle: 2D graphs of the absorption, scattering, and EF spectra in function of the coating thickness. On right: Corresponding spectra for 5nm thick coating.

affects less the EF and preserves the plasmon frequency as compared to an uncoated nanocone. SiO_2 is transparent with respect to the near-field and can be assimilated to a simple spacer from the metallic surface and the sample to be probed, which fatally reduces the EF intensity but does not change the plasmon excitation properties. A SiO_2 coating, therefore, seems to be the best candidate to drive future fabrication step in the case where a protecting coating will be needed, obtained by atomic layer deposition (ALD) [222] for instance.

Conclusion

In this chapter, we have presented a new prototype of a tunable AFM-TERS probe with a fabrication process that is compatible with reproducible mass production. First of all, to take advantages of metallic substrates that significantly enhance the plasmon effect, we have numerically designed an original optical nano-antenna where a metal step shaped as a nanodisk is introduced under the nanocone. The size of the nanocone and the metal involved are the principal actors in the EF tunability that reigns at the apex.

Secondly, we have shown how to batch fabricate an AFM probe exhibiting such nanostructure at its extremity. Statistical studies of the lithographically-patterned nanocone conception were performed to obtain parameters chosen after numerical modelling. This fabrication method reveals high reproducibility of the nano-object and should offer plasmon tunability in the visible range. On silicon wafers, we have seen how MEMS technology allows the integration of each isolated nano-antenna onto a costumed and AFM probe. The complete nano/microfabrication process open the way to mass production of such probe promising plasmonic response control for upstream TERS spectroscopy experiment.

Then, we described the critical alignment procedure between the excitation laser and the designed nano-antenna to test our first prototype on reference samples. The probes achieved satisfactory AFM images on carbon nanotube and graphene oxide flakes. Local TERS measurements have been successfully obtained with an approximation of the recorded Raman EF respectively around 10^4 and 10^5, rather than 10^6 that promises theoretical modelling.

Finally, an additional numerical study suggested the use of SiO_2 as an eventual protecting coating for the metallic nano-antenna in order to prevent the low lifetime of AFM-TERS probes due to mechanical or oxidation damages.

Chapter 5

Control metallic nanoparticle shape using tilted evaporation

Over the last few decades there has been much work on lithographic techniques for resist profiling, oblique [223] and glancing angle evaporation [224], and shadow deposition phenomenon [225] – and combinations of these techniques – to control materials' deposition shape on the sub-micrometer-scale. The classic example of lithographic profiling combined with shadowing is the well-known 'lift-off' technique which can be employed using both ultraviolet-sensitive photoresists [226] and electron beam resists [227].

Here, we demonstrate the combination of the previous Ebeam lithography with tilted thermal evaporation to open a new way to control original shapes of metallic nano-objects. The technique allows the 3- dimensional tailoring of a range shapes from sharp, flat bottomed spikes to hollow cylinders and rings whose critical dimensions are much smaller than the lithographic feature size. The generic technique can be readily incorporated into any standard planar process and could be adapted to suit other thin-film materials.

As the optical properties of nanoparticles depend heavily on the shape of the particles – such structuration will be very beneficial for photonics and optical nanoprobes (such as nano-spectroscopy Raman) which require sharp, tailored points. We have seen in the previous chapters that combining disks and cones in two steps brings improvements in electro-optical performance (enhanced EF). This chapter investigates the possibility of fabricating such features using a one-step process.

5.1 Individual Tailored Nanostructures

5.1.1 Fabrication process

We describe here how to manufacture a range of tailored nanostructures using lithography and tilted evaporation. Ebeam lithography is used to fabricate the lift-off masks composed of arrays of nanometre-scale openings on commercial silicon wafers. As previously, a flat wafer (3-inch diameter, polished, (100) orientated crystalline silicon) is spin coated with a 'COPO/PMMA' bilayer and is exposed under an electron beam. It is important to remember that the different dissolution rates of the COPO and the PMMA lead to the formation of 'overhang' and 'undercut' features. The openings or nano-holes have a height h, determined by the spin-coated total thickness, and a width w governed by the Ebeam exposure dose. The Ebeam writing allows several arrays of nano-holes with several values of w on the single silicon wafer. This has several advantages: (i) the resist processing conditions are the same, e.g., it is known that resist list-off profile is sensitive to development conditions and (ii) the metallization thickness and tilt angle is the same for several values of w allowing a direct nanostructure-to-nanostructure comparison. In the current study, w is varied from 400 nm down to 40 nm and h is fixed at either 950 nm (COPO/PMMA – 900/50 nm) or 500 nm (COPO/PMMA – 450/50 nm).

Figure 5.1 shows a schematic illustration of the samples containing the nano-holes in the bilayer resist being evaporated with a chromium/gold thin film under various conditions.

There are several factors which play a role in determining the final structuration. These are the height h, width w, the resist overhang length, the resist undercut profile in the lower resist of the nano-hole masking, the total thickness t of the evaporated matter, the evaporation tilt angle φ the presence of rotation parallel to the axis of the tilt. As seen for conically shaped gold nanoparticles, the evaporative deposition has a vertical and a horizontal component which tends to close the opening width of the hole as the evaporation proceeds. It is important to understand that the specific nanostructuration resulting from the deposition results from the shadowing depending on all these parameters. First, when the evaporation tilt angle is zero ($\varphi = 0^\circ$) and the opening is relatively large (w $\gg h$), thin film deposition leads to well-known mesa structures, as previously called nanodisk – Figure 5.1.a. However, if the opening is reduced ($w < h$) – whilst maintaining a zero tilt angle –

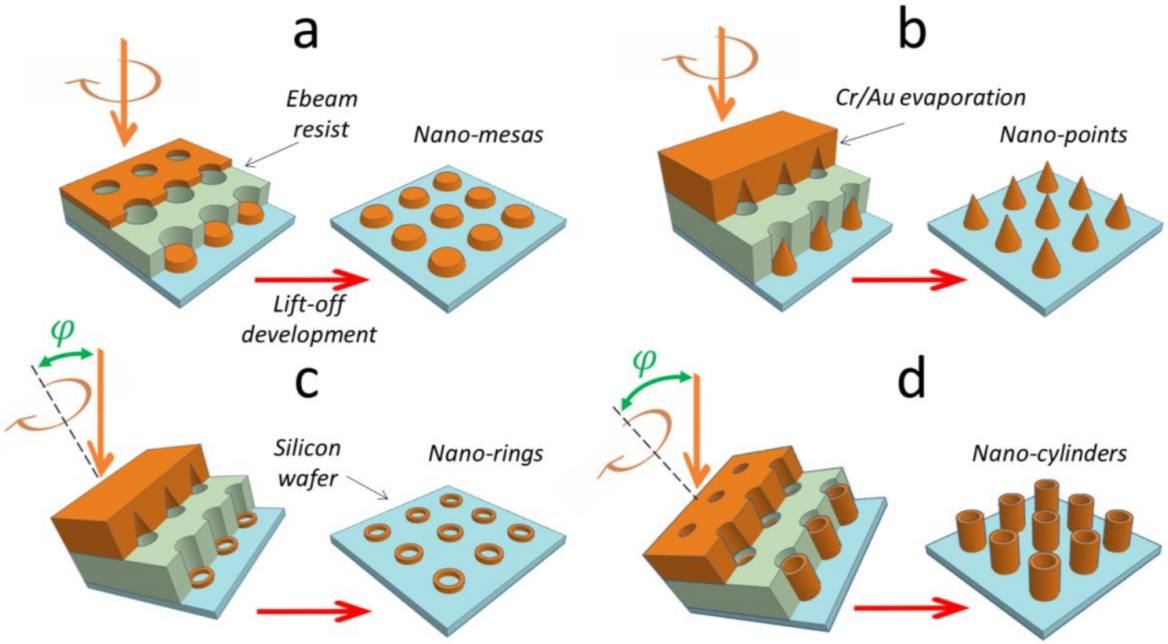

FIGURE 5.1 – Inclined rotated evaporation via a lift-off process involving a lift-off shadow mask. The formation of: a, nano-mesas and b, nano-cones at a deposition tilt angle $\varphi = 0°$. Higher tilt angles $\varphi > 0°$, lead to the formation of nano-rings (c), and eventually nano-cylinders (d). The silicon wafer (light blue) is patterned with an electron beam (Ebeam) sensitive resist mask (light green) and evaporated with chromium/gold (gold). The resist lift-off development step is indicated by the red arrow. The tilt angle φ is indicated in (c) and (d) in green relative to the rotation axis (black dashed line) which is always perpendicular to the wafer surface.

then nanometre-scale conic-like structures will be formed due to closing of the resist opening – see Figure 15.1.b. If we consider the case where $w < h$, then at small tilt angles ($0° < \varphi < 5°$) evaporation should result in nanometre-scale point-like structures where lateral growth and shadowing combine to modify the slope of the profile. At higher evaporation tilt angles ($0° < \varphi < 90°$), shadowing effects will dominate the deposition and lead to the formation of nanometre-scale rings and eventually cylinders. It is important to make a distinction between the fact that the nano-rings are deposited onto the surface of the wafer – resulting from shadowing – see Figure 5.1.c; whereas the nano-cylinders are deposited onto the sidewalls of the resist – see Figure 5.1.d. In the next section, we will see that such predicted feature can be realized practically by simply controlling bilayer resist coating conditions and evaporation tilt angle.

5.1.2 Experimental Results

The following figures show SEM images of gold nanostructures obtained by using a range of evaporation tilt angles φ (from 1° to 24°) and resist openings w (from 400 nm down to 40 nm) – for a total bilayer resist height h of 500 nm (Figure 5.2) and 950 nm (Figure 5.3).

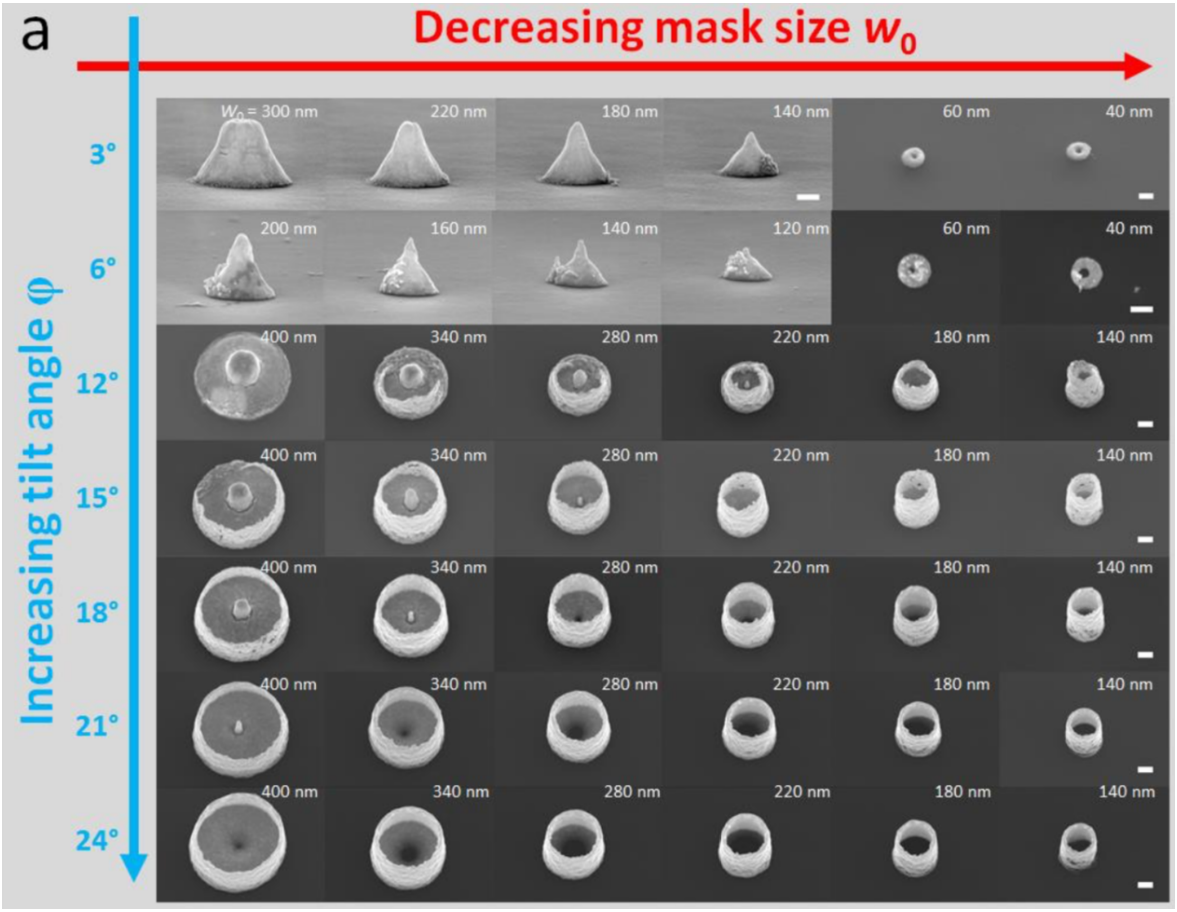

FIGURE 5.2 – SEM images showing the variety of metallic nanostructures obtained via the inclined rotating evaporation of gold via a lift-off process and shadow mask. The deposition tilt angle φ is varied from 3° to 24° (abscissa axes – blue) and the shadow mask opening width (w) from 400 nm to 40 nm (ordinate axes – red). The total thickness of the bilayer Ebeam resist (h) in this case is 500 nm and the evaporated chromium/gold thickness is 300 nm. The scale bars (white) at the right of the images indicate a length of 100 nm.

There are many specific features and trends which can be observed and remarked upon in the experimental results. We consider first the results having a mask height h = 500 nm (see Fig. 5.2). First, at low tilt angles (φ =3° and 6°), and relatively large mask openings (300 nm to 120 nm), one finds the expected mesa

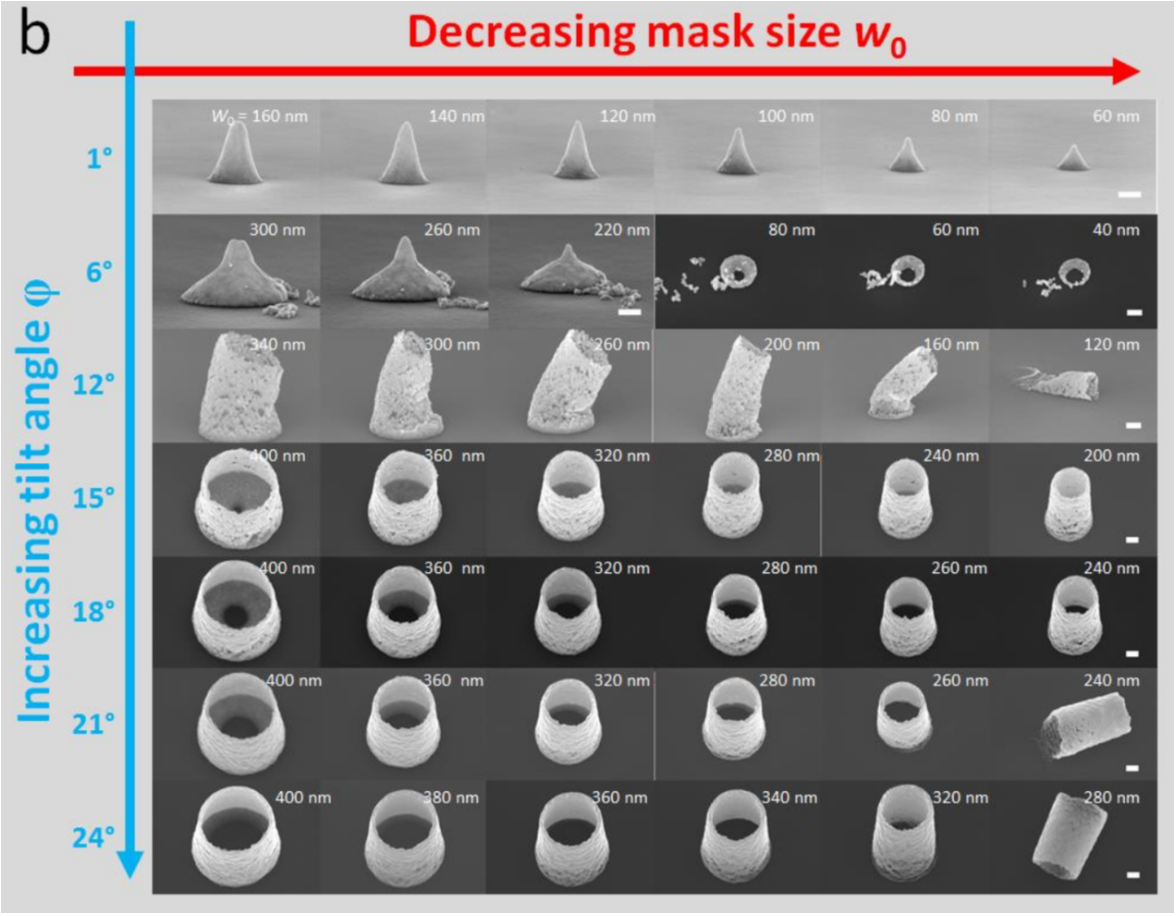

FIGURE 5.3 – SEM images showing the variety of metallic nanostructures obtained via the inclined rotating evaporation of gold via a lift-off process and shadow mask. The deposition tilt angle φ is varied from 1° to 24° (abscissa axes – blue) and the shadow mask opening width (w) from 400 nm to 40 nm (ordinate axes – red). The total thickness of the bilayer Ebeam resist (h) in this case is 950 nm and the evaporated chromium/gold thickness is 300 nm. The scale bars (white) at the right of the images indicate a length of 100 nm.

structures having a sloped edge due to the lateral deposition onto the mask edge. The flat-topped mesa features becoming sharp pointed structures below a certain critical mask opening width. When the mask opening becomes small, nano-ring features appear. For example, at a tilt angle of 3° the inner and outer diameters of the nano-rings increasing if the tilt angle is increased to 6°. When the tilt angle is increased to 12° a flat-topped feature appears which has a thinner base than a 'mesa'. Interestingly, as the mask opening width is decreased (at $\phi = 12°$) the central flat-top region becomes a small 'spike' and is surrounded by an emerging nano-cylinder. As the mask opening width is decreased, the width of the nano-cylinder diminishes.

We can now see how increasing the tilt angle affects a specific feature size. As φ is increased from 15° to 24°, at a large mask opening (w = 400 nm) the central

flat-top region becomes a nano-spike (at $\varphi = 21^\circ$) and becomes a 'hole' to form a nano-ring on the wafer surface (at $\varphi = 24^\circ$). In all cases – at w = 400 nm – there is a nano-cylinder surrounding, and indeed attached to, the surface feature. This trend is seen as the feature size is reduced, with the transition from nano-spike to 'hole' happening at a small tilt angle. Interestingly, all feature sizes studied (w = 400 nm to 40 nm) result in nano-cylinders having diminishing diameter. Indeed, SEM images reveal that the thickness of the nano-cylinders increases as the tilt angle is increased.

For the structures of Figure 5.3 the total resist thickness h is 950 nm. We observed a similar trend compared to the smaller value of h. First, classic nano-conic-like feature formation occurs at low tilt angle (3°) and for all feature sizes. Next, we observe nano-spike formation at low angle ($\varphi = 6^\circ$) intermediate feature size (w = 320 nm). At $\varphi = 6^\circ$, nano-ring formation occurs at a lower feature size (w <100 nm). For $\varphi = 6^\circ$, we see the vestiges of nano-cylinder formation – but they are clearly not robust to the lift-off process – which involves a heated solvent bath. Again, we can focus on specific features sizes as the tilt angle φ is increased. At larger feature sizes, we observe nano-ring formation having an inner diameter which increases with tilt angle – the ring is connected to an accompanying nano-cylinder whose wall thickness increases with tilt angle. At intermediate feature size, the nano-ring disappears at a lower tilt angle. At low feature sizes, the nano-cylinder is not attached to the wafer surface. The nano-cylinders become detached or released from the surface (during the lift-off solvent bath) at larger feature size as the tilt angle is increased.

Scanning electron microscopy enables an overall view of the individual nanostructures and can provide information concerning certain dimensions of the nanostructures e.g. cylinder heights and diameters. However, SEM cannot be used to measure topographic details of the structures inside the nano-cylinders, e.g., the profile information of the nano-rings and nano-spikes with modifying the structures. In order to obtain this data focused ion beam (FIB) techniques can be used to produce cross-sectional nanostructured samples for scanning transmission electron microscopy (STEM). Figure 5.4 shows the results of the STEM measurements.

The STEM allows one to measure with some accuracy the topography of the deposition on the wafer surface inside the nanocylinder. One can also obtain an approximate measurement of the thickness of the nanocylinders ($\sim$15-25 nm). The granularity and the non-uniformity of the deposition on the sidewall are also apparent.

This work shows that tilted evaporation using small lift-off profile bilayer resist

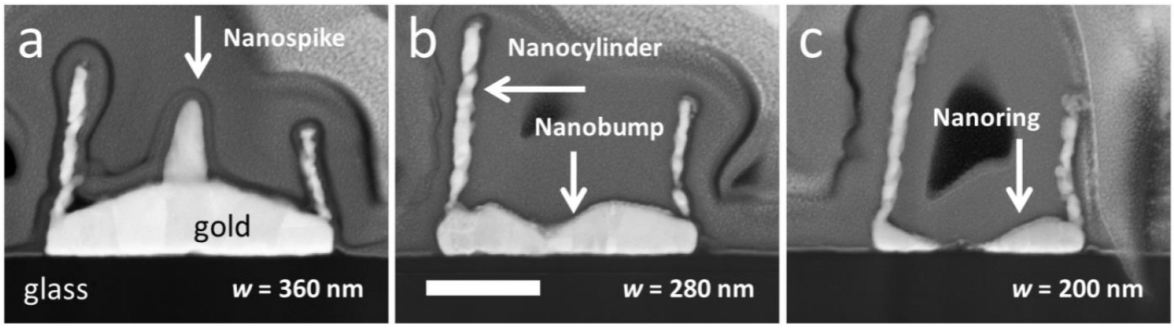

FIGURE 5.4 – Scanning transmission electron microscopy (STEM) images of 3 nanostructures fabricated using tilted rotated evaporation. The resist opening widths are: a, 360 nm, b, 280 nm, and c., 200 nm. The cross-section of the nanostructures was made using Focused ion beam (FIB) etching (see Supplementary Information for details). The evaporation tilt angle $\varphi = 15°$. The bilayer resist thickness h = 500 nm.

masking can result in a range of 3D nanostructures whose critical dimensions are less than the resist feature size. The specific nanostructures revealed by the study range from nano-spikes and nano-bumps to nano-rings and nano-cylinders. The generic fabrication process of the structures uses top-down methods which are – in principle – compatible with most micro and nanofabrication processes for microelectronics and micro/nanoelectromechanical systems. Finally, despite using metallic deposition here as a proof-of-concept demonstration, in principle, any evaporative material could be used to form such features.

5.1.3 Numerical modelling of nano-cylinders to determine their optical properties.

The previous nano-objects obtained under tilted gold deposition present sub-wavelength dimension and should exhibit plasmonic properties. In the case of Au nano-cylinders, their porous walls show a very large number of nano-pores and nano-protrusions under a random organization. The average thickness of the cylinders is 25 nm. However, the size of the protrusions can be smaller down to 5 nm. This original characteristic should allow strong EM enhancement over the porous surfaces and may drive these structures to be used in biological applications.

Numerical modelling (managed by Gaëtan Lévêque) was performed to evaluate the optical properties of such porous structure, using finite element method on a single nano-cylinder deposited on a glass substrate and excited under TIR illumination – p-polarized EM wave through the glass and at 45° from the normal of the interface.

The nano-porous cylinder has been modeled with the software Blender [1], then embedded in the simulation environment (air and SiO_2 media including PMLs) with gmsh [2], and the FEM simulation performed with Freefem++ [3] For the geometrical model, the roughness of the cylinder walls was structured to mimic the porosity of the fabricated structures observed under SEM. To better understand the influence of this porosity on the optical responses – here absorption and average enhancement factor in amplitude E/E_0 over the entire surface – four different random structurations of the cylinder have been studied, noted S1 to S4.

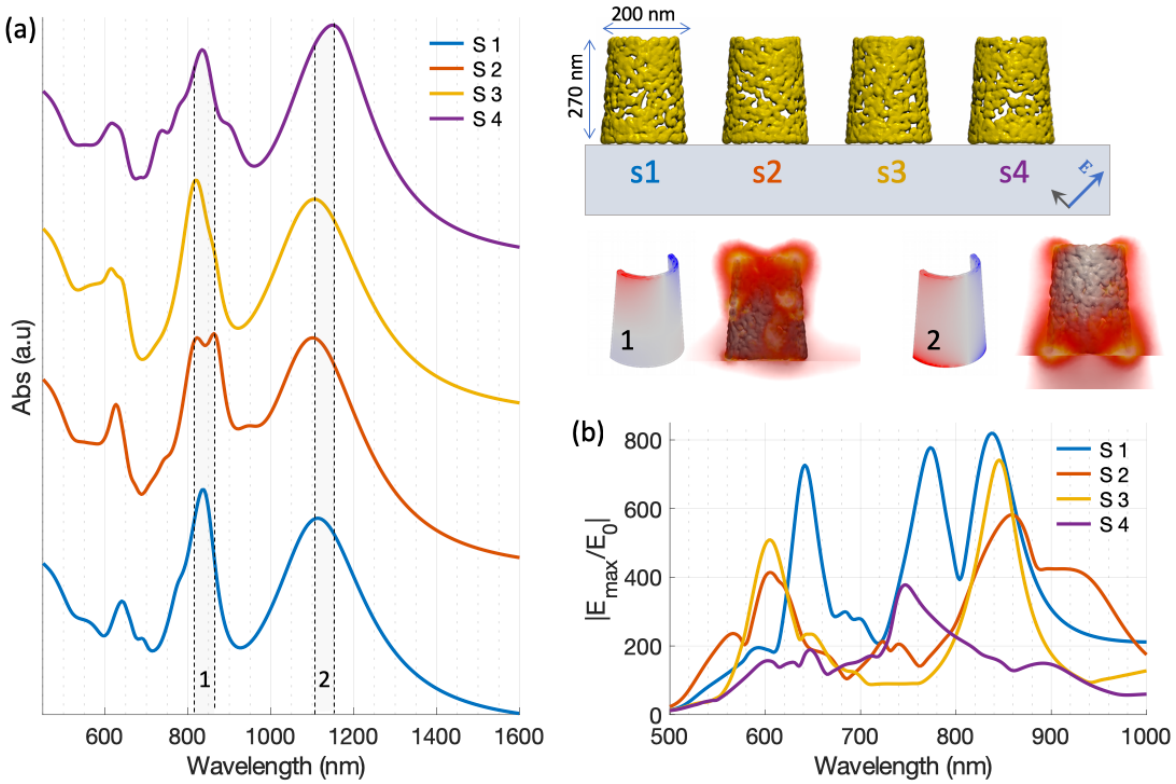

FIGURE 5.5 – (a) On the left, absorption spectra for the four structurations, noted S1 to S4, illustrated on the right with surface charges and near-field distribution for two resonance modes (at 835 nm and 1120 nm). (b) Surface-averaged EF spectra in amplitude for each structurations (E_0 the incident field).

Figure 5.5.a presents the absorption spectra for the four structurations, and each response exhibits two resonance peaks respectively located around 835 and 1120 nm. We observe that the signal does not seem to be strongly affected by the porosity. These plasmonic modes are referred to the "flat" cylinder, without any porosity or

1. https://www.blender.org/
2. Geuzaine, C. et al. International Journal for Numerical Methods in Engineering 2009, 79, 1309–1331. [228]
3. Hecht, F. Journal of Numerical Mathematics 2012,20, 251–265. [229]

roughness, as shown on the charge surfaces labeled 1 and 2. We can assume that the resonances are a horizontal plasmonic dipole, one located in the upper part of the cylinder and one for the lower part. Those modes are consistent with what has been observed on nano-cylinders designed on a glass substrate, which support a short wavelength (550 nm) mode with charges close to the top surface, barely sensitive to diameter, and the main dipolar resonance for which the field is enhanced close to the substrate, red-shifted when the diameter increase [230, 231]. Those two mode result from the combination of an in-plane dipole with an out-of-plane quadrupole [232, 233]. Moreover, Figure 5.5.b groups EF spectra, in amplitude, calculated and averaged along the whole surfaces. As expected, the EM enhancement strongly depends on the random arrangement of the different protrusions and cavities.

These last results suggest that a large number of porous metallic nano-cylinder organized as a dense array could potentially be used to create substrates for enhanced spectroscopy.

5.2 Nano-cylinder Array Micro-surfaces

5.2.1 Fabrication process

We went from individual tailored nanostructures to the development to macroscopic arrays ($200\times200\ \mu m^2$) nanostructured with hundreds of thousands of porous gold nano-cylinders. The challenge here was to find the right compromise between the Ebeam lithography parameters. The electron beam dose (from 200 to 1300 $\mu C/cm^2$) influences the cylinder diameter, while the pitch array (350-450 nm) separates each nano-objects. To uniformly expose the resist along the surface, a correction file was applied to take into account both the backscattered electrons and secondary electrons. A 950 nm thick resist was used with an angle Au evaporation of 15°. Each sample wafer was performed varying both the Ebeam dose and the pitch array Λ. Figure 5.6 presents the best result of a first try.

We see on the SEM images that nanotubes seem too close to each other, which groups them in random islands, certainly due to the capillarity forces of the different solvents used in the fabrication process or/and the electrostatic forces between each object. Interestingly, optical microscopy (VHX-5000 KEYENCE) reveals no reflexion in bright-field (BF) (at least in the normal direction) and colored reflexion

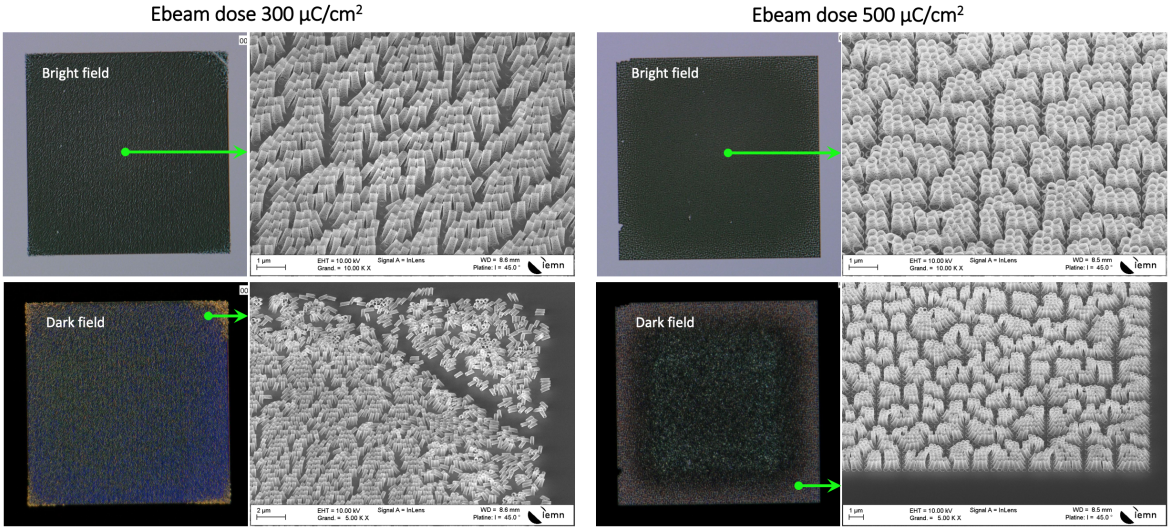

FIGURE 5.6 – Ebeam lithography dose study on 450 nm pitch arrays pattern on positive resit to lead surface of Au nano-cylinders with a average diameter around 250 and 300 nm respectively for 300 and 500 $\mu C/cm^2$. Bright field images reveal a strong extinction signal, while tiny variation of the dose and the nano-cylinder dispersion reveals different dark-field responses.

in dark-field (DF) mode, certainly due to plasmonic absorption and scattering, and grating diffraction. The irregular spacing between the islands of nano-cylinders and their distribution is likely the cause of the color variation along the nanostructured surface in DF. Regarding the diameter and the pitch array, the gap between each cylinder should be around 150 - 200 nm, which seems not required to obtain perfectly arranged nano-objects. On these first fabrication samples, preliminary confocal Raman spectroscopy tests reveal the presence of impurities probably coming from rest of PMMA. To clean the sample substrates before any depositions of the interest molecule, we performed short cleaning processes (1-30 min) into an oxygen plasma chamber with low flow and power (**XXX** sccm, 100-200W). On the same sample area, Figure 5.7 shows the plasma effect on the structure and roughness of the porous wall of the nano-cylinders.

We observe the coalescing or aggregating of Au grains under more round shapes. It is similar to the change in the morphology of gold NP films upon thermal annealing, known in the literature [234], and represents one of the most effective methods that applied for tuning the optical properties [235]. A Cleaning oxygen plasma during 10 min at 200 Watts followed by a Raman analysis revealed a pure nanostructured Au surface free of any impurities and damages of the nano-cylinders shape or the distribution, according to SEM observations.

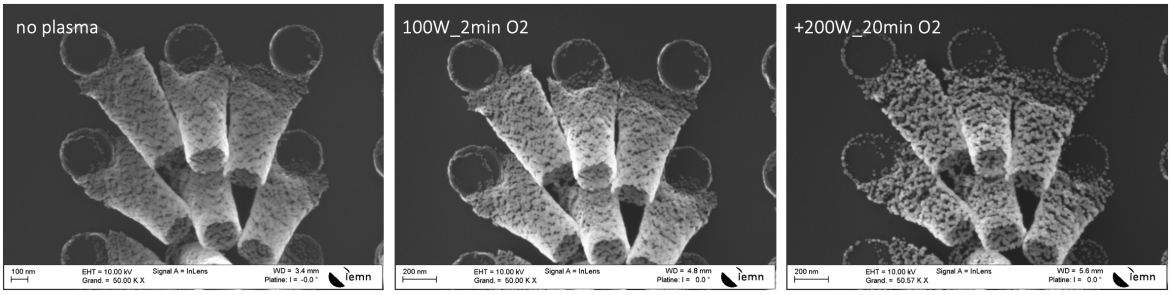

FIGURE 5.7 – Oxygen plasma study on Au nano-cylinders lithographically pattern in order the clean off the surface from rest of PMMA, which has consequently reshaped the nano-cylinder surfaces. On an original sample (left), a quick plasma O_2 cleaning was performed at 100 W for 2 min (middle), with an additional and stronger cleaning step at 200 W during 20 min (right).

A gap above 200 nm between each nano-object seems to be large enough to avoid grouping them and form disordered islands. Figure 5.8 shows successive SEM images zooming on the framed zones (white dash frame) of a nanostructured array composed of nano-cylinders with an average diameter around 140 nm and dispersed along a pitch array about 375 nm. We also observe that the oxygen plasma process does not seem to weaken the cylinders structure. The Ebeam correction has been successfully settled which leads to a perfect distribution of around 285 000 nanostructures along the whole surface of the array of $200 \times 200\ \mu m^2$. The previous numerical studies on individual structures, combined with a fabrication process solution offering such arrays suggests interesting applications in the nanophotonics field involving molecular spectroscopy.

5.2.2 Optical characterization

As before, a characterization approach was performed using optical microscopy under bright and dark-field mode. The observed samples are nanostructured surfaces, each composed of a Au nano-cylinder array with an increasing pitch Λ from 345 to 433 nm (from left to right in Figure 5.9). In this case, the nano-cylinders diameter is around 200 nm and we observe a value of Λ located between the first (345 nm) and the second array (364 nm) which delimits the minimum gap required to obtain a perfection distribution of the nano-cylinder – from the center to the edges of the patterned array. Then, both BF and DF images exhibit no emission from the structures, nevertheless with the emergence of the blue emission from the largest

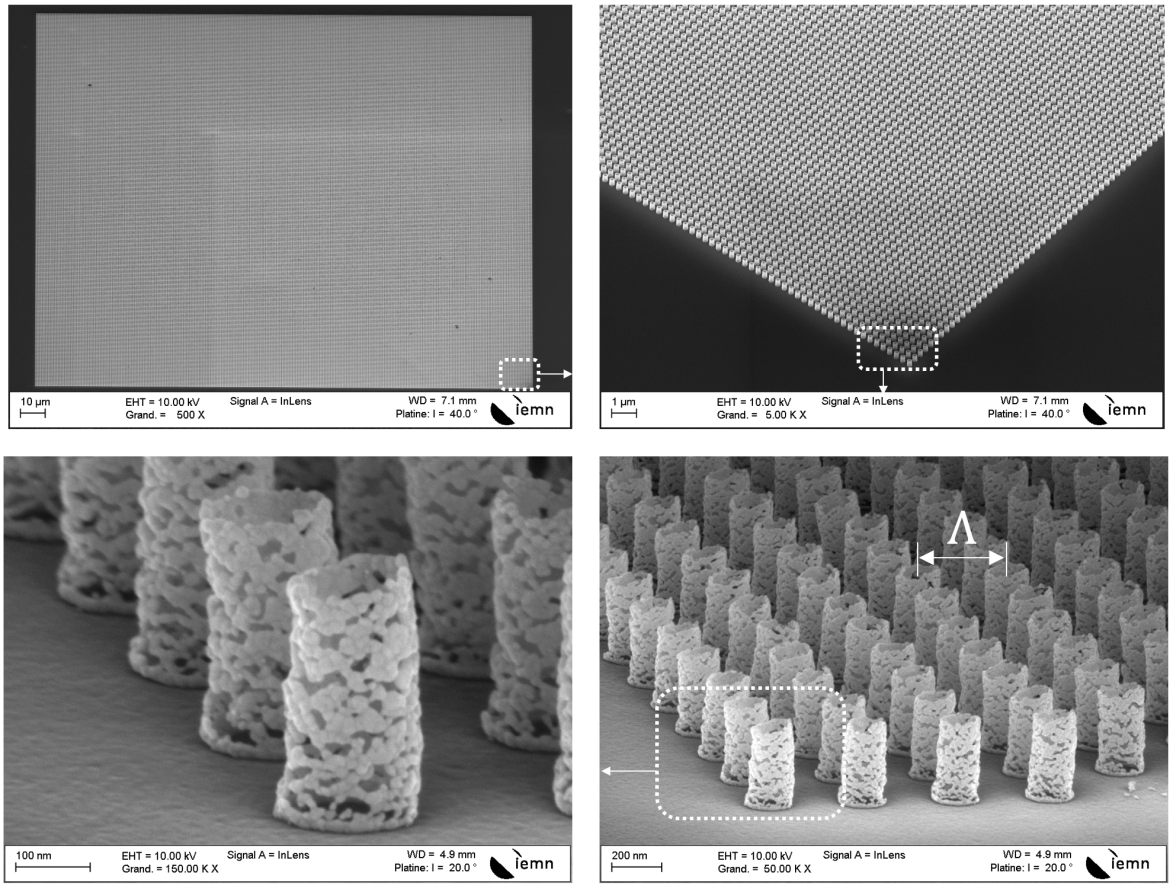

FIGURE 5.8 – Successive SEM imaging zooming of 200μm wide nano-cylinder array with a pitch about 375 nm, showing a perfect distribution of nano-cylinders with a diameter around 140 nm. A 200 Watts oxygen plasma was performed on the sample for 10 min to remove PMMA residues.

pitch arrays certainly due to a grating effect.

To better understand what we see and confirm the apparent grating effect, we need to consider the BF/DF configurations of the optical microscope (data company ?). With Λ the pith array, θ_{inc} the incident light angle at a wavelength λ, and θ_m the diffracted light of order $m \in \mathbb{N}$, the known grating equation:

$$m\lambda = \Lambda \left[\sin(\theta_{inc}) \pm \sin(\theta_m)\right] \tag{5.1}$$

As for our last set of samples (see Figure 5.9), we assumed that the appearing blue color corresponds to a wavelength with a value around 440 nm. We have then represented in Figure 5.10 the numerical aperture (NA) of the excitation $\sin(\theta_{inc})$ as a function of the first diffracted order collection $\sin(\theta_1)$ for 440 nm and for all Λ measured with SEM observations of the samples. On the sides of the graphic,

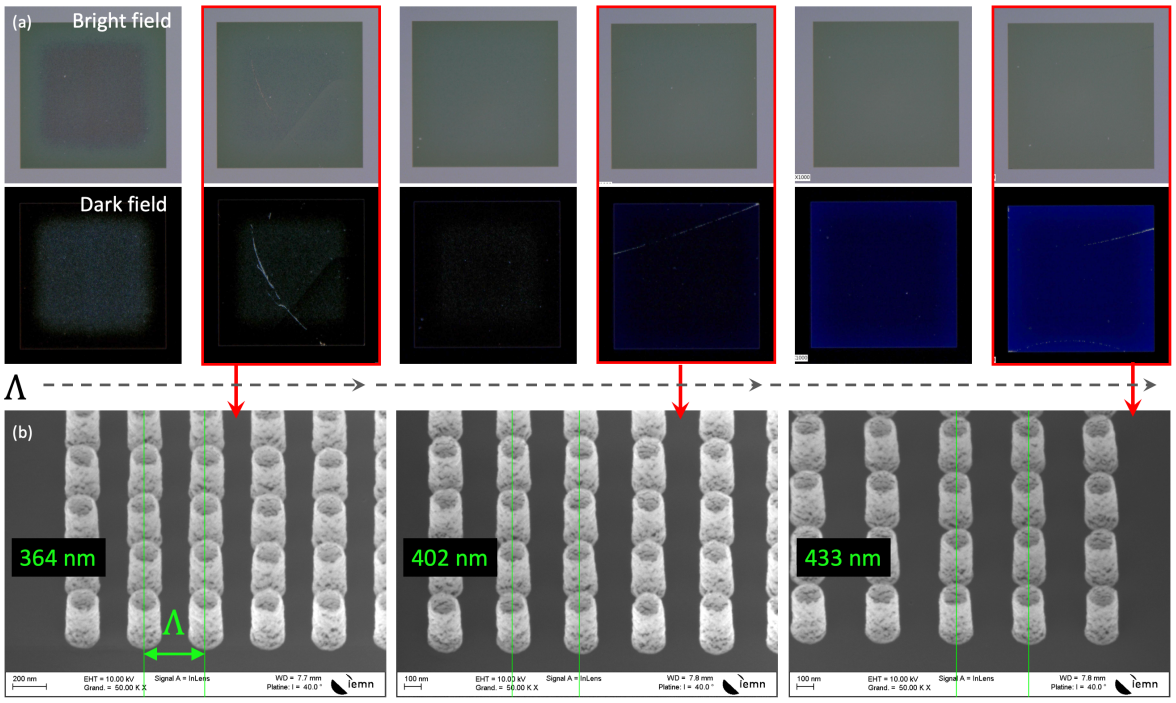

FIGURE 5.9 – (a) Bright and dark field images of nano-cylinder array lithographically patterned with a diameter about 200 nm and a pitch array of 345, 364, 402, 417, 433 nm (from left to right). (b) SEM images for samples with Λ of 364, 402, 433 nm showing the beginnings of the grating effect.

we have illustrated the BF et DF configuration used here. Using the same lens, excitation et collection angles are identical in BF mode, represented by the black dashed line ($x = y$). However, DF mode uses parabolic mirrors which encompass the lens to focus the excitation with higher angles (or NA) and the lens at the center is used only for the collection.

We observe that the small variation of the pitch array strongly affects the diffraction. We can confirm that the optical observations of our nanostructured surface are resulting from grating effects. The detection limit of this effect (in DF mode) depends on the used microscope and the pitch array. These stud also confirmed why no reflexion in BF mode is observed.

Other optical characterizations on such nanostructured surface are required to complete the list of optical properties to better understand the EM distribution between the far-field emission part from the grating effect and the plasmonic interaction part (absorption and diffusion).

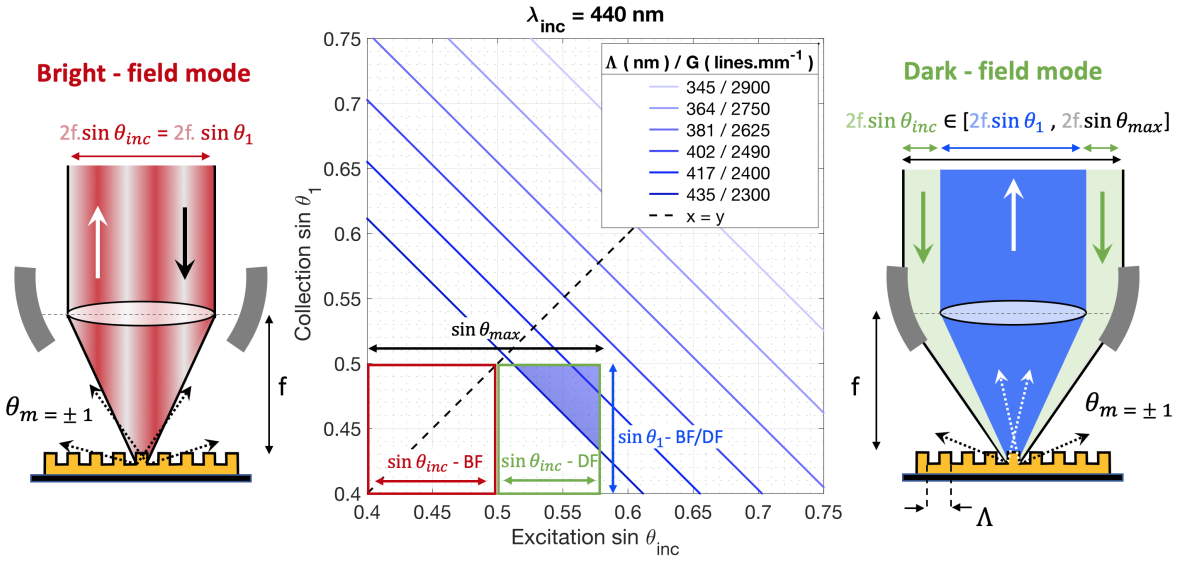

FIGURE 5.10 – Middle: first diffracted order angle as a function of the incident angle – respectively represented by $\sin\theta_1$ and $\sin\theta_{inc}$ – for incident wavelengths of 440 nm and pitch array from 345 to 435 nm (or grating characteristic from 2900 to 2300 grooves.mm^{-1}). Left and right, illustration of respectively the bright-field and dark-field modes.

5.2.3 Raman scattering application

To evaluate the near-field enhancement of the localized plasmons of the Au nano-cylinders arrays, we have performed confocal Raman spectroscopy on dithiothreitol (DTT) molecules, $C_4H_{10}O_2S_2$, adsorbed on the metallic nanostructured surfaces. We expect that these surfaces will act as SERS substrates and reveal Raman signatures of molecules. First of all, an aqueous solution of DTT concentration at 10 mM was prepared. This concentration of molecules is not important enough to detect Raman signal using standard confocal spectroscopy. The substrates are then immersed in the solution between 1 and 2 hours to ensure that the molecules are well adsorbed onto gold pillar (incubation). Water rinsing removes the excess of the solution and then Raman acquisition can be achieved after that the substrates are completely dry.

Hyperspectral imaging (each pixel of the image contains a spectrum) of the sample has been achieved on the same area (30×40 μm). Figure 5.11.a shows examples of different mappings representing the general distribution of a selection of spectra (spectrum A, B, C, D, E and F from 5.11.b). A CLS (classical least square) fitting is applied to these input spectra to generate these distributions.

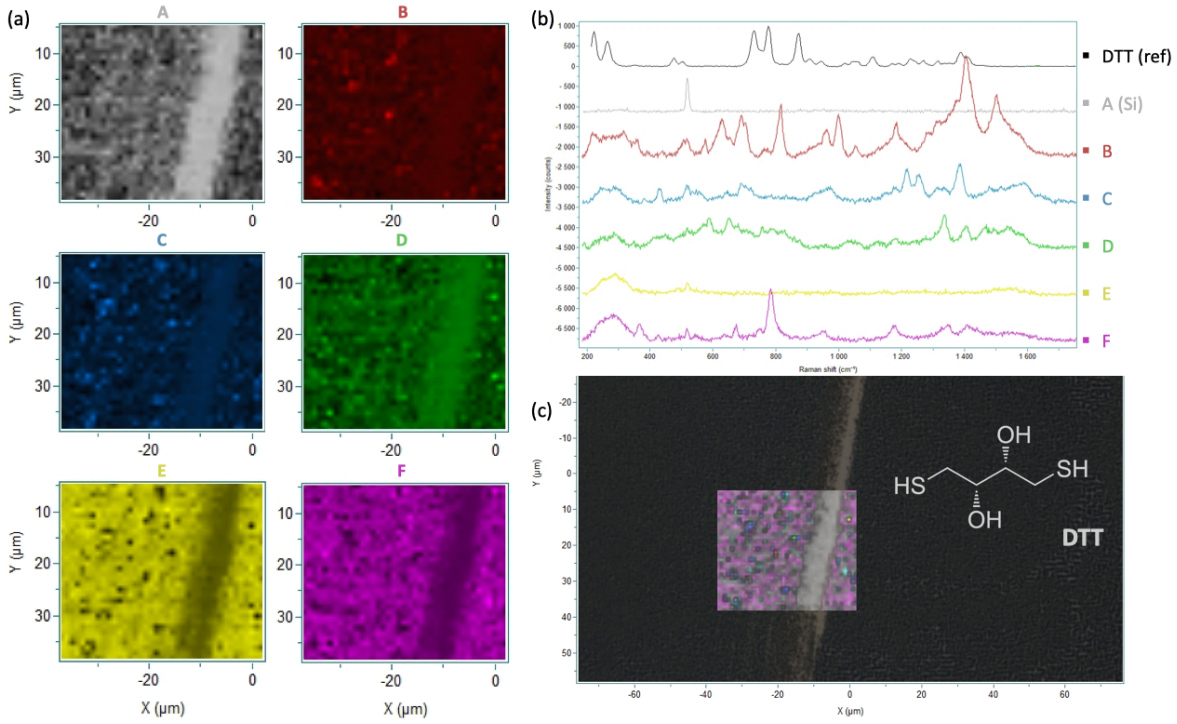

FIGURE 5.11 – Confocal Raman spectroscopy experiment on dithiothreitol (DTT) molecules deposited on nano-cylinder array surfaces. (a) 30×40 μm intensity Raman imaging of the sample according to the corresponding spectra (from A to F) in (b) with the black spectra the DTT powder reference. (c) Overlapping of all Raman imaging with the optical image of the sample.

The black spectrum is the DTT reference (power) and the grey spectrum (A) corresponds to the silicon signal of the substrate under the metal. Other Raman peaks – locally found over the surface – are relative to the DTT molecules, identified by the C-S bonds at around 750 cm^{-1} and the Au-S bonds at 280 cm^{-1} corresponding to the adsorption of the molecules on gold. On the Raman images, we observe that background signals dominate (A, E and F) with nevertheless the rare presence of very enhanced signals localized at a few positions (B, C, and D). We also observe on the Raman spectra a large number of peaks certainly due to a strong inhomogeneity of the molecules and their many possible orientations with respect to the multitude nano-pores and protrusions of the Au nano-cylinder arrays.

Qualitative and quantitative SERS studies are very complex since each SERS substrate should be dedicated to a specific molecule. Several factors need to be considered and optimized such as incubation conditions (time, method), and surface functionalization (to eliminate random orientations of molecules for example). Here, it is complicated to know how the molecules are adsorbed (and in which orientation) since our Au nano-cylinders are extremely roughed with random porosity.

It is therefore not possible at this stage to obtain an exaltation factor of the Raman scattering by the lack of information regarding the selectivity of molecules with our substrates.

Conclusion

In this chapter, we have seen that lithographically patterned nanostructures obtained under tilted metallic evaporation offer the possibility to combine a wide range of tailored nano-objects. Among all other, matrices of gold porous nano-cylinders represent a new interest for near-field optics application since the wall roughness exhibits required geometry to achieve a multitude of localized field enhancement. Numerical calculation helps us to estimate the optical responses of the isolated nano-object better. Two plasmon resonances have been identified around 800 nm and 1100 nm and correspond to the cylindrical shape of the structure. Moreover, the infinite combination of nano-pores and nano-protrusions constituting the porous walls exhibits significant EF from 550 nm to 900 nm.

We have decided to create dense arrays of Au porous nano-cylinders to obtain SERS substrates. Additional critical parameters regarding the electron beam and the pitch array need to be considered to obtain perfectly organized nanostructured surfaces. Optical microscopy achieved on the surfaces reveals the emergence of a grating effect. Finally, we have tested such surfaces as being substrates for SERS experiments on dithiothreitol molecules. Very localized enhancement Raman signal was successfully detected even in a significant inhomogeneity of the signal suggests other applications, such as new multi-modal tools for achieving SERS and matrix-free mass spectrometry analysis. This approach overcomes the limitations of both conventional SERS and MALDI techniques [236], allowing for sensitive and reliable detection of small molecules that play essential biological functions, like metabolites, illicit drugs, and neurotransmitters. The main advantages are related to the possibility to monitor chemical reactions with precise spatial localization with both mass and vibrational spectroscopies.

General Conclusion

The subject of optical nano-antennas is a developing field with fascinating promises for fundamental science as well as for various potential applications. The ability to confine an electromagnetic field to nanometer length scales makes plasmons an interesting research object for studying light-matter interactions for applications such as in Tip Enhancement Raman Scattering (TERS). In this thesis, we have seen that TERS probes incorporating a single optical nano-antenna can be a excellent candidate to solve the current problems associated with commercial TERS probes regarding the control of the plasmonic tunability caused by the poor reproducibility of the fabrication processes and their incompatibility with a mass production manufacturing. These issues have been approached from several angles and connections between the literature, theoretical and experimental results.

In the introduction chapters 1 and 2, we have seen how scanning near-field optical microscopy (SNOM) can overcome the light diffraction limit to enter the evanescent waves domain and allows sample imaging with a sub-wavelength spatial resolution. A scattering-SNOM probe made from noble metals exhibits, under EM illumination, surface plasmons either propagating along a surface or localized nearby its extremity. The resonance frequency and the enhancement amplitude of localized plasmons strongly depend on the shape, size, and nature of each material (metal, environment, substrate), which might respond in the visible range to form optical nano-antennas used for TERS. We have seen the basics of the Raman scattering phenomenon and the instrumentation that couples confocal Raman microscopy with SPM techniques for co-localized AFM-Raman and TERS experiments. To bring the chemical resolution towards a nanometric resolution, plasmonic probes are required for EM confinement of the Raman nano-source. This technique provides an excellent non-destructive characterization tool for nano-spectroscopy Raman with an enhancement factor (EF) of up to 10^8. There are different optimization probe fabrication processes of TERS probe that machine of the apex probe to isolate a single metallic nanostructure.

The work conducted for the Ph.D. has been reported in the next chapters (3 - 5)

In chapter 3, I have focused on the investigation of the resonance properties of metal optical nano-antenna through finite element simulations in which I have studied the influence of the shape and the environment properties onto the plasmonic behavior. A particular focus on nanocones has been reported for the optimization of plasmon properties required for TERS, i.e., the large plasmon tunability in air (250 nm) and intense EF of the electromagnetic field in terms of intensity (3000). I have also studied the dependence of the illumination polarizations and total internal reflexion configurations on basic plasmonic modes. I have finally shown with numerical modelling how it is possible to go beyond the 'non-resonant' aspect of a perfectly smoothed tip probe by customizing the apex tip. I have developed an optical bench for the characterization of isolated metallic nanostructures on a glass substrate. The experimental results have been compared with numerical predictions and reveal an excellent agreement. The experimental set-up groups altogether evanescent excitation and dark-field collection under an inverted microscope which allows the adaption with an AFM to also collect the optical signatures of marketed AFM-TERS probe. The different results between metallic lithographically-patterned nano-object and probes commonly used in TERS experiments suggest the use of optical nano-antenna for TERS probe to take advantage of well defined localized surface plasmon resonances.

In chapter 4, I focused on the elaboration and the design of a new prototype of tunable AFM-TERS probes with a fabrication process compatible with reproducible mass production. I have designed an original optical nano-antenna where a metal nanodisk is supporting a nanocone in order to obtain the best plasmonic responses in the visible range that reigns at the apex. I have also undertaken statistical studies of the fabrication of the metallic nanostructures show- ing a high reproducibility and plasmon tunability. I have also developed a fabrication process – using silicon-on-insulator (SOI) wafers – which integrates a single optical nano-antenna onto a costumed AFM probe compatible with mass production with plasmonic tunability to match with the excitation laser of upstream TERS spectroscopy experiment. I have tested our first prototype which achieved satisfactory AFM images on carbon nanotube and graphene oxide flakes. These probes have performed local TERS measurements with approximative Raman EF up to 10^5, while theoretical calculations predicted 10^6. The potential reasons for these discrepancies were discussed.

In chapter 5, I have tested the influence of tilted metallic evaporation for the fabrication of lithographically patterned nanostructures which offer the possibility to

obtain tailored nano-objects: conical or cylindrical, basic or complex, with smooth or porous surfaces. A particular interest has been focused on matrices of gold porous nano-cylinders where numerical calculations help us to better estimate their optical responses such as a significant EF from 550 nm to 900 nm. I have looked for the right parameters to create dense arrays of Au porous nano-cylinders potentially applicable for SERS. Optical microscopy has revealed the emergence of a grating effect and enhanced Raman signals of dithiothreitol molecules have been recorded during SERS experiments.

In chapter 5, I have tested the influence of tilted metallic evaporation for the conception of lithographically patterned nanostructures which offer the possibility to obtain tailored nano-objects: conical or cylindrical, basic or complex, with smoothed of porous surfaces. A particular interest has been focused on matrices of gold porous nano-cylinders where numerical calculation help us to better estimate their optical responses such as a significant EF from 550 nm to 900 nm. I have looked after the right parameters to create dense arrays of Au porous nano-cylinders potentially applicable for SERS. Optical microscopy has revealed the emergence of a grating effect and enhanced Raman signals of dithiothreitol molecules have been recorded during SERS experiments.

In terms of the outlook and potential future work following the thesis, one can imagine a continued optimization of the nanofabrication and investigation of other metals for the nano-antennas (e.g., silver, aluminum) in the interest of TERS in terms of better tunability of the plasmon frequency (not tested in this thesis). The work presented in chapter 5 could be applied to TERS probes and SERS surfaces. Finally, fully optimized high-performance high-EF AFM-TERS probes would have a significant impact in the measurement of *inter alia* low concentration chemical species, two-dimensional materials, and localized stress measurements in nanoelectronics.

Annexes

Intellectual property and scientific Output

Patents

— **Eschimèse,** D., De Bettignies, P., Schreiber, J., Lévêque, G., Mélin, T., Arscott, S. Patent WO/2017/178746, October, 10th 2017 - France;

Publications

— **Eschimèse, D.** et al. Modelling and characterization of lithographically-patterned metallic nanostructures for tip-enhanced Raman spectroscopy.
submitted October 2018;

— **Eschimèse, D.** et al. Metallic nano-rings, nano-cylinders, and nano-spikes via tilted rotating evaporation and electron beam lithographic lift-off technique.
submitted December 2018;

— **Eschimèse, D.** et al. Conception and Nano-/Micro-fabrication of a next-generation high-performance tip-enhanced Raman spectroscopy.
in preparation;

— **Eschimèse, D.** et al. Nanostructured surface based on porous gold nanotube with SERS application.
in preparation

Fundings

— **Start-AiRR**: TERS-Tips 2016

— **ANR**: TipTop 2016-2019

— **Equipe Mixte**: TERS-Tips 2018

International conferences

Talks:

Eschimèse, D. et al. – Study and realization of High performance TERS probe based on AFM silicon cantilever.

— EMRS Fall, Warsaw, POLAND – *July 2016*;

— Nanophotonics and Micro/Nano Optics International Conference NANOP16 – Paris, FRANCE – *December 2016*;

— Sixth International Conference on Tip Enhanced Raman Spectroscopy TERS VI – NIST, Gaithersburg, USA – *August 2017*;

Poster:

— 15^{th} International Conference on Near- Field Optics, Nanophotonics and Related Techniques NFO15 – UTT, Troyes, FRANCE – *August 2018* – *Poster*

• **Eschimèse, D.** et al. – Study and fabrication of high performance *top-down* nano/microfabricated ters probes based on afm silicon tip.

Other

— Initiation school to Raman Spectroscopy of Carbon Nanostructures – Laboratoire Charles Coulomb, Montpelier, FRANCE — *July 2015*

— Talk at GdR PMSE – Groupement de Recherche Plasmonique Moléculaire et Spectroscopies Exaltées – ICMCB-CNRS, Pessac, FRANCE – *November 2016*

— Talk at GdR NACRE – Groupement de Recherche Nanocristaux dans des diélectriques pour l'électronique et pour l'optique – Paris, FRANCE *November 2018*

Bibliography

[1] E. Abbe, "Beiträge zur Theorie des Mikroskops und der mikroskopischen Wahrnehmung: I. Die Construction von Mikroskopen auf Grund der Theorie," *Archiv für Mikroskopische Anatomie*, vol. 9, pp. 413–418, Dec. 1873.

[2] L. Rayleigh, "On the Theory of Optical Images, with special reference to the Microscope," *Journal of the Royal Microscopical Society*, vol. 23, pp. 474–482, Aug. 1903.

[3] E. Synge, "XXXVIII. A suggested method for extending microscopic resolution into the ultra-microscopic region," *The London, Edinburgh, and Dublin Philosophical Magazine and Journal of Science*, vol. 6, pp. 356–362, Aug. 1928.

[4] R. Young, J. Ward, and F. Scire, "The Topografiner: An Instrument for Measuring Surface Microtopography," *Review of Scientific Instruments*, vol. 43, pp. 999–1011, July 1972.

[5] G. Binnig, H. Rohrer, C. Gerber, and E. Weibel, "Tunneling through a controllable vacuum gap," *Applied Physics Letters*, vol. 40, pp. 178–180, Jan. 1982.

[6] G. Binnig, H. Rohrer, C. Gerber, and E. Weibel, "7x7 Reconstruction on Si(111) Resolved in Real Space," *Physical Review Letters*, vol. 50, pp. 120–123, Jan. 1983.

[7] G. Binnig, C. F. Quate, and C. Gerber, "Atomic Force Microscope," *Physical Review Letters*, vol. 56, pp. 930–933, Mar. 1986.

[8] J. A. Stroscio and D. M. Eigler, "Atomic and Molecular Manipulation with the Scanning Tunneling Microscope," *Science*, vol. 254, pp. 1319–1326, Nov. 1991.

[9] J. K. Gimzewski, "Nanoscale Science of Single Molecules Using Local Probes," *Science*, vol. 283, pp. 1683–1688, Mar. 1999.

[10] H. Guo, Y. Wang, S. Du, and H.-j. Gao, "High-resolution scanning tunneling microscopy imaging of Si(111)-7x7 structure and intrinsic molecular states," *Journal of Physics: Condensed Matter*, vol. 26, p. 394001, Oct. 2014.

[11] A. Kramer, J.-M. Segura, A. Hunkeler, A. Renn, and B. Hecht, "A cryogenic scanning near-field optical microscope with shear-force gapwidth control," *Review of Scientific Instruments*, vol. 73, pp. 2937–2941, Aug. 2002.

[12] S. Rützel, S. I. Lee, and A. Raman, "Nonlinear Dynamics of Atomic-Force-Microscope Probes Driven in Lennard-Jones Potentials," *Proceedings: Mathematical, Physical and Engineering Sciences*, vol. 459, no. 2036, pp. 1925–1948, 2003.

[13] D. J. Muller, "Conformational changes in surface structures of isolated connexin 26 gap junctions," *The EMBO Journal*, vol. 21, pp. 3598–3607, July 2002.

[14] R. C. Reddick, R. J. Warmack, and T. L. Ferrell, "New form of scanning optical microscopy," *Physical Review B*, vol. 39, pp. 767–770, Jan. 1989.

[15] J.-C. Diels, "Apodized aperture using frustrated total reflection," *Applied Optics*, vol. 14, pp. 2810–2811, Dec. 1975.

[16] M. L. M. Balistreri, A. Driessen, J. P. Korterik, L. Kuipers, and N. F. van Hulst, "Quasi interference of perpendicularly polarized guided modes observed with a photon scanning tunneling microscope," *Optics Letters*, vol. 25, p. 637, May 2000.

[17] E. Betzig, P. L. Finn, and J. S. Weiner, "Combined shear force and near-field scanning optical microscopy," *Applied Physics Letters*, vol. 60, pp. 2484–2486, May 1992.

[18] K. Lieberman, S. Harush, A. Lewis, and R. Kopelman, "A Light Source Smaller Than the Optical Wavelength," *Science, New Series*, vol. 247, no. 4938, pp. 59–61, 1990.

[19] L. Novotny, D. W. Pohl, and B. Hecht, "Scanning near-field optical probe with ultrasmall spot size," *Optics Letters*, vol. 20, p. 970, May 1995.

[20] U. C. Fischer and D. W. Pohl, "Observation of Single-Particle Plasmons by Near-Field Optical Microscopy," *Physical Review Letters*, vol. 62, pp. 458–461, Jan. 1989.

[21] M. Specht, J. D. Pedarnig, W. M. Heckl, and T. W. Hänsch, "Scanning plasmon near-field microscope," *Physical Review Letters*, vol. 68, pp. 476–479, Jan. 1992.

[22] F. Zenhausern, Y. Martin, and H. K. Wickramasinghe, "Scanning Interferometric Apertureless Microscopy: Optical Imaging at 10 Angstrom Resolution," *Science, New Series*, vol. 269, no. 5227, pp. 1083–1085, 1995.

[23] M. Schnell, A. García-Etxarri, A. J. Huber, K. Crozier, J. Aizpurua, and R. Hillenbrand, "Controlling the near-field oscillations of loaded plasmonic nanoantennas," *Nature Photonics*, vol. 3, pp. 287–291, May 2009.

[24] F. Keilmann and R. Hillenbrand, "Near-field microscopy by elastic light scattering from a tip," *Philosophical Transactions of the Royal Society of London. Series*

A: Mathematical, Physical and Engineering Sciences, vol. 362, pp. 787–805, Apr. 2004.

[25] C. Westermeier, A. Cernescu, S. Amarie, C. Liewald, F. Keilmann, and B. Nickel, "Sub-micron phase coexistence in small-molecule organic thin films revealed by infrared nano-imaging," *Nature Communications*, vol. 5, Dec. 2014.

[26] J. Chen, M. Badioli, P. Alonso-González, S. Thongrattanasiri, F. Huth, J. Osmond, M. Spasenović, A. Centeno, A. Pesquera, P. Godignon, A. Zurutuza Elorza, N. Camara, F. J. G. de Abajo, R. Hillenbrand, and F. H. L. Koppens, "Optical nano-imaging of gate-tunable graphene plasmons," *Nature*, vol. 487, pp. 77–81, July 2012.

[27] C. Wang, W. Zhang, Z. Zhao, Y. Wang, P. Gao, Y. Luo, X. Luo, C. Wang, W. Zhang, Z. Zhao, Y. Wang, P. Gao, Y. Luo, and X. Luo, "Plasmonic Structures, Materials and Lenses for Optical Lithography beyond the Diffraction Limit: A Review," *Micromachines*, vol. 7, p. 118, July 2016.

[28] C.-W. Lee, D. K.-T. Ng, A. L. Tan, and Q. Wang, "Fabrication and Demonstration of III–V/Si Heterocore Microcavity Lasers via Ultrathin Interlayer Bonding and Dual Hard Mask Techniques," *ACS Photonics*, vol. 3, pp. 2191–2196, Nov. 2016.

[29] K. P. Lim, V. Krishnamurthy, J. F. Ying, J. Pu, and Q. Wang, "Ultrahigh Index and Low-loss Silicon Rich Nitride Thin film for NIR HAMR Optics," *IEEE Transactions on Magnetics*, vol. 53, pp. 1–7, May 2017.

[30] D. K.-T. Ng, C. W. Lee, V. Krishnamurthy, and Q. Wang, "Sub-Micron Anisotropic InP-based III-V Semiconductor Material Deep Etching for On-Chip Laser Photonics Devices," *Advanced Engineering Materials*, vol. 20, p. 1700465, Feb. 2018.

[31] W. L. Barnes, "Particle plasmons: Why shape matters," *American Journal of Physics*, vol. 84, pp. 593–601, Aug. 2016.

[32] M. Hu, A. Ghoshal, M. Marquez, and P. G. Kik, "Single Particle Spectroscopy Study of Metal-Film-Induced Tuning of Silver Nanoparticle Plasmon Resonances," *The Journal of Physical Chemistry C*, vol. 114, pp. 7509–7514, Apr. 2010.

[33] M. L. Brongersma and P. G. Kik, eds., *Surface plasmon nanophotonics*. No. 131 in Springer series in optical sciences, Dordrecht: Springer, 2007. OCLC: 255029476.

[34] Z. Han and S. I. Bozhevolnyi, "Radiation guiding with surface plasmon polaritons," *Reports on Progress in Physics*, vol. 76, p. 016402, Jan. 2013.

[35] V. Lotito, C. Hafner, U. Sennhauser, and G.-L. Bo, "Novel SNOM Probes Based on Nanofocusing in Asymmetric Structures," in *Plasmonics - Principles and Applications* (K. Y. Kim, ed.), InTech, Oct. 2012.

[36] A. V. Kabashin, P. Evans, S. Pastkovsky, W. Hendren, G. A. Wurtz, R. Atkinson, R. Pollard, V. A. Podolskiy, and A. V. Zayats, "Plasmonic nanorod metamaterials for biosensing," *Nature Materials*, vol. 8, pp. 867–871, Nov. 2009.

[37] C. Mu, J.-P. Zhang, and D. Xu, "Au nanoparticle arrays with tunable particle gaps by template-assisted electroless deposition for high performance surface-enhanced Raman scattering," *Nanotechnology*, vol. 21, p. 015604, Jan. 2010.

[38] F. J. Beck, A. Polman, and K. R. Catchpole, "Tunable light trapping for solar cells using localized surface plasmons," *Journal of Applied Physics*, vol. 105, p. 114310, June 2009.

[39] V. Yannopapas, "Circular dichroism in planar nonchiral plasmonic metamaterials," *Optics Letters*, vol. 34, pp. 632–634, Mar. 2009.

[40] C. Lumdee, S. Toroghi, and P. G. Kik, "Post-fabrication Voltage Controlled Resonance Tuning of Nanoscale Plasmonic Antennas," *ACS Nano*, vol. 6, pp. 6301–6307, July 2012.

[41] R. J. Walters, R. V. A. van Loon, I. Brunets, J. Schmitz, and A. Polman, "A silicon-based electrical source of surface plasmon polaritons," *Nature Materials*, vol. 9, pp. 21–25, Jan. 2010.

[42] S. P. Burgos, S. Yokogawa, and H. A. Atwater, "Color Imaging via Nearest Neighbor Hole Coupling in Plasmonic Color Filters Integrated onto a Complementary Metal-Oxide Semiconductor Image Sensor," *ACS Nano*, vol. 7, pp. 10038–10047, Nov. 2013.

[43] J. Mihaljevic, S. Slama, R. Röpke, and A. J. Meixner, "Geometric tailoring of plasmonic nanotips for atom traps," *Physical Review A*, vol. 90, July 2014.

[44] N. C. Lindquist, J. Jose, S. Cherukulappurath, X. Chen, T. W. Johnson, and S.-H. Oh, "Tip-based plasmonics: squeezing light with metallic nanoprobes: Tip-based plasmonics: squeezing light with metallic nanoprobes," *Laser & Photonics Reviews*, vol. 7, pp. 453–477, July 2013.

[45] P. B. Johnson and R. W. Christy, "Optical Constants of the Noble Metals," *Physical Review B*, vol. 6, pp. 4370–4379, Dec. 1972.

[46] I. R. Hooper and W. L. Barnes, "The Basics of Plasmonics," in *Handbook of Surface Science*, vol. 4, pp. 37–74, Elsevier, 2014.

[47] A. E. Rider, K. Ostrikov, and S. A. Furman, "Plasmas meet plasmonics: Everything old is new again," *The European Physical Journal D*, vol. 66, Sept. 2012.

[48] A. D. Rakić, A. B. Djurišić, J. M. Elazar, and M. L. Majewski, "Optical properties of metallic films for vertical-cavity optoelectronic devices," *Applied Optics*, vol. 37, p. 5271, Aug. 1998.

[49] Z. Han and S. I. Bozhevolnyi, "Waveguiding with Surface Plasmon Polaritons," in *Handbook of Surface Science*, vol. 4, pp. 137–187, Elsevier, 2014.

[50] E. Kretschmann, "Decay of non radiative surface plasmons into light on rough silver films. Comparison of experimental and theoretical results," *Optics Communications*, vol. 6, pp. 185–187, Oct. 1972.

[51] A. Otto, "Excitation of nonradiative surface plasma waves in silver by the method of frustrated total reflection," *Zeitschrift für Physik A Hadrons and nuclei*, vol. 216, pp. 398–410, Aug. 1968.

[52] A. J. Wood, B. Chen, S. Pathan, S. Bok, C. J. Mathai, K. Gangopadhyay, S. A. Grant, and S. Gangopadhyay, "Influence of silver grain size, roughness, and profile on the extraordinary fluorescence enhancement capabilities of grating coupled surface plasmon resonance," *RSC Advances*, vol. 5, no. 96, pp. 78534–78544, 2015.

[53] J. Park and B. Lee, "An Approximate Formula of the Effective Refractive Index of the Metal–Insulator–Metal Surface Plasmon Polariton Waveguide in the Infrared Region," *Japanese Journal of Applied Physics*, vol. 47, pp. 8449–8451, Nov. 2008.

[54] E. Devaux, J.-Y. Laluet, B. Stein, C. Genet, T. Ebbesen, J.-C. Weeber, and A. Dereux, "Refractive micro-optical elements for surface plasmons: from classical to gradient index optics," *Optics Express*, vol. 18, p. 20610, Sept. 2010.

[55] I. Freestone, N. Meeks, M. Sax, and C. Higgitt, "The Lycurgus Cup — A Roman nanotechnology," *Gold Bulletin*, vol. 40, pp. 270–277, Dec. 2007.

[56] M. R. Gartia, A. Hsiao, A. Pokhriyal, S. Seo, G. Kulsharova, B. T. Cunningham, T. C. Bond, and G. L. Liu, "Colorimetric Plasmon Resonance Imaging Using Nano Lycurgus Cup Arrays," *Advanced Optical Materials*, vol. 1, pp. 68–76, Jan. 2013.

[57] A. B. Evlyukhin and S. I. Bozhevolnyi, "Point-dipole approximation for surface plasmon polariton scattering: Implications and limitations," *Physical Review B*, vol. 71, Apr. 2005.

[58] X. Fan, W. Zheng, and D. J. Singh, "Light scattering and surface plasmons on small spherical particles," *Light: Science & Applications*, vol. 3, pp. e179–e179, June 2014. arXiv: 1407.2345.

[59] B. M. Ross, S. Tasoglu, and L. P. Lee, "Plasmon resonance differences between the near- and far-field and implications for molecular detection," (San Diego, CA), p. 739422, Aug. 2009.

[60] X. Wei and P. Mulvaney, "Optical Properties of Strongly Coupled Plasmonic Nanoparticle Clusters," in *Handbook of Surface Science*, vol. 4, pp. 75–108, Elsevier, 2014.

[61] H. Oka and Y. Ohdaira, "Simple model of saturable localised surface plasmon," *Scientific Reports*, vol. 8, Dec. 2018.

[62] K. M. McPeak, S. V. Jayanti, S. J. P. Kress, S. Meyer, S. Iotti, A. Rossinelli, and D. J. Norris, "Plasmonic Films Can Easily Be Better: Rules and Recipes," *ACS Photonics*, vol. 2, pp. 326–333, Mar. 2015.

[63] S. Lal, S. Link, and N. J. Halas, "Nano-optics from sensing to waveguiding," *Nature Photonics*, vol. 1, pp. 641–648, Nov. 2007.

[64] E. Simsek, "Effective Refractive Index Approximation and Surface Plasmon Resonance Modes of Metal Nanoparticle Chains and Arrays," *PIERS Online*, vol. 5, no. 7, pp. 629–632, 2009.

[65] A. Abass, S. R.-K. Rodriguez, J. Gómez Rivas, and B. Maes, "Tailoring Dispersion and Eigenfield Profiles of Plasmonic Surface Lattice Resonances," *ACS Photonics*, vol. 1, pp. 61–68, Jan. 2014.

[66] Z. Yong, D. Lei, C. Lam, and Y. Wang, "Ultrahigh refractive index sensing performance of plasmonic quadrupole resonances in gold nanoparticles," *Nanoscale Research Letters*, vol. 9, no. 1, p. 187, 2014.

[67] L. Novotny and B. Hecht, *Principles of nano-optics*. Cambridge university press, 2012.

[68] E. Cubukcu and F. Capasso, "Optical nanorod antennas as dispersive one-dimensional Fabry–Pérot resonators for surface plasmons," *Applied Physics Letters*, vol. 95, p. 201101, Nov. 2009.

[69] W. Kim, N. Kim, J. W. Park, and Z. H. Kim, "Nanostar probes for tip-enhanced spectroscopy," *Nanoscale*, vol. 8, pp. 987–994, Dec. 2015.

[70] P. J. Schuck, D. P. Fromm, A. Sundaramurthy, G. S. Kino, and W. E. Moerner, "Improving the Mismatch between Light and Nanoscale Objects with Gold Bowtie Nanoantennas," *Physical Review Letters*, vol. 94, p. 017402, Jan. 2005.

[71] H. Mertens, J. S. Biteen, H. A. Atwater, and A. Polman, "Polarization-Selective Plasmon-Enhanced Silicon Quantum-Dot Luminescence," *Nano Letters*, vol. 6, pp. 2622–2625, Nov. 2006.

[72] E. Cubukcu, E. A. Kort, K. B. Crozier, and F. Capasso, "Plasmonic laser antenna," *Applied Physics Letters*, vol. 89, p. 093120, Aug. 2006.

[73] P. Bharadwaj, B. Deutsch, and L. Novotny, "Optical Antennas," *Advances in Optics and Photonics*, vol. 1, p. 438, Nov. 2009.

[74] L. Novotny, "A New Technology That Can Enhance Light-Matter Interactions," p. 7, 2009.

[75] L. Novotny, "Effective Wavelength Scaling for Optical Antennas," *Physical Review Letters*, vol. 98, June 2007.

[76] C. V. Raman and K. S. Krishnan, "A New Type of Secondary Radiation," *Nature*, vol. 121, pp. 501–502, Mar. 1928.

[77] G. Herzberg and B. L. Crawford, "Infrared and Raman Spectra of Polyatomic Molecules.," *The Journal of Physical Chemistry*, vol. 50, pp. 288–288, Mar. 1946.

[78] I. Vlasov, V. Ralchenko, E. Obraztsova, A. Smolin, and V. Konov, "Analysis of intrinsic stress distribution in grains of high quality CVD diamond film by micro-Raman spectroscopy," *Thin Solid Films*, vol. 308-309, pp. 168–172, Oct. 1997.

[79] N. Piluso, M. Camarda, R. Anzalone, A. Severino, A. La Magna, G. D'Arrigo, and F. La Via, "Raman Stress Characterization of Hetero-Epitaxial 3c-SiC Free Standing Structures," *Materials Science Forum*, vol. 679-680, pp. 141–144, Mar. 2011.

[80] K. Wasmer, T. Wermelinger, A. Bidiville, R. Spolenak, and J. Michler, "In situ compression tests on micron-sized silicon pillars by Raman microscopy—Stress measurements and deformation analysis," *Journal of Materials Research*, vol. 23, pp. 3040–3047, Nov. 2008.

[81] Q. Li, W. Qiu, H. Tan, J. Guo, and Y. Kang, "Micro-Raman spectroscopy stress measurement method for porous silicon film," *Optics and Lasers in Engineering*, vol. 48, pp. 1119–1125, Nov. 2010.

[82] A. C. Albrecht, "On the Theory of Raman Intensities," *The Journal of Chemical Physics*, vol. 34, pp. 1476–1484, May 1961.

[83] J. Cosas Fernandes, V. Mareau, and L. Gonon, "Co-localized AFM-Raman: A powerful tool to optimize the sol-gel chemistry of hybrid polymer membranes for fuel cell," *Polymer*, vol. 137, pp. 231–244, Feb. 2018.

[84] M. Fleischmann, P. Hendra, and A. McQuillan, "Raman spectra of pyridine adsorbed at a silver electrode," *Chemical Physics Letters*, vol. 26, pp. 163–166, May 1974.

[85] C. Otto, T. J. J. van den Tweel, F. F. M. de Mul, and J. Greve, "Surface-enhanced Raman spectroscopy of DNA bases," *Journal of Raman Spectroscopy*, vol. 17, pp. 289–298, June 1986.

[86] E. Prodan, "A Hybridization Model for the Plasmon Response of Complex Nanostructures," *Science*, vol. 302, pp. 419–422, Oct. 2003.

[87] Y. Zhang, Y.-R. Zhen, O. Neumann, J. K. Day, P. Nordlander, and N. J. Halas, "Coherent anti-Stokes Raman scattering with single-molecule sensitivity using a plasmonic Fano resonance," *Nature Communications*, vol. 5, Dec. 2014.

[88] S. Abdali, C. Johannessen, J. Nygaard, and T. Nørbygaard, "Resonance surface enhanced Raman optical activity of myoglobin as a result of optimized resonance surface enhanced Raman scattering conditions," *Journal of Physics: Condensed Matter*, vol. 19, p. 285205, July 2007.

[89] S. Nie, "Probing Single Molecules and Single Nanoparticles by Surface-Enhanced Raman Scattering," *Science*, vol. 275, pp. 1102–1106, Feb. 1997.

[90] K. Kneipp, Y. Wang, H. Kneipp, L. T. Perelman, I. Itzkan, R. R. Dasari, and M. S. Feld, "Single Molecule Detection Using Surface-Enhanced Raman Scattering (SERS)," *Physical Review Letters*, vol. 78, pp. 1667–1670, Mar. 1997.

[91] M. Moskovits, "Surface-enhanced Raman spectroscopy: a brief retrospective," *Journal of Raman Spectroscopy*, vol. 36, pp. 485–496, June 2005.

[92] J.-F. Li, Y.-J. Zhang, S.-Y. Ding, R. Panneerselvam, and Z.-Q. Tian, "Core–Shell Nanoparticle-Enhanced Raman Spectroscopy," *Chemical Reviews*, vol. 117, pp. 5002–5069, Apr. 2017.

[93] E. Le Ru and P. Etchegoin, "Rigorous justification of the $|E|4$ enhancement factor in Surface Enhanced Raman Spectroscopy," *Chemical Physics Letters*, vol. 423, pp. 63–66, May 2006.

[94] D. J. Masiello and G. C. Schatz, "Many-body theory of surface-enhanced Raman scattering," *Physical Review A*, vol. 78, Oct. 2008.

[95] S. Efrima and H. Metiu, "Classical theory of light scattering by an adsorbed molecule. I. Theory," *The Journal of Chemical Physics*, vol. 70, pp. 1602–1613, Feb. 1979.

[96] M. S. Anderson, "Locally enhanced Raman spectroscopy with an atomic force microscope," *Applied Physics Letters*, vol. 76, pp. 3130–3132, May 2000.

[97] N. Hayazawa, Y. Inouye, Z. Sekkat, and S. Kawata, "Metallized tip amplification of near-field Raman scattering," *Optics Communications*, vol. 183, pp. 333–336, Sept. 2000.

[98] R. M. Stöckle, Y. D. Suh, V. Deckert, and R. Zenobi, "Nanoscale chemical analysis by tip-enhanced Raman spectroscopy," *Chemical Physics Letters*, vol. 318, pp. 131–136, Feb. 2000.

[99] B. Pettinger, B. Ren, G. Picardi, R. Schuster, and G. Ertl, "Nanoscale Probing of Adsorbed Species by Tip-Enhanced Raman Spectroscopy," *Physical Review Letters*, vol. 92, Mar. 2004.

[100] W. Su, N. Kumar, A. Krayev, and M. Chaigneau, "In situ topographical chemical and electrical imaging of carboxyl graphene oxide at the nanoscale," *Nature Communications*, vol. 9, Dec. 2018.

[101] Y. Okuno, O. Lancry, A. Tempez, C. Cairone, M. Bosi, F. Fabbri, and M. Chaigneau, "Probing the Nanoscale Light Emission Properties of CVD-grown MoS2 Monolayer by Tip-enhanced Photoluminescence," *Nanoscale*, p. 14055, 2018.

[102] N. Kumar, A. Zoladek-Lemanczyk, A. A. Y. Guilbert, W. Su, S. M. Tuladhar, T. Kirchartz, B. C. Schroeder, I. McCulloch, J. Nelson, D. Roy, and F. A. Castro, "Simultaneous topographical, electrical and optical microscopy of optoelectronic devices at the nanoscale," *Nanoscale*, vol. 9, no. 8, pp. 2723–2731, 2017.

[103] K. K. H. Smithe, A. V. Krayev, C. S. Bailey, H. R. Lee, E. Yalon, O. B. Aslan, M. Munoz Rojo, S. Krylyuk, P. Taheri, A. V. Davydov, T. F. Heinz, and E. Pop, "Nanoscale Heterogeneities in Monolayer MoSe $_2$ Revealed by Correlated Scanning Probe Microscopy and Tip-Enhanced Raman Spectroscopy," *ACS Applied Nano Materials*, vol. 1, pp. 572–579, Feb. 2018.

[104] A. G. Milekhin, M. Rahaman, E. E. Rodyakina, A. V. Latyshev, V. M. Dzhagan, and D. R. T. Zahn, "Giant gap-plasmon tip-enhanced Raman scattering of MoS $_2$ monolayers on Au nanocluster arrays," *Nanoscale*, vol. 10, no. 6, pp. 2755–2763, 2018.

[105] H. K. Wickramasinghe, M. Chaigneau, R. Yasukuni, G. Picardi, and R. Ossikovski, "Billion-Fold Increase in Tip-Enhanced Raman Signal," *ACS Nano*, vol. 8, pp. 3421–3426, Apr. 2014.

[106] B. Pettinger, P. Schambach, C. J. Villagómez, and N. Scott, "Tip-Enhanced Raman Spectroscopy: Near-Fields Acting on a Few Molecules," *Annual Review of Physical Chemistry*, vol. 63, pp. 379–399, May 2012.

[107] N. Kumar, A. Rae, and D. Roy, "Accurate measurement of enhancement factor in tip-enhanced Raman spectroscopy through elimination of far-field artefacts," *Applied Physics Letters*, vol. 104, p. 123106, Mar. 2014.

[108] S. Kharintsev, A. Alekseev, and J. Loos, "Etchant-based design of gold tip apexes for plasmon-enhanced Raman spectromicroscopy," *Spectrochimica Acta Part A: Molecular and Biomolecular Spectroscopy*, vol. 171, pp. 139–143, Jan. 2017.

[109] M. Lopes, "Etude de nanoantennes optiques : application aux diffusions Raman exaltées de surface et par pointe," p. 171.

[110] B. Ren, G. Picardi, and B. Pettinger, "Preparation of gold tips suitable for tip-enhanced Raman spectroscopy and light emission by electrochemical etching," *Review of Scientific Instruments*, vol. 75, pp. 837–841, Apr. 2004.

[111] P. R. Brejna and P. R. Griffiths, "Electroless Deposition of Silver onto Silicon as a Method of Preparation of Reproducible Surface-Enhanced Raman Spectroscopy Substrates and Tip-Enhanced Raman Spectroscopy Tips," *Applied Spectroscopy*, vol. 64, pp. 493–499, May 2010.

[112] A. Sanders, L. Zhang, R. W. Bowman, L. O. Herrmann, and J. J. Baumberg, "Facile Fabrication of Spherical Nanoparticle-Tipped AFM Probes for Plasmonic Applications," *Particle & Particle Systems Characterization*, vol. 32, pp. 182–187, Feb. 2015.

[113] A. Taguchi, "Plasmonic tip for nano Raman microcopy: structures, materials, and enhancement," *Optical Review*, vol. 24, pp. 462–469, June 2017.

[114] Y. You, N. A. Purnawirman, H. Hu, J. Kasim, H. Yang, C. Du, T. Yu, and Z. Shen, "Tip-enhanced Raman spectroscopy using single-crystalline Ag nanowire as tip," *Journal of Raman Spectroscopy*, vol. 41, pp. 1156–1162, Oct. 2010.

[115] P. Brodard, M. Bechelany, L. Philippe, and J. Michler, "Synthesis and attachment of silver nanowires on atomic force microscopy cantilevers for tip-enhanced Raman spectroscopy: Synthesis and attachment of Ag nanowires on AFM cantilevers for TERS," *Journal of Raman Spectroscopy*, vol. 43, pp. 745–749, June 2012.

[116] S. H. Christiansen, M. Becker, S. Fahlbusch, J. Michler, V. Sivakov, G. Andrä, and R. Geiger, "Signal enhancement in nano-Raman spectroscopy by gold caps on silicon nanowires obtained by vapour–liquid–solid growth," *Nanotechnology*, vol. 18, p. 035503, Jan. 2007.

[117] M. Becker, V. Sivakov, U. Gösele, T. Stelzner, G. Andrä, H. J. Reich, S. Hoffmann, J. Michler, and S. H. Christiansen, "Nanowires Enabling Signal-Enhanced Nanoscale Raman Spectroscopy," *Small*, vol. 4, pp. 398–404, Mar. 2008.

[118] T. Kim, K.-S. Jeon, K. Heo, H. M. Kim, J. Park, Y. D. Suh, and S. Hong, "Multilayered nano-prism vertex tips for tip-enhanced Raman spectroscopy and imaging," *The Analyst*, vol. 138, no. 19, p. 5588, 2013.

[119] T. H. Taminiau, R. J. Moerland, F. B. Segerink, L. Kuipers, and N. F. van Hulst, "Lambda/4 Resonance of an Optical Monopole Antenna Probed by Single Molecule Fluorescence," *Nano Letters*, vol. 7, pp. 28–33, Jan. 2007.

[120] M. Mivelle, T. S. van Zanten, L. Neumann, N. F. van Hulst, and M. F. Garcia-Parajo, "Ultrabright Bowtie Nanoaperture Antenna Probes Studied by Single Molecule Fluorescence," *Nano Letters*, vol. 12, pp. 5972–5978, Nov. 2012.

[121] Leinhos, Rudow, Stopka, Vollkopf, and Oesterschulze, "Coaxial probes for scanning near-field microscopy," *Journal of Microscopy*, vol. 194, pp. 349–352, May 1999.

[122] T. W. Johnson, Z. J. Lapin, R. Beams, N. C. Lindquist, S. G. Rodrigo, L. Novotny, and S.-H. Oh, "Highly Reproducible Near-Field Optical Imaging with Sub-20-nm Resolution Based on Template-Stripped Gold Pyramids," *ACS Nano*, vol. 6, pp. 9168–9174, Oct. 2012.

[123] N. C. Lindquist, T. W. Johnson, P. Nagpal, D. J. Norris, and S.-H. Oh, "Plasmonic nanofocusing with a metallic pyramid and an integrated C-shaped aperture," *Scientific Reports*, vol. 3, Dec. 2013.

[124] A. Rasmussen, C. Budich, and V. Deckert, "Tip-enhanced Raman scattering of a DNA binding compound," (San Jose, CA), p. 60930Z, Feb. 2006.

[125] B.-S. Yeo, W. Zhang, C. Vannier, and R. Zenobi, "Enhancement of Raman Signals with Silver-Coated Tips," *Applied Spectroscopy*, vol. 60, pp. 1142–1147, Oct. 2006.

[126] V. Poborchii, T. Tada, T. Kanayama, and P. Geshev, "Optimization of tip material and shape for near-UV TERS in Si structures," *Journal of Raman Spectroscopy*, vol. 40, pp. 1377–1385, Oct. 2009.

[127] E. Lipiec, A. Japaridze, J. Szczerbiński, G. Dietler, and R. Zenobi, "Preparation of Well-Defined DNA Samples for Reproducible Nanospectroscopic Measurements," *Small*, vol. 12, pp. 4821–4829, Sept. 2016.

[128] K.-D. Park, Y. H. Kim, J.-H. Park, J. S. Park, H. S. Lee, S.-Y. Yim, Y. H. Lee, and M. S. Jeong, "Ultraviolet tip-enhanced nanoscale Raman imaging: Ultraviolet tip-enhanced nanoscale Raman imaging," *Journal of Raman Spectroscopy*, vol. 43, pp. 1931–1934, Dec. 2012.

[129] Z. Yang, Q. Li, Y. Fang, and M. Sun, "Deep ultraviolet tip-enhanced Raman scattering," *Chemical Communications*, vol. 47, no. 32, p. 9131, 2011.

[130] L. Opilik, U. Dogan, J. Szczerbiński, and R. Zenobi, "Degradation of silver near-field optical probes and its electrochemical reversal," *Applied Physics Letters*, vol. 107, p. 091109, Aug. 2015.

[131] C. A. Barrios, A. V. Malkovskiy, R. D. Hartschuh, A. M. Kisliuk, A. P. Sokolov, and M. D. Foster, "Extending lifetime of plasmonic silver structures designed for high-resolution chemical imaging or chemical and biological sensing," (Orlando, FL), p. 69540C, Apr. 2008.

[132] S. S. Kharintsev, A. I. Noskov, G. G. Hoffmann, and J. Loos, "Near-field optical taper antennas fabricated with a highly replicable ac electrochemical etching method," *Nanotechnology*, vol. 22, p. 025202, Jan. 2011.

[133] S. S. Kharintsev, G. G. Hoffmann, A. I. Fishman, and M. K. Salakhov, "Plasmonic optical antenna design for performing tip-enhanced Raman spectroscopy and microscopy," *Journal of Physics D: Applied Physics*, vol. 46, p. 145501, Apr. 2013.

[134] S. Berweger, J. M. Atkin, R. L. Olmon, and M. B. Raschke, "Light on the Tip of a Needle: Plasmonic Nanofocusing for Spectroscopy on the Nanoscale," *The Journal of Physical Chemistry Letters*, vol. 3, pp. 945–952, Apr. 2012.

[135] R.-H. Jiang, C. Chen, D.-Z. Lin, H.-C. Chou, J.-Y. Chu, and T.-J. Yen, "Near-Field Plasmonic Probe with Super Resolution and High Throughput and Signal-to-Noise Ratio," *Nano Letters*, vol. 18, pp. 881–885, Feb. 2018.

[136] C. Ropers, C. C. Neacsu, T. Elsaesser, M. Albrecht, M. B. Raschke, and C. Lienau, "Grating-Coupling of Surface Plasmons onto Metallic Tips: A Nanoconfined Light Source," *Nano Letters*, vol. 7, pp. 2784–2788, Sept. 2007.

[137] B. S. Archanjo, T. L. Vasconcelos, B. S. Oliveira, C. Song, F. I. Allen, C. A. Achete, and P. Ercius, "Plasmon 3d Electron Tomography and Local Electric-field Enhancement of Engineered Plasmonic Nano-antennas," *ACS Photonics*, June 2018.

[138] T. L. Vasconcelos, B. S. Archanjo, B. Fragneaud, B. S. Oliveira, J. Riikonen, C. Li, D. S. Ribeiro, C. Rabelo, W. N. Rodrigues, A. Jorio, C. A. Achete, and

L. G. Cançado, "Tuning Localized Surface Plasmon Resonance in Scanning Near-Field Optical Microscopy Probes," *ACS Nano*, vol. 9, pp. 6297–6304, June 2015.

[139] T. J. Dill, M. J. Rozin, S. Palani, and A. R. Tao, "Colloidal Nanoantennas for Hyperspectral Chemical Mapping," *ACS Nano*, vol. 10, pp. 7523–7531, Aug. 2016.

[140] T. Umakoshi, T.-a. Yano, Y. Saito, and P. Verma, "Fabrication of Near-Field Plasmonic Tip by Photoreduction for Strong Enhancement in Tip-Enhanced Raman Spectroscopy," *Applied Physics Express*, vol. 5, p. 052001, Apr. 2012.

[141] A. Taguchi, J. Yu, P. Verma, and S. Kawata, "Optical antennas with multiple plasmonic nanoparticles for tip-enhanced Raman microscopy," *Nanoscale*, vol. 7, no. 41, pp. 17424–17433, 2015.

[142] I. Maouli, A. Taguchi, Y. Saito, S. Kawata, and P. Verma, "Optical antennas for tunable enhancement in tip-enhanced Raman spectroscopy imaging," *Applied Physics Express*, vol. 8, p. 032401, Mar. 2015.

[143] H. Du, "Mie-scattering calculation," *Applied Optics*, vol. 43, no. 9, pp. 1951–1956, 2004.

[144] F. Papoff and B. Hourahine, "Geometrical Mie theory for resonances in nanoparticles of any shape," *Optics Express*, vol. 19, p. 21432, Oct. 2011.

[145] P. I. Geshev, U. Fischer, and H. Fuchs, "Calculation of tip enhanced Raman scattering caused by nanoparticle plasmons acting on a molecule placed near a metallic film," *Physical Review B*, vol. 81, Mar. 2010.

[146] O. J. F. Martin and M. Paulus, "Influence of metal roughness on the near-field generated by an aperture/apertureless probe," *Journal of Microscopy*, vol. 205, pp. 147–152, Feb. 2002.

[147] Z. Yang, J. Aizpurua, and H. Xu, "Electromagnetic field enhancement in TERS configurations," *Journal of Raman Spectroscopy*, vol. 40, pp. 1343–1348, Oct. 2009.

[148] N. Kazemi-Zanjani, S. Vedraine, and F. Lagugné-Labarthet, "Localized enhancement of electric field in tip-enhanced Raman spectroscopy using radially and linearly polarized light," *Optics Express*, vol. 21, p. 25271, Oct. 2013.

[149] S. D'Agostino, F. Della Sala, and L. C. Andreani, "Dipole Decay Rates Engineering via Silver Nanocones," *Plasmonics*, vol. 8, pp. 1079–1086, June 2013.

[150] C. Huber, A. Trügler, U. Hohenester, Y. Prior, and W. Kautek, "Optical near-field excitation at commercial scanning probe microscopy tips: a theoretical and experimental investigation," *Phys. Chem. Chem. Phys.*, vol. 16, no. 6, pp. 2289–2296, 2014.

[151] P. I. Geshev, S. Klein, T. Witting, K. Dickmann, and M. Hietschold, "Calculation of the electric-field enhancement at nanoparticles of arbitrary shape in close proximity to a metallic surface," *Physical Review B*, vol. 70, Aug. 2004.

[152] F. Demming, J. Jersch, K. Dickmann, and P. I. Geshev, "Calculation of the field enhancement on laser-illuminated scanning probe tips by the boundary element method," *Applied Physics B*, vol. 66, pp. 593–598, May 1998.

[153] R. Esteban, R. Vogelgesang, and K. Kern, "Full simulations of the apertureless scanning near field optical microscopy signal: achievable resolution and contrast," *Optics Express*, vol. 17, p. 2518, Feb. 2009.

[154] L. Novotny, R. X. Bian, and X. S. Xie, "Theory of Nanometric Optical Tweezers," *Physical Review Letters*, vol. 79, pp. 645–648, July 1997.

[155] A. Haidary, Y. Miyahara, and P. Grütter, "Antenna and Plasmonic Properties of Scanning Probe Tips at Optical and Terahertz Regimes," p. 6, 2014.

[156] J. Cui, L. Yang, and Y. Wang, "Simulation study of near-field enhancement on a laser-irradiated AFM metal probe," *Laser Physics*, vol. 23, p. 076003, July 2013.

[157] e. I. L. a. A. E. l. c. Alex, "Fresnel Equations," p. 7.

[158] M. I. Mishchenko, "The electromagnetic optical theorem revisited," *Journal of Quantitative Spectroscopy and Radiative Transfer*, vol. 101, pp. 404–410, Oct. 2006.

[159] J. Dorfmüller, R. Vogelgesang, R. T. Weitz, C. Rockstuhl, C. Etrich, T. Pertsch, F. Lederer, and K. Kern, "Fabry-Pérot Resonances in One-Dimensional Plasmonic Nanostructures," *Nano Letters*, vol. 9, pp. 2372–2377, June 2009.

[160] V. J. Sorger, R. F. Oulton, J. Yao, G. Bartal, and X. Zhang, "Plasmonic Fabry-Pérot Nanocavity," *Nano Letters*, vol. 9, pp. 3489–3493, Oct. 2009.

[161] Y. Sonnefraud, A. Leen Koh, D. McComb, and S. Maier, "Nanoplasmonics: Engineering and observation of localized plasmon modes," *Laser & Photonics Reviews*, vol. 6, pp. 277–295, May 2012.

[162] M. Rycenga, C. M. Cobley, J. Zeng, W. Li, C. H. Moran, Q. Zhang, D. Qin, and Y. Xia, "Controlling the Synthesis and Assembly of Silver Nanostructures for Plasmonic Applications," *Chemical Reviews*, vol. 111, pp. 3669–3712, June 2011.

[163] T. Huang, W. Cao, H. E. Elsayed-Ali, and X.-H. N. Xu, "High-throughput ultrasensitive characterization of chemical, structural and plasmonic properties of EBL-fabricated single silver nanoparticles," *Nanoscale*, vol. 4, no. 2, pp. 380–385, 2012.

[164] S. Sun, M. Gao, G. Lei, H. Zou, J. Ma, and C. Huang, "Visually monitoring the etching process of gold nanoparticles by KI/I2 at single-nanoparticle level using scattered-light dark-field microscopic imaging," *Nano Research*, vol. 9, pp. 1125–1134, Apr. 2016.

[165] T. Itoh, Y. S. Yamamoto, T. Suzuki, Y. Kitahama, and Y. Ozaki, "Darkfield microspectroscopy of nanostructures on silver tip-enhanced Raman scattering probes," *Applied Physics Letters*, vol. 108, p. 021604, Jan. 2016.

[166] H. Liu, C. Dong, X. Huang, and J. Ren, "Spatially Resolved Scattering Correlation Spectroscopy Using a Total Internal Reflection Configuration," *Analytical Chemistry*, vol. 84, pp. 3561–3567, Apr. 2012.

[167] I. Ament, J. Prasad, A. Henkel, S. Schmachtel, and C. Sönnichsen, "Single Unlabeled Protein Detection on Individual Plasmonic Nanoparticles," *Nano Letters*, vol. 12, pp. 1092–1095, Feb. 2012.

[168] B. Hoffmann, S. Vassant, X.-W. Chen, S. Götzinger, V. Sandoghdar, and S. Christiansen, "Fabrication and characterization of plasmonic nanocone antennas for strong spontaneous emission enhancement," *Nanotechnology*, vol. 26, p. 404001, Oct. 2015.

[169] P. von Olshausen and A. Rohrbach, "Coherent total internal reflection dark-field microscopy: label-free imaging beyond the diffraction limit," *Optics Letters*, vol. 38, p. 4066, Oct. 2013.

[170] D. Talaga, M. Comesaña-Hermo, S. Ravaine, R. A. L. Vallée, and S. Bonhommeau, "Colocalized dark-field scattering, atomic force and surface-enhanced Raman scattering microscopic imaging of single gold nanoparticles," *Journal of Optics*, vol. 17, p. 114006, Nov. 2015.

[171] J.-H. Yang and K.-P. Chen, "Evanescent Wave-Assisted Symmetry Breaking of Gold Dipolar Nanoantennas," *Scientific Reports*, vol. 6, Oct. 2016.

[172] C. Langhammer, M. Schwind, B. Kasemo, and I. Zorić, "Localized Surface Plasmon Resonances in Aluminum Nanodisks," *Nano Letters*, vol. 8, pp. 1461–1471, May 2008.

[173] T. Wu, W. Zhang, R. Wang, and X. Zhang, "A giant chiroptical effect caused by the electric quadrupole," *Nanoscale*, vol. 9, no. 16, pp. 5110–5118, 2017.

[174] K. Guo, Y.-L. Zhang, C. Qian, and K.-H. Fung, "Electric dipole-quadrupole hybridization induced enhancement of second-harmonic generation in T-shaped plasmonic heterodimers," *Optics Express*, vol. 26, p. 11984, Apr. 2018.

[175] L. Ma, S. Sun, T. Zhang, R. Li, Q. Du, J. Zhang, and M. Li, "Highly-symmetrical plasmonic nanoantenna for fluorescence enhancement and polarization preservation of arbitrarily oriented fluorophore," *Optical Materials Express*, vol. 8, p. 3770, Dec. 2018.

[176] J. Marae-Djouda, R. Caputo, N. Mahi, G. Lévêque, A. Akjouj, P.-M. Adam, and T. Maurer, "Angular plasmon response of gold nanoparticles arrays: approaching the Rayleigh limit," *Nanophotonics*, vol. 6, pp. 279–288, Jan. 2017.

[177] J. M. Kontio, J. Simonen, J. Tommila, and M. Pessa, "Arrays of metallic nanocones fabricated by UV-nanoimprint lithography," *Microelectronic Engineering*, vol. 87, pp. 1711–1715, Nov. 2010.

[178] O. Saison-Francioso, G. Lévêque, R. Boukherroub, S. Szunerits, and A. Akjouj, "Dependence between the Refractive-Index Sensitivity of Metallic Nanoparticles and the Spectral Position of Their Localized Surface Plasmon Band: A Numerical and Analytical Study," *The Journal of Physical Chemistry C*, vol. 119, pp. 28551–28559, Dec. 2015.

[179] M. I. Stockman, "Nanofocusing of Optical Energy in Tapered Plasmonic Waveguides," *Physical Review Letters*, vol. 93, Sept. 2004.

[180] A. Dmitriev, C. Hägglund, S. Chen, H. Fredriksson, T. Pakizeh, M. Käll, and D. S. Sutherland, "Enhanced Nanoplasmonic Optical Sensors with Reduced Substrate Effect," *Nano Letters*, vol. 8, pp. 3893–3898, Nov. 2008.

[181] L. Xia, M. Chen, X. Zhao, Z. Zhang, J. Xia, H. Xu, and M. Sun, "Visualized method of chemical enhancement mechanism on SERS and TERS," *Journal of Raman Spectroscopy*, vol. 45, pp. 533–540, July 2014.

[182] P. West, S. Ishii, G. Naik, N. Emani, V. Shalaev, and A. Boltasseva, "Searching for better plasmonic materials," *Laser & Photonics Reviews*, vol. 4, pp. 795–808, Nov. 2010.

[183] C. Prasad, S. K. Shrivastav, and L. K. Mishra, "A Theoretical Evaluation of Quality Factor of Surface Plasmon-Polaritons (QSPP) As a Function of Wavelength (Nm) and Comparative Studies of Metals for Better Plasmonic Materials," *Journal of Chemical, Biological and Physical Sciences*, vol. 6, pp. 546–555, Apr. 2016.

[184] G. M. Whitesides, "Self-Assembly at All Scales," *Science*, vol. 295, pp. 2418–2421, Mar. 2002.

[185] T. Ito and S. Okazaki, "Pushing the limits of lithography," *Nature*, vol. 406, pp. 1027–1031, Aug. 2000.

[186] C. Vieu, F. Carcenac, A. Pépin, Y. Chen, M. Mejias, A. Lebib, L. Manin-Ferlazzo, L. Couraud, and H. Launois, "Electron beam lithography: resolution limits and applications," *Applied Surface Science*, vol. 164, pp. 111–117, Sept. 2000.

[187] B. Wu and A. Kumar, "Extreme ultraviolet lithography: A review," *Journal of Vacuum Science & Technology B: Microelectronics and Nanometer Structures*, vol. 25, no. 6, p. 1743, 2007.

[188] J. Goldsmith, D. T. Attwood, and J. S. Taylor, "Extreme ultraviolet lithography: Optics - the next generation," in *Conference on Lasers and Electro-Optics/International Quantum Electronics Conference and Photonic Applications Systems Technologies (2004), paper PThC2*, p. PThC2, Optical Society of America, May 2004.

[189] A. Tseng, Kuan Chen, C. Chen, and K. Ma, "Electron beam lithography in nanoscale fabrication: recent development," *IEEE Transactions on Electronics Packaging Manufacturing*, vol. 26, pp. 141–149, Apr. 2003.

[190] Y. Chen, "Nanofabrication by electron beam lithography and its applications: A review," *Microelectronic Engineering*, vol. 135, pp. 57–72, Mar. 2015.

[191] B. S. Flavel, J. G. Shapter, and J. S. Quinton, "Nanosphere lithography using thermal evaporation of gold," (Adelaide, Australia), p. 64151J, Dec. 2006.

[192] C. S. Smith, "Piezoresistance Effect in Germanium and Silicon," *Physical Review*, vol. 94, pp. 42–49, Apr. 1954.

[193] J. S. Kilby, "Miniaturized electronic circuits," June 1964.

[194] R. N. Noyce, "Semiconductor device-and-lead structure," Apr. 1961.

[195] R. P. Feynman, "There's Plenty of Room at the Bottom," p. 13, Dec. 1959.

[196] H. C. Nathanson, W. E. Newell, R. A. Wickstrom, and J. R. Davis, "The resonant gate transistor," *IEEE Transactions on Electron Devices*, vol. 14, pp. 117–133, Mar. 1967.

[197] S. C. Terry, J. H. Jerman, and J. B. Angell, "A gas chromatographic air analyzer fabricated on a silicon wafer," *IEEE Transactions on Electron Devices*, vol. 26, pp. 1880–1886, Dec. 1979.

[198] K. E. Petersen, "Silicon as a mechanical material," *Proceedings of the IEEE*, vol. 70, pp. 420–457, May 1982.

[199] T. R. Albrecht, S. Akamine, T. E. Carver, and C. F. Quate, "Microfabrication of cantilever styli for the atomic force microscope," *Journal of Vacuum Science & Technology A: Vacuum, Surfaces, and Films*, vol. 8, pp. 3386–3396, July 1990.

[200] G. T. A. Kovacs, N. I. Maluf, and K. E. Petersen, "Bulk micromachining of silicon," *Proceedings of the IEEE*, vol. 86, pp. 1536–1551, Aug. 1998.

[201] J. M. Bustillo, R. T. Howe, and R. S. Muller, "Surface micromachining for microelectromechanical systems," *Proceedings of the IEEE*, vol. 86, pp. 1552–1574, Aug. 1998.

[202] X. M. Henry Huang, C. A. Zorman, M. Mehregany, and M. L. Roukes, "Nanoelectromechanical systems: Nanodevice motion at microwave frequencies," *Nature*, vol. 421, p. 496, Jan. 2003.

[203] M. J. Madou, *Fundamentals of Microfabrication: The Science of Miniaturization, Second Edition*. CRC Press, Mar. 2002. Google-Books-ID: 9bk3gJeQKBYC.

[204] A. S. Gangnaik, Y. M. Georgiev, and J. D. Holmes, "New Generation Electron Beam Resists: A Review," *Chemistry of Materials*, vol. 29, pp. 1898–1917, Mar. 2017.

[205] W. Lu and C. M. Lieber, "Nanoelectronics from the bottom up," *Nature Materials*, vol. 6, pp. 841–850, Nov. 2007.

[206] F. D. Laermer and A. Schilp, "A method for anisotropic etching of silicon," May 1994.

[207] F. Roozeboom, F. van den Bruele, Y. Creyghton, P. Poodt, and W. M. M. Kessels, "Cyclic Etch/Passivation-Deposition as an All-Spatial Concept toward High-Rate Room Temperature Atomic Layer Etching," *ECS Journal of Solid State Science and Technology*, vol. 4, no. 6, pp. N5067–N5076, 2015.

[208] B. Pettinger, K. F. Domke, D. Zhang, G. Picardi, and R. Schuster, "Tip-enhanced Raman scattering: Influence of the tip-surface geometry on optical resonance and enhancement," *Surface Science*, vol. 603, pp. 1335–1341, June 2009.

[209] G. Picardi, M. Chaigneau, and R. Ossikovski, "High resolution probing of multi wall carbon nanotubes by Tip Enhanced Raman Spectroscopy in gap-mode," *Chemical Physics Letters*, vol. 469, pp. 161–165, Feb. 2009.

[210] L. G. Cançado, A. Hartschuh, and L. Novotny, "Tip-enhanced Raman spectroscopy of carbon nanotubes," *Journal of Raman Spectroscopy*, vol. 40, pp. 1420–1426, Oct. 2009.

[211] M. Böhmler and A. Hartschuh, "Tip-Enhanced Near-Field Optical Microscopy of Quasi-1 D Nanostructures," *ChemPhysChem*, vol. 13, pp. 927–929, Mar. 2012.

[212] Y. Okuno, Y. Saito, S. Kawata, and P. Verma, "Tip-Enhanced Raman Investigation of Extremely Localized Semiconductor-to-Metal Transition of a Carbon Nanotube," *Physical Review Letters*, vol. 111, Nov. 2013.

[213] "Front Matter," in *Raman Spectroscopy in Graphene Related Systems*, pp. I–XIV, Weinheim, Germany: Wiley-VCH Verlag GmbH & Co. KGaA, Jan. 2011.

[214] N. Hayazawa, T. Yano, H. Watanabe, Y. Inouye, and S. Kawata, "Detection of an individual single-wall carbon nanotube by tip-enhanced near-field Raman spectroscopy," *Chemical Physics Letters*, vol. 376, pp. 174–180, July 2003.

[215] K. L. A. Chan and S. G. Kazarian, "Finding a needle in a chemical haystack: tip-enhanced Raman scattering for studying carbon nanotubes mixtures," *Nanotechnology*, vol. 21, p. 445704, Nov. 2010.

[216] C. Chen, N. Hayazawa, and S. Kawata, "A 1.7 nm resolution chemical analysis of carbon nanotubes by tip-enhanced Raman imaging in the ambient," *Nature Communications*, vol. 5, Dec. 2014.

[217] N. Kazemi-Zanjani, P. Gobbo, Z. Zhu, M. S. Workentin, and F. Lagugné-Labarthet, "High-resolution Raman imaging of bundles of single-walled carbon nanotubes by tip-enhanced Raman spectroscopy," *Canadian Journal of Chemistry*, vol. 93, pp. 51–59, Jan. 2015.

[218] L. Opilik, U. Dogan, C.-Y. Li, B. Stephanidis, J.-F. Li, and R. Zenobi, "Chemical Production of Thin Protective Coatings on Optical Nanotips for Tip-Enhanced Raman Spectroscopy," *The Journal of Physical Chemistry C*, vol. 120, pp. 20828–20832, Sept. 2016.

[219] R. L. Agapov, A. P. Sokolov, and M. D. Foster, "Protecting TERS probes from degradation: extending mechanical and chemical stability: Protecting TERS probes from degradation," *Journal of Raman Spectroscopy*, vol. 44, pp. 710–716, May 2013.

[220] M. Dhanalakshmi, K. Saravanakumar, S. Lakshmi Prabavathi, M. Abinaya, and V. Muthuraj, "Fabrication of novel surface plasmon resonance induced visible light driven iridium decorated SnO2 nanorods for degradation of organic contaminants," *Journal of Alloys and Compounds*, vol. 763, pp. 512–524, Sept. 2018.

[221] J. Martin and J. Plain, "Fabrication of aluminium nanostructures for plasmonics," *Journal of Physics D: Applied Physics*, vol. 48, p. 184002, May 2015.

[222] S. M. George, "Atomic Layer Deposition: An Overview," *Chemical Reviews*, vol. 110, pp. 111–131, Jan. 2010.

[223] L. Abelmann and C. Lodder, "Oblique evaporation and surface diffusion," *Thin Solid Films*, vol. 305, pp. 1–21, Aug. 1997.

[224] M. M. Hawkeye and M. J. Brett, "Glancing angle deposition: Fabrication, properties, and applications of micro- and nanostructured thin films," *Journal of Vacuum Science & Technology A*, vol. 25, pp. 1317–1335, July 2007.

[225] R. F. Bunshah, ed., *Handbook of deposition technologies for films and coatings: science, technology, and applications*. Materials science and process technology series, Park Ridge, N.J: Noyes Publications, 2nd ed ed., 1994.

[226] M. Hatzakis, B. J. Canavello, and J. M. Shaw, "Single-Step Optical Lift-Off Process," *IBM Journal of Research and Development*, vol. 24, pp. 452–460, July 1980.

[227] W. Chen, "Fabrication of sub-10 nm structures by lift-off and by etching after electron-beam exposure of poly(methylmethacrylate) resist on solid substrates," *Journal of Vacuum Science & Technology B: Microelectronics and Nanometer Structures*, vol. 11, p. 2519, Nov. 1993.

[228] C. Geuzaine and J.-F. Remacle, "Gmsh: A 3-d finite element mesh generator with built-in pre- and post-processing facilities," *International Journal for Numerical Methods in Engineering*, vol. 79, pp. 1309 – 1331, 09 2009.

[229] F. Hecht, "New development in freefem++," *Journal of Numerical Mathematics*, vol. 20, Jan. 2012.

[230] S. Zhang, K. Bao, N. J. Halas, H. Xu, and P. Nordlander, "Substrate-Induced Fano Resonances of a Plasmonic Nanocube: A Route to Increased-Sensitivity Localized Surface Plasmon Resonance Sensors Revealed," *Nano Letters*, vol. 11, pp. 1657–1663, Apr. 2011.

[231] N. Mahi, G. Lévêque, O. Saison, J. Marae-Djouda, R. Caputo, A. Gontier, T. Maurer, P.-M. Adam, B. Bouhafs, and A. Akjouj, "In Depth Investigation of Lattice Plasmon Modes in Substrate-Supported Gratings of Metal Monomers and Dimers," *The Journal of Physical Chemistry C*, vol. 121, pp. 2388–2401, Feb. 2017.

[232] A. Movsesyan, A.-L. Baudrion, and P.-M. Adam, "Extinction measurements of metallic nanoparticles arrays as a way to explore the single nanoparticle plasmon resonances," *Optics Express*, vol. 26, p. 6439, Mar. 2018.

[233] A. Movsesyan, A.-L. Baudrion, and P.-M. Adam, "Revealing the Hidden Plasmonic Modes of a Gold Nanocylinder," *The Journal of Physical Chemistry C*, vol. 122, pp. 23651–23658, Oct. 2018.

[234] A. Bonyar, B. Wimmer, and I. Csarnovics, "Investigation of thermally generated gold nanoparticles with AFM," in *2013 IEEE 19th International Symposium for Design and Technology in Electronic Packaging (SIITME)*, (Galati, Romania), pp. 31–34, IEEE, Oct. 2013.

[235] R. R. Abbas, T. H. Richardson, A. Hobson, A. Hassan, and T. R. Abbas, "Effect of annealing on the surface plasmon resonance of dodecanethiol encapsulated gold nanoparticles Langmuir–Schafer thin films," *Colloids and Surfaces A: Physicochemical and Engineering Aspects*, vol. 444, pp. 95–103, Mar. 2014.

[236] M. Kurita, R. Arakawa, and H. Kawasaki, "Silver nanoparticle functionalized glass fibers for combined surface-enhanced Raman scattering spectroscopy (SERS)/surface-assisted laser desorption/ionization (SALDI) mass spectrometry via plasmonic/thermal hot spots," *The Analyst*, vol. 141, no. 20, pp. 5835–5841, 2016.